

PROCEEDINGS



May 10 - 11, 2012
Boca Raton, FL

FCCRAR '12

KEYNOTE SPEAKERS

Dr. Stephanie Carey
Researcher, USF, College of Engineering,
Center for Assistive, Rehabilitative and
Robotics Technologies (CARRT).
"Overview of the CARRT Center."

Dr. Paul B. Rasband
Senior Consulting Engineer, Tyco Retail
Solutions. "Smarter Dumb Nodes for Truly
Distributed Computing in Wireless Sensor
Networks."

TOPICS

Fault Tolerance and Automotive
Applications
Medical Applications
Vision, Detection and Recognition
Autonomous Robots
Education and Support Technologies
Applications
Design, Control Systems
Autonomous Vehicles

INVITED SESSION

Naval Surface Warfare Center
Panama City

SPONSORED BY



COLLEGE OF ENGINEERING
& COMPUTER SCIENCE
Florida Atlantic University



DEPARTMENT OF COMPUTER &
ELECTRICAL ENGINEERING
& COMPUTER SCIENCE
College of Engineering & Computer Science
Florida Atlantic University

Motorcycle Accident Reconstruction

Part I - Physical Models

Oren Masory

Dept. of Ocean & Mechanical Engr. Mechanical Forensics Engineering Services

Florida Atlantic University

Boca Raton, FL 33431

masoryo@fau.edu

Wade Bartlett

Mechanical Forensics Engineering Services

179 Cross Road

Rochester NH 03867

wade.bartlett@gmail.com

Bill Wright

IPTM

14939 99th Street North

West Palm Beach, FL 33412

bwright@tarorigin.com

ABSTRACT

The purpose of this paper is to evaluate different formulas which are used to estimate the motorcycle's pre-collision speed in motorcycle-to-car accidents. These formulas are based on measurable physical parameters such as motorcycle's wheelbase change and fundamental physical laws such as conservation of momentum.

The evaluation used data from crash experiments performed by the authors as well as published experimental data. The results of these evaluations indicate that the motorcycle's pre-collision speed cannot be estimated with high accuracy.

Keywords

Motorcycle Accidents, Motorcycle Accidents Reconstruction, Vehicle Accidents.

1. INTRODUCTION

According to the National Highway Traffic Safety Administration (NHTSA), in 1969, there were 2.3 million motorcycles registered in the United States. This number increased dramatically during the next 40 years and currently there are over seven million motorcycles registered in the United States. Obviously, as the number of motorcycles on the road increased, so did the accident rate. In 1969, there were 69,500 motorcycle accidents reported, in which 1,855 persons were killed. In 2004, 4,008 motorcyclists were killed in the US, an 8% increase from 2003. The death rate per 100 million vehicle miles traveled for a motorcyclist is over 35 times higher than of an automobile occupant [1]. One of the main and unequivocal reasons motorcyclists are killed in crashes is because the motorcycle itself provides virtually no protection in a crash. For example, approximately 80 percent of reported motorcycle crashes result in injury or death while a comparable figure for automobiles is about 20 percent.

The earliest and the most frequently cited testing was published by Severy in 1970 [2], which included one test at 20mph, one test at 40mph, and 5 tests at 30mph. That paper included a chart showing a linear relationship between wheelbase reduction and speed with high correlation factor of 0.975. The Severy data is not relevant to today's motorcycles: chassis design, wheels, materials, engine mounting, and front end suspension styles have changed enough that his data is not applicable.

In 1976, Professor Harry Hurt [3] of the University of Southern California conducted a study of 3,600 motorcycle

accidents in the Los Angeles area. The results of this study have become the basis for much motorcycle rider training and research. The study found that in 65 percent of the multi-vehicle cases the automobile violated the motorcycle right of way. A similar survey conducted by the Philadelphia police Department showed that such a violation is the cause in only 45 percent of all motorcycle accidents in the city of Philadelphia. Hurt's study also found that in 64 percent of single-vehicle motorcycle accidents, the operator was responsible for his accident. The majority of accidents occurred on a clear, dry day during daylight hours and typically, the motorcycle operator had less than six months riding experience and no formal training.

For many years there has been some controversy over the use of conservation of linear momentum to estimate the speed of motorcycles involved in collisions with other motor vehicles. Fricke and Riley stated in [4] that "occasionally a momentum analysis is attempted" and that this technique "rarely... works well" in accurately estimating the speed of the motorcycle. They explained that the heading and departure angles become sensitive "when the angles of approach are nearly collinear and the weight difference between the colliding vehicles is fairly large."

In 1990, Brown and Obenski write that a momentum analysis "can sometimes be used in motorcycle accidents," and give a graphical example of a momentum vector diagram of a motorcycle/automobile collision. [5]

In 1994, Obenski [6] further clarified this position by stating "Generally it is tricky to use momentum analysis in accidents between vehicles with a big weight difference," but gives the same graphical example as in his previous work. Obenski specifically cautioned against using a momentum analysis where the automobile has been moved very little after impact with the motorcycle.

In 1990, Niederer [7] wrote about techniques that may be used to reconstruct motorcycle/vehicle collisions, with the emphasis of the paper on the use of conservation of linear and angular momentum. Niederer specifically cautioned that "due to the often unfavorable mass ratio an accurate reconstruction may be impeded," but concluded that when used cautiously, the use of momentum and other available information "represents a powerful tool for motorcycle-vehicle collision reconstruction." He further concluded that reconstructionists should assess the sensitivity of the momentum analysis to changes in variation of impact configuration and post impact trajectory.

In [8] the principles of linear and angular momentum conservation were investigated. It was concluded that “Use of the sensitivity analysis will allow the reconstructionist to determine if the techniques should be applied to the given analysis or be abandoned in favor of other methods of speed analysis”.

In [9], the validity of 10 different relationships, which are to evaluate a motorcycle’s pre-collision speed strikes a passenger car, were evaluated. In contrary to expectations, the correlations between speed and crush were always stronger than any relations involving energy. When contemplating speed-from motorcycle-crush, it has been commonly assumed that that the type of wheel, cast or spiked, was an important consideration. This analysis showed that while wheel type does affect the motorcycle-to-car crush ratio, the total crush was not significantly affected.

The equations that most accurately predicted the reported impact speed of the test motorcycles were the Eubanks-form equations, with the modifications suggested by this analysis that account for the differences between the door/fender impact areas and the pillar/axle areas. The door/fender collision speeds were found to be predicted with a 95% confidence range of plus or minus 20% of the nominally calculated value, while the pillar/axle speeds were predicted within a range of plus or minus 28%.

From accident reconstruction point of view there is a limited amount of data, compared with vehicle collision data which makes accurate modeling very difficult. Collision tests involving cars moving at high enough speeds to affect the motorcycle’s trajectory are very rare. In these cases it appears to reduce the total measured crush, such that using the relationships developed here will under predict speeds, typically by 15%. The additional complication of a moving target vehicle also increases the data spread significantly. The limited car-bumper impact testing appeared to be very similar in crush characteristics to the pillar/axle impacts, but the data set was too small for significant analysis.

This paper provides analysis of test results of 13 different tests in which the motorcycles were crushed into the side of a car. The impact velocity ranged from 40-58[mph] and the impact point on the car varied. The motorcycle’s wheelbase change, width and the maximum indentation and the movement of the vehicle were recorded. In addition, data from previous 56 tests were used to check the analysis results.



Figure 1: Photos of some of the motorcycle

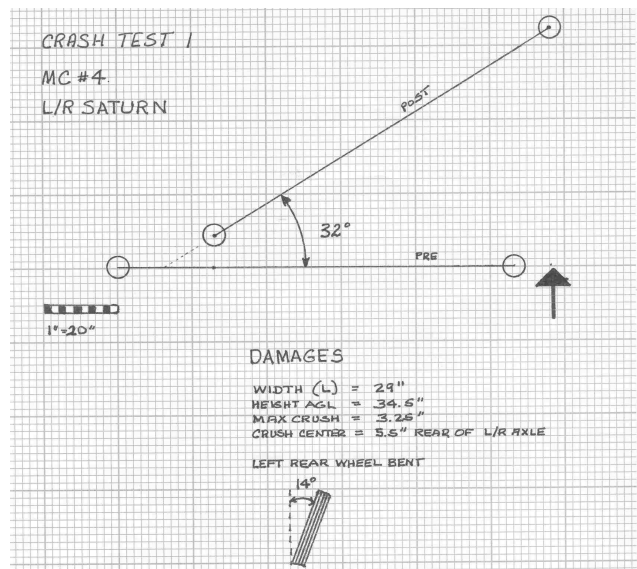


Figure 2: Data collected for each test.

1. CRASH TESTS

Sixteen motorcycles were used in the crash-tests. Figure 1 shows some photos these motorcycles. The data collected for each test is shown in Figure 2. The information on each motorcycle is given in App. I.

2. DATA ANALYSIS

2.1 Model I – Wheelbase reduction

In this model the pre-impact speed of the motorcycle is correlated with the wheelbase reduction. This model is the earliest model, proposed by Severy. The wheelbase reduction data of the previous 56 tests were graphed versus the pre-impact speed as shown in Figure 3. As shown the data is scattered and does not fit a straight line since correlation factor 0.27 which indicates a poor correlation.

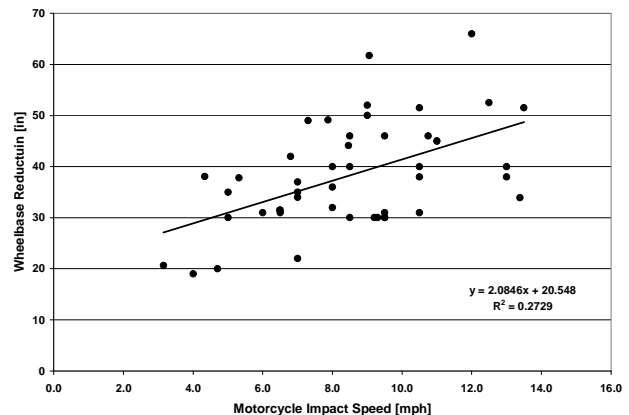


Figure 3: Results of model I.

2.2 Model II – “Total” crush

With this method the motorcycle speed is correlated with the “Total Crush” which is the sum of the motorcycle’s wheelbase reduction and the maximum indentation of the vehicle’s crush. The correlation, if exists, eliminates the need of knowing the stiffness of the motorcycle structure as well as the local stiffness of the vehicle at the impact location.

However, two different cases are being considered: 1) The motorcycle strikes vehicle at a “soft” location such as a door or a fender; and 2) A “hard” point is being struck such as a pillar or within 3 inches of an axle.

For the first case the following linear relationship with a correlation factor of 0.8 was obtained (see Figure 4):

$$V = 1.43(L + C) + 10.4 \quad (1)$$

where: V – Motorcycle impact speed (mph)

L – Motorcycle wheelbase reduction (inches)

C - Maximum indentation in the vehicle’s crush zone (inches)

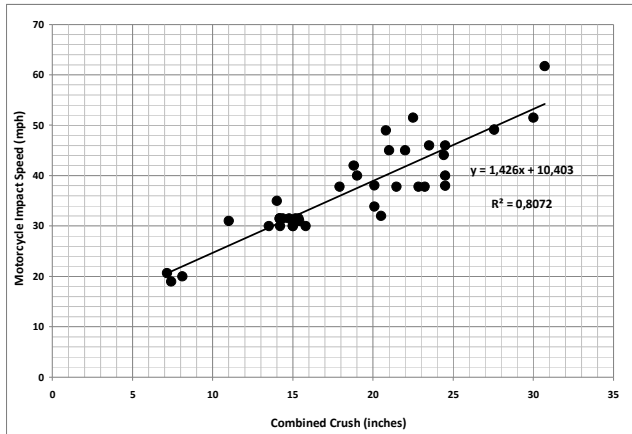


Figure 4: Motorcycle speed estimate “Soft location”

Similarly, for impacts at “hard” The following relationship with a correlation factor of 0.76 was obtained (see Figure 5):

$$V = 1.59(L + C) + 14.72 \quad (2)$$

Using the model, pre-collision speed of the motorcycle was estimated. The estimation errors are illustrated in Figure 6 through 8 for different impact location on the car. As shown, in cases where the impact location is “hard” (pillar or axle) the largest estimation errors are approximately 30% while when the impact location is “soft” the error reach 40%. In both cases, the results are not acceptable.

The data was separated according to the location of the impact: 1) Fenders and door; 2) Pillar ± 3 inches; and 3) Axle ± 3 inches. The reason behind this classification is the difference in the stiffness at these locations. The results are shown in Figure 7.

As shown in Figure 7, the only “good” correlation is when the impact location is around the axle, probably because the stiffness at this point is very high for every vehicle.

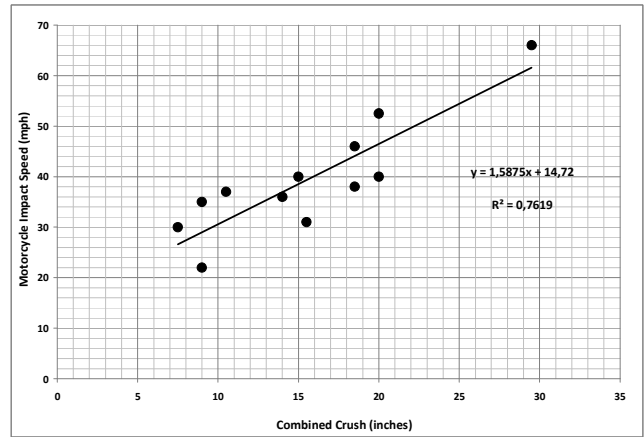


Figure 5: Motorcycle speed estimate “Hard location”

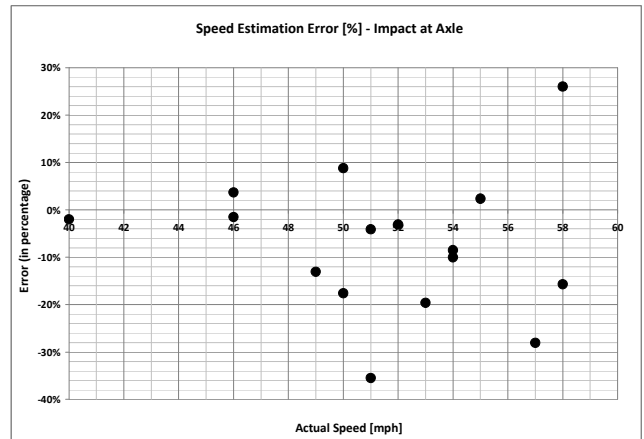


Figure 6: Motorcycle speed estimation error where impact at the axle.

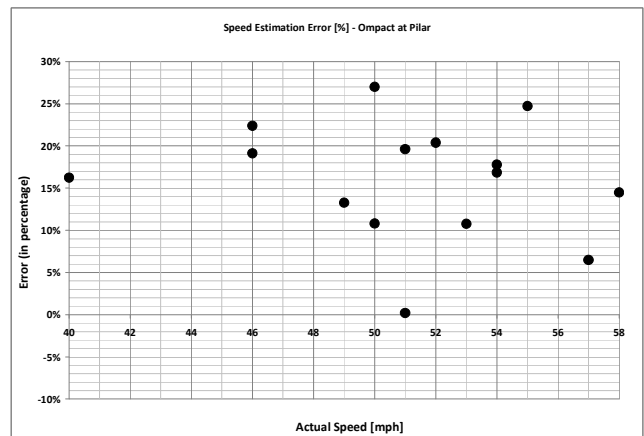


Figure 7: Motorcycle speed estimation error where impact at the pillar.

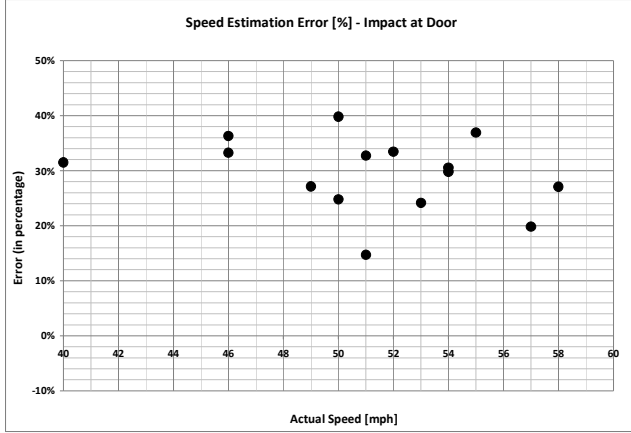


Figure 8: Motorcycle speed estimation error where impact at the door.

2.3 Model III – Conservation of linear momentum

The Law of Conservation of Momentum dictates that the total momentum just prior to two elements colliding is the same as the total momentum just after the collision. In most motorcycle collisions this basic formula must be expanded to include both motorcycle and rider post-impact velocity, since the motorcycle and rider seldom stay together following the collision. This relationship is given by:

$$(M_m + M_r)V = M_c V_c + M_m V_m + M_r V_r \quad (2)$$

where:

- M_m - Motorcycle's mass
- M_r - Rider's mass
- M_c - Vehicle's mass
- V_c - Vehicle's post impact speed
- V_m - Motorcycle's post impact speed
- V_r - Rider's post impact speed

In test conditions Eq. 2 is simplified in this case since there was no rider on the bike,

$$M_m V = M_c V_c + M_m V_m \quad (3)$$

To estimate post impact speed of the motorcycle conservation of energy relationship is used:

$$V_m = \sqrt{2\mu_m g l} \quad (4)$$

Where:

- g - Gravitational acceleration
- l - Motorcycle's skid marks length
- μ_m - Coefficient of friction between the motorcycle and the skidding surface

The same way the post impact of the vehicle can be calculated.

$$V_c = \sqrt{2\mu_c g L} \quad (5)$$

Where:

- L - Vehicle's skid marks length
- μ_c - Coefficient of friction between the vehicle and the skidding surface

Using conservation of linear momentum principle, the pre-impact speed of the motorcycle can be found by:

$$V = \frac{\sqrt{2g}}{M_m} (M_c \sqrt{\mu_c L} + M_m \sqrt{\mu_m l}) \quad (6)$$

As shown in Figure 9, the use of the principle of linear conservation principle yields poor results with some cases where the estimation errors exceeding 100%. It is interesting to note that all errors are negative which means that the model overestimate the actual speed.

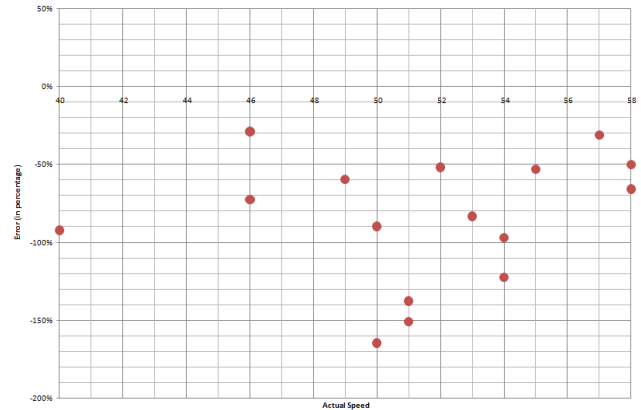


Figure 9: Estimation errors of the pre-impact motorcycle speed using linear momentum conservation.

2.5 Model IV – Conservation of Angular momentum

The McNally Rotational Momentum Method [8] utilizes vehicle information (weights, weight distributions, impact location, vehicle rotation), and scene information (post impact speed and direction of both vehicles).

The first step in the rotational analysis is to determine the total amount of torque acting through the tires/roadway interaction to slow the angular velocity of the vehicle following the collision.

In side collisions the impulse applied to the vehicle results in the struck end of the vehicle “sliding,” while the opposite end acts a pivot point. When this type of vehicular motion occurs, it is possible to calculate the torque acting on the vehicle by:

$$\tau_{tire} = M_c g W_b \mu_c \quad (7)$$

where: τ_{tire} - Torque caused by the tires sliding sideways
 W_b - Vehicle’s wheelbase

The value of torque calculated above can then be used in the following formula, which calculates the rotational velocity of the vehicle.

$$\omega = \sqrt{\frac{2\tau_{tire}\theta}{I + M_c d^2}} \quad (8)$$

where: ω - Angular velocity of the vehicle
 θ - Vehicle’s angle of rotation
 I - Yaw moment of inertia
 d - Distance of the farthest axle from the impact point to the center of gravity of the vehicle

At this point the change in the motorcycle speed, due to the impact, can be determined:

$$\Delta V_m = \frac{(I + M_c d^2)\omega}{SM_m} \quad (9)$$

where S is the length of moment arm determined by measuring the perpendicular distance from the principal direction of force to the center of mass of the vehicle.

If we know the direction of travel of the motorcycle at impact and its post-impact velocity, are know, the impact speed of the motorcycle can be determined. Figure 10 show the estimation errors of the motorcycle’s pre-impact speed. As in the previous case, the errors are large and reaching 80%. Similarly, in most cases the pre-impact speed is over estimated.

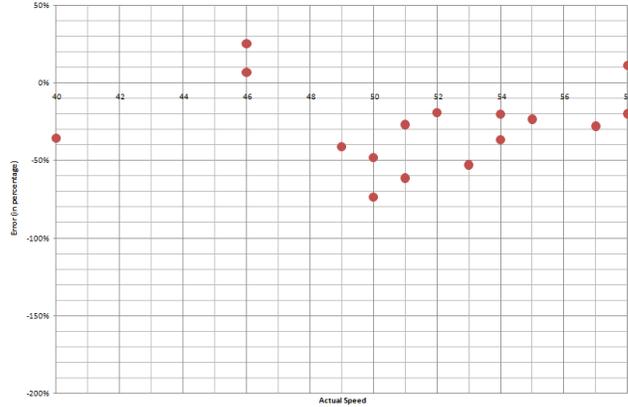


Figure 10: Estimation errors of the pre-impact motorcycle speed using angular momentum conservation.

3. CONCLUSIONS

The paper describes 5 different methods, by which the pre-impact speed of a motorcycle during a collision with the side of a vehicle, can be estimated.

While the momentum conservation methods are based on principles on mechanics, their estimate of is very poor. Out of the other 3 methods only the combined crush method produced good results.

From accident reconstruction point of you, these are encouraging results since in many cases the information available is very limited. For example, in many cases the accident site went through changes or some time passed since the accident and as a result skid marks are not available. However, at the best both vehicles are still available for inspection and the required two parameters, required for the combined crush method, can be measured.

4. REFERENCES

- [1] <http://www.edgarsnyder.com/motorcycle-accidents/statistics.html>
- [2] Severy, D., Brink, H., and Blaisdell, D., "Motorcycle Collision Experiments," SAE Technical Paper 700897, 1970.
- [3] [1] Motorcycle Accident Cause Factors and Identification of Countermeasures, Volume 1: Technical Report, Hurt, H.H., Ouellet, J.V. and Thom, D.R., Traffic Safety Center, University of Southern California, Los Angeles,
- [4] Fricke, Lynn B., and Riley, Warner W., *Reconstruction of Motorcycle Traffic Accidents*, Topic 874 of the Traffic Accident Investigation Manual, Northwestern University Traffic Institute, 1990
- [5] Brown, John F., and Obenski, Kenneth S., *Forensic Engineering Reconstruction of Accidents*, Charles C. Thomas, 1990.
- [6] Obenski, Kenneth S., *Motorcycle Accident Reconstruction: Understanding Motorcycles*, Lawyers & Judges Publishing Co., 1994

- [7] Niederer, Peter F., *Some Aspects of Motorcycle-Vehicle Collision Reconstruction*, SAE Paper 900750, Society of Automotive Engineers, 1990.
- [8] Bruce F. McNally, Wade Bartlett, 20th Annual Special Problems in Traffic Crash Reconstruction at the Institute of Police Technology and Management, University of North Florida, Jacksonville, Florida, April 15-19, 2002
- [9] Adamson, Kelley S.; Alexander, Peter; Robinson, Ed L.; Burkhead, Claude I.; McMannus, John; Anderson, Gregory C.; Aronberg, Ralph; Kinney, J. Rolley; Sallmann, David W.; Johnson, Gary M.; *Seventeen Motorcycle Crash Tests Held at WREX2000*, WREX2000 Conference Results, 2002.

APPENDIX I – Motorcycles data

CRASH TEST DATA			MOTORCYCLE DATA				WEIGHT		
TEST #	IMPACT SPEED	MC NUMBER	YEAR	MAKE	MODEL	VIN	FRONT	REAR	TOTAL
1	46	4	1984	Yamaha	FJ600L	JYA49A003EA000195	179	181	360
2	46	15	1980	Suzuki	GN400	GN400506260	143	172	315
3	54	10	1986	Honda	VT1100C Shadow	1HFSC1802GA109239	242	256	498
4	54	2	1982	Yamaha	Maxim	15R002812	221	253	474
5	51	5	1997	Kawasaki	ZX600	JKAKZ4E14VB512801	219	227	446
6	50	6	1986	Suzuki	GS550ESG	JS1GN74A3G2100744	224	212	436
7	49	9	2002	Suzuki	GSX600F	JS1GN79A022101478	205	205	410
8	52	3	1985	Suzuki	GS550ESG	JS1GN74A7G2101623	193	179	372
9	50	16	1987	Yamaha	Virago XV535T	JYA2GV002HA005753	191	214	405
10	51	1	1982	Yamaha	Virago XV920J	JYA10L009CA015001	203	215	417
11	40	13	2003	Qingqi	Unknown (Scooter)	LAEAD41053B920286	58	84	144
12	53	14	1981	Suzuki	GN400X	JS1NK41A5B2108405	128	162	290
13	58	7	1981	Honda	CB900 Custom	JH25C04058C107905	276	310	586

Motorcycle Accident Reconstruction

Part II - Self Learning Models

Oren Masory

Department of Ocean & Mechanical Engineering

Florida Atlantic University

Boca Raton, FL 33431

masoryo@fau.edu

Wade Bartlett

Mechanical Forensics Engineering Services

179 Cross Road

Rochester NH 03867

wade.bartlett@gmail.com

Hanri Peyrard

12 cours de la fontaine

77600 Bussy Saint Georges

France

henri.peyrard.13@eigsi.fr

Bill Wright

Institute of Police Technology and Management

14939 99th Street North

West Palm Beach, FL 33412

bwright@tarorigin.com

ABSTRACT

In this paper a self learning method, based on Abductive Networks, is being used for the development of a model that related pre-impact motorcycle speed to post-impact measurable data. The best results were obtained where the motorcycle wheel base reduction and the maximum crush of the vehicle were used as input the model. This result is, to some degree, similar to the results obtained in previous paper where these two parameters were assumed to be linearly related to the motorcycle pre-impact speed.

Keywords

Motorcycle Accident Reconstruction, Accidents Reconstruction, Motorcycle Accidents.

1. INTRODUCTION

The increasing number of motorcycle accidents is a major concern to policy makers. The understanding the causes of these accidents by accident reconstruction tools, will allow law makers to address this issue by regulating design features, safety requirements, road design modifications etc.[1].

Different models, based both vehicle damage and on on-site measurements, were reported in literature [2-9]. Some are based on physical principle like conservation of linear and/or angular momentum, and some based on correlation between measurable data. In both cases the results are not satisfactory in part due to the fact that very few crash tests are performed on motorcycles.

The method described in this paper falls into the second category where a correlation between measurable data and the motorcycle's pre-impact speed is being searched. Previously, a specific model was assumed and then the measured data was correlated to it. Thus, the produced models were not necessarily the best ones and mostly simple as linear polynomials. In this case, a self learning method is being used which automatically will find the best model that will fit the data. As a result higher

order polynomial might be found. In any case it should be emphasize that since the model are "just" correlation to measured data they do not shed any light on the physics of the crash.

This self learning method, which will be described in the following section, is called "Abductive Networks. This method was used successfully in many application one of which was to determine impact force and crush energy in vehicle collisions [10].

2. AIM – ABDUCTIVE NETWORKS

AIM [11] is a powerful supervised inductive learning tool for automatically synthesizing network models from a database of input and output values. The model emerging from the AIM synthesis process is a robust and compact transformation implemented as a layered abductive network of feed-forward functional elements as shown in Figure 1. Figure 1

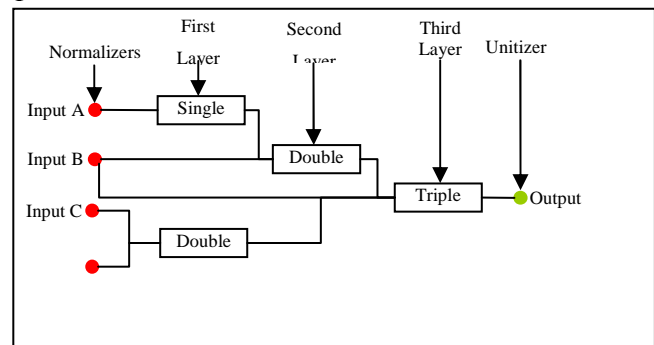


Figure 1: Example of Abductive Network.

All the functional and connection elements are learned from the input data. Currently AIM has seven types of elements.

The algebraic form of each element is a polynomial where W_n are the coefficients determined by AIM and X_n are the input variables (Table 1 shows sample elements). All terms in an element's equation may not appear in a node since AIM will throw out or carve terms which do not contribute significantly to the solution.

Table 1: Example of elements definition.

Single	$W_0 + W_1 * X_1 + W_2 * X_1^2 + W_3 * X_1^3$
Double	$W_0 + W_1 * X_1 + W_2 * X_2 + W_3 * X_1^2 + W_4 * X_2^2 + W_5 * X_1 * X_2 + W_6 * X_1^3 + W_7 * X_2^3$

The eligible inputs for each layer and the network synthesis strategy are defined in a set of rules and heuristics which are an inherent part of the synthesis algorithm.

AIM automatically determines the best network structure, element types, coefficients and connectivity by minimizing a modeling criterion which attempts to select as accurate a network as possible without over fitting the data. The modeling criterion used within AIM is the Predicted Squared Error (PSE). The PSE is a heuristic measure of the expected network squared error for independent data not in the training database. The PSE is given by:

$$PSE = FSE + KP \quad (1)$$

where FSE is the fitting squared error of the model to the training data and KP is a complexity penalty term determined in AIM by the equation:

$$KP = CPM * \frac{2K}{N} s_p^2 \quad (2)$$

where K, N and s_p^2 are determined by the database of examples used to synthesize the network and CPM, the Complexity Penalty Multiplier, is a variable the user can select. The default value of CPM is 1; a lower value decreases the complexity penalty impact and results in a more complex network and inversely for a higher value.

To create a model using AIM one has to follow these steps:

1. Decide what are the inputs and the output of the model.
2. Create a database which includes sets of inputs and the corresponding outputs from the process being modeled.
3. Train the abductive network using the above database.
4. Evaluate model performance of the model using sets of inputs/outputs which were not used to train the network.
5. Once the network (model) performs to satisfaction an explicit model can be derived and implemented.

3. THE DATA SETS AND DATA ALLOCATION

Two data sets with experimental data were available to the authors:

1. Data Set I: contains data from 47 crush tests that were performed by previously different investigators.
2. Data Set II: contains data from 13 crush test that were performed by the authors.

Both data sets include the following information:

- a) Pre-collision motorcycle's speed (V_M).
- b) Motorcycle's wheelbase reduction due to the impact (W_R).
- c) Vehicle's maximum crush (see Figure 2) (D_C).
- d) The impact location with the car, "Hard" or "Soft" locations. "Hard" location is considered as a location 3" from a pillar or axle and a "Soft" location is any other place on the car (e.g. doors or fenders) (H or S).
- e) The weight of the motorcycle (W_M).



Figure 2: Vehicle's maximum car crush.

As mentioned before, the first step is to "train" the system by providing a set on input and the corresponding outputs to the system. The inputs are post impact measurable quantities such as motorcycle's wheelbase reduction. The output, in the particular case, is only the pre-collision motorcycle's speed. The training data set is selected randomly from the entire data set. Once a model is established (the network converged), the rest of the data is used to evaluate the prediction achieved by the model.

4. MODELING

Model # 1

This model relates to the model proposed in [2] where the motorcycle's pre-collision impact speed was related only to its wheelbase reduction. Thus, the only input to this model is the wheelbase reduction of the motorcycle (W_R) and the only output is the speed. The model has been trained using measurements from 24 different crash tests from Set I.

Upon convergence, the model was used to predict the motorcycle speed of the other 23 crash tests, from the same set, which were not used for training. The average error of the predicted speed was 8.45% and the maximum error was 23.8%.

At this point the model was used to predict the motorcycle's speed user data set II. The average prediction error was 17.8%.

This first model was more of a test to see how the prediction would be using only one variable and training the model with the data set #1. It's surprisingly successful as the average errors are under 20%.

Model # 2

This model relates to the model proposed in [2] where the motorcycle's pre-collision speed (V_M) was related to its wheelbase reduction (W_R) and the maximum crush of the car (D_C). Again, 24 different crushes, which were selected randomly, used to train the network. Once the model was obtained, upon convergence, an explicit formula can be extracted:

$$V_M = 13.48 + 2.05W_R + 0.40(D_C) + 0.038(D_C)^2 \quad (3)$$

The capability to obtain an explicit relationship is very advantageous compared to other self-learning methods. For example, we can determine the sensitivity of the speed prediction to the errors in the measurements of the wheelbase reduction and the vehicle's maximum crush:

$$(\Delta V_M) = \frac{\partial(V_M)}{\partial(W_R)} (\Delta W_R) + \frac{\partial(V_M)}{\partial(D_C)} (\Delta D_C) \quad (4)$$

$$(\Delta V_M) = 2.05(\Delta W_R) + 0.40(\Delta D_C) + 0.076(D_C)(\Delta D_C)$$

where: (ΔV_M) – Error in motorcycle's speed
 (ΔW_R) – Error in the measurement of the motorcycle's wheelbase reduction
 (ΔD_C) – Error in the measurement of the vehicle's maximum crush

As an example assume that $(\Delta W_R) = (\Delta D_C) = 0.25$ ". It will result:

$$(\Delta V_M) = 0.6125 + 0.019(D_C) \quad (5)$$

Eq. (5) indicates that the error in the prediction of the motorcycle's speed is linear with the value of the vehicle's maximum crush measurement. Meaning that during the accident reconstruction process this value has to be measure with high accuracy.

The model was used to predict the motorcycle's pre-impact speed of the other 23 cases in data set #1. The errors in the predictions of the motorcycle's speed had average of 4.64% and the maximum of 11.47%.

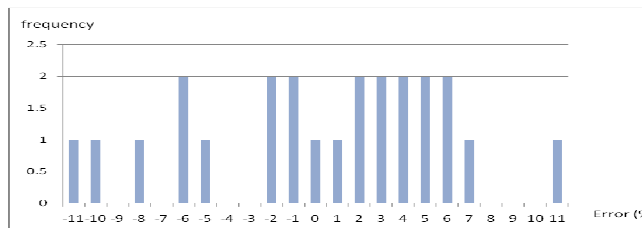


Figure 3: Histogram of the errors in prediction of the motorcycle speed using data set I.

The same model was used to predict the motorcycle's pre-impact speed of the cases provided in data set II. It resulted in an average error of 12.8% and maximum error of 22%. The histogram of these prediction errors are shown in Figure 4.

Other Models

Few other models, which differ from each other by: 1) The set of inputs; 2) Inputs configuration; and 3) Training sets, were tried (see Table2). Observing the results given in Table 1, one can reach the following conclusions:

1. One the training data and the verification data are from the same data set, the models are better (smaller errors)(tests 1,2 5,6 and 7).
2. Some set of input produces better results (within the same set). Compare the results of models 1 and 2 and 5 and 6.
3. The fact that the mixed data set produced relatively inferior results is that the tests were probably controlled differently.

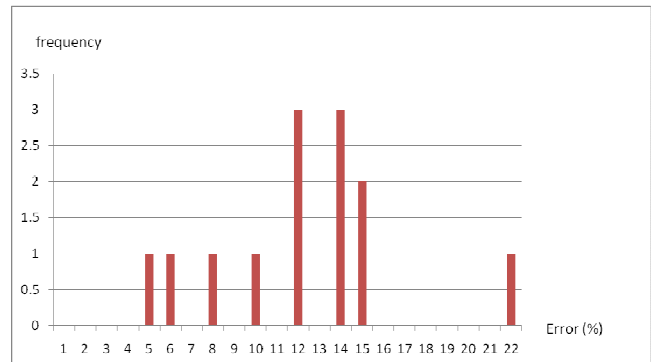


Figure 4: Histogram of the errors in prediction motorcycle's speed using model #2 and data set II

Table 2: Other models

	Inputs	Data Set I		Data Set II	
		Average Error [%]	Max. Error [%]	Average Error [%]	Max Error [%]
1 ¹	$(W_R), (D_C), (H) \text{ or } (S)$	4.24	11.6	25	
2 ¹	$(W_R), (W_M)$	6.27	21.74	23	
3 ²	$(W_R), (D_C)$	5.61	20		
4 ²	$(W_R), (W_M)$	7.49	17.42		
5 ³	$(W_R), (D_C)$	59.78		8.64	13.69
6 ³	$(W_R), (D_C)$	48	102	1.89	7.63
7 ¹	$(W_R), (D_C)$ (W_M)	6.94	17.92	180.47	

- (1) Training with data set I
- (2) Training with a mix from both data sets

- (3) Training with data set II

4. CONCLUSIONS

A simple self learning model for the estimation of a motorcycle's pre-impact speed was presented. The model is not physical model and is based on the correlation of experimental data to the motorcycle speed. It was obtained automatically using the AIM system and it is reasonably accurate. The model is explicit in contrast to non-explicit model that can be obtained by other learning procedures such a Artificial Neural Networks. As such it provides better understanding to the effect of each measurement on the model and to the sensitivity of the model to each of the inputs.

5. REFERENCES

- [1] National Highway Transportation Safety Administration. <http://www.edgarsnyder.com/motorcycle-accidents/statistics.html>
- [2] Severy D. Brink, H. and Blaisdell, D., "Motorcycle Collision Experiments," SAE Technical Paper 700897, 1970.
- [3] Motorcycle Accident Cause Factors and Identification of Countermeasures, Volume 1: Technical Report, Hurt, H.H., Ouellet, J.V. and Thom, D.R., Traffic Safety Center, University of Southern California, Los Angeles.
- [4] Fricke, Lynn B., and Riley, Warner W., Reconstruction of Motorcycle Traffic Accidents, Topic 874 of the Traffic Accident Investigation Manual, Northwestern University Traffic Institute, 1990.
- [5] Brown, John F., and Obenski, Kenneth S., Forensic Engineering Reconstruction of Accidents, Charles C. Thomas, 1990.
- [6] Obenski, Kenneth S., Motorcycle Accident Reconstruction: Understanding Motorcycles, Lawyers & Judges Publishing Co., 1994
- [7] Niederer, Peter F., Some Aspects of Motorcycle-Vehicle Collision Reconstruction, SAE Paper 900750, Society of Automotive Engineers, 1990.
- [8] Bruce F. McNally, Wade Bartlett, 20th Annual Special Problems in Traffic Crash Reconstruction at the Institute of Police Technology and Management, University of North Florida, Jacksonville, Florida, April 15-19, 2002
- [9] Adamson, Kelley S.; Alexander, Peter; Robinson, Ed L.; Burkhead, Claude I.; McMannus, John; Anderson, Gregory C.; Aronberg, Ralph; Kinney, J. Rolley; Sallmann, David W.; Johnson, Gary M.; Seventeen Motorcycle Crash Tests Held at WREX2000, WREX2000 Conference Results, 2002.
- [10] O. Masory, N. Putod, "Determination of Impact Force and Crush Energy Using Abductive Networks", Proc. 20th Florida Conference on Recent Advances in Robotics, May 31-June 1, 2007.
- [11] AIM User's Manual, AbTech Corporation, 1990
- [4] Fricke, Lynn B., and Riley, Warner W., Reconstruction of Motorcycle Traffic Accidents, Topic 874 of the Traffic

An Example of a Fault Tolerant Wrist Design

Salman Siddiqui and Rodney Roberts
Department of Electrical and Computer Engineering
FAMU-FSU College of Engineering
2525 Pottsdamer Street,
Tallahassee, FL 32310, USA
siddiqui@eng.fsu.edu, rroberts@eng.fsu.edu

ABSTRACT

In this article, the authors present a methodology for analyzing and designing a fault tolerant 4-DOF spherical wrist type mechanism. The proposed method uses a local approach based on the manipulator Jacobian. Once the form of an optimal Jacobian is identified, a family of mechanisms can be designed so that the device possesses an optimally fault tolerant nominal configuration. The method is illustrated for a specific device and the DH parameters of this device are given.

Keywords

Kinematic redundancy, fault tolerance, manipulability, spherical wrist.

1. INTRODUCTION

Robotic manipulators are designed to perform tasks that are either difficult for human beings or too time consuming. With this benefit comes the downside that the robotic manipulators are not free from failures. Failures in robots have significant consequences ranging from economic impact in industrial applications to potentially catastrophic losses in remote and hazardous environments like space exploration, deep sea exploration, nuclear waste cleanup, etc. [1]-[12].

One way to address the issue of failure of individual joints is to use kinematically redundant manipulators. These manipulators have more degrees of freedom than necessary to position and/or orient the end-effector so that there is generally a continuous family of joint configurations corresponding to an interior point of the workspace. However, kinematic redundancy should be added strategically to ensure optimal fault tolerance.

One approach to designing kinematically redundant fault-tolerant robots is to optimize some measure of fault tolerance. This measure can be either global, i.e., over a specified region of the workspace, or local, i.e., at a specific configuration. Global measures are more appropriate for tasks that require large motions throughout the workspace, whereas local measures are more appropriate for dexterous operations in a relatively small location, e.g., laser pointing [6] and manipulation of nuclear material [9]. Both of these measures are related since workspace boundaries result in manipulator singularities that are easily identified through the Jacobian. In this work, we will focus on a local measure of fault tolerance called the relative manipulability index, which was first introduced in [13] to quantify the fault tolerance of kinematically redundant serial manipulators.

In the next section, we describe the relative manipulability index for serial manipulators and discuss isotropy and fault tolerance. In Section 3, the relationship between the relative manipulability index and the null space of the manipulator Jacobian is illustrated. Section 4 discusses the design of a kinematically redundant wrist design that is fault tolerant. Lastly, conclusions appear in Section 5.

2. RELATIVE MANIPULABILITY INDEX

In the next two sections, we will review previous work by the authors on the relative manipulability index [13], [14]. In this section, the application of the relative manipulability index measure for serial manipulators is summarized. This measure has also been shown to be applicable for parallel manipulators in [15] and [16].

For a serial manipulator, the relative manipulability index is defined in terms of the manipulator Jacobian J , which relates the manipulator's joint velocity $\dot{\theta}$ to its end-effector velocity v by the equation

$$v = J\dot{\theta}.$$

In this work, we will assume that the manipulator is not operating at a kinematic singularity so that J has full rank.

When a locked-joint failure occurs, say in joint i , that component of the joint velocity vector is zero. Consequently, the end-effector motion is characterized by iJ , i.e., the Jacobian J with its i -th column removed. Multiple locked-joint failures are handled in the same way, i.e., the corresponding columns of the Jacobian are removed.

The relative manipulability index corresponding to a locked-joint failure in joint i is defined as

$$\rho = \frac{w({}^iJ)}{w(J)},$$

where once again iJ denotes the manipulator Jacobian after column i corresponding to the failed joint is removed and where

$w(J) = \sqrt{\det(JJ^T)}$ is the manipulability index of J [17]. This quantity is a local measure of the amount of dexterity that is retained when a manipulator suffers a locked-joint failure. The value of a relative manipulability index ranges from zero to one. A zero value would indicate a loss of full end-effector motion at that configuration after the failed joint is locked. In other words, a zero relative manipulability index means that the reduced

manipulator Jacobian ${}^i J$ does not have full rank. A relative manipulability index of one would indicate that no dexterity is lost at that configuration. In this case the joint in question does not contribute to end-effector motion at the operating configuration prior to its failure, i.e., that joint only produces self-motion [18], [13]. Similar statements concerning multiple failures hold for manipulators with multiple degrees of redundancy; however, in this paper, we will only consider manipulators with a single degree of redundancy.

Other measures of fault tolerance have been used in the literature such as the minimum singular value [19] and the condition number [20]. The minimum singular value gives a measure of proximity to singular configurations. The condition number is the ratio of the largest and the smallest singular values with a lower bound of one i.e., $C = \sigma_{\max}/\sigma_{\min}$, where a singularity is characterized by an infinite condition number while a condition number of one indicates an isotropic configuration of the robot where the singular values of the manipulator Jacobian are all equal [21], [22]. One disadvantage of measures such as the minimum singular value and the condition number is their dependence on the singular values of the manipulator Jacobian, which are not invariant under changes in units. This is also true of the manipulability index.

An advantage of using the relative manipulability index as compared to the other local measures discussed is that it is not dependent upon the units of the Jacobian. However, while the relative manipulability index is defined in terms of the manipulability index, it is a ratio of the manipulability index of two Jacobians and is not dependent upon the units chosen. In fact, as a function of the null space of the manipulator Jacobian, the relative manipulability index is a geometric property of the manipulator and is independent of the coordinate frame and units chosen by the operator.

In the next section, we describe a natural relationship between the relative manipulability index and the null space of the manipulator Jacobian J .

3. THE RELATIVE MANIPULABILITY INDEX AND THE NULL SPACE OF THE MANIPULATOR JACOBIAN

The amount of fault tolerance that a manipulator possesses is closely related to the null space of the manipulator Jacobian [RYM08]. Indeed, the relative manipulability index can be completely characterized in terms of the null space of the manipulator Jacobian. Let J be a full rank $m \times n$ matrix with $m < n$ and let $r = n - m$. For a manipulator, m denotes the dimension of the workspace, n denotes the number of joints, and r denotes the degree of redundancy. We will call an $n \times r$ matrix N a *null space matrix* of J if the columns of N form an orthonormal basis for the null space of J . Although the null space matrix N is not unique for a given J , any two null space matrices N and N' of J are related by an orthogonal matrix Q in the following way: $N' = NQ$.

In [RM96], it was shown that the relative manipulability index ρ_i is given by the norm of the i -th row of N . In the case of a single degree of redundancy, one has

$$\rho_i = |n_i| \quad i = 1, 2, \dots, n.$$

where n_i is the i -th component of the unit length null vector \hat{n}_J . Thus the relative manipulability is strictly a function of the null space of J . This important observation allows for the design of a fault tolerant manipulator based on the null space of the manipulator Jacobian.

Before concluding this section, we note that

$$\sum_{i=1}^n \rho_i^2 = 1,$$

so that the minimum relative manipulability index is less than or equal to $1/\sqrt{n}$. Since one would want to maximize the minimum relative manipulability index, it is desirable to have configurations where the components of the unit length null vector are all equal, i.e., where

$$\hat{n}_J = \frac{1}{\sqrt{n}} \begin{bmatrix} 1 \\ 1 \\ \vdots \\ 1 \end{bmatrix}.$$

4. DESIGN OF A FAULT TOLERANT KINEMATICALLY REDUNDANT WRIST

In Section 3 we observed that a manipulator with a single degree of redundancy is in an optimally fault tolerant configuration in the sense of maximizing the minimum relative manipulability if and only if its null vector has components of equal magnitude. We will use this observation to design an optimally fault tolerant 4-DOF spherical wrist type mechanism.

Consider a full rank 3×4 orientational Jacobian

$$J = [J_1 \ J_2 \ J_3 \ J_4].$$

The columns of such a matrix have unit length and represent the axes of rotation for the corresponding joints. Without loss of generality we assume that the components of the unit length null vector are all equal so that

$$\hat{n}_J = 1/2 [1 \ 1 \ 1 \ 1]^T.$$

We can accomplish this by multiplying certain columns of the Jacobian by -1 if necessary, which does not essentially change the structure of the robot. Hence, an optimally fault tolerant 3×4 orientational Jacobian has the property that its columns have unit length and their sum is the zero vector. Traditionally, the first column of an orientational Jacobian is given by

$$J_1 = [0 \ 0 \ 1]^T.$$

If the first twist angle is denoted by α , we can assume without loss of generality that the second column of J is

$$J_2 = [0 \ -\sin \alpha \ \cos \alpha]^T$$

by applying a suitable rotation about the z-axis, i.e., we can choose the first angle so as to zero out the first element of the J_2 .

The properties that the remaining two columns also have unit length along with the requirement that the sum of the four

columns is the zero vector allow us to write a closed form expression for the optimal Jacobian:

$$J = \begin{bmatrix} 0 & 0 & \sin\frac{\alpha}{2}\sin 2\psi & -\sin\frac{\alpha}{2}\sin 2\psi \\ 0 & -\sin\alpha & \sin\alpha\sin^2\psi & \sin\alpha\cos^2\psi \\ 1 & \cos\alpha & -\cos^2\psi - \sin^2\psi\cos\alpha & -\sin^2\psi - \cos^2\psi\cos\alpha \end{bmatrix}. \quad (1)$$

As an example, let $\alpha = 120^\circ$ and $\psi = 60^\circ$. In this case, the orientational Jacobian in (1) becomes

$$J = \begin{bmatrix} 0 & 0 & \frac{3}{4} & -\frac{3}{4} \\ 0 & \frac{-\sqrt{3}}{2} & \frac{3\sqrt{3}}{8} & \frac{1\sqrt{3}}{8} \\ 1 & -\frac{1}{2} & \frac{1}{8} & -\frac{5}{8} \end{bmatrix}. \quad (2)$$

Table 1 gives the DH Table [23] corresponding to (2) while Figure 1 shows a generic 4-DOF spherical wrist type mechanism that can be placed in a fault tolerant configuration.

Table 1. DH Table

i	α_i	θ_i
1	120°	0°
2	128.6822°	-106.1021°
3	-120°	-73.8979°
4	0	-153.5890°

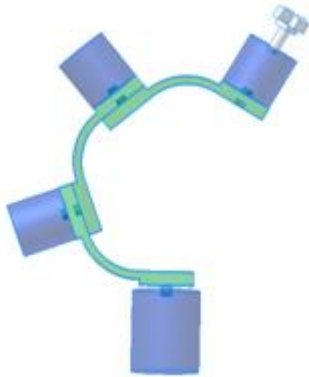


Figure 1. A spherical wrist type mechanism that can be placed in an optimally fault tolerant configuration.

The singular values for this particular Jacobian are $3/2$, 1 , and $\sqrt{3}/2$, and the manipulability index is 1.299 . By design, the relative manipulability index is $\rho_i = 1/2$ for any joint failure. This is the optimal value for maximizing the minimum relative manipulability index over all possible failures.

In designing a suitable fault tolerant orientational Jacobian, one would want to make sure that the original manipulability at the design point is relatively large. One can show that the largest possible value for the manipulability index of a 3×4 orientational Jacobian is $8\sqrt{3}/9$, which is obtained precisely when the manipulator is in an isotropic configuration, i.e., a configuration where all three singular values of the orientational Jacobian are equal (in this case $2\sqrt{3}/3$). Interestingly, it can be shown that an isotropic orientational Jacobian is also optimally fault tolerant in the sense of maximizing the minimum relative manipulability index. To see this, observe that the singular value decomposition of a 3×4 isotropic Jacobian has the form $J = \sigma V_1^T$ where the output vector matrix V_1 consists of the first three columns of an orthogonal matrix $V = [V_1 \ V_2]$ and σ is equal to the value of the three singular values of J . The requirement that the columns of an orientational Jacobian $J = \sigma V_1^T$ are of unit length dictates that the columns of V_1^T each have the same norm. Consequently, the magnitudes of the elements of the vector V_2 are all equal owing to the fact that V is an orthogonal matrix. Since V_2 is equal to the unit length null vector \hat{n}_J , it follows that the manipulator is also optimally fault tolerant.

5. CONCLUSION

In this article, the authors presented a methodology for designing an optimally fault tolerant 4-DOF spherical wrist type mechanism. This approach was based on maximizing the minimum relative manipulability index. It was shown that the orientational Jacobian must have a certain form for the manipulator to have the best possible relative manipulability index value of $1/2$. An optimal configuration along with the corresponding DH parameters was presented. It was also pointed out that isotropic configurations of a 4-DOF spherical wrist type mechanism are fault tolerant in this sense and furthermore, isotropic configurations for these types of mechanisms are also optimal in the sense that they have the largest possible manipulability index prior to a failure.

6. ACKNOWLEDGMENTS

The authors gratefully acknowledge the support of the National Science Foundation under Contract IIS-0812437.

7. REFERENCES

- [1] Y. Chen, J. E. McInroy, and Y. Yi, "Optimal, fault-tolerant mappings to achieve secondary goals without compromising primary performance," *IEEE Trans. Robot. Autom.*, vol. 19, no. 4, pp. 680-691, Aug. 2003.
- [2] R. Colbaugh and M. Jamshidi, "Robot manipulator control for hazardous waste-handling applications," *J. Robot. Syst.*, vol. 9, no. 2, pp. 215-250, Mar. 1992.

- [3] J. D. English and A. A. Maciejewski, "Fault tolerance for kinematically redundant manipulators: Anticipating free-swinging joint failures," *IEEE Trans. Robot. Autom.*, vol. 14, no. 4, pp. 566-575, Aug. 1998.
- [4] K. N. Groom, A. A. Maciejewski, and V. Balakrishnan, "Real-time failure-tolerant control of kinematically redundant manipulators," *IEEE Trans. Robot. Autom.*, vol. 15, no. 6, pp. 1109-1116, Dec. 1999.
- [5] M. L. Leuschen, I. D. Walker, and J. R. Cavallaro, "Investigation of reliability of hydraulic robots for hazardous environment using analytic redundancy," *Proc. Annu. Rel. Maintain. Symp.*, Washington, D.C., Jan. 18-21, 1999, pp. 122-128.
- [6] J. E. McInroy, J. F. O'Brien, and G. W. Neat, "Precise, fault-tolerant pointing using a Stewart platform," *IEEE/ASME Trans. Mechatronics*, vol. 4, no. 1, pp. 91-95, Mar. 1999.
- [7] L. Notash and L. Huang, "On the design of fault tolerant parallel manipulators," *Mech. Mach. Theory*, vol. 38, pp. 85-101, Jan. 2003.
- [8] E. C. Wu, J. C. Hwang, and J. T. Chladek, "Fault-tolerant joint development for the space shuttle remote manipulator system: Analysis and experiment," *IEEE Trans. Robot. Autom.*, vol. 9, no. 5, pp. 675-684, Oct. 1993.
- [9] Y. Yi, J. E. McInroy, and Y. Chen, "Fault tolerance of parallel manipulators using task space and kinematic redundancy," *IEEE Trans. Robot.*, vol. 22, no. 5, pp. 1017-1021, Oct. 2006.
- [10] Y. Yi, J. E. McInroy, and F. Jafari, "Optimum design of a class of fault tolerant isotropic Gough-Stewart platforms," *Proc. IEEE Int. Conf. on Robot. Autom.*, New Orleans, LA, Apr. 26-May 1, 2004, pp. 4963-4968.
- [11] C. J. J. Paredis and P. K. Khosla, "Designing fault-tolerant manipulators: How many degrees of freedom?," *Int. J. Robot. Res.*, vol. 15, no. 6, pp. 611-628, Dec. 1996.
- [12] S. Tosunoglu and V. Monteverde, "Kinematic and structural design assessment of fault-tolerant manipulators," *Intell. Autom. Soft Comput.*, vol. 4, no. 3, pp. 261-268, 1998.
- [13] R. G. Roberts and A. A. Maciejewski, "A local measure of fault tolerance for kinematically redundant manipulators," *IEEE Trans. Robot. Autom.*, vol. 12, no. 4, pp. 543-552, Aug. 1996.
- [14] R. G. Roberts, S. A. Siddiqui, and A. A. Maciejewski, "Designing equally fault-tolerant configurations for kinematically redundant manipulators," *Proc. IEEE Southeastern Symp. on Syst. Theory*, Tullahoma, TN, Mar. 15-17, 2009, pp. 335-339.
- [15] C. S. Ukidve, J. E. McInroy, and F. Jafari, "Orthogonal Gough-Stewart platforms with optimal fault tolerant manipulability," *Proc. IEEE Int. Conf. on Robot. Autom.*, Orlando, FL, May 15-19, 2006, pp. 3801-3806.
- [16] R. G. Roberts, H. G. Yu, and A. A. Maciejewski, "Fundamental limitations on designing optimally fault-tolerant redundant manipulators," *IEEE Trans. Robot.*, vol. 24, no. 5, pp. 1224-1237, Oct. 2008.
- [17] T. Yoshikawa, "Manipulability of robotic mechanisms," *Int. J. Robot. Res.*, vol. 4, no. 2, pp. 3-9, Jun. 1985.
- [18] J. W. Burdick, "On the inverse kinematics of redundant manipulators: Characterization of the self-motion manifolds," *IEEE Int. Conf. Robot. Autom.*, Scottsdale, AZ, May 14-19, 1989, pp. 264-270.
- [19] C. L. Lewis and A. A. Maciejewski, "Dexterity optimization of kinematically redundant manipulators in the presence of failures," *Comput. Elect. Eng.*, vol. 20, no.3, pp. 273-288, 1994.
- [20] H. Abdi and S. Nahavandi, "Well-conditioned configuration of fault-tolerant manipulators," *Robot. and Auton. Syst.*, vol. 60, pp 242-251, 2012.
- [21] C.A. Klein and T. A. Miklos, "Spatial robotic isotropy," *Int. J. Robot. Res.*, vol. 10, no. 4, pp. 426-437, Aug. 1991.
- [22] D. Chablat and J. Angeles, "The Computation of All 4R Serial Spherical Wrists with An Isotropic Architecture," *ASME J. Mech. Des.*, vol. 125, pp: 275-280, 2003.
- [23] K. M. Ben-Gharbia, A. A. Maciejewski, and R. G. Roberts, "An illustration of generating robots from optimal fault-tolerant Jacobians," *15th IASTED Int. Conf. on Robot. Applic.*, Cambridge, MA, Nov. 1-3, 2010, pp. 453-460.

Robotic Surgery - A Review on Recent advances in Surgical Robotic Systems.

Jyotsna Dwivedi
Department of Computer & Electrical Engineering &
Computer Science
Florida Atlantic University
Boca Raton, FL 33431
Jdwived1@fau.edu

Imad Mahgoub
Department of Computer & Electrical Engineering &
Computer Science
Florida Atlantic University
Boca Raton, FL 33431
mahgoubi@fau.edu

ABSTRACT

Robotic surgery has been around for over two decades, and has been a revolutionary step in improving surgical procedures. The use of robotics in medical procedures has become common place in the past decade. With the wide acceptance in robotic surgery, the drive to provide smaller, more efficient and less expensive equipment is driving researchers to reach unheard of heights. Robotic surgery has been successfully implemented in several hospitals around the globe and has received world wide acceptance.

The focus of this paper is to provide a review of the latest robotic surgical technology. We classify and compare the surgical robotic systems and discuss their future directions.

Keywords

Robotic Surgery, Medical Robotics, Surgical Robots, Robots, Surgery and Surgical Advances.

1. INTRODUCTION

1.1 Background

The term "robot" was coined by Karel Capek, who was a Czech playwright. The origin coming from the root 'Robota', which means forced labor-like the machines that do repeated, menial work [17].

Over time robots have become highly evolved as compared to their predecessors. The robots of today are very precise, highly specific, and a godsend for hazardous jobs, which just decades ago, had to be done by the human workforce.

1.2 Evolution of Surgical Robots

Robots have been around for a long time, but only recently have these machines entered the medical field. This change can be attributed to the recent advances in technology that have lead to more reliability, and therefore wider acceptance by the general populace and the medical community. Technology has advanced to the point that the present generation expects everything at their fingertips, and medicine has not been far behind. Online doctor visits and tele-consults are the norm for most non-emergency situations. Telesurgical robots are presently being used for transcontinental surgeries as well.

As technology advances in the area of robotics, newer and more reliable surgical robots created. The field of surgical robotics really took off after the late 1980's in minimally invasive

surgery (MIS), where surgeons performed surgery laparoscopically. Before this, traditional surgery involved opening up the patient to get a visual of the procedure as shown in Figure 1.

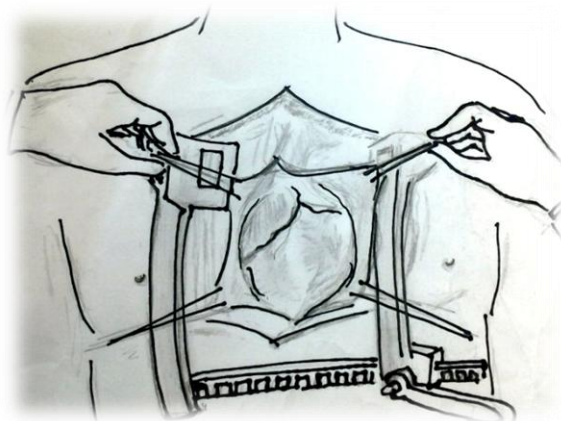


Figure 1. Traditional Open Surgery.

There were many benefits of minimally invasive techniques over traditional techniques, which was immediately apparent to both surgeons and patients. The tiny incisions lead to lower risk of infection and less recovery time after surgery. Surgeons especially liked the precision and enhanced vision that this provided [13]. Figure 2 illustrates how the use of a laparoscope to see inside the patient without having to make a large incision.

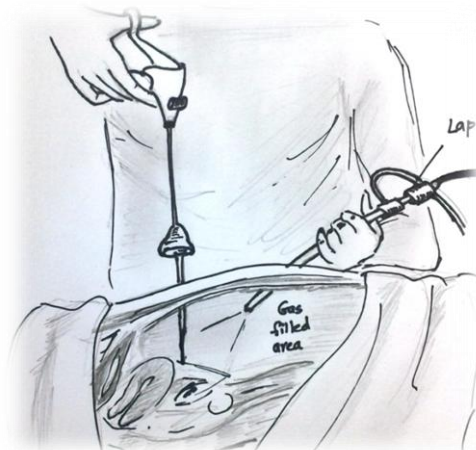


Figure 2. Minimally Invasive Surgery.

However, minimally invasive surgery isn't without several drawbacks. There is no haptic feedback, as well as the loss of natural dexterity and hand-eye co-ordination.

Minimally invasive surgery also has its limitations. Some of the more prominent limitations involve the technical and mechanical nature of the equipment. Surgeons found it somewhat difficult to manipulate the instruments while watching a 2-D image. The fulcrum effect, where every motion of the surgeon is in reversed order, is counter-intuitive for the surgeon. The greatest disadvantage was that the tremors of surgeons, especially evident during long surgical procedures, were translated through the instruments. These limitations are what fueled further development of surgical robots [10]. Figure 3 is an outline of a robotic surgical system.

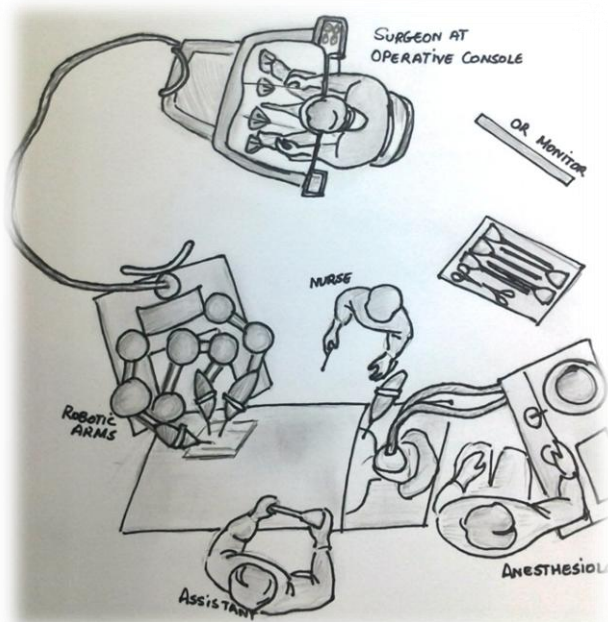


Figure 3. Minimally Invasive Robotic Surgery.

Surgical Robots of today originate from the 1985 Robot, Programmable Universal Manipulation Arm (PUMA) 560 used by Kwoh [1] to perform high precision neurological biopsies. Over time this robot led to the PROBOT which was used in the transurethral resection of prostate, and then the first FDA approved robot used for hip replacement surgery, the ROBODOC. The design of the computer-aided surgery resulted in a clean cut cavity, with precision and a perfect fit of the prosthesis [10].

In the 80's, NASA's Ames Research Center began working on virtual reality and introduced the concept of telepresence in surgery [10]. The Stanford Research Institute joined forces with NASA in the 1990's, which led to the development of an agile telemanipulator and which went a long way to overcoming the limitations of normal MIS. [10].

Soon afterwards, the US Army began funding medical and surgical robotic technology hoping to eventually develop a

remote surgical robotic system, which they coined 'MASH', which stands for 'Mobile Advanced Surgical Hospital' [10]. Telepresence was initially the domain of US Department of Defense with a goal, to provide immediate assistance to wounded soldiers. This was because a survey showed that 90% of fatalities of combat situations were caused by the delay in reaching a medical center [10].

In 1996, the Automated Endoscopic System for Optimal Positioning (AESOP) 2000 was created by Computer Motion, using voice control technology. In 1998, with a few modifications to the degree of freedom of movement, the AESOP 3000 released. This technology was later used as a part of the surgical robotic systems like ZEUS [1].

With funding available in the field of robotics many companies took advantage of this opportunity, leading to the integration of robotic surgery in the medical system.

Table 1 shows a comparison between tradition open surgery, minimally invasive surgery and robotic surgery.

Table 1. Comparison between Open, MIS and MIRS Surgeries

	Open Surgery	Minimally invasive Surgery	Minimally Invasive Robotic Surgery
Shorter operative time	✗	✓	✓
Shorter post op stay	✗	✓	✓
Shorter recovery time	✗	✓	✓
Less blood loss	✗	✓	✓
Less post op pain	✗	✓	✓
Less scarring	✗	✓	✓
Less complications	✗	✓	✓
Less infection risk	✗	✓	✓
Less transfusion requirement	✗	✓	✓
Less fatigue (surgeon)	✗	✗	✓
Less expensive equipment	✓	✓	✗
Less specialized training	✓	✓	✗
Compensate for hand tremors	✗	✗	✓
Enhanced view	✗	✓	✓
Small incisions	✗	✓	✓
Less anesthesia required	✗	✓	✓
Fewer doctors in OR	✗	✗	✓
Motion scaling	✗	✗	✓
Improved dexterity	✓	✗	✓
Fulcrum effect	✗	✓	✗
Longer setup time	✗	✗	✓
Significant haptic-feedback	✓	✗	✗

2. ROBOTIC SURGICAL SYSTEMS

Robotic surgical systems cost on average range from 0.5 million to 1.5 million dollars [4]. Despite this fact, it has proven to be profitable in the long run for society as a whole.

There are three major categories when it comes to surgical robots.

2.1 Supervisory Controlled System (SCS)

The SCS are the most automated type of surgical robot, though not fully automated. A lot of surgeon-involved prep-work must be done before the robots can perform. This system follows an

extremely detailed set of instructions, which depend on input from the surgeon.

The drawbacks of this is once the instructions have been input and the sequence initiated, there is no room for error as there is no way to make any adjustments to the procedure in real time. These types of surgeries are common in hip and knee replacements.

There are three steps to this process. In the first step the surgeon takes a lot of details, mapping the body as well as the region of interest and collects pertinent data. The second step is registration, where the surgeon uses the collected body image of the patient and connects it to a set of corresponding spots on the real-time image of the patient. The third and final step is the actual surgery, where the surgeon places the robot in the first position. Then the robot, while following its programmed path, completes its instruction [4].

Robotic Radiosurgery Systems are a subset of SCS, used to deliver radiation treatment for tumors from a remote location. This system has lowered the risk of overexposure of medical professionals.

2.2 Telesurgical

These systems are better known as Remote Surgical Systems. The surgeon is at a console manipulating the arms of the robot in real time. While technically the procedure is performed by the robot, the surgeon is controlling its movement throughout the procedure.

2.3 Shared Control System

In the Shared Control System the surgeon is involved the most. The surgeons perform the procedure with the help of a robot as an assistant to offer steady manipulations of the instrument. Shared Control systems are often used in neurosurgery and orthopedic surgery.

3. RECENT ADVANCES

3.1 Building Blocks

The AESOP was produced by Computer Motion and approved by the FDA in 1994 [2]. Computer Motion later merged with Intuitive Surgical. While previous versions of AESOP were foot or hand switch controlled cameras, the latest ones were voice-activated.

The main feature of this robot is the robotic arm that holds a voice-activated endoscope. This feature allows for greater control on behalf of the surgeon in terms of guidance of the camera positioning thus removing the cost of an additional assistant. The surgeon guides the camera using foot pedals and voice-activated software [2].

The robotic arm was later incorporated into the *ZEUS* and other systems [9].

The Hermes Control Center was developed as a robotic system which, unlike the *da Vinci* and *ZEUS* robots does not make use of robotic arms. Hermes is a centralized networking platform used to connect all the intelligent tools in the Operating Room (OR).

Networking all the components in the room also gave the robotic system more control over the operating room environment. Hermes can integrate lights, video cameras, tables and surgical equipment as well as equipment outside the sterile area[11]. This reduces cost of hiring additional personnel.

Hermes was implemented using a system known as the Socrates System to form a telesurgical system for remote surgical Control.

The *ZEUS* System or the *ZEUS* Robotic Surgical System, released by Computer Motion, in 1995, was a prototype but did not receive FDA approval until 2001. *ZEUS* is different from the *da Vinci* robot as it is voice-activated [1]. The three robotic arms of the *ZEUS* System are attached to the side of the surgery table. One robotic arm uses the voice-activated AESOP technology, while the other two arms of *ZEUS* are the extensions of the right and left arms of the surgeon. Surgeons sit at the console with special polarized glasses that create a 3-D image [1].

Using a small joystick, the surgeons control the micromovement of the robotic arms which contains the incision and surgical instruments. The third arm contains a 3-D high quality digital camera. The video is streamed in real time. Like the *da Vinci* robot, the *ZEUS* system also has the capability of filtering out tremors that would otherwise cause issues. The hand controls provide the surgeon with 6 degrees of freedom [1, 9].

The original design was initially geared towards minimally invasive microsurgical procedures like Endoscopic Coronary Artery Bypass Graft (E-CABG) and evolved to complex procedures like mitral valve surgery and gallbladder surgery [1].

Advanced versions may carry out surgical procedures in space by surgeons on the Earth surface. [7]

ZEUS systems are no longer produced.

3.2 *da Vinci* Surgical System

3.2.1 Overview

The *da Vinci* Surgical System is a telesurgical robotic device manufactured by Intuitive Surgical (IS) and is one of the most well known and most widely used robotic surgical devices in the world. As with all telesurgical robots, the *da Vinci* Surgical System is directed by the surgeon. It was originally developed by the United States Department of Defense in 1991 before IS acquired the prototype and commercialized it.

On July 11, 2000, the *da Vinci* System became the first robotic surgical system to be implemented in an American OR after the U.S. FDA approved this robot for laparoscopic procedures [3].

With a net worth of approximately 1.5 million dollars, the *da Vinci* is one of the most expensive tools used by surgeons today [3].

Recent advances have been made to the *da Vinci* System in 2006 when the Type S *da Vinci* robotic system was released by Intuitive Surgical and again in 2009 when Type Si *da Vinci* robotic system was released.

3.2.2 Standard Features

The *da Vinci* Surgical System has the following standard components:

- Surgeons console
- Patient side cart
- EndoWrist instruments
- Vision System

Small incisions are made in the area of interest, the number of which are determined by the number of surgical arms of the model. The two or three surgical arms, varying by model, made of miniaturized wrist instruments and one arm fitted with a high-definition 3-D Dual channel endoscopic camera are introduced into the incisions [6, 15].

Sitting at the control console away from the surgical table, the surgeon receives a stereoscopic, magnified version (up to 12 times magnified) of the high resolution image from the camera. The control console has joystick-like controls which the surgeon then uses to manipulate the surgical instruments for suturing and dissecting [6].

The *da Vinci* computer sends out an electronic signal to the corresponding instruments, which mimic the movement of the surgeons. The instruments were created with the patented Endowrist technology that provides the surgeon with 6 degrees of freedom. The motion is then scaled down, filtered and translated. Unwanted tremor motions are filtered by the 6 Hz motion filter. Clutch pedal disconnects arms/instruments [10].

Motion sensors on the console halt movement of the instruments when sensors on the head-rest pad detect the movement of the surgeon away from the console. Sensors on the tips of the robotic arm prevent the movement of the instrument from crossing the incision area.

3.2.3 Applications

The *da Vinci* Surgical System has been used in many surgeries including cardiothoracic surgeries (mitral valve prolapse, revascularization, CABG an adrenal tumor), in general surgery (gastric bypass, bariatric, etc.), as well as gynecological (hysterectomy) and urological (prostatectomy) [1].

Overall, the *da Vinci* System is the most popular system at the present moment.

3.3 CyberKnife- Mako Surgical Corp

3.3.1 Overview

The CyberKnife is a radio-surgical robotic system, falling under the category of shared control systems. In October of 2001, the CyberKnife was cleared by the FDA, making it the very first image-guided robotic technology for non-invasive radiation procedures.

3.3.2 Standard Features

The CyberKnife has the following features:

- Compact, lightweight linear accelerator (LINAC) mounted on a robotic arm
- Two Flat panel cameras
- DTS - Dynamic Tracking Software

- Synchrony-tracking vest with LED markers
- Camera array with 3 CCD camera [1]

LINAC is mounted on a robotic arm which provides lesion treatments at targeted regions of the body using radiation. The stereotactic radiosurgery system (SRS) uses body's skeletal structure as a reference frame as compared to traditional SCS systems where the surgeon synchronizes the markers.

The Dynamic Tracking Software technology makes minor adjustments to compensate for patient movements, thus giving the system a higher level of accuracy. Using pre-prepared CT images of the bone structure as markers, lesions are marked. The flat panel cameras are positioned perpendicular to the X-ray which is mounted on the ceiling. During the actual surgical procedure X-ray images are used in real time for accurate positioning of the LINAC for the delivery of the radiation beam [1].

3.3.3 Applications

The CyberKnife is used for radiation treatment of lesions, tumors, and other conditions.

3.4 The Raven (I and II)

3.4.1 Overview

The Raven was designed by the army as a teleoperated system and was adapted as a research tool that allowed researchers in multi-disciplinary fields like surgery, computer science and engineering to experiment, collaborate and innovate and further the research of robotic surgery. The Raven I was released in 2005. Raven II was completed and seven prototypes have already been released to various universities.

3.4.2 Standard Features

Main features of the Raven I system include:

- The patient site (slave)
- The surgeon site (master)
- A network connecting the two

The Raven has dual arm with laparoscopic tools, a 1000Hz real-time control loop, seven degrees of freedom per arm. spherical mechanism that allows rotation around remote center, USB 2.0 computer interface, open-architecture Linux control system, PLC safety processor, interoperable network protocol, rugged hardware and software for control using two PHANTOM Omni haptic devices [12].

The patient site, or the slave, has two surgical devices positioned over the patient. The surgeon site, or the master, has two control devices and a video feed, using a communication layer consisting of any TCP/IP network, coming in from the operative site [12].

3.4.3 Improvements to Raven I in Raven II

The Raven II is a joint project between UCLA Santa Cruz Human Bionics Laboratory and the University of Washington Biorobotics Lab [8].

Raven II has the following improvements over Raven I [12].

- Tool interface redesigned for cable driven tools
- Adapted to commercial surgical robotic instruments
- Actuation for a seventh degree of freedom

- Gripper with 3-axis wrist
- More compact mechanism

3.5 The Socrates System

3.5.1 Overview

The Socrates system allows worldwide remote access of a surgeon with another operating surgeon. The surgeons can hold discussions, as well as view live video images generated by overhead or endoscopic cameras. Socrates was first used in February of 2001 [11].

3.5.2 Applications

With the use of SOCRATES, new definitions have been coined.

- Telementoring - the use of this technology in teaching surgical procedures via video-conferencing technology.
- Telesurgery - the surgeon performs the operation from a remote console. The location of the console can be within a few feet or miles.
- Telestration - Surgeon draws on a tablet to virtually illustrate on the local surgeon's video screen. This can be used to highlight a region of interest [5].

3.6 The MiroSurge Robotic Surgery System

3.6.1 Overview

The MiroSurge is a robotic surgical system designed by the German Aerospace Center DLR company for minimally invasive surgical procedures, but has the versatility to be used in open surgery. This surgical system design allows it to have intuitive interaction with the MIRO robot [16].

Two different types of interfaces are provided by MiroSurge. One type is the bimanual haptic type of force and the partial tactile feedback, gives direct perception of the remote surgical environment. In the other type the surgeon can control the instruments by optically tracked hand-held forceps [16].

3.6.2 Standard Features

The MiroSurge has the following features [16].

- Haptic feedback on two surgical arms holding instruments
- Bi-manual configuration with axis four aligned with the forearm
- One surgical arm with two endoscopic High Definition cameras which provide stereoscopic 3-D image
- Contact free interface as Surgeons console
- Dedicated left and right handed control
- 7 degrees of freedom inside a patient

The robotic arms can be angled which provides a high degree of freedom inside the patient. Sensors for each joint of the robot make it easier to grab and insert the endoscopic instrument into the body. The surgeon sits at the surgeon's remote console and teleoperates with haptic input devices. Forces exerted on the

organs are simultaneously measured and reported back to the surgeon. The inside view of the patient is provided with stereo display with no need for additional glasses, unlike with the ZEUS model. The robotic arms contain force capture sensors which transmits feedback and gives the surgeon greater touch sensitivity. Actuators allow the surgeon to move the controls with the same ease as moving a feather [16].

3.6.3 Applications

This surgical system was designed with both MIRS and open surgery in mind. Future improvements are expected to allow for compensation of heartbeat so surgeons can do heart surgery without stopping the heart [1].

3.7 Trauma Pod

3.7.1 Overview

DARPA was given a twelve million dollar contract to create a modern day MASH unit which will receive, assess and stabilize wounded soldiers. The Trauma Pod is being designed with these needs in mind. The present prototype has a team of robots to assist it, all of them controlled by a remote surgeon [1].

3.7.2 Standard Features

- The Trauma Pod has the following features:
- Three arms on a lead robot
- Bed monitors vitals, administer fluids and oxygen, and performs anesthesiologist functions.
- Voice activated robotic arm works as scrub nurse
- Tool dispensing robot acts as circulating nurse
- Software controlled monitoring to avoid collisions

The lead robot has two arms with surgical instruments under the surgeons control and one arm with an endoscope. The robot surgeon performs temporary fixes to stabilize the injured until they can reach the hospital. Specific software has been introduced to avoid collisions between interacting robotic systems and to maintain fidelity to the order of instructions. A human surgeon has complete control over all the robots in the system [1].

3.7.3 Future Applications of Trauma Pod

In the future, the plan is to implement the Trauma Pod in combat areas via telesurgery and telecommunications while protecting the actual surgeons in a remote location.

In a four step process, the first step involves loading the wounded soldier into the pod via a fully automated machine. The second step involves complete initial scan and administration of oxygen, fluid or blood infusion, as well as processing and prep work for triage and treatment.

The third step involves the remote surgeon teleoperating the instruments to stabilize the patient. The final step is airlifting the injured via evacuation helicopters to the nearest field hospital.

Table 2 gives an overview of the major advances in robotic surgery from 1980-2012 [1].

Table 2: Timeline of Major Surgical Robotic Systems

1980s	Telepresence surgical system	Stanford Research Institute (SRI) & NASA's Ames Research Center
-------	------------------------------	---

1985	Puma (Programmable Universal Manipulation Arm) 560	Developed at Imperial College (UK) as the 1 st Robot used in Neurosurgery,
1988	PROBOT	Developed Imperial College (UK), used in Transurethral prostate resection (TURP)
1992	ROBODOC	Developed by Integrated Surgical for Orthopedic surgery
1993	HERMES	Developed by Computer Motion for use as voice controlled integration of operative room components
1994	AESOP 1000	Developed by Computer Motion, approved for use in laparoscopic abdominal surgery
1997	<i>ZEUS</i> Surgical System	FDA approval for <i>ZEUS</i> developed by Computer Motion used for reanastomosis of a fallopian tube
1997	<i>da Vinci</i> Surgical System	The <i>da Vinci</i> Surgical System manufactured by Intuitive Surgical Inc
1998	Surgeon Programmable Urological Device (SPUD)	Developed by NTU & Dornier Asia Medical for TURP, prostate biopsy and brachytherapy seed placement
1999	Orthopilot	Developed and received a CE marking
1999	NeuroMate	Developed by Integrated Surgical Systems Inc. designed for stereotactic brain surgery.
2000	The ARTEMIS system	Developed by Karlsruhe Research, is a telemanipulator for the abdominal minimally invasive surgery
2001	StealthStation	Developed by Medtronic Surgical Navigation Technologies for cranial, neurologic, spinal, and ENT procedures
2001	Socrates Robotic Telecollaboration System	Developed by Computer Vision. Allows shared control of AESOP 3000 from different locations
2001	<i>ZEUS</i> Surgical System	<i>ZEUS</i> Robotic Surgical System from Computer Motion receives FDA approval for robotically assisted laparoscopic and thoracic procedures.
2001	Orthopilot	FDA approval for Orthopilot for executing large joint replacement/corrective surgeries
2001	CyberKnife	Developed by Accuray Incorporated, FDA approved for use in radiosurgery
2001	SOCRATES	Developed by Computer Motion. Received FDA approval as robotic telecollaboration system
2004	Trans-rectal Ultrasound (TRUS) Prostate Robotic System	Developed by John Hopkins University for use in trans-rectal ultrasound guided biopsy of prostate
2005	SRI's M7 Telesurgical Robot	Developed by SRI International, for use in telepresence surgery
2005	The Raven I	Developed by The University of Washington for open surgery and MIS
2006	TRUS-Guided Brachy-therapy	Developed by John Hopkins University for use in Trans-rectal ultrasound guided brachytherapy
2007	NeuroArm	Developed by University of Calgary and MacDonald Dettwiler and Associates, used in neurosurgery for both biopsy and microsurgery
2009	Robotic Doppler Micro Probe	Developed by Vascular Technology. Doppler for vascular identification during robotic microsurgical procedures
2009	The MiroSurge Robotic Surgery System	Developed at the Institute of Robotics and Mechatronics of the German Aerospace Centre for MIRS
2009	iDrive Intelligent Power Unit	Developed by Power Medical Interventions, FDA approved for resecting and transecting tissue as well as for creating anastomoses between structures
2010	SOFIE "Surgeon's Operating Force-feedback Interface Eindhoven" Surgical Robot	Developed by Eindhoven University of Technology. 1 st surgical robot to incorporate force feedback

2011	Endo Stitch Automated Suturing Device,	Developed by Covidien as an automated suturing device
2012	The Raven II	Developed and seven prototypes sent for evaluation
2012	Amadeus Robotic Surgical System	Developed by Titan Medical Inc (Canada) for laparoscopic surgery

4. CONCLUSIONS

In the past decade alone, multiple companies and universities have been taking advantage of the funding available as well as the increasing popularity of robotics to create better and more efficient robots for various fields. While cost has been an issue when it comes to the design and development of the robots, the economic feasibility of this endeavor has fueled the fires of many robotic engineers around the world. Many of the surgical robots used in modern day surgery find their origins in defense and commercial market. With advancements in telecommunications, the emergence of subfields in remote medicine, like telesurgery, has taken foreground.

In this paper, we provide a review of the latest robotic surgical technology. We classify and compare the surgical robotic systems and discuss their future directions.

Robotic surgery may have miles to go, but it has already proven its worth according to many medical professional as well as patients around the globe. Though the learning curve for these systems are a bit steep, there is no doubt that this is the surgical technology of the future. With the MASH and Trauma Pod creation in the works, the fire that fueled this area of research has found its goal. In the new digital age, with the exponential growth of technology, the next decade promises to bring even greater, more compact, versatile and precise surgical systems.

5. REFERENCES

[1] Surgical Robots. The Official Medical Robotics News Center for AVRA Surgical Inc. 2012 [cited 2012 24 April]; Available from: <http://allaboutroboticsurgery.com/surgicalrobots.html>.

[2] Berkelman, P. and J. Ma, A Compact Modular Teleoperated Robotic System for Laparoscopic Surgery. *Int J Rob Res*, 2009, 28(9): p. 1198-1215.

[3] Bonsor; Kevin; Strickland, J. How Robotic Surgery Will Work. 2000 30 October [cited 2012 04 April]; Available from: <http://science.howstuffworks.com/robotic-surgery.htm>.

[4] Childress, V.W., Resources in Technology: Robotic Surgery, in *The Technology Teacher* 2007, www.iteaconnect.org.

[5] Ghodoussi, M., S.E. Butner, and W. Yulun Wang Yulun, Robotic surgery - the transatlantic case. *CORD Conference Proceedings*, 2002. 2: p. 1882-1882.

[6] Guthart, G.S. and J.S. J.K, The IntuitiveTM telesurgery system: overview and application. *Ieee International Conference On Robotics And Automation. Proceedings*, 2000. 1: p. 618-611.

[7] Haidegger, T., J. Sándor, and Z. Benyó, Surgery in space: the future of robotic telesurgery. *Surg Endosc*, 2011. 25(3): p. 681-690.

[8] Hannaford, B. R., J. Raven II Research Surgical Robot. 2012.

[9] Holt, D., et al., Telesurgery: Advances and Trends. *University of Toronto Medical Journal*, 2004. 82: p. 3.

[10] Lanfranco, A.R., et al., Robotic surgery: a current perspective. *Ann Surg*, 2004. 239(1): p. 14-21.

[11] Lobontiu, A.L., D. ROBOTIC SURGERY AND TELE-SURGERY: BASIC PRINCIPLES AND DESCRIPTION OF A NOVEL CONCEPT. 2007.

[12] Lum, M.J.H., et al., The RAVEN: Design and Validation of a Telesurgery System. *Int J Rob Res*, 2009. 28(9): p. 1183-1197.

[13] Maan, Z.N., et al., The use of robotics in otolaryngology-head and neck surgery: a systematic review. *Am J Otolaryngol*, 2012. 33(1): p. 137-46.

[14] Speich, J.E.R., J Medical Robotics. *Encyclopedia of Biomaterials and Biomedical Engineering*, 2004. DOI: 10.1081/E-EBBE 120024154.

[15] Sung, G.T. and I.S. Gill, Robotic laparoscopic surgery: a comparison of the *Da Vinci* and *ZEUS* systems. *Urology*, 2001. 58(6): p. 893-8.

[16] Tobergte, A.H., P.; Hagn, U.; Rouiller, P.; Thielmann,S.; Grange,S.; Albu-Schäffer,A.; Conti,F.; Hirzinger, G. , The sigma.7 haptic interface for MiroSurge: A new bi-manual surgical console. . In *Proceedings of IROS*, 2011: p. 3023-3030.

[17] Valero, R., et al., Robotic surgery: history and teaching impact. *Actas Urol Esp*, 2011. 35(9): p. 540-545.

Design and Prototyping of an Interface Tool for Aphasic Patients

Oren Masory

Ocean and Mechanical Engineering Department
777 Glades Road Boca Raton, FL 33431
USA

Jonathan LATAPIE

Ecole Nationale D'Ingeniers De Tarbes
47 Avenue d'Azereix – BP 1629 65016 Tarbes
France

ABSTRACT

In hospitals aphasic patients, individuals affected by speech disorders and others are unable to communicate orally. As a result, it is very difficult for them to make the hospital employees understand their particular needs. The goal of the project was to design an interactive tool by which these patients will be able, accurately, to express their needs and feeling and to respond to inquiries from the medical team.

The proposed solution is based on creating a tool based on navigational menu which will allow the patient to express his most likely needs such as comfort and food. Moreover, the tool should provide the capability to communicate with the medical staff during the evaluation of his medical state such as pain, pain strength and duration.

The navigational menu was designed to be intuitive, complete and user-friendly. To cover the case in which the user wants to specify a need that is not included in the menu a writing tool, a virtual keyboard, was added.

The menu and the navigation process are presented graphically, which make it very easy to use by patients with motion difficulties. Also, the use of colors, large buttons and pictograms make the navigation process easier. The program was written in Visual Basic and special efforts have been made to make it reliable, robust and relatively easy to use.

Keywords

Patient interface, Interface to Aphasic patients.

1. INTRODUCTION

Speech disorders are type of communication disorder in which 'normal' speech is disrupted permanently or temporarily. Such disorders are common in people with Cerebral Palsy, these patients require several hospitalizations throughout their life and may need alternative and augmentative communication methods to create the most advantageous communication between patient and staff. This disorder can also be caused by cerebral vascular accident, neurological anomalies, stroke or other traumas. In some other cases patients cannot talk due to a particular treatment e.g. tubes are inserted through their mouth to tier lungs or stomach. In all these and other cases the individuals are unable to communicate concerns with the medical care takers and therefore an alternative communication tool, between the patient and the medical staff, should be provided in order to enhance the medical service and treatment.

In hospital environment patient's inability to speak can be

the source of a multitude of problems, for example a misunderstanding can occur while the patient is trying to describe a pain to a doctor and this situation can result in inadequate treatment.

Additionally communication disorders generates a loss of dignity, in many cases the relative who is visiting the person feels the need to speak to the patient rather than trying to allow him to be heard. At times patients need to recover psychologically even more than physically which requires the patient to express his feelings which is impossible with a communication tool. Emergency cases are another example for the need for such a tool, while the patient is being treated his speech is impaired (e.g. Oxygen mask) but he'll be able to communicate using such a device.

Beforehand the possibility to write out messages by hand or type them via typewriter or computer is a method of communicating that can both augment or replace verbal speech. However, in order for individuals to rely on this type of communication the small muscles of the hands must be strong enough and coordinated enough to make writing a viable option.

Furthermore a variety of communication aids exists for both augment and replace verbal speech as needed. Communication software, voice amplifiers, switches, and mounting or holding devices can all be used as augmentative means of communication. Words or symbol boards are another means of supporting or replacing verbal speech. These boards allow individuals to point to an item or a word that they wish to communicate. Some software, such as Boardmaker by Mayer-Johnson allows individuals to create their own symbols. Electronic communication devices may also be employed to support or replace verbal speech such as SuperVoca, an electronic display communication aid or the Liberator which is a device allowing synthesized speech.

2. SOFTWARE DESIGN

The aim of this project is to design and implement a computer program that would display a menu on a screen and would allow the user to easily navigate through it using a simple pointing device such as a touch pad or track ball. Therefore the interface between the user and the device is not included in the scope of study though it is assumed that the program would be run on a computer and would respond to variety of pointing

devices By using the system the patient will be able to communicate with his care taker as shown in Figure 1.

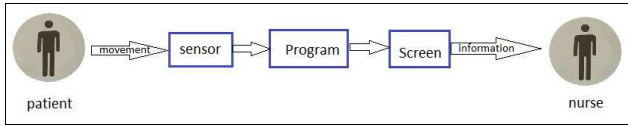


Figure 1: Communication tool structure overview

The program has to accommodate the following Main Functions (MF) and Constraint Function (CF) as shown in the diagram in Figure 2:

- MF1: Enable an interaction between the patient and the nurse
- CF1: Comply with the patient’s level of disability
- CF2: Be ergonomic and user-friendly
- CF3: Comply with Hospital or Clinic environment

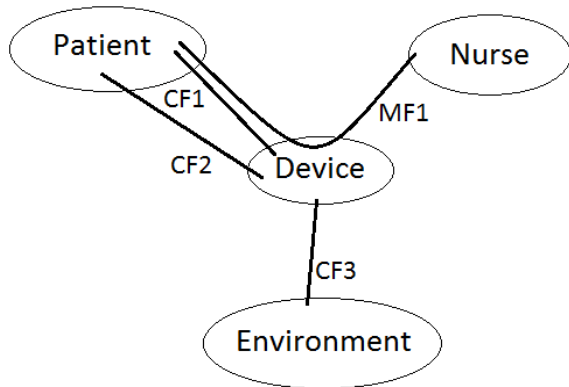


Figure 2: Specifications Diagram.

The program consists of a tree that organizes menus and submenus while the code manages both the navigation up/down tree and the different menus and displays the graphical user interface. An example of the tree structure and the navigation through the menu is illustrated in the Figure 3 The navigation process progresses by choosing a menu item and navigating down to a sub menu until the right request has been reached.

Prior to the tree design a complete list of possible patient’s requests was established in cooperation with a care provider. Once all the requests are known, the structure of the tree was determined. Then the task on hand was how to make it possible for the user to easily and intuitively to navigate through the tree. In practical terms the user would have to activate the pointing device in order to choose a menu item and as a result, the tree’s lower level menu is displayed. The process repeats until the patient finds and chooses the particular request he wanted to express.

The structure of the tree has been considered using the following guidelines:

1. The number of entities within the menu should be restricted so that the navigation is convenient.
2. The number of layers and the number of possibilities at each menu item had to be restricted.
3. The menu needs to be balanced where the more likely choices had to be on the top of the tree.
4. The flow from one level of the tree to the next has to be natural and intuitive from a patient point of view. That is to say that the way menus are classified and organized had to be logical for the patient and their particular menu’s item designation had to be familiar too.

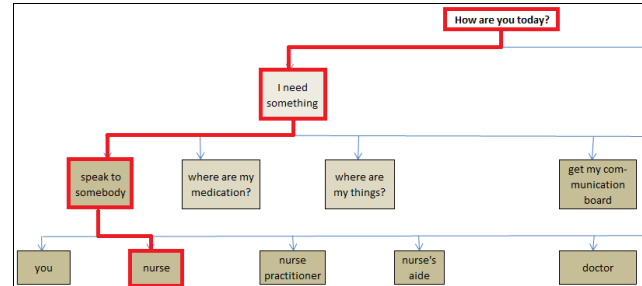


Figure 3: Navigation example.

In order to achieve the above requirements, the solution was inspired from actual oral communication between a nurse and a patient in hospitals. Thus, the navigation through the menu should “sound” like a real conversation as much as possible. Therefore, the first layer of choices (or the main menu) had to suggest replies to the question “how are you doing today?”(see figure 4).

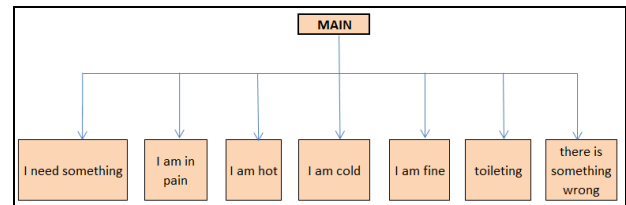


Figure 4: First menu level

3. FOCUS ON ONE CATEGORY

Menu items related to pain intensity, pain type, pain duration and part of the body were expressed in question’s form which appears like an actual diagnosis process. These items would be passed over automatically in an established order which is the most commonly used in medical diagnosis:

1. “Which part of the body hurts?”
2. “How long have you had the pain?”
3. “Can you describe the pain? “
4. “How intense is the pain?”

That means that once a particular part of the body is specified the user is directed to answer the above question in that sequence. The possibility of letting the patient to specify each of these 4 items at his own convenience was evoked. That

is to say the user would specify the intensity of the pain first and then the duration for example.

This methodology would have been a bit confusing since once the user had answered a certain question (“pain intensity” for example) he would be automatically directed to the next question (“pain form”) to which he can answer by choosing another parameter to specify. This means that the diagnosis would require a considerable number of pointing events in order to move deeper in the tree.

For example, to express a right shoulder pain the user is required to “penetrate” 12 layers deep in the tree “free choice solution” (see Figure 5) whereas it requires 7 clicks with the “diagnosis solution” (see Figure 6).

Free choice solution		
nod	click	number of clicks
main	0	0
I feel	1	1
pain	1	2
part of the body	1	3
upper part	1	4
shoulder	1	5
right	1	6
pain	0	6
type of pain	1	7
sharp	1	8
pain	0	8
duration	1	9
30 min	1	10
pain	0	10
intensity	1	11
3 over 10	1	12

Figure 5: Free choice solution table

Diagnosis solution		
nod	click	number of clicks
main	0	0
in pain	1	1
which part of the body hurts	0	1
upper part	1	2
shoulder	1	3
right	1	4
how long have you had the pain	0	4
30 min	1	5
can you describe the pain	0	5
sharp	1	6
how intense is the pain	0	6
3 over 10	1	7

Figure 6: Diagnosis solution table

4. SOME DETAILS

Navigation Control

The navigation control allows the user to step up or down the tree. Also it allows him to go back to the previous step and if necessary to go back to the main menu (top of the tree). The last two options are very important and therefore special buttons were designed for their implementation (see Figures 7 and 8).



Figure 7: “main menu” button



Figure 8: “go back” button

Nurse-patient interaction controls

Even though the main purpose of the graphical user interface is to enable the user to navigate through the tree it should be kept in mind that the main goal of the project is to assist patients with speech disability to communicate. Thus, the user should be able to answer any question by “yes”, “no” or “I don’t know” using the pointing device. For this purpose corresponding keys were added to the base menu (see Figure 9). For a nurse to be aware of the answer, it was decided to implement a function which would change the color of the button during a few seconds from the moment the user clicked above it.



Figure 9: “yes”, “I don’t know” and “no” buttons

Differentiation between menu item and requests

Every nod within the tree leads to either a request or a menu. For example, as shown on the Figure 10 the user can choose to ask for some **juice**, some **milk** or some **soda** but he can also select the **water** and then be able to specify **hot water** for instance. To indicate that a further (deeper level in the tree) selection is available a little sign on menu item was added (see Figure 11).

Writing tool

In case where the user needs to express or ask for something that is not included in the menus, a writing tool (virtual keyboard) was provided as shown in Figure 12. An item

menu that request the writing tools, shown in Figure 13, was added to the base menu.

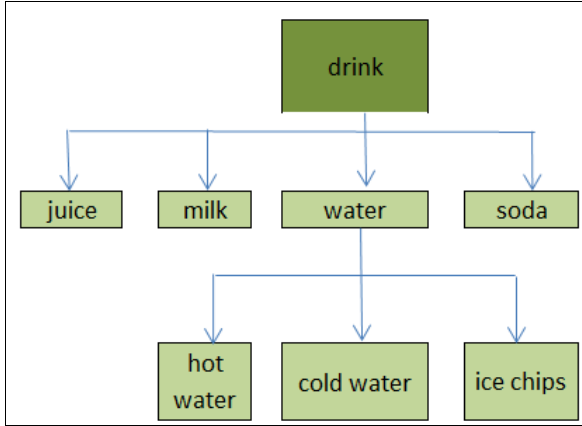


Figure 10: “drink” category

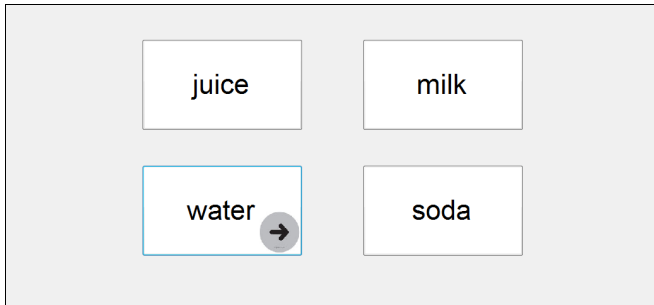


Figure11: Button sign

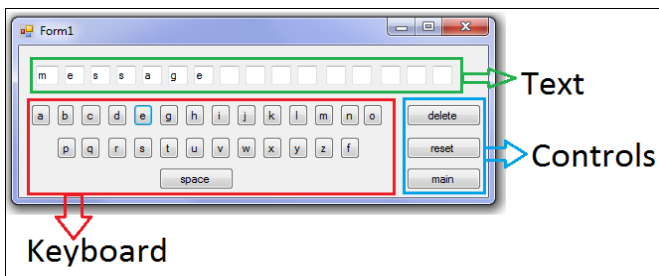


Figure 12: Writing tool structure



Figure 13: Writing tool access button

Sum-up box

While the user goes through the menu a sum-up box is being constructed. It displays all the answers that were provided by the patient during the navigation process. This summary helps the nurse in her evaluation of the patient state since all the information is displayed on one screen and she does not have to remember every answer that was given during the process (see Figure 14).

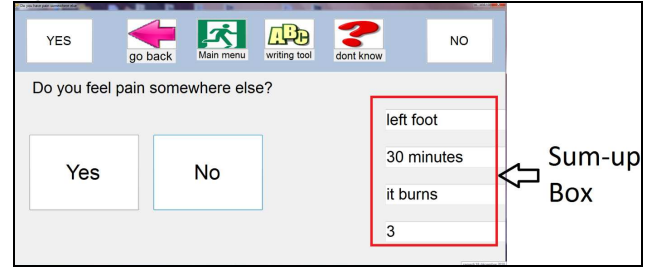


Figure14: Example of Sum-up box

Button highlighting function

Since some users have difficulties in controlling the pointing device a feature, which changes the color of menu item when the pointer is in its proximity, was added. This way the user knows clearly where which menu item is “active” and can be selected. It makes the use of the pointing device easier to use and the selection process with fewer errors (see Figure 15).

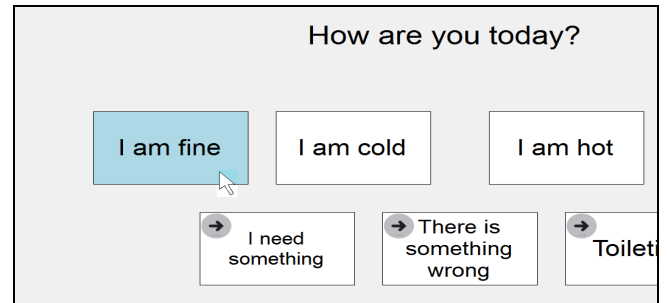


Figure 15: Example of the highlighting function.

5. CONCLUSIONS

The final program implemented all the menus, the tree structure and all the necessary controls. Figure 16 illustrates three consecutive steps of the graphical user interface when the user starts from the main menu to reach the “I want to speak to the nurse”.

The patient interface program has been completed and tested. Modification and additions to the program can be easily achieved due to its structure. At this point in time, the program was not evaluated by actual patients due to time and legal restrictions. This evaluation has to be done in order to determine if the menus and the tree structure is suitable, and whether or not additional items should be added. Also, testing of different pointing devices is essential in order to accommodate different patients.

Also, implementation of the tool on different platforms will make it more accessible. Another option that is being considered is to implement the tool on the hospital server. This way the nurse will be able to communicate with the patient from her station without the need to walk to his room. This way time is being save and service is quicker.

7. REFERENCCESS

- [1] Bill Sempf, Visual Basic 2008 For Dummies. ISBN-13 978-0470182383.
- [2] Todd Herman, Allen Jones, Matthew MacDonald, and Rakesh Rajan, Visual basic 2005 recipes : a problem-solution approach, ISBN-13 978-1590598528.
- [3] MSDN Library: msdn.microsoft.com
- [4] www.support.microsoft.com
- [5] www.vbfrance.com
- [6] www.vb.developpez.com

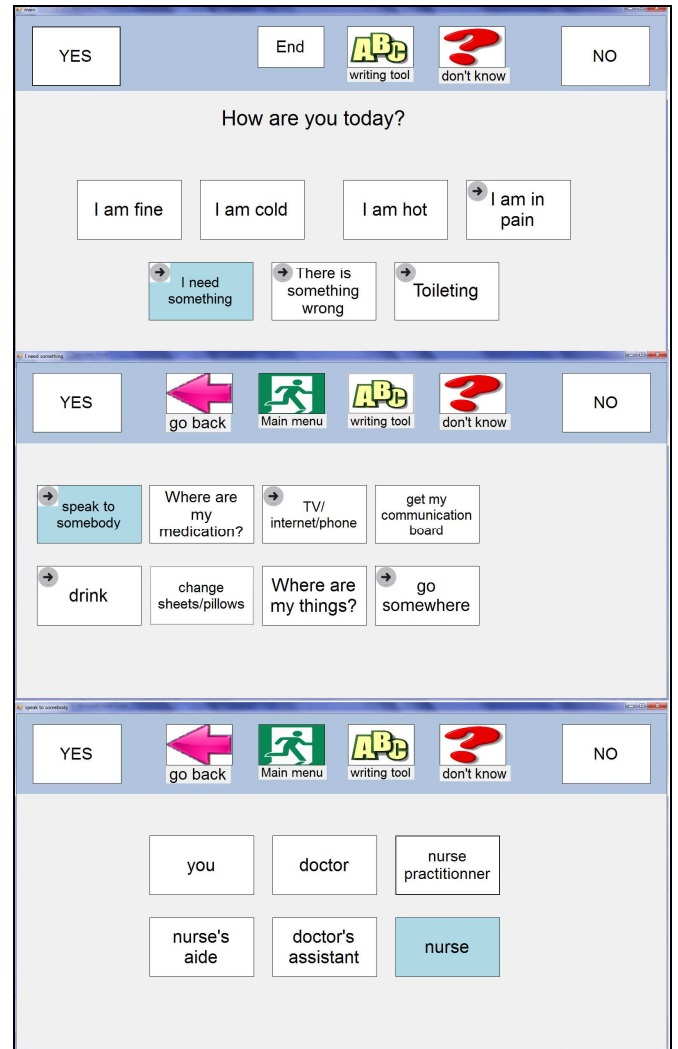


Figure 16: Succession of the 3 graphical interfaces for the “I want to speak to the nurse” request.

Using Neural Networks to Predict Cardiac Arrhythmias

Roland Adams
Mercer University
1400 Coleman Ave
Macon, GA 31207
011-1-404-310-9182

Rockin237@gmail.com

Anthony Choi
Mercer University
1400 Coleman Ave
Macon, GA 31207
011-1-478-301-2953

choi_ta@mercer.edu

ABSTRACT

Cardiac arrhythmias are classified by abnormal activities in the heart. These abnormalities can be analyzed by an electrocardiogram (ECG). Details from this electrical signal can be used to classify what type of arrhythmia, if any, the patient has by analyzing the PQRST wave properties. The arrhythmias analyzed for this study are Bundle Branch Block, Supraventricular Tachycardia, Ventricular Tachycardia, Tachycardia, and Bradycardia. Multiple data samples of normal ECG characteristics also were read by an artificial neural network (ANN) and analyzed for the differences between a normal signal and an irregular signal. The data was extracted from the MIT-BIH Supraventricular database and the MIT-BIH Arrhythmia database. A typical method used to analyze cardiac arrhythmias is to take the Fast Fourier Transform (FFT) of the signal. In this study, an alternate method is used to predict cardiac arrhythmias. A neural network is designed and programmed with this data and then tested to validate the data set. The pattern recognition tool in MATLAB is then used to analyze and predict the data. The program results were tested to validate the data set. The ANN achieved 98.6% accuracy on the test data. The findings and outcome probabilities from this study are more accurate than some current methods of analysis used today. When neural networks are further used to analyze and test medical data samples, the medical community and patients will experience improvements in the diagnosis of heart abnormalities and early detection of debilitating medical conditions.

Keywords

Cardiac Arrhythmia, Electrocardiogram, Fast Fourier Transform, MATLAB, Multilayer Feed-Forward, Neural Network.

1. INTRODUCTION

An electrocardiogram (ECG) contains a large amount of information that can be used for determining many different attributes of the electrical activities of the heart. Typically, an ECG varies from person to person due to the difference in the position, size, anatomy of the heart, age, body weight, chest configuration, and various other factors. An ECG is a representative signal of cardiac physiology, which can be very useful in diagnosing cardiac disorders [1, 2]. The ECG was originally observed by Waller in 1899. In 1903, Einthoven introduced the electrophysiological concepts still used today, which includes the labels of the waves [3]. To this day, an ECG is the main way of gathering information from the body in order to

better analyze the heart's activities [4]. The heart is one of the most important organs in the body due to the fact that it supplies the body with oxygen [5]. Furthermore, filtration of an ECG is very crucial to get the parameters of the signal in order to recognize variability's of the heart's activities [6]. Coronary care units use a 12-lead ECG. These units analyze the QRS wave in order to quickly gather information. The PQRST wave will be described in more detail in the next section. The goal is to store data each time an arrhythmia occurs, however to accomplish this, the device needs a very accurate QRS recognition capability [7]. There are multiple ways that this signal can be analyzed in order to find out the necessary information of each heartbeat. From this, we can use this data to analyze every single beat of the heart and predict problems.

There have been multiple methods as to better analyze these arrhythmias such as cardiac auscultation, phonocardiography, Discrete Wavelet Transform (DWT), Fast Fourier Transform (FFT), and using a Neural Network to analyze signals. Cardiac auscultation is widely used by physicians, but it is quite the difficult skill to master. Phonocardiography is the recording of sonic vibrations of heart and blood circulation. This can provide valuable information when dealing with heart valves and the hemodynamics of the heart [8]. Another way to analyze is the DWT. In 1989, Mallat proposed the fast DWT algorithm to decompose a signal using a set of quadrature mirror decomposition filters. These filters have band-pass and low-pass properties specific to each mother wavelet. This removes the redundancy in the signal and compresses the signal while still giving a high quality reconstruction of the signal [9]. Both the FFT and the DWT have their own advantages and disadvantages. This paper analyzes a special type of neural network in more detail.

2. PROBLEM FORMULATION

The World Health Organization has estimated that 12 million deaths occur worldwide each year due to cardiovascular diseases. The fact is that Coronary Heart Disease (CHD) has risen four-fold in 40 years. CHD is caused when the coronary arteries do not supply enough blood to the heart due to clogging [10-12]. They are responsible for one in three deaths in the world. Therefore, the goal of many medical professionals is to find a more accurate method of analyzing these cases. Ninety percent of the deaths are due to cardiac arrhythmias. Many deaths are unfortunately caused by ventricular fibrillation (VF), which is frequently initiated by ventricular tachycardia [13, 14].

A problem in the heart is referred to as a cardiac arrhythmia which is abnormal electrical activity in the heart. Cardiac arrhythmias can best be predicted by ECG. By analyzing the features in an ECG signal, certain arrhythmias such as Supraventricular Tachycardia (SVT), Ventricular Tachycardia (VT), Bundle Branch Block (BBB), Bradycardia, and Tachycardia can be better determined. There are many databases out there for personal use that make project like this possible. So, finding quality ECG signals, that does not require filtering and are relatively clean, are desired. These signals can then be analyzed by an Artificial Neural Network (ANN) to detect signal properties that can differentiate the differing cardiac arrhythmias listed above. Some typical approaches for ECG classification use timing classifiers implemented using a decision tree which use temporal criteria and amplitudes to determine the differences between normal and irregular rhythms [15]. Also, there is pattern recognition, Bayes theorem, and fuzzy logic that have been used, some of which are relatively inaccurate in correct classification [15]. Typically, ECG signal processing is time consuming and too sensitive to the amount of noise, so a good solution proposed is to analyze the RR time intervals or determining the heart rate variability (HRV) [16]. In a study conducted by Darrington and Hool, the contemporary method for reporting the performance of a beat classification algorithm involves beat-by-beat comparisons between the classes as indicated by the algorithm. Common ways are sensitivity, specificity, and positive predictivity. This is a good method for analysis; however, when there are more than two classes, problems can arise [17]. Lyapunov exponents are another type of measurement that can be used to analyze ECG signals. They are used for a qualitative measure for distinguishing among the various types of orbits based upon their sensitive dependence on the initial conditions [18].

Using an ECG is a noninvasive technique that is simple to analyze. An ECG is the most commonly used diagnostic test that can produce quick results with portable equipment. A patient is attached to few leads and then every single beat is analyzed by the equipment that makes up the ECG. A possible pitfall that can adversely affect the interpretation of an ECG signal is an artifact. Artifacts are defined as ECG abnormalities that may be due to sources other than the electrical activity of the heart. If these are not solved, then the wrong diagnosis like atrial flutter and ventricular tachycardia could be incorrectly diagnosed, which could lead to death [19]. In a previous study, the maxima of the filter output that is above a certain threshold is analyzed as long as they don't fall within a refractory period of a certain number of samples after the QRS duration is detected [20]. This is potentially a good idea for signal analysis in an ANN.

In order to better understand how an ECG works, one needs to have a better knowledge of the signal outputted by the leads that are analyzing the heart. A typical heartbeat consists of a PQRST wave as shown in Figure 1. Each of these letters represents a different part of the signal. Starting with the P wave, this represents atrial contraction. This is when the blood is flowing from the atria into the ventricles. The SA node sends out a signal to the AV node during this time. Next, the QRS wave is when the ventricles contract. This depolarization occurs after the SA node has stimulated the ventricles to contract. This has higher amplitude due to the fact that the ventricles are so powerful. They have to deliver blood through the lungs and also through the entire body, depending on whether it is the right or left ventricle. After this, the T wave represents the ventricular recovery time. Each

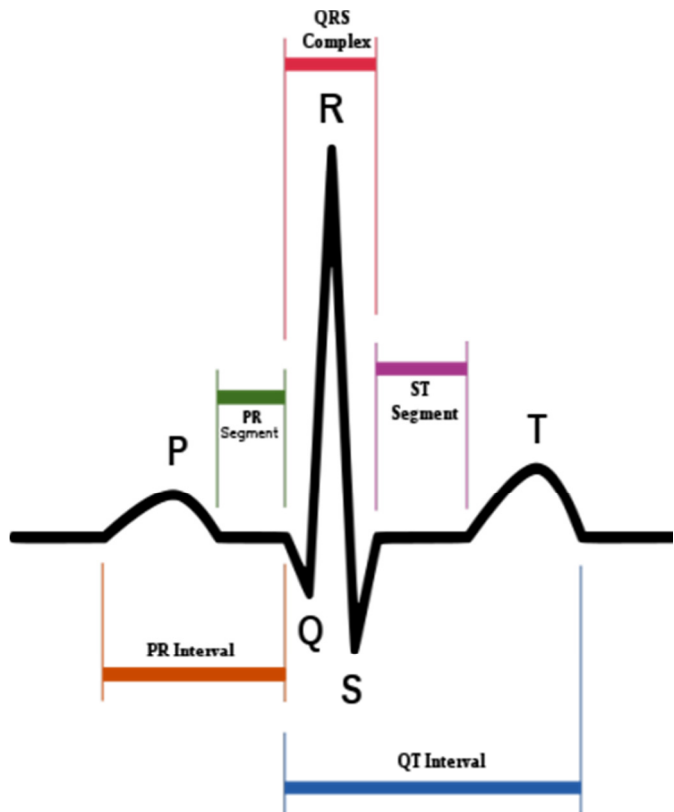


Figure 1. Diagram of the ECG signal outputted by the heart.

heartbeat contains each part of this signal except for some arrhythmia cases [4].

Each heartbeat signal is analyzed by the ECG. Certain properties help us to better determine which cardiac arrhythmia, if any, is occurring in the heart. For the arrhythmias in this paper, most of them can be analyzed due to the differences in the QRS part of the signal. The width and height help determine the differences in three of the five arrhythmias.

SVT is a heart arrhythmia that is due to a fast heartbeat in the atria. Typically, the QRS wave ranges from 40 ms to 100 ms in a healthy patient. As for the SVT case, most cases deal with the fact that the QRS wave is now less than 40 ms long. Typically, the patient will have above 150 beats per minute with a shorter than normal width of the QRS wave. This can occur in patients for a few minutes to a few days and can cause dizziness, rapid breathing, and chest pain. SVT is rarely life threatening but it can be treated by a few medications or physical maneuvers that are relatively simple [21].

VT is a heart arrhythmia that originates in the ventricle of the heart. Unlike SVT, this is a life threatening arrhythmia that can cause ventricular fibrillation and sudden death. 80% of cases of sudden cardiac death (SCD) are caused by spontaneous VT. Predicting the difference between VT and ventricular fibrillation (VF) can significantly increase the rate of the survival rate of patients [22, 23]. One way of classifying this is that it may have three or more beats in a row that originate from the ventricle. A way that VT can be diagnosed is noticing that the P wave in the PQRST wave is no longer visible because the T wave from the

previous beat has overtaken it [21]. Typically, the treatment includes a shock to the patient to get the heart back on track. There is one case that SVT and VT can be misdiagnosed as the other due to the fact that SVT has a minor case that deals with a prolonged duration of the QRS wave. An easy way to prevent this method is shown in this paper when the entire signal is analyzed instead of only the FFT characteristics of the signal [24].

BBB is due to disruption in the normal flow of electrical pulses. Typically, BBB has QRS width duration greater than 120 ms. Right and left BBB are possible and the ECG signal will be shifted left or right towards the P or T waves respectively. Some patients are born with this condition and many of these patients can be quite active. Heart disease is a possible consequence but overall, this condition is not as serious as many other types of arrhythmias. In a more extreme case, one might need a pacemaker to have enough electrical supply to the heart muscle [25].

Bradycardia is defined as a slow heartbeat below 50 beats per minute (BPM). Analyzing the time between pulses is how this arrhythmia is classified. This can be caused due to drug use or heart disease. If the person is stable, then most of the time treatment is not needed. However, if the patient is not stable, then atropine can be administered to speed the heart back up.

Tachycardia is defined as a fast resting heart rate of above 100 beats per minute. Like Bradycardia, this is quite similar other than the heart is racing due to bad diet or poor heart condition. The heart is essentially working harder than it has to in order to achieve the same result. Treatment may include adenosine to slow down the heart.

The FFT is a great way to determine frequency characteristics of a signal and many ECG's still use this today. The only problem occurs when the frequency characteristics of two differing arrhythmias have similar characteristics like the SVT case that looks like VT. Analyzing the signal will show that there is no P wave and there is a much higher amplitude in the VT signal. On average, taking the FFT of a signal to analyze arrhythmias is about 85% accurate [4]. Using this knowledge, one could better analyze signal characteristics and maybe even bypass the FFT analysis.

3. METHODS

The analysis of this data is done by an artificial neural network. An ANN is a computer network consisting of artificial neurons that are used to solve problems without creating a model of a real system. This is used by a computer program MATLAB to create the desired results. Data is inputted and trained by this neural network and then some of the data is used for validation and actual testing. For the data in this project, 350 data samples of an ECG beat are used to train the data, 75 are used for validation, and 75 are used for testing the network on accuracy. As seen in Figure 2, the proposed network has 177 input data points, 8 hidden layer neurons, and 6 outputs.

The data collected was very precise to the point. The data consisted of 177 data points which was 1.40 seconds of the signal in the MIT-BIH Supraventricular Database. The data pre-processing consisted of finding the peak point for each data point and making that point 89. An example of this can be seen in Figure 3. The center point is defined as the highest peak in the entire signal with analysis on that individual beat. Some signals,

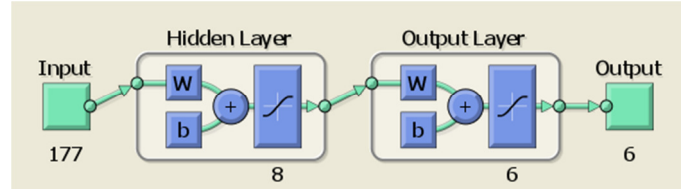


Figure 2. Neural Network setup for beat analysis of ECG.

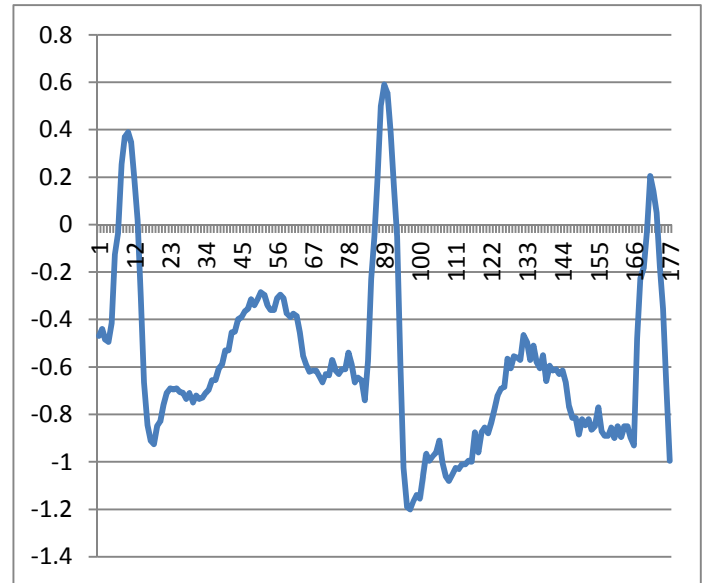


Figure 3. A 1.40 second sample of data from the MIT database.

like figure 3 shows, did have 3 multiple peaks due to the fact that the person's heart started to beat faster. So, the center peak is the highest point for the beat being analyzed. This was done to prevent discrepancies in all of the data being analyzed. This prior work is not necessarily needed, but it does help to get better results and have very few issues in analyzing data. This is the center point of the data to prevent any abnormalities in all of the 500 data points collected. This idea came from Ayub and Saini, which they analyzed the heartbeats [26]. 125 regular heartbeats, 75 SVT, 75 VT, 75 BBB, 75 Bradycardia, and 75 Tachycardia points were collected. For each case, two to six patients were used to get all of the data to add to the diversity of the data points being analyzed. The data was stored in Excel for easier processing.

The ANN used for this dataset was the pattern recognition tool in MATLAB. This tool is great for analyzing patterns of data inputted into the network especially for the nonlinear data. This tool is a multilayer feed-forward network with back propagation [27]. The 500 data points were inputted into this network and analyzed. The outputs are:

- 1) Regular heartbeat
- 2) SVT
- 3) VT
- 4) BBB
- 5) Bradycardia
- 6) Tachycardia



Figure 4. View of ECG classification and heart analysis.

From this, each data point that makes up a signal is inputted into the network and analyzed. Since the FFT of the signal is not taken, this is a very reliable way to analyze the signals for these cases only. There are other arrhythmias that would probably benefit from taking the FFT to analyze the signal characteristics.

The actual data being analyzed is the beats. Beat analysis consists of analyzing just a single beat and then classifying it. So, a supraventricular premature beat (S) is classified as SVT. A premature ventricular contraction (V) is classified as VT. Left bundle branch block (L) is classified as BBB, however, there is R and B used to also classify this arrhythmia. Regular heartbeats (N or \bullet) is an ECG's way of showing that the heart has a normal sinus rhythm. This is also shown in Figure 4. As the figure shows, when an abnormal beat occurs, the beat is classified based on the analysis done by the machine. This irregular beat is classified as a ventricular premature beat because the beat was premature and the T wave is of higher amplitude as well. Typically, an ECG used today gives a blue dot for every healthy beat. This can be seen on the MIT database as well.

4. RESULTS

The neural network trained properly and efficiently. The network analyzed the 500 data samples and used 350 for training, 75 for validation, and 75 for testing. The validation stopped after 147 epochs, which was the best validation point that had a mean squared error of 0.008. As shown in Figure 5, the data takes more to train while analyzing the signal characteristics but this is only recommended for the certain cardiac arrhythmias being analyzed. As shown in Figure 6, the testing went well and the ANN did not over train.

The error of the entire data analyzed is 1.3%. The goal of doing better than just taking the FFT for analysis of 85% was achieved. Neural Networks have the potential to have much more accuracy if trained correctly; however, there are still exceptions in all ECG signals. This does not take this into account. As shown in Figure 7, the final results of the data analyzed and the two errors are shown. One regular heartbeat was misclassified as SVT and one BBB was misclassified as a regular heartbeat.

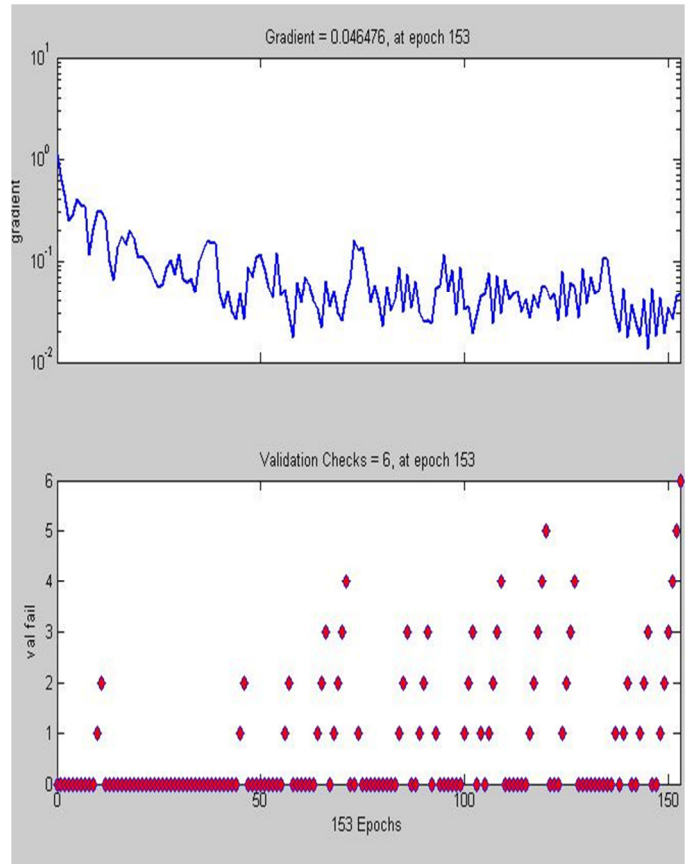


Figure 5. Gradient and validation results of the ANN

5. DISCUSSION

The errors arose from not having enough variation in the data set. The typical QRS width of a regular heartbeat is from 40 ms to 100 ms. BBB is classified by data having a QRS width above 100 ms and SVT is below 40 ms for all but one minor case. VT is classified by data having a QRS width of greater than 100 ms as well, but VT also has a higher amplitude signal because the P wave has been overtaken by this premature beat. The regular heartbeat data had 125 samples to try to avoid this problem but apparently, more of a range is needed than the data collected.

The common misdiagnosis that needed to be averted was misclassifying SVT as VT. When the FFT of a signal is taken, some of the signal characteristics are lost and other than the varying frequencies. The data, therefore, doesn't analyze signal properties like amplitude or the P wave in the signal missing like in the case of VT. As previously stated, the VT case is life threatening while SVT is not. In this analysis, this common misdiagnosis was averted with no errors.

The signals analyzed here didn't have any prior filtering needed. The signals taken from patients included:

- 1) 800, 803, 811, 824, 846, 872 on the regular heartbeat
- 2) 800, 806, 822 on SVT
- 3) 803, 872, 887 on VT
- 4) 109 and 111 on BBB

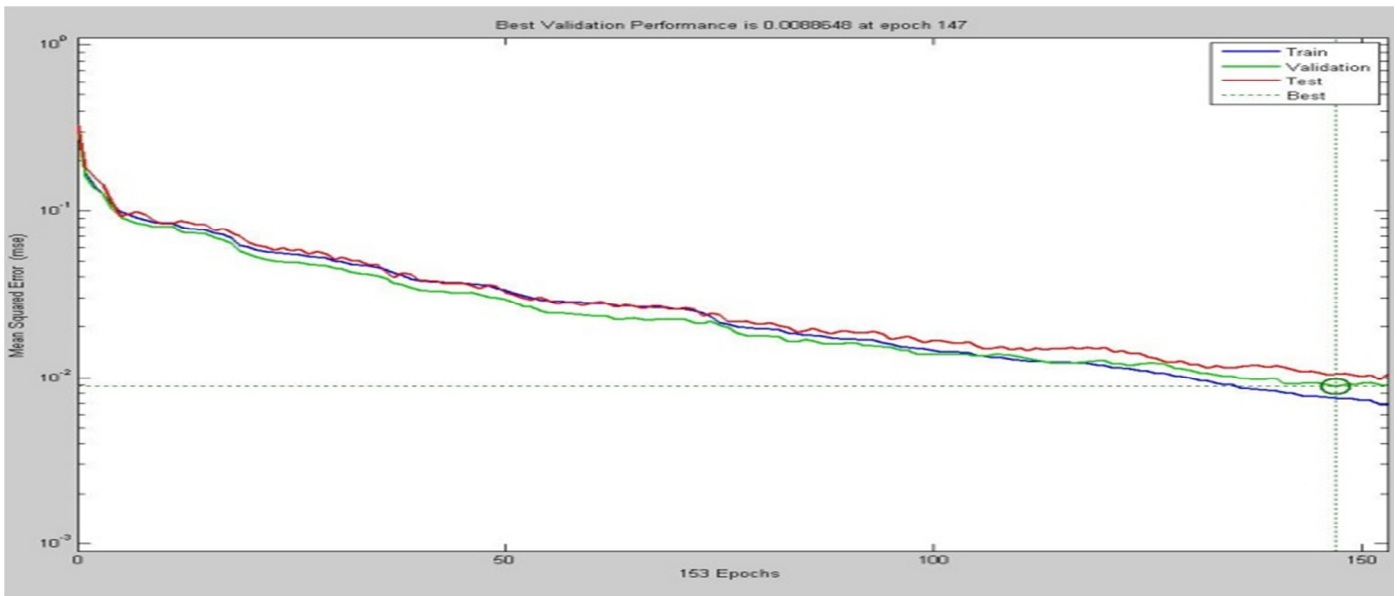


Figure 6. Validation, training, and testing performance of the ANN.

Output Class \ Target Class	1	2	3	4	5	6	Accuracy
1	23 30.7%	1 1.3%	0 0.0%	0 0.0%	0 0.0%	0 0.0%	95.8%
2	0 0.0%	9 12.0%	0 0.0%	0 0.0%	0 0.0%	0 0.0%	100%
3	0 0.0%	0 0.0%	11 14.7%	0 0.0%	0 0.0%	0 0.0%	100%
4	0 0.0%	0 0.0%	0 0.0%	12 16.0%	0 0.0%	0 0.0%	100%
5	0 0.0%	0 0.0%	0 0.0%	0 0.0%	9 12.0%	0 0.0%	100%
6	0 0.0%	0 0.0%	0 0.0%	0 0.0%	0 0.0%	10 13.3%	100%
Overall	100%	90.0%	100%	100%	100%	100%	98.7%
Overall	0.0%	10.0%	0.0%	0.0%	0.0%	0.0%	1.3%

Output Class \ Target Class	1	2	3	4	5	6	Accuracy
1	23 30.7%	0 0.0%	0 0.0%	0 0.0%	0 0.0%	0 0.0%	100%
2	0 0.0%	13 17.3%	0 0.0%	0 0.0%	0 0.0%	0 0.0%	100%
3	0 0.0%	0 0.0%	7 9.3%	0 0.0%	0 0.0%	0 0.0%	100%
4	1 1.3%	0 0.0%	0 0.0%	11 14.7%	0 0.0%	0 0.0%	91.7%
5	0 0.0%	0 0.0%	0 0.0%	0 0.0%	14 18.7%	0 0.0%	100%
6	0 0.0%	0 0.0%	0 0.0%	0 0.0%	0 0.0%	6 8.0%	100%
Overall	95.8%	100%	100%	100%	100%	100%	98.7%
Overall	4.2%	0.0%	0.0%	0.0%	0.0%	0.0%	1.3%

Figure 7. Error in final results

All had very clean signals. Multiple patients were analyzed to prove that an ANN has the capability of analyzing multiple patients. As previously noted, an ECG signal is different for each individual. Analyzing multiple patients proves the fact that ANN's have the capability of detecting minor differences and still making the correct classification on either normal or arrhythmia beats. In some signals, there was some noise. These few areas that seemed like they contained 60 Hz noise were not analyzed. A simple filtration of this signal could be done or even analyzed to test the ANN.

6. CONCLUSION

Using an ANN is more accurate than taking the FFT of an ECG signal for this case. ANN's are a great way to solve some common things in this world just by using some artificial

intelligence and training it for the right answers. By analyzing the data points in an ECG signal, many characteristics of the heart can be determined and analyzed. ANN's have much potential especially for cardiac arrhythmias. Hopefully, this type of research will continue and help make the medical field progress in the area of cardiology.

7. FUTURE WORK AND RECOMMENDATIONS

As ANN's gets better at analysis, they could be used in pacemakers [28]. There is much potential in this line of research and analysis for predicting arrhythmias.

In the future, more arrhythmias could be analyzed. Depending on the arrhythmias being analyzed, the FFT of the signals could be

taken and used to help validate the ECG. An idea is to continue analyzing the whole signal as well as the FFT. This could have the potential to correct some of the inaccuracies of just analyzing the FFT or just the signal. Also, more patients could be analyzed to better train the network. There is variation in every heart and signals that were not accounted for by only selecting a few patients. More databases could also be used to acquire more patient data.

8. ACKNOWLEDGMENTS

The research was partially supported by NASA.

9. REFERENCES

- [1] Acharya, U., Bhat, P., Iyengar, S., Rao, A., & Dua, S. (2003). Classification of heart rate data using artificial neural network and fuzzy equivalence relation. *The Journal of the Pattern Recognition Society*, 36, 61-68.
- [2] Sasikala, P., & Wahidabanu, R. (2010). Robust r peak and QRS detection in electrocardiogram using wavelet transform. (IJACSA) *International Journal of Advanced Computer Science and Applications*, 1(6), 48-53.
- [3] Belhachat, F., & Izeboudjen, N. (2009). Application of a probabilistic neural network for classification of cardiac arrhythmias. *Centre de Développement des Technologies Avancées*, 13, 397-400.
- [4] Gothwal, H., Kedawat, S., & Kumar, R. (2011). Cardiac arrhythmias detection in an ECG beat signal using fast Fourier transform and artificial neural network. *Journal of Biomedical Science & Engineering*, 4(4), 289-296.
- [5] Vijaya, V., Rao, K., & Rama, V. (2011). Arrhythmia detection through ECG feature extraction using wavelet analysis. *European Journal of Scientific Research*, 66(3), 441-448.
- [6] Qawasmi, A., & Daqrouq, K. (2010). ECG signal enhancement using wavelet transform. *WSEAS Transactions on Biology and Biomedicine*, 7(2), 62-72.
- [7] Pan, J., & Tompkins, W. (1985). A real-time QRS detection algorithm. *IEEE Transactions on Biomedical Engineering*, 32(3), 230-236.
- [8] Gupta, C., Palaniappan, R., Swaminathan, S., & Krishnan, S. (2005). Neural network classification of homomorphic segmented heart sounds. *Applied Soft Computing*, 7, 286-297.
- [9] Cervigón, R. (2011). Biomedical applications of the discrete wavelet transform. *Intec*, 1-16.
- [10] Kavitha, K., Ramakrishnan, K., & Singh, M. (2010). Modeling and design of evolutionary neural network for heart disease detection. *IJCSI International Journal of Computer Science Issues*, 7(5), 272-283.
- [11] Bulusu, S., Faezipour, M., Ng, V., Nourani, M., Tamil, L., & Banerjee, S. (2011). Transient ST-segment episode detection for ECG beat classification. *Life Science Systems and Applications Workshop*, 121-124.
- [12] Ozbay, Y., & Karlik, B. (2001). A recognition of ECG arrhythmias using artificial neural networks. *Proceedings – 23rd Annual Conference*, 23, 1-5.
- [13] Benchaib, Y., & Chikh, M. (2009). A specialized learning for neural classification of cardiac arrhythmias. *Journal of Theoretical and Applied Information Technology*, 6(1), 92-100.
- [14] Harikumar, R., & Shivappriya, S. (2011). Analysis of QRS detection algorithm for cardiac abnormalities - a review. *International Journal of Soft Computing and Engineering*, 1(5), 80-88.
- [15] Izeboudjen, N., & Farah, A. (1998). A new neural network system for arrhythmias classification. *Proceedings of the Mediterranean Conference on Medical and Biological Engineering and Computing*, 1-5.
- [16] Yaghouby, F., Ayatollahi, A., & Soleimani, R. (2009). Classification of cardiac abnormalities using reduced features of heart rate variability signal. *World Applied Sciences Journal*, 6(11), 1547-1554.
- [17] Darrington, J., & Hool, L. (2008). A new methodology for assessment of the performance of heartbeat classification systems. *BMC Medical Informatics and Decision Making*, 8(7), 1-8.
- [18] Ubeyli, E. (2009). Detecting variabilities of ECG signals by lyapunov exponents. *Neural Comput & Applic*, (18), 653-662.
- [19] Baranchuk, A., Shaw, C., Alanazi, H., Campbell, D., Bally, K., Redfearn, D., Simpson, C., & Abdollah, H. (2009). Electrocardiography pitfalls and artifacts: the 10 commandments. *Critical Care Nurse*, 29(1), 67-73.
- [20] Poli, R., Cagnoni, S., & Valli, G. (1995). Genetic design of optimum linear and non-linear QRS detectors. *IEEE Transactions on Biomedical Engineering*, 42(11), 1137-1141.
- [21] Belhachat, F., & Izeboudjen, N. (2010). Conception of intelligent classifiers for cardiac arrhythmias detection. *Centre de Développement des Technologies Avancées*, 1-10.
- [22] Joo, S., Choi, K., & Huh, S. (2010). Prediction of ventricular tachycardia by a neural network using parameters of heart rate variability. *Computing in Cardiology*, 585-588.
- [23] Clarkson, P., Chen, S., & Fan, Q. (1995). A robust sequential detection algorithm for cardiac arrhythmia classification. *Acoustics, Speech, and Signal Processing*, 2, 1181-1184.
- [24] Arumugam, S., Gurusamy, G., & Gopalasamy, S. (2009). Wavelet based detection of ventricular arrhythmias with neural network classifier. *Journal of Biomedical Science & Engineering*, 2(6), 439-444.
- [25] Ceylan, R., & Özbay, Y. (2011). Wavelet neural network for classification of bundle branch blocks. *Proceedings of the World Congress on Engineering*, 2, 1-5.
- [26] Ayub, S., Saini, J.P. (2011). ECG classification and abnormality detection using cascade forward neural network. *International Journal of Engineering, Science, and Technology*, 3(3), 41-46.
- [27] Arumugam, S., Gurusamy, G., & Gopalasamy, S. (2009). Neural network based arrhythmia classification using heart rate variability signal. *Control and Intelligent Processing Center of Excellence*, 14, 1-12.
- [28] Almassy, R., Itchhaporia, D., Oetgen, W., Snow, P. (1996). Artificial neural networks: current status in cardiovascular medicine. *Journal of the American College of Cardiology*, 28(2), 515-521

A Novel Control Algorithm for Ankle-Foot Prosthesis

Arvind Parsan

Department of Mechanical and Materials Engineering
Florida International University
Miami, Florida 33174 USA
(954)-798-4883
apars002@fiu.edu

Sabri Tosunoglu

Department of Mechanical and Materials Engineering
Florida International University
Miami, Florida 33174 USA
(305)-348-1091
tosun@fiu.edu

ABSTRACT

Patients suffering from below knee amputation utilize ankle-foot prostheses to regain partial mobility. Research efforts have focused on improving device functionality to offer patients a higher standard of living. This study proposes a novel algorithm for device control, which utilizes input from two sensors to relay data into the control system. The system processes the data according to a set of rules, and outputs a respective foot angle value to mimic the normal motion of the ankle-foot complex in natural cadence. Matlab Simulink offers exceptional utility in developing a computational model for evaluating the efficacy of the rule system. Comparison of the true and theoretical foot angle values produced low levels of error underlining the overall effectiveness of the algorithm.

Keywords

Gait, Controller, Ankle-Foot Prosthesis, Micro-controller, Matlab, Simulink, Natural Cadence, Smart Prosthesis, Biomechanics, biomimetic, Ankle-Foot Emulator, Below-Knee Prosthesis

1. INTRODUCTION

Gait is the most basic of human actions, and has been the subject of considerable study for many decades. Many people learn to walk at a young age, and take for granted the 15 independent degrees of freedom which the body regulates to create the gait cycle. Gait studies can be divided into several segments including: temporal and stride measurements, kinematics, kinetics, electromyography, balance, posture, pathology, and age. Cadence is defined as the number of steps per unit of time and differs based upon someone's weight, height, age, gender, and pathology. Cadence can be further divided into three categories: slow, natural, and fast walking. Fast, natural, and slow walkers have an average cadence of 123.1, 105.3, and 86.8 steps per minute respectively. Our study focuses exclusively on natural cadence, and aims to replicate the foot angle of the smart prosthesis using input from sensors placed in strategic positions on the device [1].

Gait is cyclic in nature, and this fact has been utilized by researchers to simplify the gait cycle into smaller segments. The gait cycle can be divided into two distinct phases: the stance phase, and the swing phase [2]. The cycle begins with heel strike of one foot, proceeds to a foot-flat stance of the same foot, moves

into heel strike of the opposite foot, continues with toe off of the original foot, proceeds with a forward swing of the original foot in air, and culminates with the heel strike of the original foot [3]. The stance phase consists of the first ~60% of the gait cycle beginning with the heel strike of the original foot and ending directly before toe off. The swing phase accounts for ~40% of the gait cycle and begins directly after toe off and continues until heel strike is once again initiated, beginning a new gait cycle [2].

The ankle-foot complex is of particular importance in human movement. During locomotion the complex plays a pivotal role in the support of body weight and the control of walking kinetics [4-7]. Three stages of the gait cycle are particularly significant in gait kinetics. At heel strike the heel absorbs the reaction forces that are created by contact between the heel and the ground. At this stage the total body weight of the individual is dually supported by the heel of one foot, and the toes of the opposite foot. As the opposite foot moves into its swing phase the ankle-foot complex solely supports the weight of the individual in the foot-flat stance. As opposite heel strike occurs the complex pushes off of the floor propelling the body forward into the subsequent swing phase. The ankle-foot complex supplies the body with the necessary kinetics required to drastically reduce the metabolic energy required for locomotion [7].

Currently there are 2 million Americans who suffer from an amputation and millions more worldwide. One in 190 Americans lives without a limb, and the number is expected to double by the year 2050 [8]. Every year 185,000 amputations occur in the United States alone [9]. Several factors contribute to the growing number of amputees such as diet, disease, and trauma. After surgery patients are presented with a limited number of options. They can use the traditional passive prosthesis that contains purely mechanical components, or they can opt for a more advanced micro-processor controlled prosthesis. Ankle-foot prostheses are designed specifically for patients suffering from below-knee amputations that require a device to replace the functions of the lower part of the leg [2]. Traditional prostheses do not offer the patient any form of intelligent control or powered assistance for walking, and because of this amputated patients can expend up to 60% more metabolic energy in level walking than healthy subjects [10, 11].

Metabolic energy expenditure is a major concern with patients suffering from limb loss. Patients forced to exert an unusually high level of energy to complete basic tasks necessary for daily

life are drastically discouraged from pursuing other activities, such as sports and hobbies, which would enrich their lives. Studies by the Kaufman group have confirmed that patients with microprocessor-controlled prosthesis have increased physical activity, and enhanced quality of life compared to those with traditional prosthesis. For this reason it is imperative that microprocessor-controlled prosthesis be a topic of continued research and development for the purpose of giving amputees a higher standard of life [12].

The objective of this study focuses exclusively on the control of an ankle-foot prosthesis. Ankle-foot prostheses have been under development for several decades and their progress is a process of continued improvement. Researchers have investigated ankle-foot prosthesis from a multitude of perspectives including: mechanical design and kinetics [13, 14], assistance in pathology [15], and overall gait control [16, 17]. Most ankle-foot prostheses work by regulating the movement of a single linear actuator mounted where the tendon would be located in a healthy individual. During intended use the actuator moves up and down causing the foot to move through various angles.

Control of this device can be divided into four categories: biomechanical signals, electromyographic signals, peripheral nervous system signals, and central nervous system signals [4]. This investigation has focused on using biomechanical signals to control the prosthesis, because of the large amount of readily available data published in human gait studies. By using two sensors (heel contact, and knee angle) we propose a rule system for controlling the foot angle of the prosthesis. The goal is to mimic the motion of a healthy foot in natural cadence in order to produce enhanced device performance to ultimately minimize the metabolic energy required to walk. To evaluate the efficacy of the algorithm a simulation was developed in Matlab Simulink. Matlab Simulink was selected for computational modeling because of its ease of use, block programming language, and previous applications in the modeling of gait and robotic systems [18-21].

2. NOMENCLATURE

θ_h = Hip Angle

θ_{th} = Thigh Angle

θ_{tr} = Trunk Angle

θ_k = Knee Angle

θ_{lg} = Leg Angle

θ_a = Ankle Angle

θ_{ft} = Foot Angle

$\omega_k = \frac{d\theta_k}{dt}$ = Knee Angular Velocity

3. METHODS

3.1 Gait Modeling

The human leg can be modeled in three-dimensional space as having a total of seven degrees of freedom (DOF), where three DOF are in the hip, one is in the knee, and three are in the ankle

[3]. Together both legs have fourteen DOF, but in actuality fifteen degrees of freedom are required to model the gait of the human body entirely. The additional DOF is the trunk angle which is depicted as θ_{tr} in Figure 1 [1]. Taking into consideration all 15 DOF can be a daunting task, and poses significant challenges in studying gait. For this study one of the two legs is healthy removing the need to model 7 DOF, and the trunk angle remains constant at 90 degrees in natural cadence which removes an additional DOF. The hip and the knee of the amputated leg are intact which removes an additional 4 DOF, leaving behind only the 3 DOF corresponding to the ankle-foot complex. In two dimensional motion studies of the ankle-foot prosthesis 2 DOF are unused reducing the study to examining 1 DOF. The sole DOF is represented in Figure 1 by the foot angle (θ_{ft}).

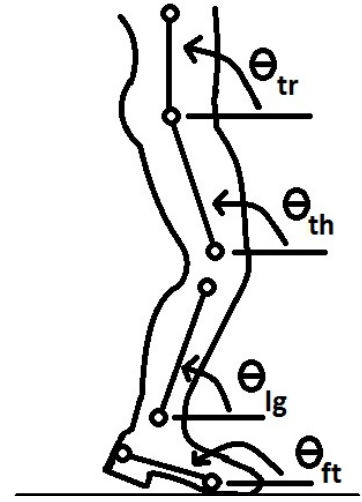


Figure 1. Outline of Major Angles in a Single Leg

Equations 1, 2, and 3 were acquired from [1], and represent three major angles that are reported extensively in literature. As one can see these angles are not directly measured in data collection, but are calculated from other angles.

As previously stated in natural cadence the trunk angle remains constant at 90 degrees [1]. Taking this into consideration equations 1-3 can be used to solve for the foot angle (θ_{ft}). The algorithm aims to match the foot angle, and its ability to do so is studied closely in the simulation. The derivation of equation 4 is included in the Appendix at the end.

$$\text{Equation 1: } \theta_h = \theta_{th} - \theta_{tr}$$

$$\text{Equation 2: } \theta_k = \theta_{th} - \theta_{lg}$$

$$\text{Equation 3: } \theta_a = \theta_{ft} - \theta_{lg} - 90^\circ$$

$$\text{Equation 4: } \theta_{ft} = \theta_a + \theta_h - \theta_k + 180^\circ$$

$$\text{Equation 5: } \omega_k = \frac{d\theta_k}{dt} = \text{Knee Angular Velocity}$$

Table 3.32b of [1] details a collection of data for hip, knee, and ankle degrees recorded every 2% in stride for natural cadence. This data was input into equation 4 to compute the true foot angle value at various points of percent stride, which can be seen in Figure 8.

The values of true foot angle are input into the model as a standard for comparison against the theoretical foot angle values produced by the algorithm for the prosthesis.

3.2 Sensor Selection and Knee Analysis

3.2.1 Sensor Selection

Many ankle-foot prostheses use a multitude of sensors to feed information into the controller. These sensors include: accelerometers, rotary potentiometers, and force transducers [7]. In our algorithm the system receives input from only two sensors: a rotary potentiometer measuring knee angle, and a force transducer mounted at the bottom of the heel. Input from the rotary potentiometer undergoes a derivation with respect to time to produce the knee angular velocity, as seen in Equation 5. The heel sensor functions as a switch, and is only activated when the heel is in contact with the ground. Therefore, the rotary potentiometer delivers a quantitative measurement to the system, while the heel sensor delivers a purely qualitative measurement.

3.2.2 Knee Angle Examination

As one can see in Figures 2 and 3 both the knee angle and the foot angle exhibit non-linear behavior throughout the percent stride. This poses a significant challenge in developing the rule system. If the relationship was more linear fewer sensors would be needed to differentiate between different stages of the gait cycle. The knee angle exhibits two peaks: one in the stance phase, and the other in the swing phase. The foot angle plateaus near 175 degrees for a significant portion of the stance phase, and drops substantially prior to the initiation of the swing phase where the foot angle proceeds in a steep upward climb.

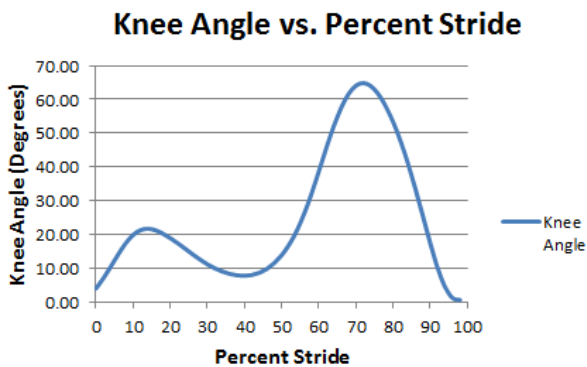


Figure 2. Knee Angle vs. Percent Stride

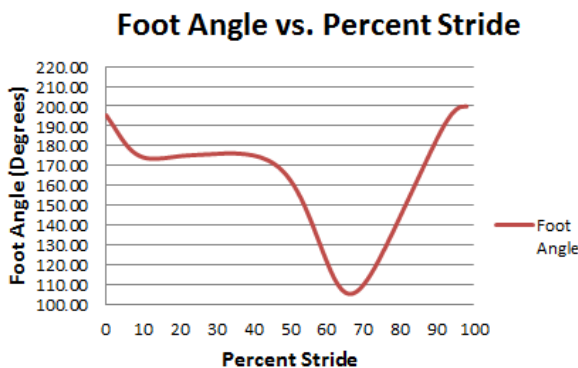


Figure 3. Foot Angle vs. Percent Stride

3.2.3 Knee Angular Velocity and Stride Segmentation

Figure 4 illustrates the knee angular velocity throughout a complete stride. As one can see the angular velocity is positive from 0-14 and from 40-72 percent of the stride. The angular velocity is negative from 14-40 and approximately 72-98 percent of the stride. This information is particularly important in developing the algorithm that will be discussed in greater detail. Taking into consideration that the angular velocity can be divided into two positive regions and two negative regions, and the heel sensor is on for one major region (0-40 percent of stride), and off for one major region (40-98 percent of stride) Figure 2 can be divided into 4 segments listed in Table 1.

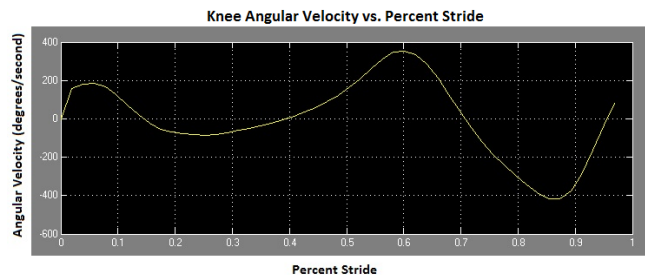


Figure 4. Knee Angular Velocity vs. Percent Stride

Table 1. Segmentation of Knee Angle vs. Stride Plot

Segment	Range of Percent Stride	Heel Sensor	Angular Velocity
1	0-14	On	Positive
2	14-40	On	Negative
3	40-72	Off	Positive
4	72-98	Off	Negative

3.3 Selection of Control Mechanism

Several system identification techniques were examined for potential in prosthesis control. Neural networks were considered, but ultimately dismissed due to the large amount of data required to properly develop an accurate control system. Fuzzy logic exhibited some promise for controlling the system, but modeling with the Fuzzy Logic Toolbox in Matlab produced large errors that could not be reduced. This was mostly likely because of the non-linear interaction between knee angle and foot angle in a complete stride. After these two techniques were discarded the model was developed using two switches placed in series to control the filtering of four functions. The objective is to use the correct function in the correct portion of the stride to accurately relate knee angle to foot angle throughout a complete stride.

3.4 Control Algorithm

Figure 5 displays the control algorithm for governing the foot angle of the prosthesis. The overall system aims to use the angle of the knee, the status of the heel sensor, and the value of the knee's angular velocity to determine the corresponding foot angle. Due to the non-linear behavior of the knee angle through a complete stride the graph in Figure 2 has been divided into four

segments listed in Table 1. In the algorithm the first sensor reading is the knee angle measurement acquired from the rotary potentiometer. The derivative is taken to determine the angular velocity, and based upon the positive or negative value of the velocity the algorithm proceeds to evaluate either Segments 1 and 3, or Segments 2 and 4. Next, the heel sensor is read, and based upon the on/off status the algorithm determines which segment to use. In Table 2 it is seen that each segment has a corresponding function where the dependent variable is the knee angle, and the independent variable is the foot angle. In this manner the rule system is able to output a foot angle for each knee angle value across all four segments of the stride.

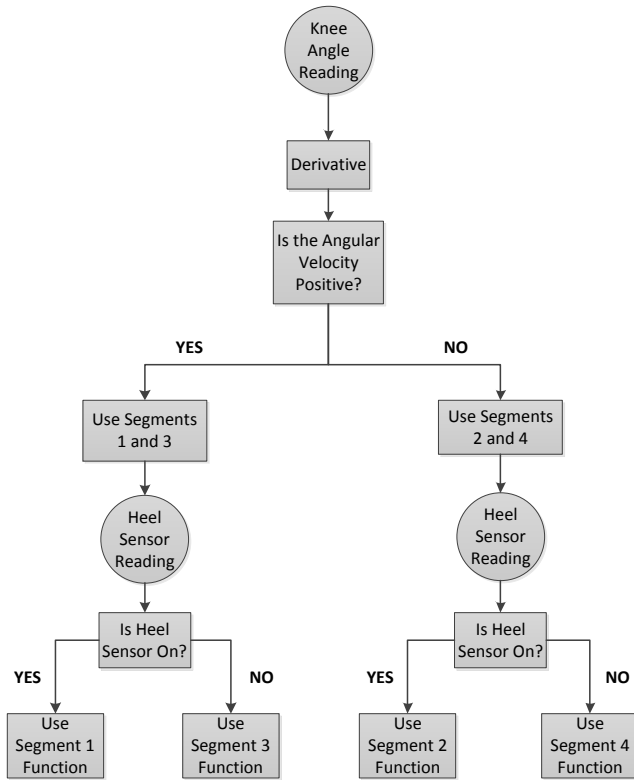


Figure 5. Algorithm governing use of functions

Table 2. Functions Governing Foot Angle

Segment	Segment Function
1	$y = -1.2643x + 198.72$
2	$y = -0.1432x + 177.2$
3	$y = -1.2165x + 178.28$
4	$y = -1.1964x + 195.83$

3.5 Matlab Simulink Model

Figure 6 exhibits the model that was built in Matlab Simulink. A magnification of this model is more clearly displayed in the Appendix. The model begins with the input of a series of physiologically relevant knee angles. A derivative is immediately taken to determine the knee angular velocity, and this value is the

input for the velocity switch. As described in the algorithm segment functions 1 and 3 proceed through the model when the velocity is positive, and segment functions 2 and 4 move forward when the value is negative. The two signals which pass through the velocity switch are separated by the “demux” block, and input into the heel switch. The values for the heel sensor are input into the model as a source block, and provide the input for the heel switch. The switch behaves according to the rule system displayed in Figure 5. The output from the heel switch is the foot angle of the ankle-foot prosthesis. Other blocks function to calculate the error of the foot angle, and visually display the true value of the foot angle superimposed against the calculated value.

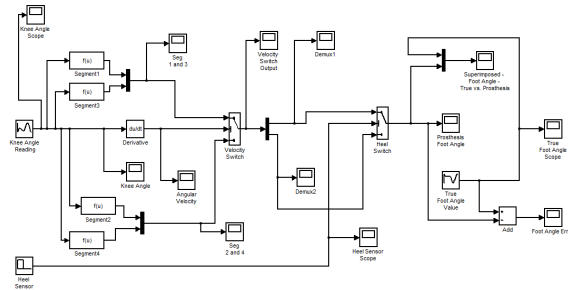


Figure 6. Simulink Model for Testing Algorithm

4. RESULTS AND DISCUSSION

Figures 2 and 4 display plots of the knee angle and the knee angular velocity utilized in the model. Figure 7 illustrates the spectra for the heel sensor seen over one complete stride. The heel sensor is activated in first 40% of the stride, noted by the value of one, and deactivated in the remaining 60% of the stride, noted by a value of zero. The heel switch contains a threshold of 0.9 allowing it to distinguish between the on and off statuses.

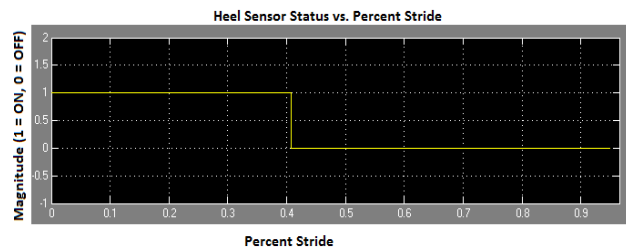


Figure 7. Heel Sensor vs. Percent Stride

Figure 8 displays the true foot angle utilized for evaluation of the theoretical results. Figure 9 illustrates the output of the control system referred to as the prosthesis foot angle. Figure 10 represents a superimposed plot of the true foot angle and the prosthesis foot angle versus percent stride. In this figure one can see that the algorithm functions well in mimicking the true value of the foot angle for the first two segments (0-40%) of the stride. In segment three (40-72%) there are regions of varying accuracy. From 41% to 52% there is a noticeable difference between the theoretical and true values. The largest deviation occurs at approximately 72% of the stride, and is subsequently followed by the beginning of the fourth segment. The function of the fourth

segment maintains a fairly consistent error, and follows the overall path of the true foot angle plot.

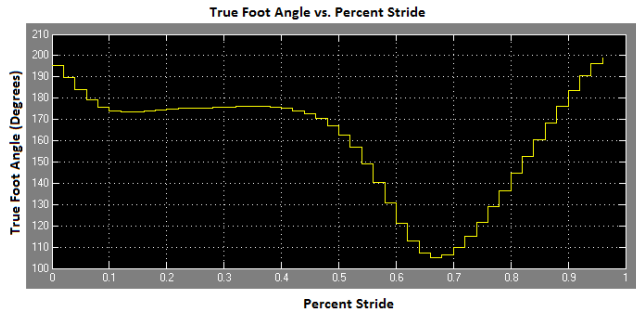


Figure 8. True Foot Angle vs. Percent Stride

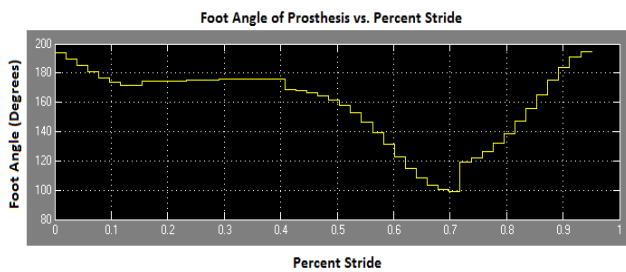


Figure 9. Prosthesis Foot Angle vs. Percent Stride

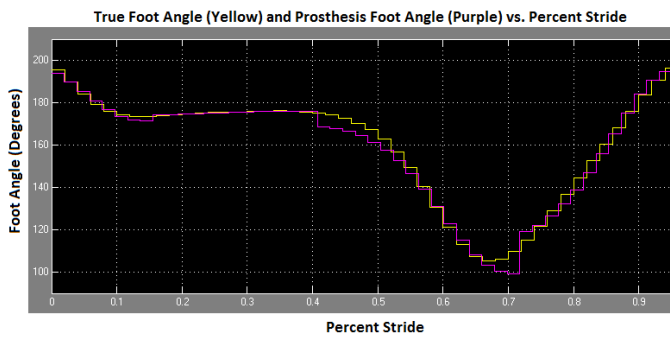


Figure 10. True and Prosthesis Foot Angles Superimposed

In Figure 11 one can see that each of the four segments have drastically different levels of error. In the first segment (0-14%) the error fluctuates from +5.5 to -1.7 degrees. Then, in the second segment (14-40%) the error ranges from +2.1 to -1 degrees. Subsequently, in the third segment (40-72%) the error varies from +10.4 to -9.9 degrees. Lastly, in the fourth segment the error ranges from +5.6 to -7.9 degrees. As one can observe different functions are more accurate at following the true path of the foot angle. At 67 percent stride the true foot angle makes a sharp change in slope that is difficult for the control methodology to follow. This change sets the precedent for the error observed at 70 percent stride.

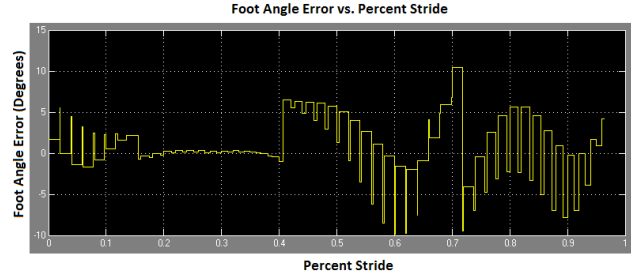


Figure 11. Foot Angle Error vs. Percent Stride

5. CONCLUSION AND FUTURE WORK

This study has successfully simulated a novel algorithm for controlling an ankle-foot prosthesis. The results indicate that this rule system has potential for direct application in micro-processor controlled prosthetics. Matlab Simulink has exhibited utility in modeling the complex nature of human gait, and provided a medium for evaluating the functionality of the algorithm. Matlab Simulink is an indispensable tool in computational modeling, and provides great utility in accelerated modeling and evaluation of control mechanisms.

The reported error is minimal, and can be further reduced through additional studies. Suggestions for future work include implementing advanced numerical method techniques to develop more sophisticated functions, and utilizing additional sensors to better mimic the natural motion of the ankle-foot complex. The study can be further expanded to develop additional control methods for governing foot angle positions in patients with slow and fast cadence. Furthermore, control of kinematics is but one of several important factors to consider in prosthesis design. Additional studies are recommended to investigate mimicking the natural kinetics of human gait to produce enhanced functionality of the prosthesis.

6. REFERENCES

- [1] Winter, David. *The Biomechanics and Motor Control of Human Gait: Normal, Elderly, and Pathological*. Second Edition. Waterloo, Ontario: Waterloo Biomechanics, 1991.
- [2] Au S., et al. "An Ankle-Foot Emulation System for the Study of Human Walking Biomechanics". *2006 IEEE International Conference on Robotics and Automation (2006)*: 2939-2945.
- [3] Dollar M., et al. "Lower Extremity Exoskeletons and Active Orthoses: Challenges and State-of-the-Art". *IEEE Transactions on Robotics*. 24, NO. 1 (2008): 1-15.
- [4] Zwipp H., et al. "Ankle Joint Biomechanics". *European Journal of Food and Ankle Surgery*. 1 (1994): 21-27.
- [5] Dul J., et al. "A Kinematic Model of the Human Ankle". *Journal of Biomedical Engineering*. 7 (1985): 137-143.
- [6] Surer E., et al. "A markerless estimation of the ankle-foot complex in 2D kinematics during stance". *Gait and Posture*. 33 (2011): 532-537.
- [7] Jimenez-Fabian R., et al. "Review of control algorithms for robotic ankle systems in lower-limb orthoses, prostheses, and

- exoskeletons”. *Medical Engineering & Physics*. 34 (2012): 397-408.
- [8] Ziegler-Graham K., et al. “Estimating the Prevalence of Limb Loss in the United States: 2005 to 2050”. *Archives of Physical Medicine and Rehabilitation* 2008; 89 (3): 422-429.
- [9] Owings M., et al. “Ambulatory and Inpatient Procedures in the United States, 1996”. Hyattsville, Md.: U.S. Dept. of Health and Human Services, Centers for Disease Control and Prevention, National Center for Health Statistics; 1998.
- [10] Varol H., et al. “Multiclass Real-Time Intent Recognition of a Powered Lower Limb Prosthesis”. *IEEE Transaction of Biomedical Engineering*. 53 (2010): 542-551.
- [11] Mohanty R.K., et al. “Comparison of energy cost in transtibial amputees using “prosthesis” and “crutches without prosthesis” for walking activities”. *Annals of Physical and Rehabilitation Medicine*. In Press Available Online April 9th, 2012.
- [12] Kaufman K., et al. “Energy Expenditure and Activity of Transfemoral Amputees Using Mechanical and Microprocessor-Controlled Prosthetic Knees”. *Archives of Physical Medicine and Rehabilitation*. 89 (2008): 1380-1385.
- [13] Bellman R., et al. “SPARKy 3: Design of an Active Robotic Ankle Prosthesis with Two Actuated Degrees of Freedom Using Regenerative Kinetics”. *Proceedings of the 2nd Biennial IEEE/RAS-EMBS International Conference on Biomedical Robotics and Biomechatronics*. (2008): 511-515.
- [14] Holgate M., et al. “The SPARKy (Spring Ankle Regenerative Kinetics) Project: Choosing a DC Motor Based Actuation Method”. *Proceedings of the 2nd Biennial IEEE/RAS-EMBS International Conference on Biomedical Robotics and Biomechatronics*. (2008): 163-168.
- [15] Blaya J., et al. “Adaptive control of a variable-impedance ankle-foot orthosis to assist drop-foot gait”. *IEEE Transactions on Neural Systems and Rehabilitation Engineering* (2004): 968-977.
- [16] Eilenberg, MF., et al. “Control of a powered anklefoot prosthesis based on a neuromuscular model”. *IEEE Transactions on Neural Systems and Rehabilitation Engineering*. (2010): 164-173.
- [17] Holgate M., et al. “Control Algorithms for Ankle Robots: A Reflection on the State-of-the-Art and Presentation of Two Novel Algorithms”. *Proceedings of the 2nd Biennial IEEE/RAS-EMBS International Conference on Biomedical Robotics and Biomechatronics*. (2008): 97-102.
- [18] Lim C.M., et al. “Modeling of knee joint muscle during the swing phase of gait – a forward dynamics approach using Matlab/Simulink”. *Simulation Modeling Practice and Theory*. 11 (2003): 91-107.
- [19] Gill H.S., et al. “Heelstrike and the pathomechanics of osteoarthritis: a simulation study”. *Journal of Biomechanics*. Volume 36, Issue 11 (2003): 1617-1624.
- [20] Mansouri M., et al. “A platform for dynamics simulation and control of movement based on OpenSim and MATLAB”. *Journal of Biomechanics*. Volume 45, Issue 8 (2012): 1517-1521.
- [21] Wang Z., et al. “Mobility analysis of the typical gait of a radial symmetrical six-legged robot”. *Mechatronics*. Volume 21, Issue 7 (2011): 1133-1146.

7. APPENDIX

Derivation of Equations:

$$\theta_h = \theta_{th} - \theta_{tr}$$

$$\theta_{tr} = 90^\circ \text{ in natural cadence}$$

$$\theta_h = \theta_{th} - 90^\circ$$

$$\theta_{th} = \theta_h + 90^\circ$$

$$\theta_k = \theta_{th} - \theta_{lg}$$

$$\theta_{lg} = \theta_{th} - \theta_k = \theta_h - \theta_k + 90^\circ$$

$$\theta_a = \theta_{ft} - \theta_{lg} - 90^\circ$$

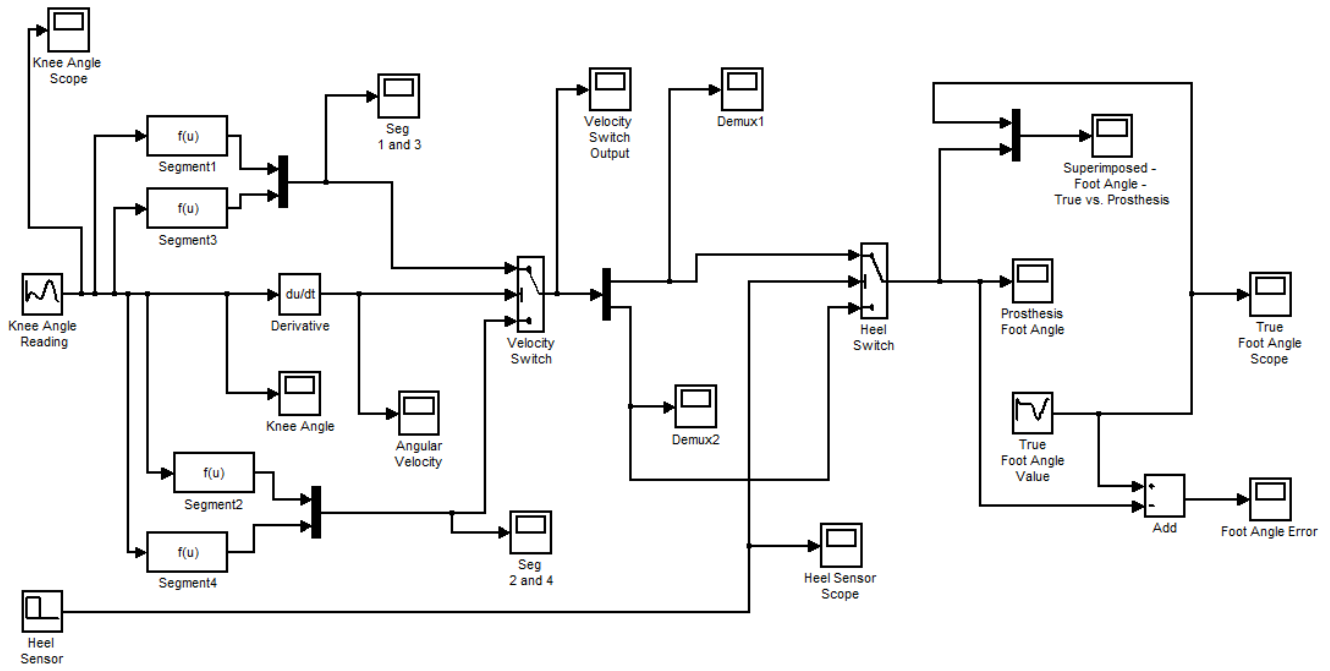
$$\theta_{ft} = \theta_a + \theta_{lg} + 90^\circ$$

$$\theta_{ft} = \theta_a + \theta_h - \theta_k + 90^\circ + 90^\circ$$

$$\theta_{ft} = \theta_a + \theta_h - \theta_k + 180^\circ$$

$$\omega_k = \frac{d\theta_k}{dt} = \text{Knee Angular Velocity}$$

Simulink Model:



A New Generation of Health Monitoring Robots

Wuqayan Alwuqayan

Department of Mechanical and Materials Engineering
Florida International University
Miami, Florida, U.S.A.

(305) 903-8455
walwu001@fiu.edu

Sabri Tosunoglu

Department of Mechanical and Materials Engineering
Florida International University
Miami, Florida, U.S.A.

(305) 348-1091
tosun@fiu.edu

ABSTRACT

This research paper ventures through a cutting-edge technology behind personal service robots that are aimed towards the elderly population. The technology uses sensors that measure several characteristics about the habits of elderly people and provide vital feedback on their health. The sensors are specially designed to fulfill their objectives which may range from face recognition and/or detecting people's motion all the way to measuring their pulse and body temperature. The technology will enable the service robots to create personal health profiles of their owners. Through pattern recognition the robots then can detect any abnormality or irregularity in their owners' health or habits and act accordingly to prevent potential health mishaps. The robots will feature modular design that will incorporate different needs for different users.

Key element about this new breed of robots is their controller system which allows them to mimic human reasoning in handling complex nonlinear systems. There are number of methods to conduct such kind of controllers. However when dealing with imprecise input signal in real-time operations, fuzzy-logic controller proven to be the best suit for the job. A detailed research work in fuzzy-logic controller is compiled by a number of researchers and there have been many books and articles on the subject as reported in [1-4]. For simulation purposes a fuzzy logic controller was constructed using Fuzzy Logic Toolbox provided by MATLAB software, a performance test of the system was carried out, and the results were analyzed. Simulation and analysis provide designers with information on how the fuzzy-logic controller can affect the output speed and stability of a system with multivariable inputs. Thus, designers can proceed with a larger and more complex system. The objective behind this technology is to improve life quality of the elderly.

KEYWORDS

Fuzzy Logic, Fuzzy-Logic Controller (FLC), Proportional-Integral-Derivative (PID) Control, Mobile Platform

INTRODUCTION

The population of people age 65 and older is increasing rapidly. According to the 2010 U.S. census 13% of the population is over 65, The U.S. Census Bureau projects that number will increase to 19.7% in 2030. Current living conditions for the majority of elderly people are already alarmingly unsatisfactory. According to US Department of Health and Human Services, nearly 9% of non-institutionalized persons 70 years of age and over were unable to perform one or more activities of daily living such as

bathing, dressing, using the toilet, and getting in and out of bed [5]. At the same time, the health-care sector is undergoing a dramatic cost increase, according to US Department of Health and Human Services current nursing home costs range between \$30,000 and \$60,000 a year which has been doubled over the last decade. Therefore, an alternative ways of providing quality care for elderly people have to be considered. Such ways must not only lower the cost, but they must also increase the comfort of living while approaching the elderly with a level of privacy and dignity that they deserve.

One approach would be a tailor made service robot that will open the gate for new generation of artificial intelligence robots. These new service robots are powered with Fuzzy-Logic Controller (FLC) system that gives them the ability to imitate humans in decision making when dealing with multivariable inputs. Integrated with specially designed high tech sensors, these robots are capable of creating health profiles of their owners through pattern recognition thus sensing any potential risk ahead of time.

Furthermore they can detect and report sudden break downs. Their fuzzy-logic controller is proven to be far more superior to the commonly used Proportional-Integral-Derivative (PID) controller [6]. FLC has more robust against disturbances and faster transient response with less overshoot and oscillation than the PID controller. Robotic technology is going through major revolution and now would be the time to take advantage of such revolution and find an optimum solution for a potentially growing problem.

PLATFORM MOBILITY

Mobility is an essential component for all service robots. The robot platform must be able to efficiently commute and navigate through its environment in order to effectively execute its task. Furthermore the robot must be able to avoid obstacles or constraints that may come along its path. All of which indicate the robot platform ought to be agile and versatile.

There are a number of options to be considered when designing a powered mobile platform. Degree of freedom, level of stability, and the required speed are just to name a few. For simulation purpose, a three-wheel platform robot was chosen. The two rear wheels are powered via servomotors; which have been proven to be more controller-friendly than most of the other robotic propulsion. The front wheel is left to be the idle wheel (Figure 1).

The wheels turning motion is controlled by the servomotors, who receive their operating signals from the microcontroller.

Depending on the output command, the servomotors turn CW or CCW and with a specified pluses, thus turning the rear wheels in a particular direction with the desired speed.

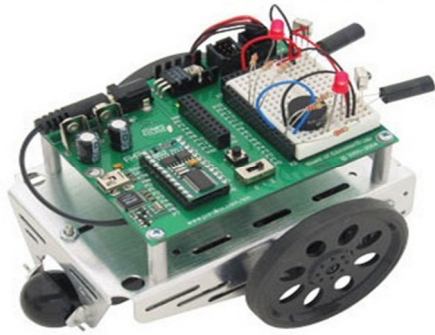


Figure 1. Three wheel mobile platform [1]

PLATFORM NAVIGATION

One of the crucial tasks the service robot has to perform is environmental scanning. The robot platform must scan its surroundings and identify the appropriate route to take during commuting. For instance, the platform must be capable to identify its user in the midst of household obstacles i.e. furniture, walls, doors, etc, and select the shortest, most practical path for approaching when necessary. The robot platform should also distinguish between a station obstacle or a moving one and act accordingly. There are various types of sensors that can be used in this application.

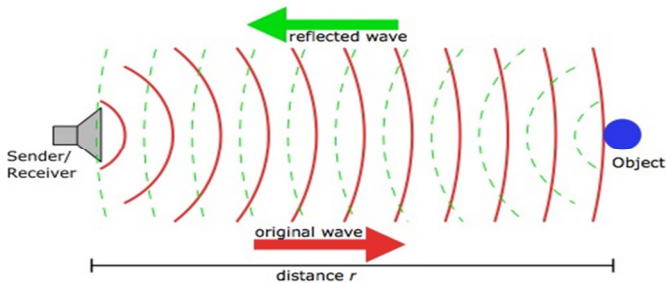


Figure 2. Ultrasound surroundings scan

Ultrasound and infrared sensors are the most cost-efficient and commercially available. Though infrared provide a better accuracy, the ultrasound is preferable for its wider beam, which enables it to perform better detection. Ultrasound sensors use a time-of-flight logic to figure the distance between the sensor and the next object in front of it. The sensor emits an ultrasonic wave and waits for it to be reflected off an object in front of it (Figure 2).

The microcontroller tallies the time between emission and reception and calculates the distance by counting the time it took for a one-way trip and multiplying it by the speed of sound. Once the object is detected and its distance is measured, the platform can act according to the preset program.

For demonstration purposes a set of ultrasound sensors were mounted on a platform and used to perform an environmental

scan. The platform has to identify the furthest object, move towards it, and stop within five inches.

OBJECT AVOIDANCE

Avoiding obstacles is an integral part of the platform navigation and mobility. Simply detecting an object or a target alone would not be practical. The platform must be capable to reach its target while avoiding obstacles along its way or bypass obstruction during its normal commute. This is typically done through set of commands and subroutines that are preset in the robot's memory and using a variety of sensors readings to trigger those commands and subroutines. Figure 03 illustrates a program code flowchart that belongs to line-following robot and the commands/subroutines it executes based on the sensors inputs.

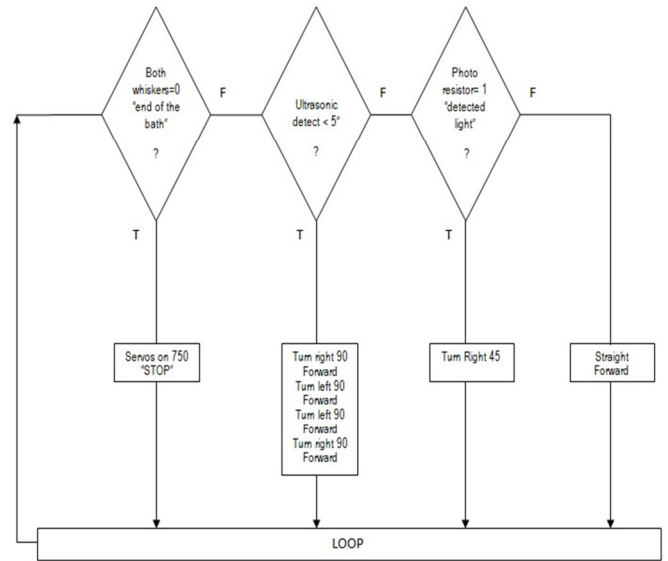


Figure 3. Flowchart of line-following robot

There are a Variety of sensors that can be used for object avoidance and each would serve a specific need. Photo resistors are commonly used to detect light/dark areas and objects some can be used for color recognition. Infrared and ultrasound sensors are widely used for object scanning, and touch-sensors are used for object sensing. Typically all of these types of sensors send an input signals to the robot's microcontroller through the I/O ports.

The microcontroller then automatically triggers a preset commands and subroutines in the form of an output. The input signal can be either digital (0 or1) as in a touch-sensor (whiskers), or it can be analog signal as in ultrasound sensor. Either way a conventional microcontroller simply execute a preset of commands based on incoming signals without analyzing or cross checking these signals.

It is one of the areas where the new breed of service robots really shines. The platform will be powered by a Fuzzy-Logic controller which enables it to make an inelegant decision on whether or not to trigger an output solely based on an input signal. Thus, the robot will efficiently chose which route to take and/or which maneuvers to implement in order to avoid or bypass an obstacle. All of which results in a superior performance in object avoidance that would enhance agility and varsity of the platform.

FUZZY THEORY

Fuzzy-logic control system can replace many of today's complicated control systems. It simplifies the control design which can save time and money. The main feature of fuzzy logic is that it is able to deal with imprecise linguistic information. Compared with traditional logic, fuzzy-logic is more suitable for analyzing complex nonlinear systems, such as the ones that involve humans.

Fuzzy algorithms can be implemented with software on standard hardware such as microprocessors. However, for complex and real-time control systems hard-wired fuzzy algorithms are required (Fuzzy hardware); one type of such hardware is the Fuzzy-Logic Controller (FLC). The FLC is a rule-based system (see Figure 1) where fuzzy control rules and membership functions are stored in the knowledge base. Control operations then can be divided into three parts. The first part is fuzzification, which converts crisp input data into linguistic values (fuzzy values). The second part is fuzzy inference that executes the fuzzy approximate reasoning. The third and final part is defuzzification which yields a none-fuzzy crisp data action as output. In depth analysis on FLC construction is reported in [7, 8].

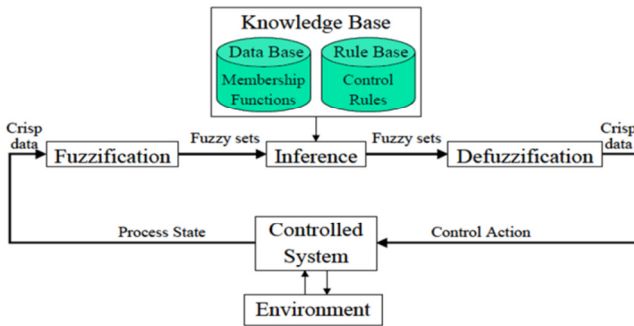


Figure 4. Fuzzy logic based control

PROPOSED METHOD

Utilize fuzzy-logic controller to design a state-of-the-art personal service robot. The model involves specially developed sensors that enable face recognition, motion detection, and monitoring vital characteristics such as pulse and respiration [9]. These high tech motion sensors can be installed throughout the owner's home; i.e., doorways, mattress, showers, chairs, etc. The sensors send their signals to the robot's control panel.

The collected data are then used to create a personal health profile via fuzzy-logic controller embedded within the service robot which enables it to detect potential medical alerts. Furthermore, by incorporating the gathered data the robot will be able to distinguish between similar sounds that belong to different sources; i.e. owner's cry for help vs. a loud sound from a TV set, which will reduce the number of false alarms. In order to construct a fuzzy logic controller inputs and outputs variables must be defined. The membership functions can then be created via set of rules and equations. Figure 2 demonstrates a general design scheme of a fuzzy logic controller.

CONTROL SYSTEM CONSTRUCTION

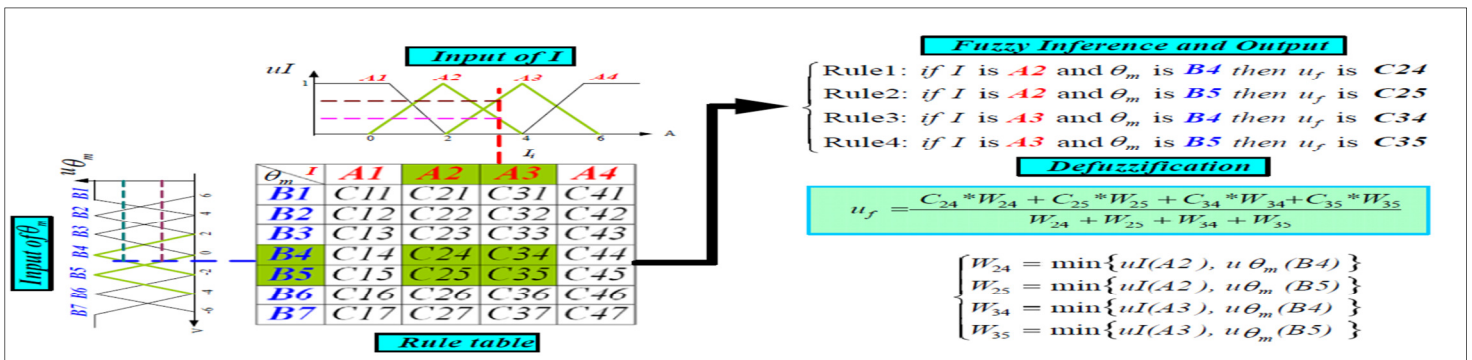
In order to simulate the robot's performance, a fuzzy-logic controller had to be constructed. For simplicity, a system of three inputs and two outputs was chosen (Figure 3). The input variables were defined as *Pulse Rate*, *Body Temperature* and *Room Temperature*, each of which was assigned five levels; Alarmingly Low, Low, Normal, High, and Alarmingly High. The corresponding values for each level were picked according to nursing practice [10]. Output variables were defined as *Robot's Mode* and *Temperature Control*. The *Robot's Mode* has four levels; Normal, Standby, Alert, and Emergency. For each input variable a set of membership functions were constructed (Figure 4). Table 1 and 2 contain the values of input and output variables respectively.

Table 1. Input membership functions variables

Definition	Pulse Rate	Body Temp	Room Temp
Alarmingly Low	40-49	< 31.5	64-55
Low	50-59	31.3-32.9	72-65
Normal	60-100	32.5-38.5	73-79
High	101-120	38.1-39.9	77-85
Alarmingly High	121-200	39.5-40.9	83-90

Table 2. Output membership functions variables

Robot's Mode	Factor
Normal	0-0.3
Standby	0.31-0.5
Alert	0.51-0.75
Emergency	0.76-1.00



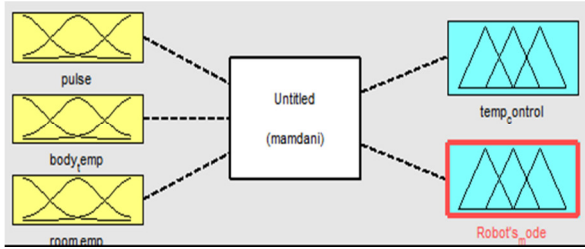


Figure 6. Control system outline

The inputs and outputs membership functions were defined, a set of membership functions rules were created using the *IF-THEN* rule base. As mentioned, one of the important features of fuzzy logic is the ability to efficiently handle multiple-state logic as demonstrated below:

1. *IF* pulse is Alarmingly Low *OR* body temp is Alarmingly Low *THEN* it is an Emergency.
2. *IF* pulse is Alarmingly High *OR* body temp is Alarmingly High *THEN* it is an Emergency.
3. *IF* pulse is Normal *AND* body temp is Normal *THEN* it is Normal.
4. *IF* pulse is Normal *AND* body temp is High *THEN* it is an Alert.
5. *IF* pulse is Normal *AND* body temp is Low *THEN* it is an Alert.
6. *IF* room temp is Low *AND* body temp is Low *THEN* it is a Standby.
7. *IF* room temp is High *AND* body temp is Low *THEN* it is an Alert.
8. *IF* room temp is Low *AND* pulse is Alarmingly Low *OR* body temp is Alarmingly Low *THEN* it is an Emergency.

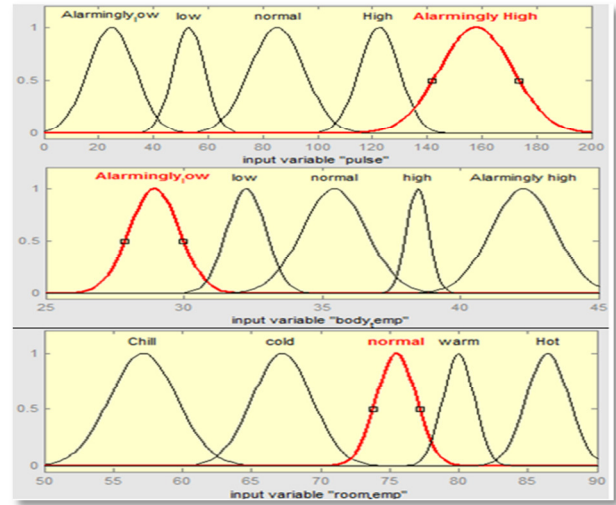


Figure 7. Input variables membership functions

Membership functions rules are very essential for any fuzzy logic controller. They provide the FLC with more options to choose from for each possible scenario. However, having too much set of membership functions rules can affect the performance of the controller which may yield some inconsistency output results. It can also slow the system response speed which is a very vital aspect of the controller. Therefore an optimum set of membership functions rules must be sought after.

When the fuzzy logic controller is constructed, the controller guides the robot to perform tasks and make decisions based on the specified membership rules to incorporate a preset commands. The controller enables the robot to mimic human-like reasoning when handling none-linear multivariable inputs. The output responses would be predefined as well. For instance, an “Emergency” output means a 911 call, while an “Alert” output means a call to a doctor or relative. On the other hand a “Cool” output would require the robot to cool down the air condition unit. By interface with specially developed sensors, the controller can read the transmitted signals from the sensors and gather all the data to create a health profile of the robot’s owner. The controller then can compare trends and/or detect potential health risks. The robot’s response will be according to the FLC membership functions rules (see Figure 5).

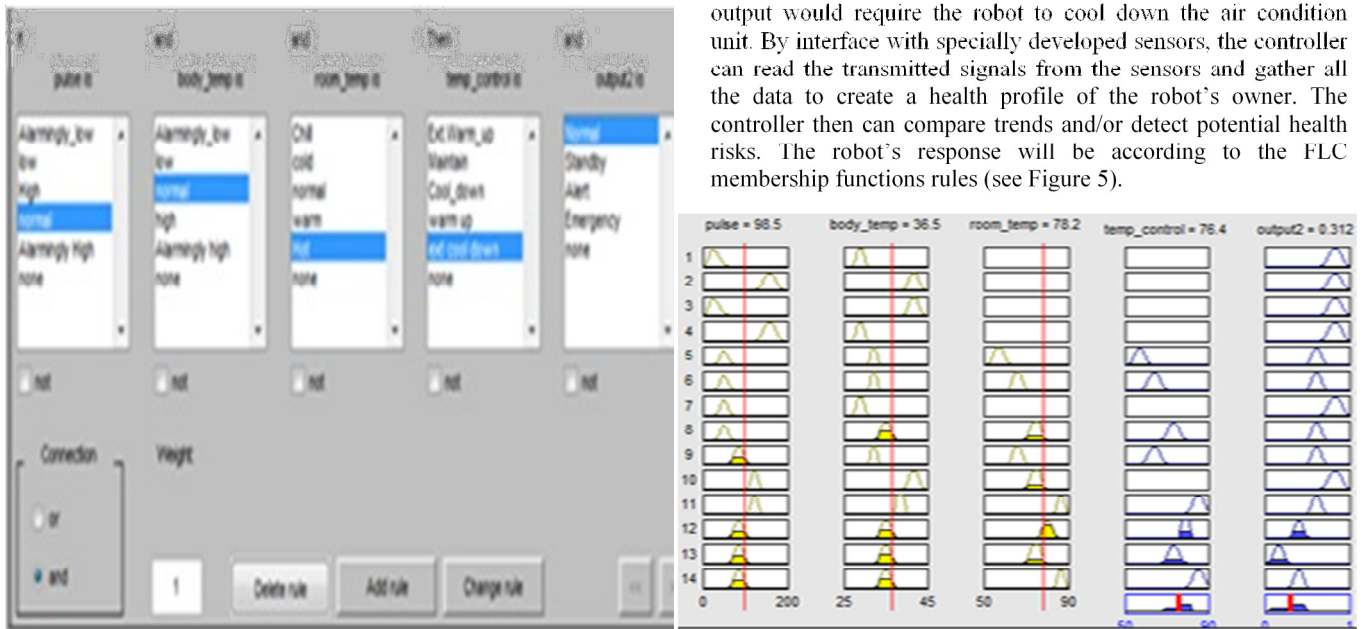


Figure 8. Membership rules

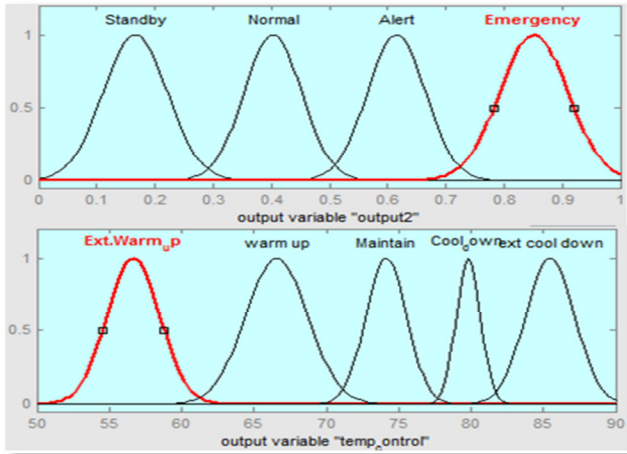


Figure 9. Output variables membership functions

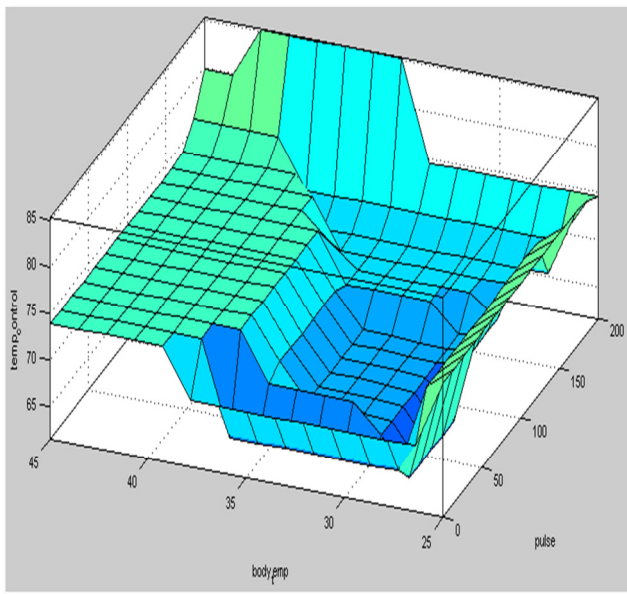


Figure 10. Performance plot of FLC

SIMULATION RESULTS

The assigned inputs and outputs variables were run through a fuzzy logic controller to simulate the outcome based on the specified rules. The system showed that it can handle a wide range of possibility combinations and the ability to process nonlinear variables.

Some set-value modifications were needed to reach optimum results. A performance test of the system was conducted and the results were plotted (Figures 6 and 7). The performance plot shows a generally coherent and smooth surface with no significant spikes or breakouts which is an indication of the system success.

CONCLUSION

With the rapidly growing number of elderly population and the dramatically increasing cost of nursing homes and home-care services, a serious social problem is on the rise. In an effort to control such a problem, a cutting-edge service robot is proposed that can mimic human control via a set of specially developed sensors and a fuzzy logic controller embedded within the robot. For simulation purposes some of the robot's features were demonstrated in smaller scale such as the environment scan, object avoidance and the control logic. A fuzzy logic controller was constructed and its performance was tested. The results have showed that the system can handle multiple inputs and outputs variables successfully. The results have also demonstrated that the system can be easily modified to reach optimum results.

REFERENCES

- [1] Ellis, Justin, Morelli, Tony, Sohal, Amandeep, *Autonomous Mobile Robots*, 2005.
- [2] Ahmad, M. Ibrahim, *Fuzzy Logic for Embedded Systems Applications*, Elsevier Science, Burlington, Massachusetts, 2003.
- [3] Kevin, M. Passino, Stephen, Yurkovich, *Fuzzy Control*, Addison Wesley Longman Inc., Menlo Park, California, 1998.
- [4] Bandemer, H., Gottwald, S., *Fuzzy Sets, Fuzzy Logic, Fuzzy Methods with Applications*, Wiley, New York, 1995.
- [5] Nicholas, Roy, Gregory, Baltus, Dieter, Fox, Francine, Gemperle, Jinnifer, Goetz, Tad, Hirsch, Dimitris, Margaritis, Mike, Montemerlo, Joelle, Pineau, Jamie, Schulte, and Sebastian, Thrun, *Towards Personal Service Robots for the Elderly*, Computer Science and Robotics, Carnegie Mellon University, 1999.
- [6] Herbert, Eichfield, Thomas, Kiinemund, and Manfred, Menke, *A 12b general fuzzy logic controller chip*, IEEE Transaction on Fuzzy Systems, vol 4, no 4, 1996.
- [7] Faizal, A. Samman, Eniman, Y. Syarnsuddin, *Programmable Fuzzy Logic Controller Circuit on CPLD Chip*, IEEE, 2002.
- [8] Khan, Sheroz, Salami, Femi Abdulazeez, Adetunji, Lawal Wahab, Zahirul, Alam, Momoh Jimoh, E. Salami, Hameed, Shihab Ahmed, Abdalla, Aisha Hasan, Islam, Mohd Rafiqul, *Design and Implementation of an Optimal Fuzzy Logic Controller Using Genetic Algorithm*, Journal of Computer Science, 2008.
- [9] Glascock, Anthony, Kutzik, David, *The Impact of Behavioral Monitoring Technology on the Provision of Health Care in the Home*, Journal of Universal Computer Science, 2006.
- [10] McDermott, M., *Central Venous Pressure*, Nursing Standard, Vol. 9, No. 35, March 1995.
- [11] Alwuqayan, Wuqayan, Tosunoglu, Sabri, *Fuzzy-Logic Health Monitoring Robots for the Elderly*, ASME ECTC 2011.

Visual Servoing Control of a 9-DoF WMRA to Perform ADL Tasks

William G. Pence
University of South Florida
4202 E Fowler Ave, ENB118
Tampa, FL 33620
+1 813 974-2115
wpence@mail.usf.edu

Fabian Farelo
University of South Florida
4202 E Fowler Ave, ENB118
Tampa, FL 33620
+1 813 974-2115
ffarelo@mail.usf.edu

Redwan Alqasemi
University of South Florida
4202 E Fowler Ave, ENB118
Tampa, FL 33620
+1 813 974-2115
alqasemi@usf.edu

Yu Sun
University of South Florida
4202 E Fowler Ave, ENB118
Tampa, FL 33620
+1 813 974-2115
yusun@cse.usf.edu

Rajiv Dubey
University of South Florida
4202 E Fowler Ave, ENB118
Tampa, FL 33620
+1 813 974-2115
dubey@usf.edu

ABSTRACT

The wheelchair-mounted robotic arm (WMRA) is a mobile manipulator that consists of a 7-DoF robotic arm and a 2-DoF power wheelchair platform. Previous works combined mobility and manipulation control using weighted optimization for dual-trajectory tracking [7]. In this work, we present an image-based visual servoing (IBVS) approach with scale-invariant feature transform (SIFT) using an eye-in-hand monocular camera for combined control of mobility and manipulation for the 9-DoF WMRA system to execute activities of daily living (ADL) autonomously. We also present results of the physical implementation with a simple “Go to and Pick Up” task and the “Go to and Open the Door” task previously published in simulation, using IBVS to aid the task performance.

Keywords

WMRA, ADL, Rehabilitation, Visual Servoing.

1. INTRODUCTION

The 2010 US Census Bureau report on disability shows that about 10 percent of the working age population has some sort of disability, with most of these disabilities being ambulatory [1]. It has been shown that robotic arms can serve as effective assistive devices for users with impaired upper-body functions [2]. Two prototype WMRAs have been developed at the Center for Assistive, Rehabilitation and Robotics Technologies at the University of South Florida that outperform traditional 6-DoF WMRAs that are commercially available [3, 4].

Several user interfaces have been implemented on the 9-DoF WMRA system such as the 3D SpaceBall joystick, laptop touch screen, voice recognition, eye gaze tracking [6], and P300 brain-computer interface (BCI) [5]. Although the system has executed several ADL tasks successfully, it is difficult to teleoperate the 9-DoF system with combined mobility and manipulation.

In [7], dual-trajectory control was implemented to provide sub-trajectories in order to execute a “Go to and Open the Door” task

in simulation. In this work, we theorize a visual servoing technique to control combined mobility and manipulation on the 9-DoF WMRA system for execution of ADL tasks. We use a simple 2D visual servoing method while approaching the goal object such that it will be in the workspace of the manipulator, then after a threshold distance from the goal object we use IBVS with SIFT [8], where the manipulator translates and orients to grasp the goal object and depth is estimated with a proximity sensor. Weighted optimization is used throughout the control system to control mobility and manipulation simultaneously in a coordinated manner. Finally, physical results of “Go to and Pick Up” and “Go to and Open the Door” ADL tasks are presented. This work presents a novel application of visual servoing to a combined 9-DoF mobile manipulator for the execution of assistive ADL tasks, and also presents a hardware implementation of previously published work in simulation [7], using IBVS with SIFT to enhance task execution robustness.

2. BACKGROUND

Redundant mobile manipulators have become increasingly popular in the research field and can be used in various different applications. Having a mobile platform greatly increases the workspace of a manipulator since the system is able to navigate around in the environment. Control systems for a 7-DoF mobile manipulator consisting of a 5-DoF robotic arm mounted to a nonholonomic 2-DoF mobile platform were described in [9]. In this work, control of mobility and manipulation were decoupled such that the mobile platform moved to an area that put the goal object in the workspace of the manipulator, and then the manipulator grasped the goal object. In [10], combined kinematics for a nonholonomic platform with a manipulator were presented. In this work, redundancy in the system was resolved using the projected gradient and reduced gradient optimization methods. A sample trajectory was followed where the manipulator stayed in a pre-specified orientation while the mobile platform followed a circle.

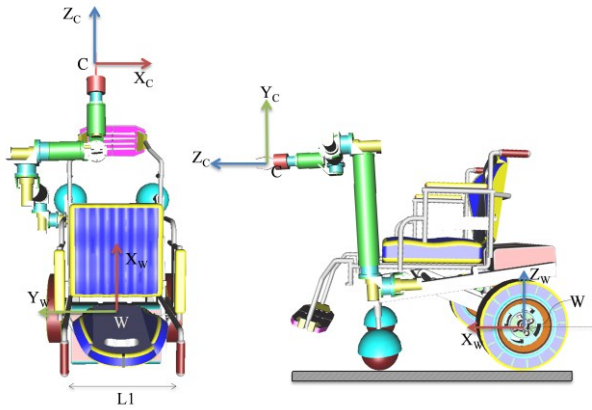


Figure 1. WMRA coordinate frames. W shows the wheelchair frame and C shows the camera frame.

Weighted least norm solution is one method of redundancy resolution, described in [11]. This method resolves redundancies in redundant manipulators while at the same time minimizing unnecessary motion of the joints. This can also be extended to avoid joint limits by using specific criterion functions described in [12]. In a similar fashion, we will coordinate mobility and manipulation using weighted optimization in this work.

Visual servo control has become increasingly popular due to its simplicity and robustness, especially for physical applications in real-world environments. These methods have been described in great detail in tutorials such as [13, 14]. Two main forms of visual servoing exist, but we mainly focus on IBVS where velocity control for the system is computed based strictly on features immediately available in the image. Position-based visual servoing (PBVS) is another form that relies on estimation of 3D positions in the image. Essentially, visual servoing provides a correspondence between matched features in a goal and camera image and robot movement, and gives as output a velocity controller for a robot system. The goal image contains a view of the goal object from the desired grasping position and orientation. Visual servoing minimizes the error between this goal image and camera image until it becomes zero, such that the goal object can then be grasped. This error is computed by matching features in the goal and camera image, and virtually any feature matching algorithm can be used.

Several works have demonstrated the success of visual servoing on fixed-base manipulators. In [15], the commercially-available Manus arm was controlled using a visual servoing technique relying on color-based feature extraction. This implementation was reliable, but depended on good color information for goal objects to be grasped. An extension to this work described in [16] used SIFT to match features between the goal and camera image. This provided a much more robust system working towards autonomous grasping. In [17], a similar approach was used by implementing a 2 1/2D homography-based visual servoing using SIFT. This work split the grasping task into gross and fine motion with separate control systems for each phase. While this work did not implement a full 3D visual servoing technique, it did provide a beginning to end solution for autonomous grasping.

Visual servoing applications on mobile manipulators have typically consisted of very simple manipulators on two-wheeled

platforms. The 7-DoF mobile manipulator mentioned above was controlled using visual servoing in [18]. This work integrated IBVS and Q-learning to control the nonholonomic 2-DoF platform and 5-DoF manipulator. Control was decoupled such that the mobile platform first approaches the goal object, and then the manipulator grasps it. One of the problems with the application of visual servoing to mobile manipulators is that the mobile platform can easily move such that the visual features move outside the view of the camera and are therefore lost. Q-learning is used to aid the system in [18] to overcome this problem.

Although these applications to both fixed-base and mobile manipulators prove that the implementation of visual servoing control can be very successful, they still have some shortcomings. Fixed-base manipulators are constrained to their local workspace, which is undesirable for assisting users with daily ADLs. Applications of visual servoing to mobile manipulators typically decouple the control systems. In this work, we use a combined approach based on weighted optimization to integrate IBVS for full 3D control using SIFT on the 9-DoF WMRA system so that all DoF are controlled simultaneously throughout the entire task. This provides for a smoother and more seamless application specifically for the execution of ADL tasks.

3. CONTROL SYSTEMS

3.1 WMRA Combined Kinematics

For the 7-DoF manipulator, numerical solutions exist to have it follow a desired trajectory. The other 2-DoF in the WMRA system are provided by the nonholonomic power wheelchair. The 2-DoF mobile platform consists of linear translation and rotation about a fixed axis. When controlling the mobile platform, velocities must be given for the linear translation as well as rotation. We use the weighted least-norm solution with singularity-robust pseudo inverse to resolve redundancies. As we will discuss later, we also use this weighted optimization to control coordination of the wheelchair platform and robotic arm during executed ADL tasks. Combination of the robotic arm and wheelchair kinematics is done using Jacobian augmentation, which can give the flexibility of using conventional control and optimization methods without compromising the total combined control [10]. Full kinematics and detailed equations can be found in a previous work concentrating on the control system [3].

The wheelchair will move forward when both wheels have the same speed and direction while rotational motion will be created when both wheels rotate at the same velocity but in opposite directions. Since the wheelchair's position and orientation are our control variables rather than the left and right wheels' velocities, a relationship between the wheels' rotational velocities and the linear and rotational velocities of the wheelchair was derived ($X; \theta$):

$$\begin{bmatrix} \dot{\theta}_l \\ \dot{\theta}_r \end{bmatrix} = \begin{bmatrix} 1 & -L_1 \\ L_5 & 2 \cdot L_5 \\ 1 & L_1 \\ L_5 & 2 \cdot L_5 \end{bmatrix} \cdot \begin{bmatrix} \dot{X} \\ \dot{\theta} \end{bmatrix} \quad (1)$$

Where L1 is the distance between the wheels and L5 is the wheels radius (see Figure 1). Seven DoFs are provided by the robotic arm mounted on the wheelchair from the Denavit-Hartenberg parameters of the robotic arm specified in earlier publications [3].



Figure 2. USB camera mounted on end effector in eye in hand configuration.

3.2 Redundancy Resolution and Optimization

Redundancy is resolved in the algorithm using singularity-robust inverse of the Jacobian [20] to give a better approximation around singularities, and use the optimization for different subtasks. Manipulability measure [21] is used as a factor to measure how far the current configuration is from singularity.

Weighted Least Norm solution proposed by [11] is integrated to the control algorithm to optimize for secondary tasks. In order to put a motion preference of one joint rather than the other (such as the wheelchair wheels and the arm joints), a weighted norm of the joint velocity vector can be defined as:

$$|V|_W = \sqrt{V^T W V} \quad (2)$$

where W is a 9×9 symmetric and positive definite weighting matrix, and for simplicity, it can be a diagonal matrix that represent the motion preference of each joint of the system. The weighted least norm solution integrated to the S-R inverse is:

$$|V|_W = W^{-1} J^T (J W^{-1} J^T + k * I_6)^{-1} \dot{r} \quad (3)$$

where J is the augmented Jacobian of the WMRA system combining the robotic arm and wheelchair kinematics explained in [3], k is a parameter defined by the manipulability measure [3, 22] and \dot{r} represents the Cartesian velocities of the end effector.

The above method has been used in simulation of the 9-DoF WMRA system with the nine control variables (V) that represent the seven joint velocities of the arm and the linear and angular wheelchair's velocities. An optimization of criteria functions can be accomplished when used in the weight matrix W .

3.3 Criteria for Weighted Optimization

The criteria functions used in the weight matrix for optimization can be defined based on different requirements. For the robotic arm, the physical joint limits can be avoided by minimizing an objective function that represents this criterion. One of these mathematical representations was proposed by [11] as follows:

$$H(q) = \sum_{i=1}^7 \frac{1}{4} \cdot \frac{(q_{i,max} - q_{i,min})^2}{(q_{i,max} - q_{i,current}) \cdot (q_{i,current} - q_{i,min})} \quad (4)$$

where q_i is the angle of joint i . This criterion function becomes 1 when the current joint angle is in the middle of its range, and it

becomes infinity when the joint reaches either of its limits. The gradient projection of the criterion function can be defined as:

$$\frac{\partial H(q)}{\partial q_i} = \frac{(q_{i,max} - q_{i,min})^2 \cdot (2 \cdot q_{i,current} - q_{i,max} - q_{i,min})}{4 \cdot (q_{i,max} - q_{i,current})^2 \cdot (q_{i,current} - q_{i,min})^2} \quad (5)$$

When any particular joint is in the middle of the joint range, (5) becomes zero for that joint, and when it is at its limit, (5) becomes infinity, which means that the joint will carry an infinite weight that makes it impossible to move any further.

The diagonal weight matrix W can now be constructed as:

$$W = \begin{bmatrix} w_1 + \left| \frac{\partial H(q)}{\partial q_1} \right| & 0 & \dots & \dots & 0 \\ 0 & w_2 + \left| \frac{\partial H(q)}{\partial q_2} \right| & 0 & \dots & 0 \\ \vdots & 0 & \ddots & \dots & \vdots \\ \vdots & \vdots & \vdots & w_x & 0 \\ 0 & 0 & \dots & 0 & w_\phi \end{bmatrix} \quad (6)$$

where w_i is a user-set preference value for each joint of the arm, and w_x and w_ϕ are the translation/rotation of the wheelchair.

3.4 Visual Servoing for Approach

At the beginning of the task, the user selects the goal object on a GUI, and then the wheelchair and arm work to center on the goal object and approach it. Coordination is controlled by criterion functions we define below. We initially set a rough velocity for the system depending on the distance to the goal object, and then control system movement with weights. We desire to initially use mostly wheelchair motion, but as we approach the goal object wheelchair motion should decrease as arm motion increases. We use an eye in hand monocular camera mounted on the end effector, as seen in Figure 2.

For the initial approach, it is only necessary for simple 2D visual servoing. We use camshift color tracking implemented in the OpenCV open source computer vision library for tracking the goal object [22]. Camshift returns the centroid of the matched template in the scene image, so in order to center on the selected area, we must adjust motion so that the tracked object's centroid reaches the center of the image plane, $a=(c_u, c_v)$.

The wheelchair translation w_x is directly related to the distance from the camera frame to the goal object, in the camera frame's Z-direction. We approximate this distance by means of proximity sensor mounted on the end effector. Since w_x should be directly proportionate to the distance on Z, we have:

$$w_x = \frac{Z_i}{\lambda_1 Z} \quad (7)$$

where λ_1 is an appropriate gain, Z is the distance from the camera frame to the goal object estimated with a proximity sensor, and Z_i is the initial distance from the camera frame to the goal object.

The desired wheelchair rotation w_ϕ is directly related to the 2D visual servoing error. Since setting w_ϕ is only able to minimize the error in the camera frame's X-direction, we compute the error $e(t)_x$ using:

$$e(t)_x = s_x - c_u \quad (8)$$

where s_x is the current x-location of the centroid of the matched template, and c_u is the desired x-location of the template which is the center of the image plane in the camera frame's X-direction.

Since w_ϕ should be directly proportionate to $e(t)_x$ computed in (8), we have:

$$w_\phi = \frac{e(t)_x \max}{\lambda_2 e(t)_x} \quad (9)$$

where λ_2 is an appropriate gain and $e(t)_x \max$ is the maximum possible error in the x-direction, in our case half of the image width in pixels.

We also desire to set the user-set preference values for w_i through w_7 in order to control arm motion. We should use mostly wheelchair motion when the goal object is far away, and use mostly arm motion when the goal is very close. Therefore, we define the arm's user-set preference values for all 7 joints as:

$$w_1 = w_2 = \dots = w_7 = \lambda_3 Z \quad (10)$$

where λ_3 is an appropriate gain.

Using equations (7), (9), and (10) we can set motion so that the WMRA will approach the selected goal object area. Based on these criteria functions, initially when the distance Z is very large, primarily the wheelchair will move. As the WMRA approaches the goal object and z is reduced, the arm will begin moving as the wheelchair slows. Finally, when the WMRA has approached the goal object, strictly the arm will move. We then transition to grasping using IBVS when a defined threshold distance has been reached, while continuing use of the same weight equations (7), (9), and (10).

3.5 Visual Servoing for Grasping

We now implement an IBVS control system based on [13, 14] that outputs velocities to move the WMRA system until it has reached the 3D goal position and orientation. At this point, the gripper paddles can close and grasp the goal object, and the task is completed when the object is delivered to the user.

We desire to have a reliable and accurate method of feature extraction since the accuracy of the visual servoing control relies on this. Scale-invariant feature transform (SIFT), as described in [8], is a very robust feature extraction algorithm. For our code implementation, we use the open source SIFT library developed by Rob Hess in [23] to match features between the goal and scene images.

The goal of visual servoing is to minimize an error computed by:

$$e(t) = s(m(t), a) - s^* \quad (11)$$

where $s(m(t), a)$ are extracted features, $m(t)$ is the vector of image measurements, and a is a set of camera parameters. In our case, $m(t)$ consists of the image coordinates of the matched features in the scene image. From this point forward, we can represent $s(m(t), a)$ simply as s . The vector s^* consists of the desired goal image measurements. In our case, s^* contains the image coordinates of the features in the goal image. Therefore, from (11), we see that the error $e(t)$ is simply the difference between s and s^* .

For our application, we desire to design a velocity controller that can control the WMRA system using this visual servoing control. The relationship between the time variation of s and the camera velocity is described by:

$$\dot{s} = L_s v_c \quad (12)$$

where L_s is the image Jacobian related to s , which we will define later. The vector v_c is the velocity controller for the WMRA system, which consists of v_c and ω_c , the instantaneous linear velocity and angular velocity, respectively, in all three dimensions. For visual servo control, $v_c = (v_x, v_y, v_z, \omega_x, \omega_y, \omega_z)$. Using (11) and (12), we find the relationship between the time variation of the error and the camera velocity:

$$\dot{e} = L_e v_c \quad (13)$$

where $L_e = L_s$. We wish to solve (13) for v_c so that we can use it as velocity input to the WMRA control system. Therefore, we finally find:

$$v_c = -\lambda_4 \widehat{L_e^+} e \quad (14)$$

where λ_4 is a gain for the velocity control and the Moore-Penrose pseudo-inverse of L_e is taken to solve for v_c .

We now define the image Jacobian to use in (14). We must first relate the 3D world point $X=(X,Y,Z)$ to the 2D camera point $x=(x,y)$:

$$\begin{aligned} x &= \frac{x}{z} = (u - c_u) \\ y &= \frac{y}{z} = (v - c_v) \end{aligned} \quad (15)$$

where $m=(u,v)$ from (11) above is the coordinates in pixels of the image feature point, and $a=(c_u, c_v)$ is the set of camera parameters with the principal point described by c_u and c_v . The image Jacobian is a $6 \times 2k$ matrix for k matched feature points. The image Jacobian L_x , related to x from (15) is:

$$L_x = \begin{bmatrix} \frac{-1}{z} & 0 & \frac{x}{z} & xy & -(1+x^2) & y \\ 0 & \frac{-1}{z} & \frac{y}{z} & 1+y^2 & -xy & -x \end{bmatrix} \quad (16)$$

where x and y are from (15). In order to control the WMRA system using 6-DoF Cartesian control, we must have at least $k=3$ matched feature points to determine the velocities. We stack the image Jacobians for k points:

$$L_x = [L_{x_1} \quad L_{x_2} \quad \dots \quad L_{x_k}]^T \quad (17)$$

Similarly, we also stack the errors such that e from (14) is:

$$e = [e_{x_1} \quad e_{y_1} \quad e_{x_2} \quad e_{y_2} \quad \dots \quad e_{x_k} \quad e_{y_k}]^T \quad (18)$$

We have now designed a visual servoing control system based on (14) from [13, 14] that can output velocity control for the WMRA. When the visual error has been minimized and the velocities of the system approach zero, then the robotic arm has reached its desired position and orientation. At this time, the gripper paddles can be closed to grasp the goal object and deliver it to the user in the wheelchair.

4. IMPLEMENTATIONS AND RESULTS

Physical design of the 7-DoF manipulator and implementation onto the power wheelchair can be reviewed in [3, 4]. We use a Logitech C910 USB webcam mounted in eye in hand configuration on the end effector as seen in Figure 2. For estimating the z distance from the camera to the goal object, we use a Sharp GP2Y0A21YK infrared proximity sensor mounted just beneath the camera. Users operate the system with a laptop using a GUI developed for the application.

4.1 Go to and Pick Up Task

To demonstrate an example application of IBVS combined mobility and manipulation control, we execute a simple “Go to and Pick Up” task. Initially, the user is presented with a camera view, and once the object is selected it is tracked using camshift, and feedback is presented to the user in the GUI as seen in Figure 3. During the beginning of the approach, mostly the wheelchair moves. As the distance to the goal object decreases, the wheelchair slows and the arm begins moving. This can be seen visually with the weights displayed in Figure 4.

Once the end effector has reached a threshold distance from the goal object, SIFT-based IBVS begins and the user is presented with additional feedback in the GUI as seen in Figure 5. While grasping takes place, only manipulator movement is used to correctly position and orient it. Figure 6 shows the velocity output of IBVS while grasping. After IBVS finishes and the error is minimized, the gripper paddles then close to grasp the goal object, and it is delivered to the user through pre-programmed position control as seen in Figure 7.

Physical testing of this implementation generally results in a successful grasp. In 30 trials of the task, the system completed successfully 83.3% of the time. As can be seen from Figure 4, the system is able to control the weights to coordinate the combined mobility and manipulation during approach. Figure 6 shows that with the physical results of the system, the linear and angular velocities converge such that the error is minimized at the end of grasping. Although slight noise in the data exists, the physical system stays stable during testing. In rare situations where the goal object was lost, the system halted all motion and prompted the user to re-select the goal object on the GUI.



Figure 3. GUI feedback while camshift object tracking during approach. The screen on the left is initially presented to the user to select the desired object, then it is tracked as seen on the right.

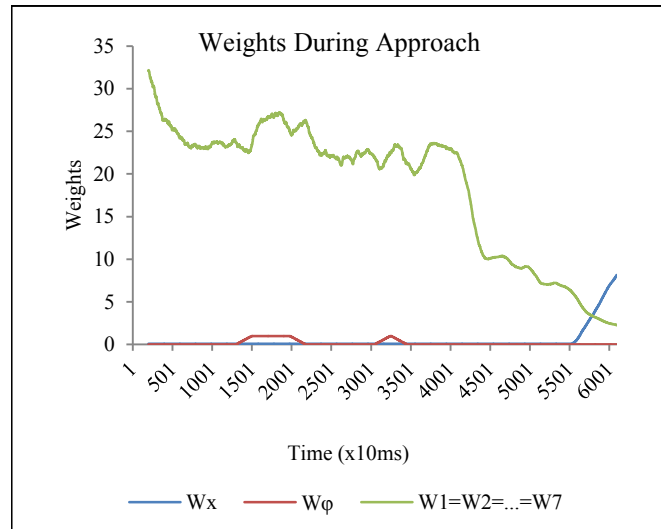


Figure 4. Weights for wheelchair (w_x and w_ϕ) and arm ($w_1...w_7$) during approach.

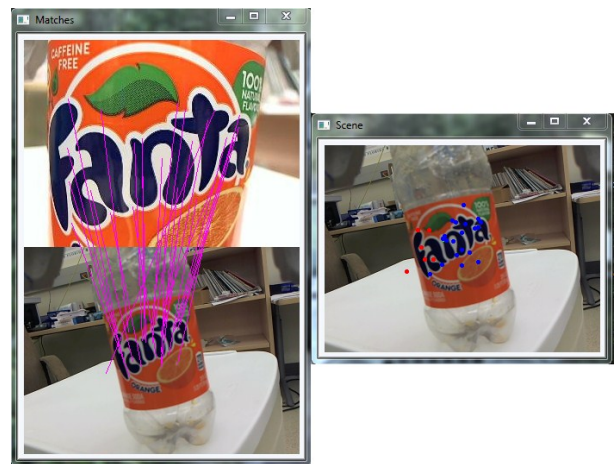


Figure 5. GUI feedback during SIFT-based IBVS control while grasping. Rob Hess’s open-source SIFT code [25] is used.

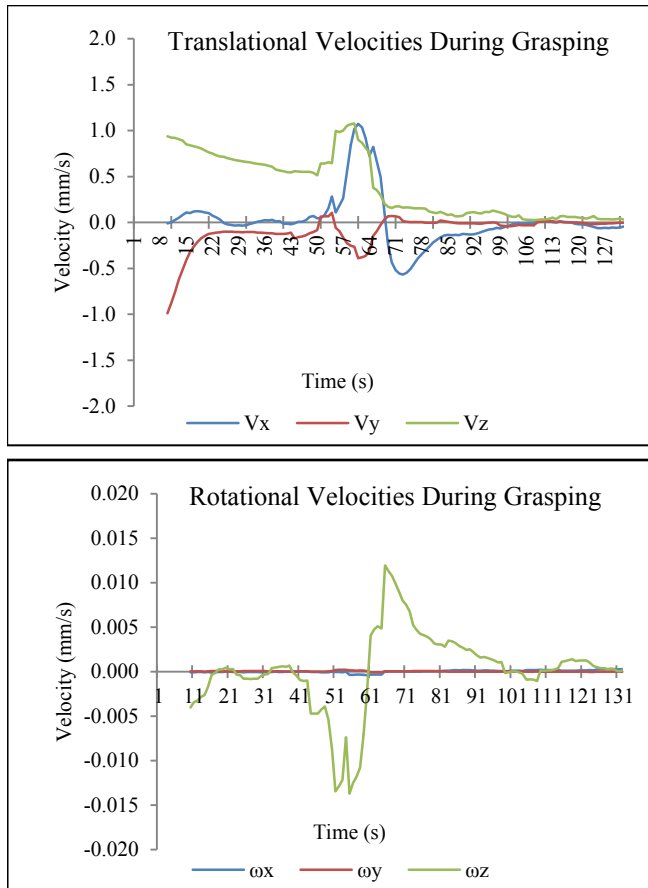


Figure 6. Velocity output from visual servoing control while grasping. Translational velocity (top) is separated from rotational velocity (bottom) for easier viewing. Velocity reaches zero as the error is minimized (11), (14).



Figure 7. Gripper grasping the goal object (top) at the end of IBVS when velocities reach zero, and then delivering the goal object to the user (bottom) through position control.

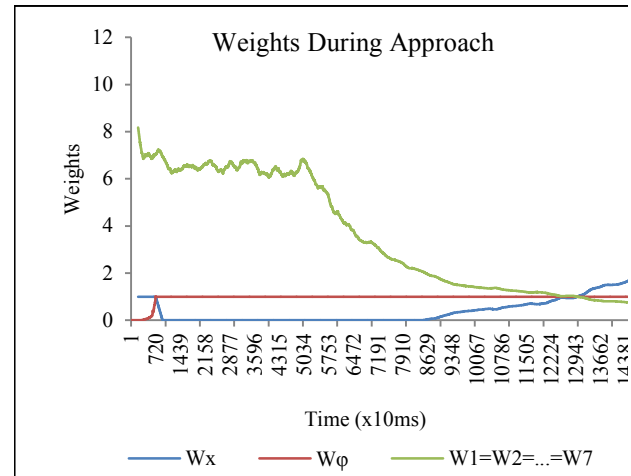


Figure 8. Weights during the “Go to and Open the Door task.” The wheelchair first rotates to face the door, then it translates straight forward until it approaches the door.

4.2 Go to and Open the Door Task

Previous work published in simulation presented the “Go to and Open the Door” task optimizing a second trajectory for the wheelchair while performing the main task with the end-effector [7]. Using a weight matrix, we successfully controlled the preference of motion for the arm or the rotation and translation of the wheelchair.

For the physical implementation, we have adopted the use of IBVS to compensate for the errors induced by the wheeled platform in the approach stage, giving a high robustness for the strategy aided by sensory information.

As with the task presented in the previous section, a weight for the arm was introduced to avoid over-stretching the arm while the WMRA is far away from the door knob.

As shown in Figure 8, the weights are controlled according to (7), (8), (9) and (10) allowing the WMRA to autonomously:

- Rotate the wheelchair towards the door
- Approach the door using IBVS to center on the door knob for grasping
- Adjust Orientation of the wheelchair and the end effector for opening the door
- Grasp the door knob and execute a circular trajectory to open the door

Note that in Figure 8 the rotational weight starts very close to zero and increases as the wheelchair orients toward the door, while translational weight behaves opposite to prioritize translation once the optimal orientation is reached [7].



Figure 9. WMRA approaching the door (up), adjusting and grasping the door knob (middle) and opening the door (down) to complete the “Go to and Open the Door” task.

5. CONCLUSION AND FUTURE WORK

In this work, we have presented a novel approach and hardware implementation for combined mobility and manipulation of a WMRA system using visual servoing. We have also presented results from an assistive application for autonomous beginning to end execution of a “Go to and Pick Up” and “Go to and Open the Door” ADL task. Although this work is implemented on an assistive WMRA device, it could be extended to any mobile manipulator system.

Future work includes implementation of a potential fields collision avoidance system fused with the visual servoing velocity control. This would allow the system to navigate around obstacles autonomously. Other work includes the application of this work to other assistive ADL tasks.

6. REFERENCES

- [1] US Census Bureau, “Disability Among the Working Age Population: 2008 and 2009,” Census Brief, September 2010, <http://www.census.gov/prod/2010pubs/acsbr09-12.pdf>
- [2] Reswick J.B., “The Moon over Dubrovnik - A Tale of Worldwide Impact on Persons with Disabilities,” *Advances in External Control of Human Extremities*, 1990.
- [3] Alqasemi, R.; Dubey, R.; , "Maximizing Manipulation Capabilities for People with Disabilities Using a 9-DoF Wheelchair-Mounted Robotic Arm System," *Rehabilitation Robotics, 2007. ICORR 2007. IEEE 10th International Conference on* , vol., no., pp.212-221, 13-15 June 2007.
- [4] P Schrock, P.; Farello, F.; Alqasemi, R.; Dubey, R.; , "Design, simulation and testing of a new modular wheelchair mounted robotic arm to perform activities of daily living," *Rehabilitation Robotics, 2009. ICORR 2009. IEEE International Conference on* , vol., no., pp.518-523, 23-26 June 2009.
- [5] Palankar, M.; De Laurentis, K.J.; Alqasemi, R.; Veras, E.; Dubey, R.; Arbel, Y.; Donchin, E.; , "Control of a 9-DoF Wheelchair-mounted robotic arm system using a P300 Brain Computer Interface: Initial experiments," *Robotics and Biomimetics, 2008. ROBIO 2008. IEEE International Conference on* , vol., no., pp.348-353, 22-25 Feb. 2009.
- [6] C. Bringes, J. Jones, M. Malek, B. Simons, W. Pence, and R. Alqasemi. *Human-Computer Interaction for the WMRA*, FCRAR 2011.
- [7] Farello, F.; Alqasemi, R.; Dubey, R.; , "Optimized dual-trajectory tracking control of a 9-DoF WMRA system for ADL tasks," *Robotics and Automation (ICRA), 2010 IEEE International Conference on* , vol., no., pp.1786-1791, 3-7 May 2010.
- [8] Lowe, David. "Distinctive Image Features from Scale-Invariant Keypoints". *International Journal of Computer Vision* 2004.
- [9] Chengjun Ding; Ping Duan; Minglu Zhang; Huimin Liu; , "The kinematics analysis of a redundant mobile manipulator," *Automation and Logistics, 2008. ICAL 2008. IEEE International Conference on* , vol., no., pp.2352-2357, 1-3 Sept. 2008.
- [10] De Luca, A.; Oriolo, G.; Giordano, P.R.; , "Kinematic modeling and redundancy resolution for nonholonomic mobile manipulators," *Robotics and Automation, 2006. ICRA 2006. Proceedings 2006 IEEE International Conference on* , vol., no., pp.1867-1873, 15-19 May 2006.
- [11] Tan Fung Chan; Dubey, R.V.; , "A weighted least-norm solution based scheme for avoiding joint limits for redundant joint manipulators," *Robotics and Automation, IEEE Transactions on* , vol.11, no.2, pp.286-292, Apr 1995.
- [12] R. Alqasemi. “Maximizing Manipulation Capabilities for People with Disabilities Using a 9-DoF Wheelchair-Mounted Robotic Arm System”. Doctoral Dissertation. University of South Florida. Tampa, 2007.
- [13] Chaumette, F.; Hutchinson, S.; , "Visual servo control. I. Basic approaches," *Robotics & Automation Magazine, IEEE*, vol.13, no.4, pp.82-90, Dec. 2006.

- [14] Hutchinson, S.; Hager, G.D.; Corke, P.I.; , "A tutorial on visual servo control," *Robotics and Automation, IEEE Transactions on* , vol.12, no.5, pp.651-670, Oct 1996.
- [15] Driessen, B.; Liefhebber, F.; Kate, T.T.; Van Woerden, K.; , "Collaborative control of the MANUS manipulator," *Rehabilitation Robotics, 2005. ICORR 2005. 9th International Conference on* , vol., no., pp. 247- 251, 28 June-1 July 2005.
- [16] Liefhebber, F.; Sijs, J.; , "Vision-based control of the Manus using SIFT," *Rehabilitation Robotics, 2007. ICORR 2007. IEEE 10th International Conference on* , vol., no., pp.854-861, 13-15 June 2007.
- [17] Kim, Dae-Jin; Lovelett, Ryan; Behal, Aman; , "Eye-in-hand stereo visual servoing of an assistive robot arm in unstructured environments," *Robotics and Automation, 2009. ICRA '09. IEEE International Conference on* , vol., no., pp.2326-2331, 12-17 May 2009.
- [18] Ying Wang; Haoxiang Lang; de Silva, C.W.; , "A Hybrid Visual Servo Controller for Robust Grasping by Wheeled Mobile Robots," *Mechatronics, IEEE/ASME Transactions on*, vol.15, no.5, pp.757-769, Oct. 2010.
- [19] Craig, J., 2003, "Introduction to robotics mechanics and control", third edition, Addison- Wesley Publishing, ISBN 0201543613.
- [20] Nakamura, Y., "Advanced robotics: redundancy and optimization," Addison- Wesley Publishing, 1991, ISBN 0201151987.
- [21] Yoshikawa, T., "Foundations of robotics: analysis and control," MIT Press, 1990, ISBN 0262240289.
- [22] G.R. Bradski, Computer video face tracking for use in a perceptual user interface, Intel Technology Journal, Q2 1998.
- [23] Rob Hess. An open-source SIFT Library. In *Proceedings of the international conference on Multimedia (MM '10)*. ACM, New York, NY, USA, 1493-1496

A Real-Time Implementation of Vision-Based Terrain Classification

Eric Coyle

Embry-Riddle Aeronautical University
600 S. Clyde Morris Blvd
Daytona Beach, FL 32114-3900
(386) 226-7441

coylee1@erau.edu

Wendell Bates,

FAMU-FSU College of Engineering
2525 Pottsdamer Street
Tallahassee, FL 32310-6046
(850) 410-6389

batesir@eng.fsu.edu

Emmanuel G. Collins, Jr.,

FAMU-FSU College of Engineering
2525 Pottsdamer Street
Tallahassee, FL 32310-6046
(850) 410-6373

ecollins@eng.fsu.edu

Hongwu Wang

Human Engineering Research
Laboratories
6425 Penn Avenue, Suite 400
Pittsburgh, PA 15206
(412)-954-5322

how11@pitt.edu

Dan Ding,

Human Engineering Research
Laboratories
6425 Penn Avenue, Suite 400
Pittsburgh, PA 15206
(412) 822-3684

Dad5@pitt.edu

Rory A. Cooper

Human Engineering Research
Laboratories
6425 Penn Avenue, Suite 400
Pittsburgh, PA 15206
(412) 822-3700

rcooper@pitt.edu

ABSTRACT

To increase vehicle safety and efficiency on all terrains (both outdoor and indoor) a ground vehicle control system should have settings tuned to individual terrains. However, to ensure the correct terrain-dependent control setting is used, a method of identifying the current terrain must be sought. This paper focuses on the real-time implementation of a vision-based terrain classification approach. A laser-stripe based structured light sensor is used in conjunction with an infrared camera that allows the traversed terrain signature to be seen during the day or at night. The classification procedure uses spatial features, extracted from the captured images, to characterize each terrain. A Parzen-window classifier is used to estimate the terrain type in real time and a history-based method is used to reject misclassifications. Experimental results based on classifying four terrains (asphalt, tile, grass, and gravel) demonstrate the overall effectiveness of the proposed method. Although, the presented results correspond to implementation on an electric powered wheelchair (EPW), the method is applicable to all ground vehicles including autonomous ground vehicles (AGVs) by simply replicating the mounting conditions of the sensor.

Keywords

Terrain Classification, Autonomous Ground Vehicles

1. INTRODUCTION

Vehicles that are expected to operate on a variety of off-road terrains have a need for separate control systems or settings for each terrain in order to ensure safe and efficient performance. Vehicles of this nature include commercial, landscaping, military and personal use vehicles such as electric powered wheelchairs (EPWs) [3]. Examples of such systems can be found on the new Land Rovers (LR4), Ford Explorers, and Jeep Cherokees [22], [17], [11]. These systems include modes for various terrains such as gravel, grass, snow, mud, sand, and rock. The modes include predefined settings that alter vehicle parameters including anti-

locking, throttle response, and differential locking. It is then the responsibility of the driver to manually switch between the control modes for each terrain. Terrain classification algorithms have been developed to assist in automating the switch between control modes since human driver awareness can be limited [8], [7].

Terrain classification methods for mobile robots primarily use one of two sensor types: proprioceptive (i.e. vibration and slip) sensors [19], [18], [16], [6], and vision sensors [1], [10]. In previous works that utilize proprioceptive sensors, it was discovered that by transforming vibration signals (measured from inertial measurement units) into the frequency domain using a Discrete Fourier Transform (DFT), distinct terrain signatures can be observed in the magnitude response [2], [8], [7]. However, terrain classification using proprioceptive sensors is speed, load and vehicle dependent. These dependencies create a lack of portability between platforms and can lead to poor classification results without the use of large training sets. Vision sensing of the terrain generally refers to the use of cameras or laser range finders to identify unique spatial or visual characteristics of the terrain [1], [10]. These methods have the advantage of being easily ported between vehicle platforms, but when the ground has superficial coverings (e.g. , leaves, dry grass, or a small amount of water), or when the environment lacks visibility due to smoke, fog, or other precipitation, vision sensors can lead to misclassifications. Surfaces that have a similar appearance, such as dry and wet sand, may also cause poor classification but are very distinct from a control perspective.

This paper presents results from one of the first examples of real-time implementation of terrain classification. The methodology is classified as vision-based and was originally presented in [13]. The system is implemented on an electric powered wheelchair (EPW), but can easily be translated to other vehicle platforms by replicating the mounting conditions. This platform was chosen since it is pre-equipped with five programmable driving profiles which can be tuned to individual terrains. It should be noted that

over 200,000 people in the United States used electric-powered wheelchairs (EPWs) as their primary means of mobility in 2000 [12] and approximately 400,000 in 2010 [4]. This has led to increased attention on terrain-dependent control systems for EPWs [23], [24], [25] which is expected to greatly increase independence and maneuverability [9], [5]. This paper also discusses the online implementation of an update rule [13] to reject misclassifications, which ultimately leads to more accurate use of EPW control modes.

The paper is organized as follows: Section 2 describes the hardware set-up used to implement the algorithm and Section 3 describes the classification algorithm itself. Section 4 describes the raw classification results and how these results are improved through the use of the update rule methodology discussed in Section 3. Section 5 gives concluding remarks and identifies areas for future work.

2. SYSTEM DESCRIPTION

The Quantum 6000Z (shown in Figure 1), which is produced by Pride Mobility, was chosen as the target EPW platform for real-time use of terrain classification as its programmable driving profiles are ideal for implementing terrain-dependent control modes in future research. The 6000Z connects to a PC based Pilot Plus programmable controller (shown in Figure 1) that allows the user to change certain settings such as: maximum velocity, acceleration, deceleration, and turning radius in up to five driving modes.



Figure 1. Quantum 6000Z Pride Mobility Wheelchair

The 6000Z weighs 300 lbs, has a maximum speed of 8 mph and a range of approximately 20 miles. The wheelchair is joystick controlled and has a passenger and personal item weight capacity of 300 lbs. Several other Pride 6000Z product specifications are given in Table 1.

Table 1. Specifications for the Pride Mobility 6000Z Electric Wheelchair

Quantum 6000Z Specifications	
Ground Clearance	3.5"
Turning Radius	22.5"
Overall Length	36" w/o foot riggings
Overall Width	25.875"
Drive Wheels	14"
Caster Wheels	6" solid
Suspension	Active-Trac ATX with integrated rear dual-strut and articulating caster beam

The online classification approach presented in this paper uses the same laser stripe based structured light sensor, or line-striper used in [13]. The laser line-striper is a high resolution, low proximity, hybrid sensor consisting of the following components: a Class IIIB GaAs laser (pulsed) with 1mW max output at 905nm donated by the line striper developers [15] at Carnegie Melon University, and a Watec WAT-902H Ultimate camera with a Computar HG1214AFCS-3 12mm lens. In order to capture the intersection of the laser plane and terrain using the Watec camera, a 900nm Omega Optical bandpass filter is attached to the lens. The line-striper is mounted on the front left of the wheelchair directly above the front caster wheel as seen in Figure 2. The laser is mounted 10 inches off the ground at an angle of 29° with respect to the horizontal. The camera is mounted 5 inches above the line-striper at an angle that places the laser plane in the center of captured images when traversing level ground. This mounting was chosen to prevent the foot platform and user from obstructing the laser line without increasing the outer dimensions of the EPW. In this configuration, the camera sees approximately 21 inches ahead of the front left caster, with a square terrain patch of approximately 9 inches by 9 inches. Figure 4 illustrates how the camera is used to perceive the laser plane and terrain intersection.

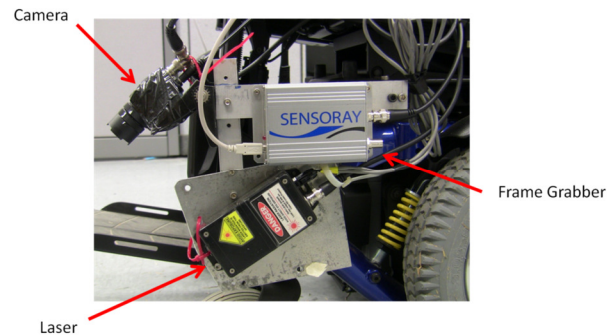


Figure 2. The laser line-striper and frame grabber mounted to the Quantum 6000Z by Pride Mobility

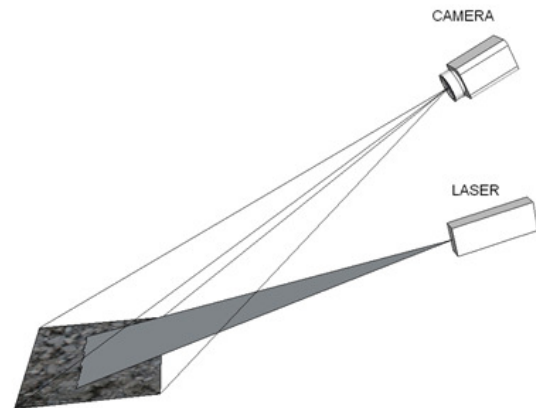


Figure 3. Demonstration of mounted camera viewing an approximately 9in x 9in area

Figure 3 shows that the light of the laser is fanned out 30° in both directions, forming a plane of light. When an object or the ground intersects the laser plane, the reflected light is observed by the camera placed at a vertical offset from the laser. The bandpass filter attached to the camera lens prevents most of the ambient light that illuminates the ground from being seen in the captured

images. Triangulation is used to extract the spatial coordinates of the laser plane and terrain intersection. The image frames are captured with a 2253S Sensoray frame grabber, which is LINUX compatible and also shown in Figure 3. The Sensoray frame grabber is capable of capturing frames at 30 fps, but the classification algorithm, presented in Section III, is only able to process the 640 x 480 images at a rate of 10-15 fps due to the use of a 1.8GHz Pentium M 745 processor used in these experiments.

3. CLASSIFICATION ALGORITHM

Due to the fact that terrain colors may change under different lighting and weather conditions (e.g., grass may be green or yellow, gravel may be white or various shades of gray, or tile may consist of different colors), the methodology used in this research for classification, unlike [1] and [10] is not heavily dependent on color. Instead the classification relies on spatial relationships in the terrain which are reflected in the gray levels of the captured images. These relationships are quantified using spatial frequency response methods to determine features for classification. Terrain classification is conducted separately on each of these feature sets using Parzen windows estimation of the probability distributions [20] similar to its use in [6], [2], [8], and [7]. The classification procedure for each feature type is shown in Figure 4 along with an alternate feature set based on image texture that was proposed in [13].

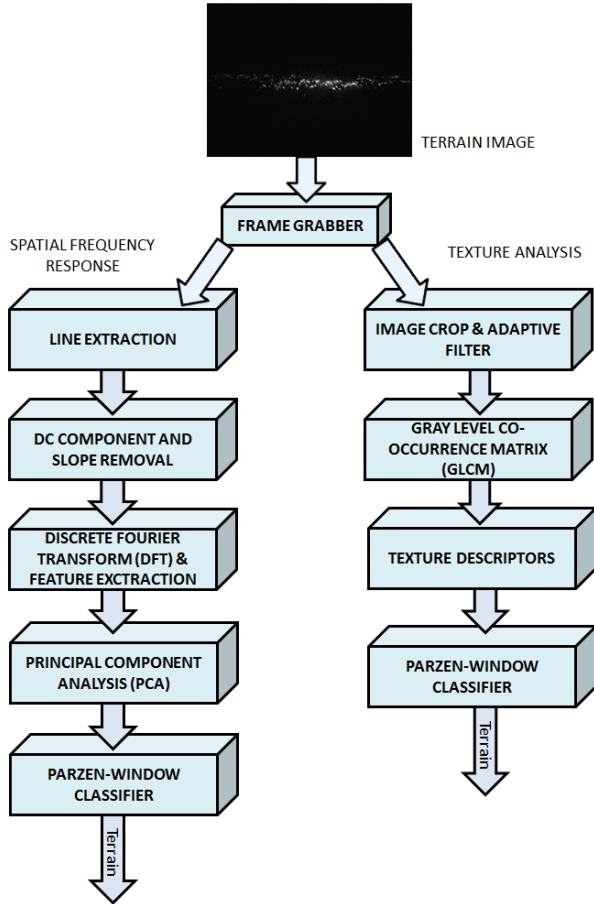


Figure 4. The Vision Based Classification Outline

3.1 Spatial Frequency Response Features

Spatial frequency analysis is designed to provide an accurate representation of the unique spatial nature of each terrain profile. To compute the spatial frequency response feature, the points on the laser line are first extracted from the image, as shown below in Figure 5, and then transformed from the image coordinates to the laser plane coordinates (X,Y). These laser plane coordinates are indicative of the terrain profile being traversed. It can also be shown that the spatial frequency response of the terrain profile has a direct link to terrain classification using proprioceptive sensors (specifically vibration-based terrain classification) [6], [2].



Figure 5. Infrared Image of the Laser Line on Grass (left) and the Extracted Laser Line (right)

Before calculating the spatial frequency response of the terrain profiles, it is important to remove any information that is not inherent to the terrain type such as the DC component (a zero frequency component) and the average slope of the profile. The DC component represents the average height of the profile in the laser plane and the average slope is with respect to the cross-slope referenced to the EPW position. The DC component and relative slope are removed from the vertical position of the terrain profile by first fitting a line in the least squares sense, which has the equation.

$$\hat{Y} = aX + b, \quad (1)$$

where X is the set of horizontal positions for the laser line in the laser plane coordinate system, \hat{Y} is the vertical position estimate in the laser plane coordinate system, a is the estimated cross-slope and b is the estimated DC component. The relative cross-slope and DC component can then be removed from the measured vertical position Y by:

$$y = Y - \hat{Y}, \quad (2)$$

which yields the new terrain profile y .

The new terrain profile y forms a discrete sequence of length n which is equal to the number of laser points that can be extracted from the camera image. To find the frequency components of y , the spatial Fourier Transform is obtained by using the Discrete Fourier Transform (DFT), which has the form

$$\tilde{y}_k = \sum_{n=0}^{N-1} y(n) e^{-i2\pi k n / N}, \quad k = 0, \dots, N-1, \quad (3)$$

where the frequency components \tilde{y}_k comprise the spatial frequency response $y(j\omega) = [\tilde{y}_1 \ \tilde{y}_2 \ \dots \ \tilde{y}_{N-1}]^T$. The spatial frequency response feature vector x_f is then the magnitude of $y(j\omega)$ as defined by

$$x_f = [|y(j\omega)|]^T. \quad (4)$$

This process for computing spatial frequency response is the same as presented in [13].

3.2 Principal Component Analysis

Classification of \mathbf{x}_f is a high-dimensional classification problem which results in large computational requirements. For this purpose, Principal Component Analysis (PCA) is used to create reduced-order feature vectors. In implementing PCA, a training matrix \mathbf{D} is first constructed such that it is comprised of a set of feature vectors for each of the considered terrains; in particular,

$$\mathbf{D} = [\mathbf{x}_{f1} \ \mathbf{x}_{f2} \ \dots \ \mathbf{x}_{fN-1}]. \quad (5)$$

Then, an unbiased set of the training data $\hat{\mathbf{D}}$ was created by subtracting the mean feature vector $\bar{\mathbf{d}} \in \mathbb{R}^{d \times 1}$ of the training matrix \mathbf{D} from each column of the training data \mathbf{D} matrix such that

$$\hat{\mathbf{D}} = \mathbf{D} - \bar{\mathbf{d}}\mathbf{1}_{1 \times r}, \quad (6)$$

where $\mathbf{1}_{m \times n}$ is an $m \times n$ matrix of ones. Computing the Singular Value Decomposition (SVD) of this unbiased training data yields orthogonal matrices \mathbf{U} and \mathbf{V} with a nonnegative diagonal matrix $\mathbf{\Sigma}$ such that

$$\hat{\mathbf{D}} = \mathbf{U}\mathbf{\Sigma}\mathbf{V}^T. \quad (7)$$

Each diagonal component of $\mathbf{\Sigma}$ corresponds to a principal component vector \mathbf{u}_i of \mathbf{U} (i.e., a column). The amount of energy ξ associated with the first k principle components is given by

$$\xi = \frac{\sum_{i=1}^k \sigma_i^2}{\sum_{i=1}^d \sigma_i^2}, \quad (8)$$

where σ_i is the i th diagonal component of the matrix $\mathbf{\Sigma}$ and $\sigma_1 \geq \sigma_2 \geq \dots \geq \sigma_d$. The parameter k serves as the reduced-order dimension and is chosen by treating ξ as a tuning parameter. Then defining

$$\mathbf{U}_k = [\mathbf{u}_1 \ \mathbf{u}_2 \ \dots \ \mathbf{u}_k] \quad (9)$$

allows $\mathbf{Y}_R \in \mathbb{R}^{k \times r}$ to be given by

$$\mathbf{Y}_R = \mathbf{U}_k^T \hat{\mathbf{D}}, \quad (10)$$

where the columns of \mathbf{Y}_R , denoted by $\bar{\mathbf{y}}_{Ri}$ are called the eigenspace coefficients and serve as the reduced-order feature vectors used in training. These $\bar{\mathbf{y}}_{Ri}$ are the projections of the unbiased feature vectors $\hat{\mathbf{d}}_i$ (the columns of $\hat{\mathbf{D}}$) onto the space spanned by \mathbf{U}_k . Hence, the eigenspace coefficients are reduced-order representations of the terrain signatures in the orthogonal basis defined by the column space of \mathbf{U}_k [7]. Note that each $\bar{\mathbf{y}}_i$ corresponds to a specific terrain type, which is the same as the feature vector \mathbf{d}_i (which is the i -th column of \mathbf{D}) [7].

3.3 Parzen Window Estimation

The Parzen-window classifier was selected to identify the terrain corresponding to \mathbf{x}_f due to its fast training speed, simplicity and robustness [20]. The Parzen window classifier is a non-parametric procedure that estimates a probability density function (pdf) by superposition of a window, i.e. replicates of a function (often a Gaussian), onto each training sample. The Parzen window classifier makes a classification decision after calculating the pdf of each class using the given training examples.

Probabilistic Neural Networks (PNNs) provide a structure for implementation of Parzen window estimation. The network structure of a typical PNN is shown in Figure 6 with an input layer, a pattern layer, a summation layer, and an output layer [14].

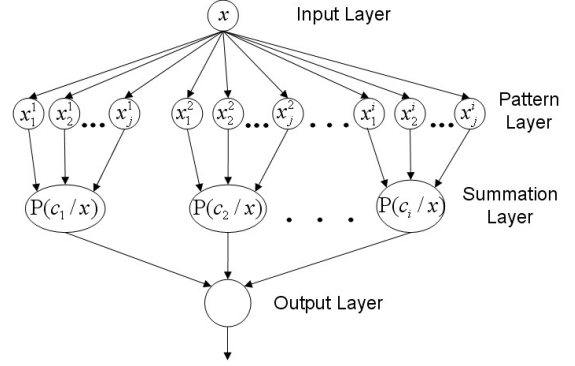


Figure 6. Parzen Probabilistic Neural Network

The input layer buffers the input feature vector \mathbf{x}_f from (4) to the neurons in the pattern layer. Then, the neuron \mathbf{x}_j^i computes its output using the Gaussian window function

$$\phi_{ij}(\mathbf{x}) = \frac{1}{(2\pi)^{\frac{N}{2}} \sigma^N} \exp \left[-\frac{(\mathbf{x} - \mathbf{x}_j^i)^T (\mathbf{x} - \mathbf{x}_j^i)}{2\sigma^2} \right], \quad (11)$$

where i is the class (or in our case the terrain type), j is the training sample in class i , σ is a smoothing factor, and N is the dimension of the pattern vector \mathbf{x} [24]. The summation layer then sums the windowing function $\phi_{ij}(\mathbf{x})$ for all the training samples, resulting in the probability $P(C_i|\mathbf{x})$ of a given input \mathbf{x} belonging to class C_i . Mathematically this is equivalent to

$$P(C_i|\mathbf{x}) = \frac{1}{(2\pi)^{\frac{N}{2}} \sigma^N} \sum_{j=1}^{n_i} \exp \left[-\frac{(\mathbf{x} - \mathbf{x}_j^i)^T (\mathbf{x} - \mathbf{x}_j^i)}{2\sigma^2} \right], \quad (12)$$

where n_i denotes the total number of samples in class C_i . The PNN output layer estimates \mathbf{x} to be from the class with the highest $P(C_i|\mathbf{x})$. This means the vector \mathbf{x} is said to belong to a particular class C_i if

$$P(C_i|\mathbf{x}) > P(C_j|\mathbf{x}), \quad \forall j = 1, 2, \dots, n, \quad j \neq i. \quad (13)$$

The key to effective use of the PNN in this manner is the selection of the smoothing factor σ . For nonlinear decision boundaries, the smoothing factor needs to be as small as possible [6]. In empirical studies such as the one presented here, a validation set can be used to select a suitable smoothing factor and the PCA energy percentage ξ discussed in Subsection 3.2.

3.4 Control Update Rule

As the classification result, regardless of whether it is a true or false positive, will be used to determine the appropriate terrain-dependent control mode, a process is needed which prevents or minimizes control mode usage based on misclassifications. The research of [4] utilizes such a process, called an update rule, by considering both the current and past terrain detection. The motivation behind the update rule is to utilize inherent consistency in terrain data that results from the fact that terrain changes are not random. This allows for misclassifications to be rejected while minimizing the delay in switching control modes when a true terrain transition is experienced. The update rule has two design parameters:

- 1) n - the width of the history window, which corresponds to the current and previously identified terrains;

- 2) η - the minimum fraction of samples in the history window required to be of a single terrain before the control mode will be updated (It can be viewed as a threshold required to switch control modes.)

When a new terrain is classified, the update rule considers the new classification and the $n-1$ prior classifications. The update rule then calculates the percentages each terrain is observed in this history window. If the highest percentage \bar{p} satisfies $\bar{p} \geq 100\eta$ then the control mode will be updated. In the case where $\bar{p} < 100\eta$, the robot will continue to use the last control mode specified by the update rule.

Update rule performance is measured in terms of robustness to misclassification and sensitivity to terrain transition. Robustness is expressed as the accuracy of control mode usage and sensitivity is defined as the average delay in updating control modes when a terrain transition is experienced. Note that higher robustness corresponds to more accurate control mode usage and a smaller delay (measured in number of samples) implies higher sensitivity. Due to the inherent trade-off in robustness and sensitivity, values of n and η that simultaneously maximize robustness and sensitivity may not exist. Therefore, in general a Pareto optimal choice of n and η is sought. A pair (n, η) is Pareto optimal if there is no way to increase the sensitivity without reducing the robustness and vice versa (see Figure 7). Determining the Pareto optimal values of n and η begins by defining finite sets of values of n and η to be considered which are: $N = \{n_1, n_2, \dots\}$ and $H = \{\eta_1, \eta_2, \dots\}$. Update rules with all possible combinations of $n \in N$ and $\eta \in H$ are then applied to the classification results obtained using the Parzen-window classifier discussed previously. For each update rule, sensitivity is computed along with the robustness, after which a set of Pareto optimal pairs (n, η) can then be determined. Selection of one pair from this set of Pareto optimal values is dependent on user's preference between sensitivity and robustness [4].

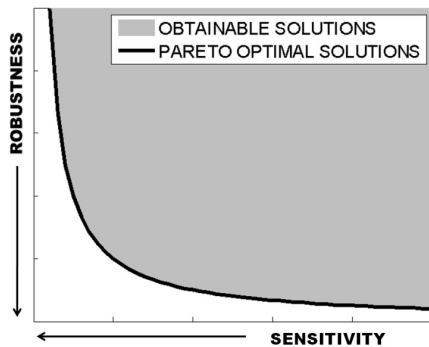


Figure 7. Explanation of Pareto Optimality

To determine an update rule for x_f , the set of considered values for n was defined as $N = \{1, 2, 3, \dots, 20\}$, while the set of considered values of η was defined as $H = \{0.5, 0.525, 0.55, \dots, 1.0\}$. A brute force search was used to determine the appropriate values of these parameters based on empirical data. The values chosen were $n = 5$, and $\eta = 0.60$ which corresponded to the highest observed robustness. For more information on the update rule, see [4].

4. REAL-TIME RESULTS

This section presents terrain classification results obtained using spatial frequency features as described in Section 3. Online classification tests were conducted at two locations: the University of Pittsburgh campus in Pittsburgh, PA and the FAMU-FSU College of Engineering campus in Tallahassee, FL. Four different surfaces were considered during testing: grass, asphalt, tile, and gravel. Figure 8 shows the four different terrains traversed by the EPW. In total 500 samples from each terrain were used in algorithm training and 1000 on-line classifications were conducted on each of the terrains below.



Figure 8. Grass (top left), gravel (top right), asphalt (bottom left), and tile (bottom right) terrains

Table 2 shows the classification accuracy that can be achieved when using spatial frequency response features for classification and Table 3 shows the result when the update rule is applied. These results show that the online algorithm is able to classify all four terrains with an accuracy of at least 84% and an overall accuracy of 89%. When paired with the presented update rule this accuracy increases to over 93% for each terrain and an overall accuracy of over 96%. This indicates that x_f is an effective online terrain signature for the EPW. When misclassifications occur it tends to be between the gravel and grass terrains or between the tile and asphalt terrains. This is due to the similarly rough nature of the grass and gravel profiles and the similarly smooth nature of the asphalt and tile profiles.

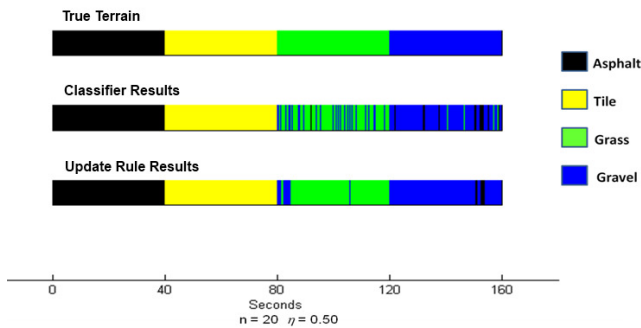
Table 2. Spatial frequency response classification results

		Tested Terrain			
		Asphalt	Tile	Grass	Gravel
Detected Terrain	Asphalt	84.3%	15.7%		
	Tile		96.7%		3.3%
	Grass			84.0%	16.1%
	Gravel			8.3%	91.7%

Table 3. Update rule results

		Tested Terrain			
		Asphalt	Tile	Grass	Gravel
Detected Terrain	Asphalt	93.6%	6.4%		
	Tile		99.3%		0.7%
	Grass			96.0%	4.0%
	Gravel			4.1%	95.9%

To determine if the classification approach could benefit from further tuning of the update rule, a sequence of three terrain-transitions was formed by concatenating 1000 samples of the four terrains (asphalt, tile, grass, and gravel) at 25Hz. This sequence is shown in the top bar graph (labeled true terrain) of Figure 9, while the middle bar gives the classifier results and the bottom bar shows the results of the update rule when applied to the classifier results.

**Figure 9. Spatial frequency response classification accuracy comparison**

While the control update rule was effective, Table 3 and Figure 9 obviously indicate it is not able to completely eliminate all of the misclassifications. However, the updater rule is primarily designed to ignore isolated, shorts stretches of misclassifications, which it does effectively based on Figure 9. From figure 9 there are only 5 instances of improper control usage with each lasting 2 seconds or less. Additional data collections or incorporating other features may be able to eliminate this all together.

5. CONCLUSIONS AND FUTURE WORK

This paper presents real-time implementation results from a terrain classification approach based on spatial terrain profiles measured from a laser line striping sensor. All experiments were conducted on the Pride Mobility Quantum 6000Z Series EPW and spatial frequency response features are used to indicate the terrain signature. When paired with the presented update rule to reject misclassifications, classification accuracies of over 93% can be achieved for each of the four terrains.

Future work is expected to incorporate real-time testing of texture features which are presented in [13]. The combined use of spatial frequency response and texture features will also be addressed through the use of parallel programming (opposed to sequential programming). Lastly, the implementation of the classification algorithm was tested with four relatively homogenous terrains. Therefore, more challenging experiments involving mixed terrains, surfaces with anisotropic features (e.g. concrete roadways

to grooves in predefined directions) and other outdoor terrains like mud should be conducted to determine the range of applicability of the online implementation.

6. ACKNOWLEDGMENTS

This research was supported by the Telemedicine and Advanced Technology Research Center (EDMS# 4532).

7. REFERENCES

- [1] A. Angelova, L. Matthies, D. Helmick, and P. Perona. *Fast terrain classification using variable-length representation for autonomous navigation*. In IEEE Computer Society Conference on Computer Vision and Pattern Recognition, pages 1–8, June 2007.
- [2] E. G. Collins Jr. and E. Coyle. *Vibration-based terrain classification using surface profile input frequency responses*. In IEEE International Conference on Robotics and Automation, pages 3276 – 3283, May 2008.
- [3] E. Coyle, E. G. Collins Jr., E. M. DuPont, D. Dang, H. Wang, R. A. Cooper and G. Grindle, *Vibration-Based Terrain Classification for Electric Powered Wheelchairs*, Proc. of the Fourth IASTED International Conference on Telehealth and Assistive Technologies (Telehealth/AT 2008), Baltimore, Maryland, pp. 139-144, April 16-18, 2008.
- [4] E. J. Coyle, J. E. G. Collins, and L. Lu, *Updating control modes based on terrain classification*, in Proceedings of International Conference on Robotics and Automation, Anchorage, Alaska, 2010.
- [5] D. Ding, R.A. Cooper, S. Guo, T.A. Corfman. *Analysis of Driving Backwards in an Electric-Powered Wheelchair*. IEEE Transactions on Control Systems Technology, 12(6): 934-943, 2003.
- [6] E. M. DuPont, R. G. Roberts, C. A. Moore, M. F. Selekw, and E. G. Collins. *Online terrain classification for mobile robots*. In Proceedings of IMECE 2005 ASME 2005 International Mechanical Engineering Congress and Exposition Conference, Orlando, FL, November 2005.
- [7] E. M. DuPont, E. G. Collins, E. J. Coyle, and R. G. Roberts. *Terrain classification using vibration sensors: theory and methods*. Chapter in New Research on Mobile Robotics, Nova Science Publishers, 2008.
- [8] E. M. Dupont, C. A. Moore, Jr. E. G. Collins, and E. Coyle. *Frequency response method for terrain classification in autonomous ground vehicles*. Autonomous Robots, 24(4):337–347, May 2008.
- [9] S. Evans, A. Frank, C. Neophytou, L. de Souza, *Older adults' use of, and satisfaction with, electric powered indoor/outdoor wheelchairs*. Age and Ageing, 2007.
- [10] I. Halatci, C. A. Brooks, and K. Iagnemma. *Terrain classification and classifier fusion for planetary exploration rovers*. In IEEE Aerospace Conference, pages 1–11, March 2007.
- [11] Jeep, Off-Road Performance, Available [Online]: September 6, 2011 http://www.jeep.com/en/2012/grand_cherokee/capability/off_road_performance
- [12] M.P. LaPlante, *Demographics of Wheeled Mobility Device Users*. Space Requirements for Wheeled Mobility, Center for

- Inclusive Design and Environmental Access, University at Buffalo, Buffalo, New York 14214-3087, 2003.
- [13] L. Lu, C. Ordonez, E. G. Collins, Jr., and E. M. DuPont. *Terrain surface classification for autonomous ground vehicles using a 2d laser stripe-based structured light sensor*. In Proceedings of Conference on Intelligent Robots and Systems, St. Louis, MO, 2009.
- [14] K. Z. Mao, K. C. Tan, and W. Ser. *Probabilistic neural-network structure determination for pattern classification*. IEEE Transactions on Neural Networks, 11(4):1009–1016, July 2000.
- [15] C. Mertz, J. Kozar, J. R. Miller, and C. Thorpe. *Eye-safe laser line stripers for outside use*. In IV 2002, IEEE Intelligent Vehicle Symposium, June, 2002, December 2001.
- [16] L. Ojeda, J. Borenstein, G. Witus, and R. Karlesen. *Terrain characterization and classification with a mobile robot*. Journal of Field Robotics, 23(2):103–122, January 2006.
- [17] J. N. Ross, Next-Gen 2011 Ford Explorer Will Feature Terrain Management System, Available [Online]: <http://www.autotropolis.com/car-tech/next-gen-2011-ford-explorer-will-feature-terrain-management-system.html>, April 2010.
- [18] D. Sadhukhan. *Autonomous ground vehicle terrain classification using internal sensors*. Master’s thesis, Florida State University, Tallahassee, FL, March 2004.
- [19] D. Sadhukhan and C. Moore. *Online terrain estimation using internal sensors*. In Proceedings of the Florida Conference on Recent Advances in Robotics, Boca Raton, FL, May 2003.
- [20] D. F. Specht. *Probabilistic neural networks*. Neural Networks, 3(1):109–118, 1990.
- [21] E. Steinfeld, and P. Paque, *Space Requirements for Wheeled Mobility*. Technical Report: U.S. Access Board, Washington D.C. March 2004.
- [22] D. Vanderwerp. *What does terrain response do?*, [Online], Available: <http://www.caranddriver.com/features/9026/what-does-terrain-response-do.html>, February 2005.
- [23] H. Wang, B. Salatin, G.G. Grindle, D. Ding, R.A. Cooper, *Real-Time Model Based Electrical Powered Wheelchair Control*, Medical Engineering and Physics, pp. 1244-1254, Vol. 31, No. 10, December 2009.
- [24] H. Wang, B. Salatin, G.G. Grindle, D. Ding, R.A. Cooper, *Real-time Slip Detection and Traction Control of Electrical Powered Wheelchairs*, Proceedings of the Rehabilitation Engineering and Assistive Technology Society of North America Conference, June 23-27, 2009.
- [25] H. Wang, B. Salatin, G.G. Grindle, D. Ding, R.A. Cooper, *Real-Time Forwarding Tipping Detection and Prevention of a Front Wheel Drive Electric Powered Wheelchair*, Proceedings of the Rehabilitation Engineering and Assistive Technology Society of North America Conference, Las Vegas, NV, June 26-30, 2010.

Aspects of Simultaneous Localization and Mapping for Change Detection

George Baltas
Florida State University
Electrical and Computer Engineering
gb11c@my.fsu.edu

Tesfaye G-Michael
Florida State University
Electrical and Computer Engineering
tg04@my.fsu.edu

Rodney Roberts
Florida State University
Electrical and Computer Engineering
rroberts@fsu.edu

ABSTRACT

The underwater object tracking procedure comprises object detection and classification with a seafloor imaging sonar, followed by identification (ID) of objects (features) by human divers or short-range ID sensors. This approach is impractical in wide area seafloor, where large concentrations of debris may saturate the procedure. Thus change detection techniques have been developed for surveillance of cluttered environments in order to automatically compare new seafloor images with historical data. These techniques track changes that occur over time using a database of historical (benign) objects created during past seafloor scans or surveys against current scans detecting the appearance of new potential threats that are inserted into the scene by adversaries. In this paper we analyze aspects of simultaneous localization and mapping (SLAM) algorithm feature recognition on the image data collected using a synthetic aperture sonar (SAS).

Keywords: SLAM, Change detection, Synthetic aperture sonar

1. Introduction

In recent years, the problem of localization and mapping of an area using imagery from sensor systems brought particular interest in the mobile robotics community Kummerle [1], where place recognition has been studied intensively in the area of mobile robotics. Techniques for localization and feature recognition are highly relevant in the context of the SLAM problem, as they can be used to solve object location. They can also be applied to detect changes in the environment such as, underwater. Our planet is mostly covered by water, yet the level of detailed knowledge about the water covered area is very limited compare to the land, for instance synthetic aperture sonar (SAS) in an underwater environment, provide high-resolution imaging that is particularly useful for object detection operations. Usually, an autonomous underwater vehicle (AUV) will be deployed to survey an area of seafloor in a pre-programmed fashion. Ideally, however, the AUV would be allowed to react to information that it collects during the mission by

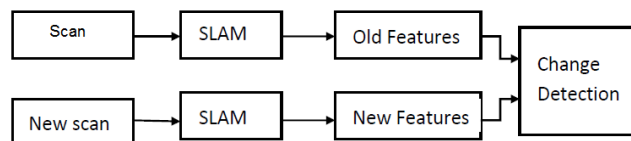


Figure 1. General Block Diagram for SLAM Based Change Detection

adapting its route so that the most useful data can be collected.

This paper will address the high level prospective of SLAM techniques for change detection potentially using synthetic aperture sonar image data. In change detection, it is important to identify anomalies in the area of high traffic water ways, which may include threats such as under water improvised explosive devices (IEDs). However, it is tedious and very difficult to compare huge number of underwater images looking for differences manually. Subtle changes may also be missed by visually comparing two images.

The SLAM based change detection process is outlined in Figure 1. The reference scan (the first scan) and new scan are surveyed in different time. Each scan is undergoing through SLAM processor, where the features/landmarks are identified. If a new feature is inserted into the scene, it will be flagged and passed onto the Change Detection module. The Change Detection module finds differences between two images and precisely identifies if the new object is a potential threat or not. This paper does not discuss any particular change detection algorithm, however the development of robust change detection algorithms is an active area of research. Recently, coherent change detection has been employed by G-Michael et al in [2,3].

2. Body of The Paper

This paper is organized as follows: Section 1 reviews the change detection and SLAM methods and their application as a feature identification and detection tool. Section 2 presents a review of SLAM, development of SLAM algorithms, such as Extended Kalman feature (EKF),

and develops a method for change detection using SLAM. And finally conclusions and future work are discussed in Section 3.

2.1 Review of Simultaneous Localization and Mapping

Simultaneous localization and mapping (SLAM) was originally developed by Smith[4] and Leonard [5]. SLAM is a technique created in the robotics community while wondering if an autonomous vehicle can start in an unknown location, without previous knowledge of the environment, and then incrementally build a map of this environment by extracting information from its sensors, while simultaneously using this map to compute the robot location. The map and the estimate of the vehicle's location that are obtained from a successful SLAM system do provide important information. In the robotics domain, SLAM is the problem of concurrently estimating in real time the structure of the surrounding scene, perceived by moving sensor, while simultaneously getting localized in it. Probabilistic technique based on estimation theory is the nerve of SLAM algorithms. Estimation theory is the process by which we infer the value of a quality of interest, x , by processing data that is some way dependent on x :

$$p(x|z) = \frac{p(z|x)p(x)}{p(z)}. \quad (1)$$

Equation 1 could be reformulated into three straightforward parts: $p(z|x)$ is the likelihood of receiving the measurement z for the given states of x , $p(x)$ is the prior probability of the states incorporating all our previous knowledge about the states and $p(z)$, the probability of the measurement, normalizes the state probabilities. Estimation theory can be divided into two categories: linear and nonlinear estimation. Linear estimation is straightforward and its results are trustworthy, nonlinear estimation on the other hand is a more difficult technique and the solutions are prone to diverge. However, nonlinear estimation is often opted due to the fact that many problems are not linear. In our problem, we use the non-linear form of Kalman filter, i.e., Extended Kalman Filter (EKF). The main reason for this choice is that the assumption of linearity does not hold for motion sequences of robotic vehicles and the extension was developed using a Taylor series expansion to handle non-linearity [6]. The EKF proposed by Smith [4], has been used as an estimator and is widely accepted by the SLAM community. It has been used here to solve the SLAM problem and allows for non-linear assumptions to be made in modeling. The Kalman filter is basically a Bayesian filter that estimates the posterior over the current pose along with the map:

$$p(x_k, m_k | z_k, u_k). \quad (2)$$

The robot pose at time k is denoted x_k , m is the map, and z_t and u_t are the measurements and controls, respectively. Maps in EKF-based SLAM approaches are feature-based. A map feature is usually represented as a point landmark m_i with coordinates x_i and y_i . The EKF algorithm consists of two main parts: Prediction and Update, its process is described in Algorithm [1] table.

Algorithm 1 : The EKF Algorithm

1. Obtain initial state estimate using vehicle data
 2. Observe and add features to the state
 3. After moving, update the new current state using vehicle data
 4. Update the estimated state from re-observing the features
 5. Add new features to the current state
-

2.2 The Extended Kalman Filter Equations

The generic equations for the EKF is based on *prediction* and *update* is given by:

2.2.1 Prediction

$$\hat{x}(k|k-1) = f(\hat{x}(k-1|k-1), u(k)) \quad (3)$$

$$\mathbf{P}(k|k-1) = \frac{\partial f}{\partial x} \mathbf{P}(k-1|k-1) \frac{\partial f^T}{\partial x} + Q(k) \quad (4)$$

$$\mathbf{z}(k|k-1) = h(\hat{x}(k|k-1)) \quad (5)$$

where $\hat{x}(k|k-1)$ is the predicted state and the right hand side of Eqn. 3 is the plant model. Eqn. 4 is the predicted covariance which is a sum of the estimated covariance and process noise. The final equation of the prediction process is the observation prediction, shown in Eqn. 5.

2.2.2 Update

$$\hat{x}(k|k) = \hat{x}(k|k-1) + \hat{W}(k)v(k) \quad (6)$$

$$\mathbf{P}(k|k) = \mathbf{P}(k|k-1) - \mathbf{W}\mathbf{S}\mathbf{W}^T \quad (7)$$

$$\mathbf{W}(k) = \mathbf{P}(k|k-1) \frac{\partial h^T}{\partial x} \mathbf{S}^{-1} \quad (8)$$

$$v(k) = \mathbf{z}(k) - \mathbf{z}(k|k-1) \quad (9)$$

$$\mathbf{S} = \frac{\partial h}{\partial x} \mathbf{P}(k|k-1) \frac{\partial h^T}{\partial x} + \mathbf{R} \quad (10)$$

The first step of the update is involved, as shown in Eqn. 6, in updating the new state estimate consisted of prediction and correction displayed on the right hand side of the equation. $\mathbf{W}(k)$, from equation 8, is the Kalman gain which minimizes the conditional mean-squared estimation error and $v(k)$ from equation 9 is the innovation. The second step of update, equation 7, is involved in updating the covariance $\mathbf{P}(k|k)$ according to the new predicted vehicle pose $\hat{x}(k|k)$. For this we need the Jacobian of the transition function relative to the state vector. Eqn. 10 is the innovation covariance.

2.3 Feature Based Mapping and Localization

In the application of the SLAM algorithm for change detection we are interested in identifying new features that are inserted into the scene between the subsequent sea-floor surveys. We assume that the underwater environment is cluttered by a set of discrete features whose location, orientation, and shape can be described by a set of parameters

which will lump into a feature vector x_f . The collection of n features is called a **Map**, such that

$$M = \{x_{f1}, x_{f2}, \dots, x_{fn}\}. \quad (11)$$

Feature maps in the sea-floor will represent specific objects of the environment. Items such as, crab traps, tires, and barrels are typical features extracted by the SAS vehicle. The use of SLAM to identify features in the laser range finder sensor is an active area of research (vandorpe). In SLAM, observation h in equation 5, occurs when a measurement of a particular feature is taken by a sensor. In feature based localization, we have a map that contains a set of features and observations of measurements between our sensor and the features. Using our prediction equations from Section 2.2.1, we can formulate an observation equation which is simply a range and bearing to the i th feature:

$$\mathbf{z}(k) = \begin{pmatrix} r \\ \theta \end{pmatrix} = h(\mathbf{x}(k), \mathbf{w}(k)). \quad (12)$$

Differentiating with respect to the x_v we arrive at the observation Jacobian model:

$$\nabla \mathbf{H}_x = \frac{\partial h}{\partial x}. \quad (13)$$

In the feature-based method, we have a map with features/landmarks of interest as depicted in Fig.[2]. This data will be processed in order to obtain well defined features which can be detected and recognized repeatedly. The confidence level of detecting a feature is boosted using n -sigma uncertainty ellipse. The n -sigma uncertainty ellipse defines the region over which the map might be visible with respect to the vehicle and then based on the value of n which sets a threshold on the uncertainty search-space. Ellipse dimensions, position, and orientation are governed by the SVD decomposition of the covariance matrix. Different n value ellipses can be defined for the same covariance matrix, the most useful ones are 2σ and 3σ , because they include probability of concentrations of 97% to 99%. For example in Fig.[3] our simulated side scan sonar vehicle sees a feature for the first time, it has an elongate ellipse. But comparing with Figs. [4] and [5], we observe that as the vehicle observes the feature repeatedly, the ellipse shrinks and almost looks like a circle, indicating more certainty.

3. Conclusions

In this paper we presented a preliminary study of the potential application of SLAM to the change detection problem. The continuation of the work presented in this paper could be quite useful in identifying features that could be used for change detection problem. In the future work, we plan to further develop the algorithm using real simulated SAS vehicle data that represents a realistic scenario.

4. Acknowledgments

We thank Professor Rodney Roberts for mentoring and giving his guidance during Spring semester 2012 when we took a directed independent study (DIS) course on studying the SLAM algorithms.

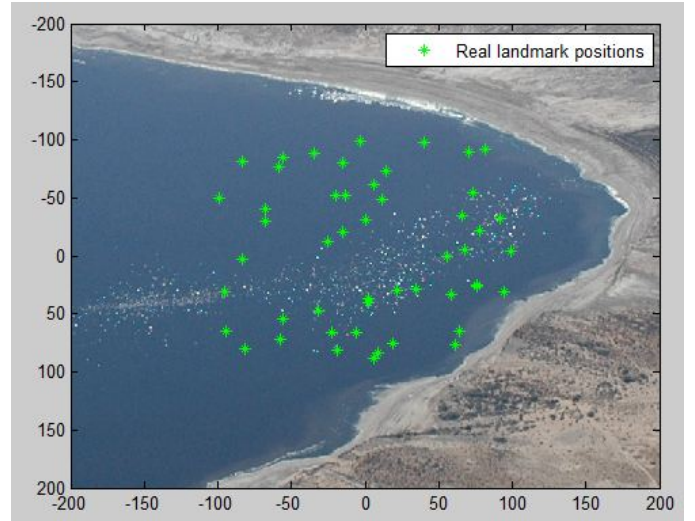


Figure 2. Representation of Features

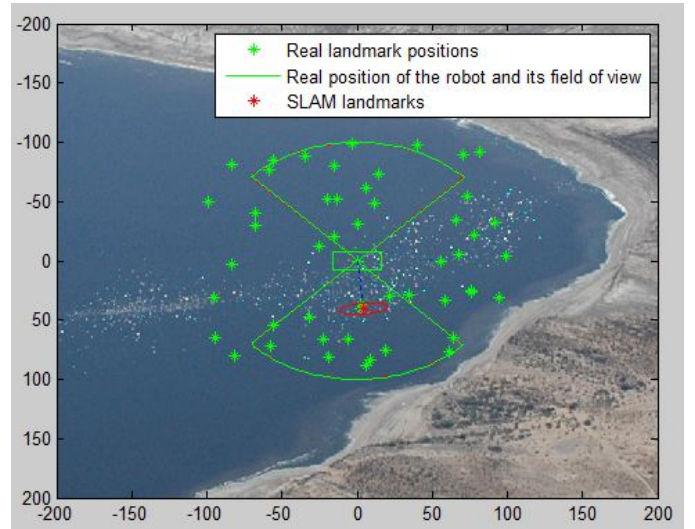


Figure 3. First Encounter of single Feature

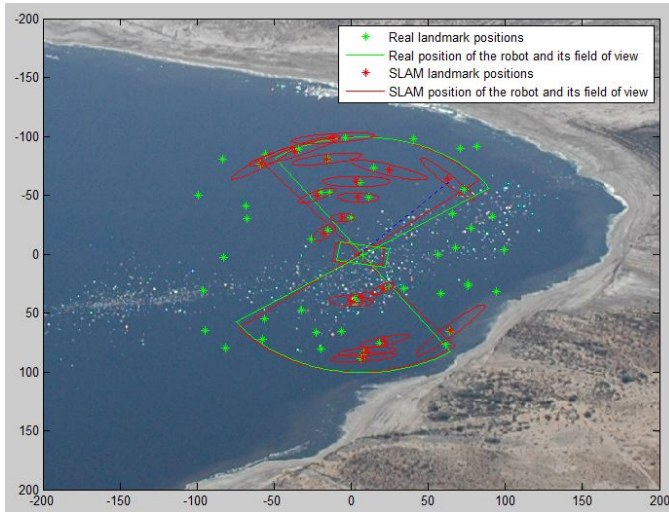


Figure 4. Intermediate Feature Detection

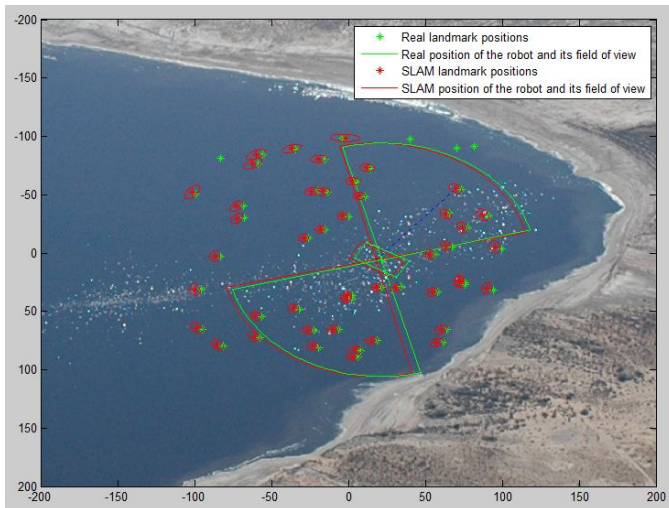


Figure 5. Final Feature Detection

5. References

- [1] R. Kummerle, B. Steder, C. Dornhege, A. Kleiner, G. Grisetti, and W. Burgard. Large scale graph-based SLAM using aerial images as prior information. *Autonomous Robots*, 30(1):25-39.
- [2] T. G-Michael and J. D. Tucker. Canonical correlation analysis for coherent change detection in synthetic aperture sonar imagery, *Institute of Acoustics Proceedings*, 32, Pt.4:87-91, September 2010.
- [3] D. D. Sternlicht, and T. G-Michael. Change detection by image correlation for synthetic aperture sonar, *Institute of Acoustics Proceedings*, 32, Pt.4:117-122, September 2010.
- [4] R. C. Smith and P. Cheeseman. On the representation and estimation of spatial uncertainty. *Int. J. Robotics Research*, 5(4), 1986.
- [5] J. J. Leonard and H. F. Durrant-Whyte. mobile robot localization by tracking geometric beacons. *IEEE Trans. on Robotics and Automation*, 7(3):376-382, June 1991.
- [6] S. Thrun. FastSLAM: An Efficient Solution to the Simultaneous Localization and Mapping Problem with unknown Data Association. *PhD thesis*, June 2003.

Information Gathering Autonomous Robot (IGAR)

John Bevis, Diego Flores
 Department of Electrical and Computer Engineering
 FAMU-FSU College of Engineering
 2525 Pottsdamer St, Tallahassee, FL 32310
 dof05@my.fsu.edu

ABSTRACT

The design of IGAR, an autonomous robot and the winner of the IEEE SoutheastCon 2012 hardware competition, is described. The purpose of the robot was to traverse through a maze-like course while taking different measurements which would indicate the correct path to follow. The data to be analyzed was temperature, capacitance, signal type (waveform or sawtooth), or voltage information for each station. A circuit was designed to incorporate the measurements of voltage, signal type, and capacitance into a single sensor, while a separate sensor measured the temperature. For navigation, a proportional derivative algorithm was used with a digital line sensor which was comprised of 8 IR emitter/receivers. The only actuators used for this project were 2 brushless DC motors controlled by a motor controller. The main controller was an 8-bit AVR microcontroller. The design was kept simple and to the point on purpose. Simplicity and efficiency were adopted as the design philosophies for this project, and they were the main factors behind the robot's success.

Keywords

SoutheastCon, line following, IGAR, voltage sensor, signal sensor, temperature sensor, capacitance sensor

1. INTRODUCTION

The IEEE SoutheastCon 2012 Hardware competition required the design of an autonomous robot that could perform electrical analysis. The robot operated in a 6 x 8ft rectangular playing field with a 5.3ft inner wall.

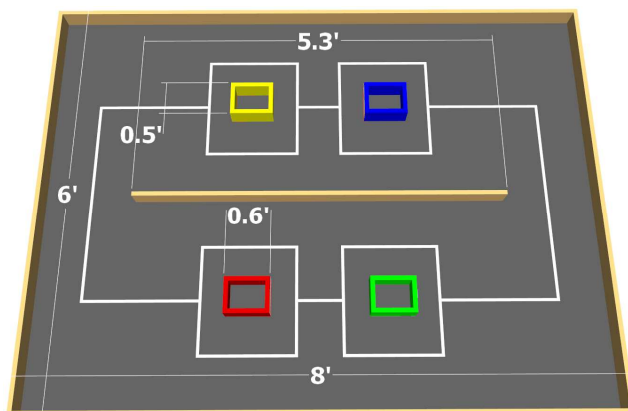


Figure 1. View of the track from the top

The robot had to run clockwise around the track. It also had to stop at four different stations to perform electrical analysis and determine the correct path to take. At each one of the four stations there was a measurement for the robot to perform. The measurements were as follows: voltage across two plates (yellow), capacitance between two plates (blue), temperature of one plate (green), and interpreting a waveform (red). Based on the information gathered the robot determined if it had to turn left or right around the station.

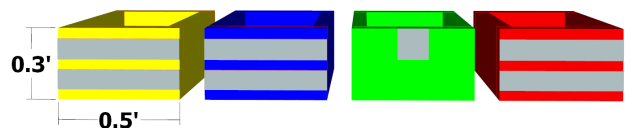


Figure 2. View of the stations from the front

Table 1. Station turns

Stations	Turn Left	Turn Right
Voltage	$\pm 5V$ to $\pm 9V$	$\pm 11V$ to $\pm 15V$
Capacitance	10nF to 100nF	1uF to 10uF
Temperature	< Ambient Temperature	> Ambient Temperature
Waveform	Sawtooth	Square

Points were granted for each completed lap (4 stations measured), and for each correctly completed task (turning in the right direction). Conversely, points were deducted for turning in the wrong direction at the stations. Four minutes was the allotted time for each run.

2. THE DESIGN

The main design approach was to keep things simple, reliable, and efficient. For instance, a single line sensor can provide all the line information needed without the need for more line sensors. Also, the robot just needed to move forward to touch the station's plates. This meant that a moving arm wasn't really necessary. Furthermore, if a two wheel differential drive system works fine, additional motors don't serve any particular purpose (provided that the two motors selected can output the appropriate torque and velocity). In other words, additional unnecessary complexity just deters from the main objective.

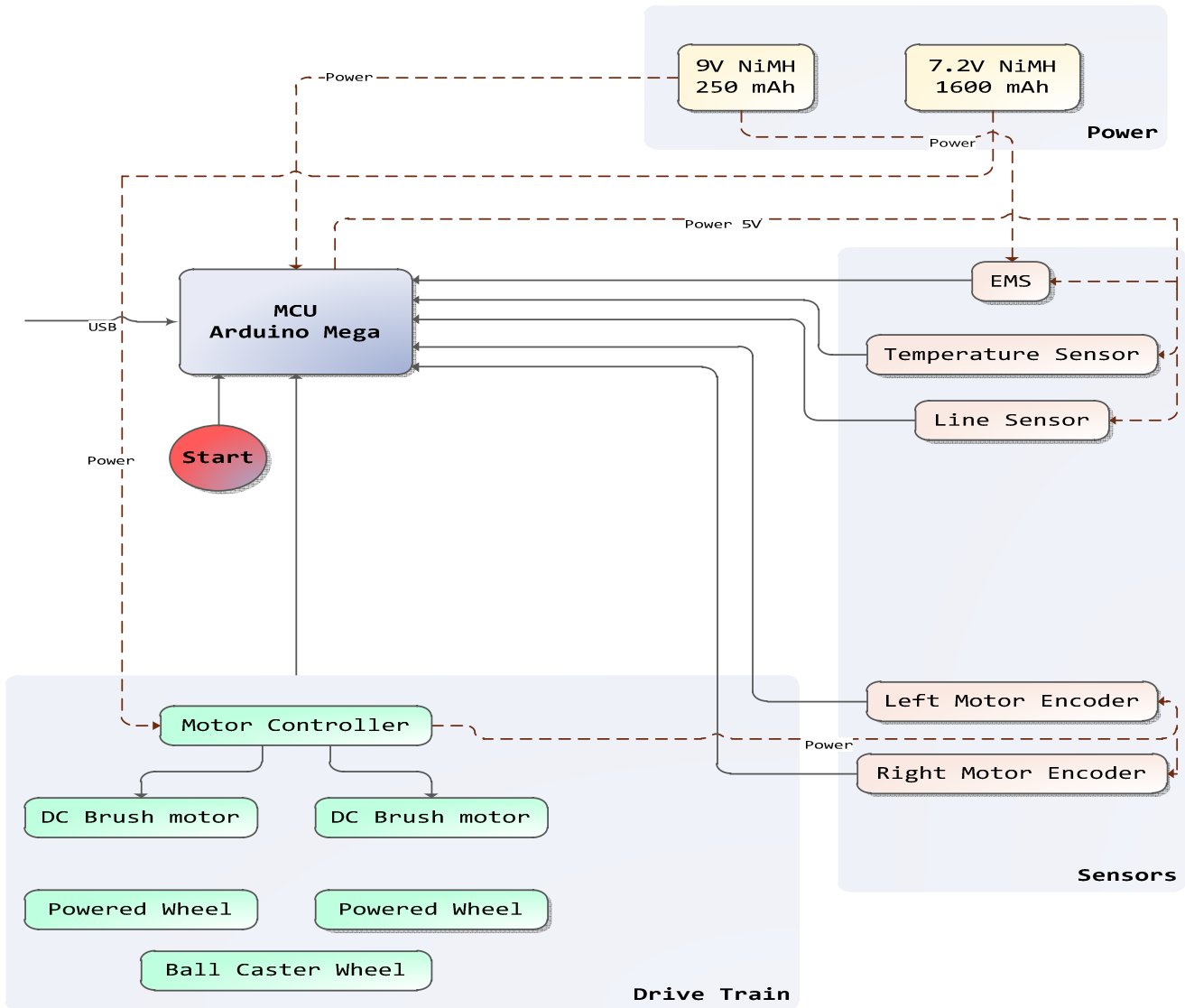


Figure 3. System Level Block Diagram

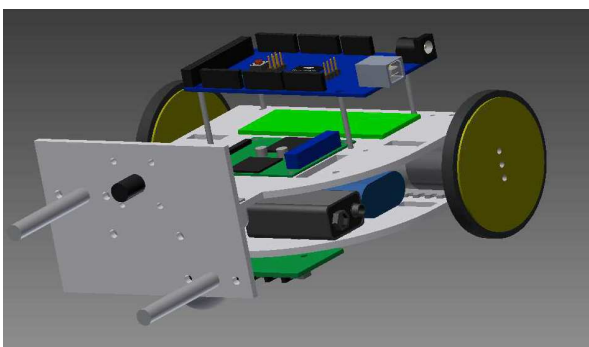


Figure 4. 3D CAD Design

2.1 Controllers

The brain of the robot was an Arduino Mega 2560 based on ATmega2560 8-bit AVR microcontroller. This controller was selected due to its abundance of digital I/O and analog ports, speed, low power consumption, and small size. The code written for the microcontroller was in C.

The second controller used was the Pololu Qik motor controller. A 2 channel controller used to send PWM signals to both motors. The use of the motor controller simplified the process of interacting with the motors by providing a higher level interface. The motor controller already had preprogrammed commands which were utilized to obtain very precise control over the motors. The main controller communicated with the motor controller serially using UART.

2.2 Navigation

2.2.1 Line Following

The line sensor used to read the line was made up of 8 IR emitter and receiver pairs. The IR light was emitted by IR LED's, and was read by IR phototransistors. The digital output of the sensor was used to determine the position of the robot with respect to the line.

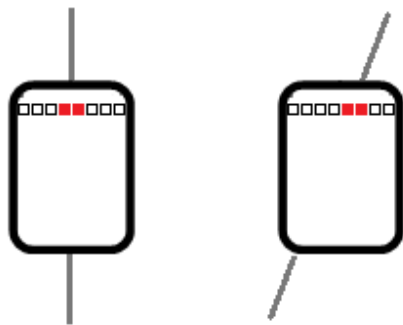


Figure 5. Line Sensor Examples

A numerical weight was assigned to each line sensor digital output, from 0 for the leftmost to 7 for the rightmost. The heading was just the average of the sum of the weights divided by the number of outputs that were high. For instance, the example on the left of Figure 5 has an average heading of 3.5, whereas the example on the right has an average heading of 4.5.

The line sensing algorithm was done by using a proportional derivative (PD) algorithm. Ideally, the robot should have been centered over the line as it went forward - this was the target position (3.5 being the half point between 0 and 7). However, as the robot moved it would slowly drift from the center of the line. To correct this, the velocity of each motor needed to be adjusted. A correction value was calculated and the value was added to the velocity of the left motor and subtracted to the velocity of the right motor.

Pseudo code:

$error = averageheading - 3.5$

$correction = error \times kp + (error - lasterror) / dt \times kd$

$leftmotorvelocity = velocity + correction$

$rightmotorvelocity = velocity - correction$

Kp, and Kd are the proportional and derivative constants respectively. Their values were determined experimentally.

2.2.2 Encoders, Corners, and Intersections

Each motor had a rotary quadrature encoder attached. The encoders were used to measure distances, and to determine how close the robot was from the corners and intersections. The encoders proved to be essential to make the line following more reliable by helping anticipate corners and intersections. With this method, the robot was able to slow down before approaching the corners or intersections (reducing the risk of missing them), and speed up (if the opposite was true).

Corners were considered special cases of the line following algorithm. When a corner was sensed, the PD algorithm would be ignored, and the robot would simply turn until it was facing in the right direction. The way corners were detected was by checking if the first or last 4 line sensor outputs were on. This approach, although simple in practice, created an additional problem: corner false positives as depicted in Figure 6.

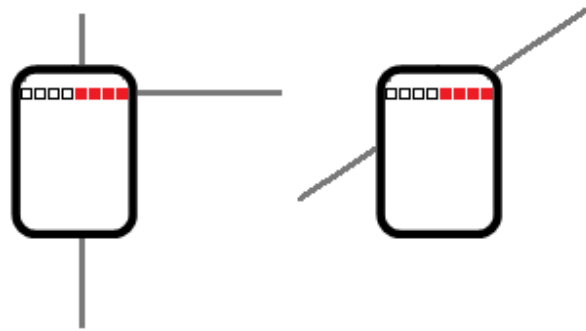


Figure 6. Corners

The way around this issue was to have a very solid line following algorithm ensuring that the robot would never be so far off the line, that the case on the right of Figure 6 would happen. This meant that the robot had to correct its heading in a quickly fashion, but at the same time not overshoot.

Intersections (stations), similarly to corners, were detected in the same way. Intersections were assumed when all the line sensor outputs were high. Since the robot started on the top left corner of Figure 1, keeping track of which measurement algorithm to perform for each station was just a matter of keeping count of the intersections.

2.3 Stations

2.3.1 Station Detection

After the robot detected an intersection, it moved forward a fixed distance based on the number of encoder pulses that were counted as the robot was advancing. In the case of the voltage station, the robot immediately stopped when the EMS detected a voltage. If a voltage was not detected at the station, the robot stopped when the fixed distance was reached.

For the capacitance and waveform stations, measuring capacitance or correctly interpreting a waveform while the robot was moving proved to be problematic, and it was decided that the robot would only stop after advancing a fixed distance toward the station. This ensured that sufficient compression of the spring probes would be present to allow for a reliable electrical contact with the station

The temperature sensor used was a noncontact IR sensor. This meant that the robot could take the temperature measurement inches before it reached the temperature station. Thus, the robot did not stop at the temperature station saving time.

2.3.2 EMS

The electrical measurement subsystem (EMS) is a configurable resistor network that was used to scale and level-shift the voltage at the input probes to the zero to five volt level that was required

by the micro-controller's A/D converter. The scaled and level-shifted output of the resistor network was also used by a pair of comparators to determine the peak amplitude of the waveform present at the waveform station. The EMS board is a printed circuit board consisting of the resistor network, a dual comparator IC, pull-up resistors, and potentiometers. The EMS board was mounted on the top of the robot chassis below the micro-controller board, and was used to analyze the voltage, capacitance, and waveform signals.

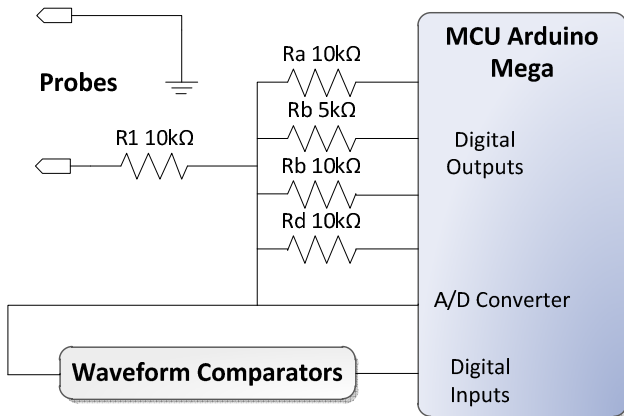


Figure 7. EMS circuit

The resistor network may be thought of as a simplified equivalent circuit (Figure 7), which has different values for R_{eq} and V_{eq} , depending on the mode that is used. The C program code for the EMS contains mode control functions that set the $R1$ and R_{eq} program variables to the correct value, and set the digital outputs that control the resistor network to the high, low or high-impedance states corresponding to the mode that was selected.

When the robot was at the capacitance station, an RC circuit was created (Figure 8), and the capacitor was charged or discharged by changing the EMS modes. Discharge mode 2 is used when the

charge of the capacitor is not known (since the initial charge may be negative). Discharge mode 1 is used when the charge of the capacitor is known to be positive and may be used to produce more accurate capacitance measurements.

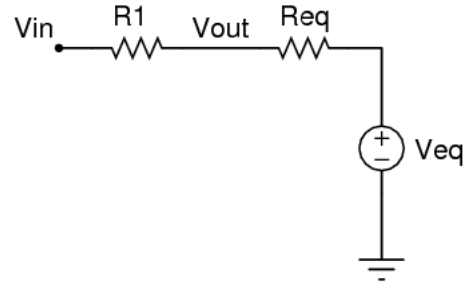


Figure 8. Equivalent Circuit

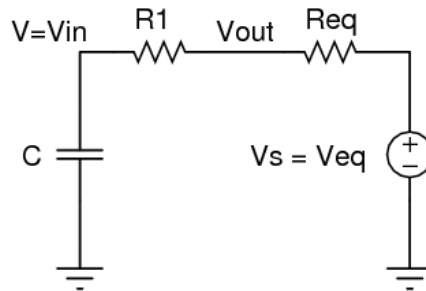


Figure 9. RC Circuit

Table 2. EMS Resistor Network Modes

Mode	Digital I/O Pins				R_{eq} (k Ω)	V_{eq} (V)	Input Range (V)	A/D Resolution (mV)
	1	2	3	4				
Voltage	H	H	L	L	2.0	3.0	-15 to 15	29.3
Wave	Z	H	Z	L	3.3	3.3	-10 to 10	19.5
Capacitance (Charge)	H	Z	Z	Z	10.0	5.0	-5 to 5	9.8
Capacitance (Discharge 1)	Z	Z	Z	L	10.0	0.0	0 to 10	9.8
Capacitance (Discharge 2)	H	Z	L	L	3.3	3.3	-5 to 10	14.6

H = High = 5V, L = Low = 0V, Z = high impedance input state

2.3.3 Voltage

V_{in} , the voltage at the spring probes, is calculated from V_{out} , the voltage measured by the A/D converter, using this formula:

$$V_{in} = \frac{V_{out}(R_1 + R_{eq}) - V_{eq}R_1}{R_{eq}} \quad (1)$$

When the robot is not making contact with a station, the C function returns a value of three volts, which is equal to the R_{eq} for voltage mode.

2.3.4 Capacitance

Capacitance was measured rapidly using the following procedure. First, the voltage across the capacitor was measured while the EMS was in Discharge 2 mode. If the voltage was less than 3.33V (which is halfway between the Charge mode voltage of 5V and the Discharge 2 voltage of 1.66V), the EMS was placed in Charge mode. Otherwise, the EMS remained in Discharge mode. As the capacitor charged or discharged the voltage was read by the A/D converter and stored as v_1 along with the time of the sample t_1 . After a brief (approximately 1ms) delay, the voltage was sampled again and stored as v_2 at time t_2 . $(v_2 - v_1) / (t_2 - t_1)$ was used to approximate the time derivative of voltage when solving the following equation for capacitance.

$$I = C \frac{dv}{dt} \quad (2)$$

$$C = \left(\frac{V_{eq} - \frac{1}{2}(V_1 + V_2)}{R_1 - R_{eq}} \right) \left(\frac{t_2 - t_1}{V_2 - V_1} \right) \quad (3)$$

This method of measuring capacitance was very fast and reasonably accurate over a range of about .1 μ F to 1 μ F. If the capacitance measured more than .5 μ F, the robot turned right, otherwise the robot turned left.

2.3.5 Waveform

The task at the waveform station was to determine if the 5V rms waveform present was a sawtooth or a square wave. The sawtooth and square waves differ in peak amplitude: the square wave has a peak of 5V, while the sawtooth wave has 8.660V peak amplitude. To determine if any waveform was present at the input probes, interrupts were enabled for the first comparator. The first comparator had a threshold (set by a potentiometer) set at 2.5V, which corresponds to zero volts at the input probe springs. The comparator triggered an interrupt for each zero crossing. If ten rising edges were detected within a one microsecond time period, a waveform (of at least 10kHz) was detected, and interrupts were then enabled for the second comparator. The second comparator had a potentiometer set at 4V. This corresponds to an input voltage of +6V. If ten rising edges were detected within a one microsecond time period, a waveform (of at least 10kHz) with a peak of six volts or greater was present. If the second comparator detected a waveform, it was assumed that it was a sawtooth wave; otherwise it was assumed that the waveform was a square wave.

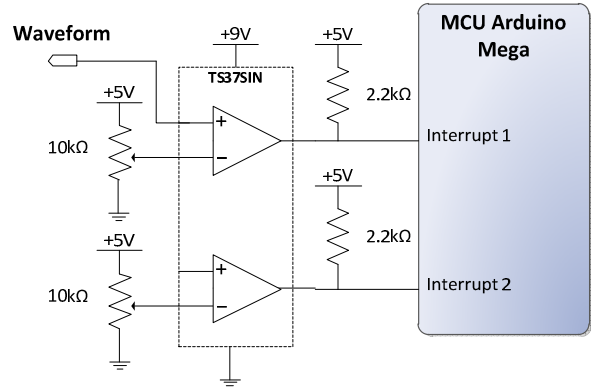


Figure 10. Waveform Circuit

Table 3. Waveforms Peak and RMS

Waveform	RMS Voltage	Peak Voltage
square	5	5
sawtooth	5	$5\sqrt{3} = 8.660$

2.3.6 Temperature

An IR temperature sensor was used to measure both the temperature of the plate, and the ambient temperature. The sensor is a Melexis MLX90614, which has a 10° field of view and communicates with the microcontroller via an I2C Digital interface. A small printed circuit board was made to hold the MLX90614 and its associated components. The field of view was an important factor when selecting the temperature sensor since it determines how far away from the station the robot could measure the temperature. The robot exploited this feature, and measured the temperature of the plate inches before reaching the intersection. So in a single fluid motion, the robot would keep going without the necessity of stopping at the temperature station at all.

3. CONCLUSION

A combination of fast line following, fast station measurements, and a simple design made this project a success. The downfall of most of the other competing robots was their overly complicated designs. Though very creative, those designs didn't really advance the ultimate goal: speed and accuracy. A brief survey of the top 10 placing robots tells the same story: differential drives, solid line following, fast measurements, simple probes, and so forth. What all these robots had in common was that their designs were straightforward.

When the design team for any given project starts drifting away from the main goal, the project starts following a path of unnecessary changes while the time of implementation and usually the cost increase. Losing track of the main goal can be very tempting when exploring solutions for open ended projects, but discipline should be maintained throughout the design phase so the project doesn't fall victim to work that doesn't lead anywhere.

GunBot: Design Concept of a Semi-Autonomous UGV with Omni-directional Mobility and Auto-Target Tracking

Cardenas Irvin, Shao Leo, Jong-Hoon Kim

Discovery Lab, School of Computing and Information Science

Florida International University, 11200 SW 8th St, Miami, Florida 33199

icard005@fiu.edu, lshao002@fiu.edu, kimj@cis.fiu.edu

Abstract

Modern day firefights during military operations in the Middle East have resulted in a high number of casualties and wounded soldiers due to the exposure of deadly attacks. However, those highly risky activities are inevitable for military operations.

Unmanned robots will lead to a new era of reduced casualties. To perform dangerous activities without those casualties, unmanned robotics is a valuable approach. We have developed a semi-autonomous Unmanned Ground Vehicle, named GunBot, which is designed for battlefield operations as well as police patrol.

GunBot has two superior features; Omni-directional Mobility based on the mecanum wheel mechanism which provides Gunbot with quick response to movement in any direction and an auto-Target Tracking system based on image processing techniques which enables one operator to drive GunBot and to track a target simultaneously. In this paper, we provide a prototype of GunBot and show the feasibility of the design of GunBot.

Keywords: UGV, Robotics, Autonomous Target Tracking, Image Processing, Mecanum wheel.

1. Introduction

During the current military operational time, many efforts are placed in reducing the life-risk factor for United States service members. Unmanned Ground Vehicles (UGVs) are the most sought option to reduce the presence of our military men and women in hostile areas.

Unmanned ground vehicles are used in important military applications, which include surveillance, unarmed/armed reconnaissance, and explosive device inspection and disposal [5]. As unmanned ground vehicles keep on becoming ever more prominent, to maximize their effectiveness in field operations more advanced methods of guidance and targeting keep on being implemented.

This has led to the global UGV market to become a growing marketplace that is providing government contract opportunities to major defense contractors and robotics research institutions [5]. As the market for UGVs grow. To distinguish ourselves we are forced to implement a more agile, more versatile and more efficient robot.

1.1 Background

Early Research Efforts

As early as the late 1960's, mobile robotics has been on the move, starting with one of the first major mobile robots named *Shakey*. *Shakey* was created to serve as a platform of experimentation for DARPA's funded artificial intelligence research work at the Stanford Research Institute. Although *Shakey* was not considered a success in its day because it never achieved the desired autonomous operation, it was the starting point for other mobile robot projects and AI research in areas such as vision. [3], [6], [7], [10], [11].

Other projects such as Hans Moravec's Stanford Cart project, a robot used to plan an obstacle-free path to its destination, at Stanford University AI Lab from 1973 to 1981 led to further involvement of the government and private agencies such as DARPA. And in the early 1980's *Shakey* was reborn as the DARPA *Autonomous Land Vehicle (ALV)*, which focused on military applications [2].

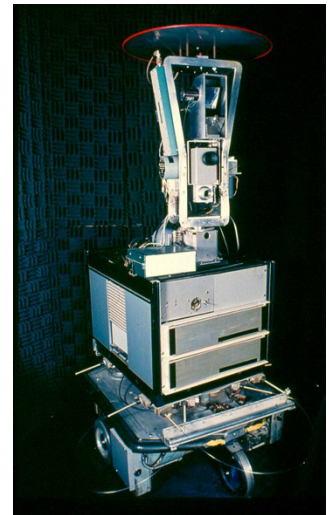


Figure 1. *Shakey* [14]

Reconnaissance, Surveillance, and Target Acquisition (RSTA)

The idea of RSTA application always drew the attention of UGV developers since it would offer non-human military battlefield "personnel" with sensing capabilities on the battlefield.

In 1990, in response to Congressional concerns, a number of Department of Defense (DoD) advanced development projects related to ground vehicle robotics were placed under the Joint Robotics Program (JRP) directed by the Office of the Secretary of Defense (OSD)

The Joint Robotics Program Master Plan (JRPMP) is prepared annually and provided to Congress. This plan provides an integrated Department of Defense document that describes the strategies for acquiring first-generation UGVs and for developing technologies critical to these systems.

The Joint Robotics Program Master Plan describes the individual projects and the management framework for their execution. It is considered an OSD management tool for fulfilling its responsibility to oversee the Joint Robotics Program [5].

Teleoperation

Teleoperation capability, or the ability for an operator to manipulate and control a UGV remotely from a safe location, is what attracts UGV developers the most. At the moment it is the most mature control technology available and therefore is an area of emphasis for all Services in developing first generation robotics programs.

Teleoperation capabilities are important to the military because they enable standoff operations and thereby reduce or remove operator risks in highly stressful and dangerous environments, such as minefields and in areas of potential explosive hazards [5].

A variety of potential UGV applications to land operations can increase mission performance, combat effectiveness, and personnel safety. These applications include assistance of military personnel, mapping of unknown areas, disaster rescue, and visual identification. In these areas it is important for an UGV to have an advanced visual interpreter and agile mobility. Advanced visual interpreter is defined here as visual mapping which will allow the mapping of unknown areas during disaster recovery and also to identify between friend and foe targets during hostile encounters. This advanced visual technology combined with agile mobility, which we define as being able to move, and change directions quickly and efficiently will create a dynamic UGV that is better equipped for a wide variety of situations.

The majorities of UGVs are designed to traverse various terrains and avoid obstacles but lack agile mobility. There is plenty of research on UGVs that operate on slow speed. There have also been experiments on higher speed performance in small sized robots; but there is not much research devoted to the turning and mobility of a UGV. The majority of UGVs designed to be agile are either Ackerman or skid-steered. Their design prevents them from being extremely agile. There are also omnidirectional UGVs such as an Active Split Offset Caster (Figure 2.), which while having 360-degree movement are lacking in speed.

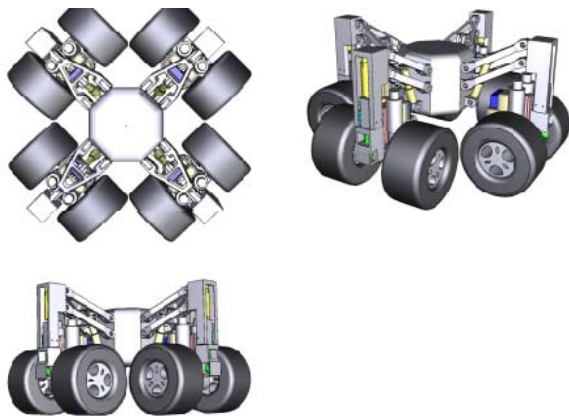


Figure 2. Active Split Offset [9]

In addition to mobility other features are taken in consideration, especially that of a UGV's teleoperation Interface. Despite advances in autonomy, there will always be a need for a human involvement in vehicle teleoperation; in particular for tasks such as exploration, and reconnaissance, and surveillance where human interference is required for monitoring and control of the vehicle [4].

There four main categories of teleoperation interfaces that we take in consideration: direct, multimodal/multisensory, supervisory control, and novel [4].

The direct interface is the most common interface, which relies on the operator using hand-controllers such as 3-axis joysticks, while watching video from vehicle-mounted cameras. Although it is the most simple form vehicle teleoperation it is the most problematic due to the operator's loss of situational awareness, inaccurate attitude judgment, and failure to detect obstacles" [4].

On the other hand multimodal and multisensory interfaces provide for efficient command tools and strong information feedback between the operator and robot. This is needed when a vehicle is operated during a complex or highly dynamic situation such as those of military operations, where it may be difficult for the operator to rapidly and accurately perceive information from the vehicles surroundings, to make correct control decisions [4].

Then we have supervisory control, which is an interface where the operators divide a problem into parts that he/she can perform and that the robot can execute, needless to say, this means that the robot should have some level of autonomy.

Lastly we have Novel interfaces, which refer to unconventional interfaces such as the hands-free remote driving interface based on brainwave and muscle movement analysis [4].



Figure 3. Digital modal sensory Interface [4]

2. State of the Art

Gladiator Tactical Unmanned Ground Vehicle is a high tech vehicle developed by the US marines. They have an array of vision devices that allow the user to see as well as if he were on the battlefield. We believe that utilizing our technology we can improve this machine. The heavily armed gladiator could greatly

benefit from an auto tracking mechanism. It already has high definition vision and weapons so this implementation will allow a fully autonomous machine, which will be able to better help the US marines [5].



Figure 4. Gladiator Tactical UGV [12]

Remote Ordnance Neutralization System (RONS) is a high level machine that was designed to dispose of waste and get rid of explosives. To increase its functionality the RONS is equipped with a specialized driving system that allows it to change its elevation and provides various other maneuvers. Unfortunately, their special drive system also limits them in their directional drive movement. If we were to implement Gunbots omnidirectional movement with RONS then we could achieve a more agile waste and explosive disposal machine, which would be beneficial in different terrains. The RONS could be further improved with the addition of a face tracking and visual interpreting mechanism. This would allow the RONS to be able to communicate with onsite workers without them having to explicitly give the commands [5].



Figure 5. RONS UGV [13]

The TALON is a lightweight versatile robot that is useful in reconnaissance and combat situations. In the development of Gunbot we took into consideration the abilities of the TALON and realized that we could improve upon it. The TALON like the Gunbot can be fitted with weapons and provides a good gun mount to shoot targets. Unfortunately the TALON only has Tele-Operational abilities and lacks the sensing and the mobility of Gunbot. Gunbot has a face detection system that allows for a more autonomous and variable robot. The face detection will take away

the clumsiness of having to train a user to track a target and allow a user to operate multiple vehicles. The TALON also uses caterpillars to drive. We believe that our use of mecanum wheels to provide Omni-directional movement adds to the survivability and efficiency of the combat robot [5].



Figure 6. TALON UGV [1]

2.1. System Overview

GunBot will be programmed in C and will run on an embedded computer inside GunBot. The computer will receive signals through various detectors attached on GunBot including high definition cameras. After being interpreted by the GunBot program, the computer will transmit serial signals to GunBot’s microcontroller, which will be programmed in C and will act accordingly. The computer will also have 4G cellular network modules, which will allow remote control of GunBot from anywhere.

3. Architecture

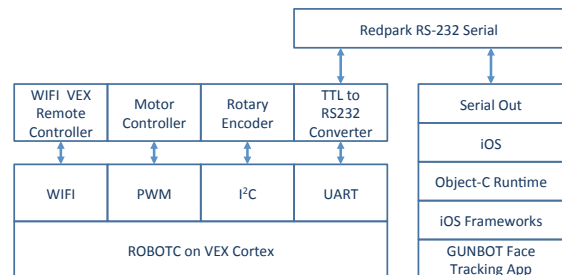


Figure 7. Architecture

GunBot has two main control components, the vex microcontroller, and the iPhone. The microcontroller has our code loaded into it and receives wireless signals to control the Gunbot via a VEX controller. The iPhone has a built in face tracking software, which we modified to send serial signals via an UART connection.

3.1 Programming Algorithm

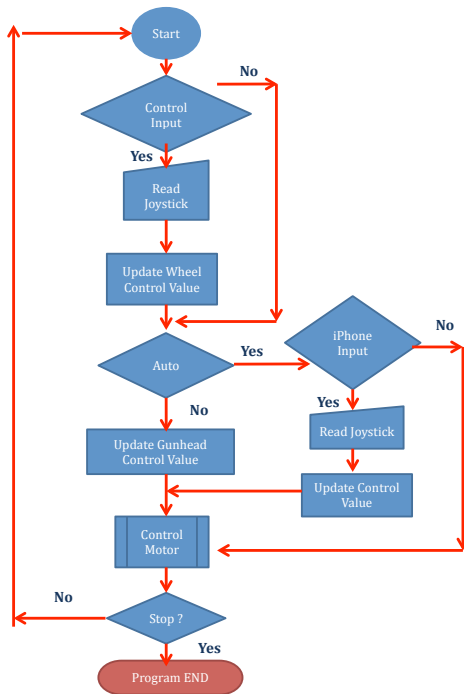


Figure 8. Control Flow

The code is set in an infinite loop to continually accept commands from the controller. The cycle starts by the microcontroller checking if the user has sent any commands for wheel motor movement. If there are commands, the relevant motors will be activated else no motors will be activated. The next step is to check whether or not the Boolean for auto-targeting has been activated. If it has been activated then the microcontroller checks whether or not a signal has been sent. If one has been sent then the Gun mount motors will activate. If no signal has been sent the microcontroller will not wait for the signal and instead continue the cycle and check again the next time it reaches this step. In the event that the Boolean for auto-tracking has not been activated the microcontroller will check what commands has been inputted in the controller for the gun mount. If commands have been inputted then the gun mount motors will act accordingly otherwise the motors won't act accordingly.

4. Implementation

The prototype design considered in this paper is of a battery powered UGV with omnidirectional mobility via the mecanum wheel mechanism and auto target tracking capability made from iPhone's API.

4.1. Implementation Plan

The Implementation Plan consists of the first phase of GunBot. Phase one consists of the proof of concept of an auto target tracking system

based on image processing and the proof of concept of omnidirectional mobility based on the mecanum wheels.

The next phase consist of a proof of concept of an advanced auto target tracking system using image processing and depth perception technology based on the Xbox Kinect sensor, and a proof of concept of an improved omnidirectional mechanism suitable for outdoor environments with less terrain constraints. In this paper we implement Phase one.

4.2. Major Structure of GunBot

A reduced scale prototype was built using VEX parts, smart phone device (mainly iPhone), and serial communication hardware.

The structure of the prototype is divided into four major parts:

- Mechanical Structure
- Electrical Structure
- Image processing and face detection.
- Logic Design and Architecture.

Mechanical Structure

GunBot has an aluminum structure that measures 15.32" x 11.61".

The base

The base is composed of four 3x3x25 cm. angle rails, two slotted angles rails that make the structure that holds the gears and mecanum wheels.

Place on top is the first part of what makes up the base for the gun mount. It is composed of four C-Channel rails, two on each side, which hold the four 2-wire 393 motors.

The final part of the base is a 1x5x1x25 cm. C-Channel rail, which connects the gun mount, and a 2-wire 393 motor for the gun mount's horizontal movement.

Gun mount

The gun mount is composed of a two Turntable gear system. The Turntable gears provide us with low friction turning which in turn provides us with more accurate reading from the encoders.

Electrical Structure

We connected 6 motors to the Cortex microcontroller. Four of the connections were for the wheels. The two others were for horizontal and vertical gun movement. The gun also has its own internal motor, which is connected to the microcontroller.

Gun Movement

The two gun movement motors were fitted with quadrature encoders connected in daisy chain. The encoders allow us to measure the movement of the motors.

Controller

WIFI connection provides communication between controller and microcontroller manual control.

iPhone and UART Connection

The UART Serial Connection allows communication between the microcontroller and iPhone.

Battery

A 7.2-volt main battery and a 9-volt backup battery power the CORTEX microcontroller.

Image processing and face detection.

Our auto-target tracking system is based off an app developed for the iPhone.

The iPhone sends serial signals to the microcontroller, which allow the gun motors to move until the target has been reached.

Logic Design and Architecture.

GunBot has two main control components, the VEX Cortex microcontroller and iPhone.

GunBot's ROBOTC code is loaded onto the VEX Cortex microcontroller. The microcontroller receives WIFI signals from the VEX remote controller to allow movement.

Our app makes use of the iPhone's face detection API, and an external hardware and software implementation that allows serial

communication between the iPhone and the CORTEX microcontroller.

5. Prototyping

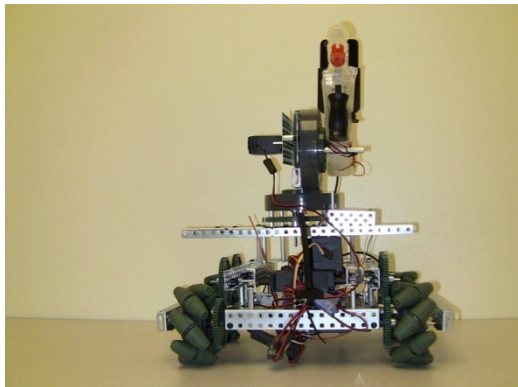
In this paper the prototype of GunBot was built from VEX Robotics parts to allow efficient and inexpensive prototyping.

Figure 7.a) shows the front view of GunBot where the gunmount design could be seen. One Turntable is laid horizontally, while another is placed vertically ontop. The gun is attached to the vertical Turntable gear.

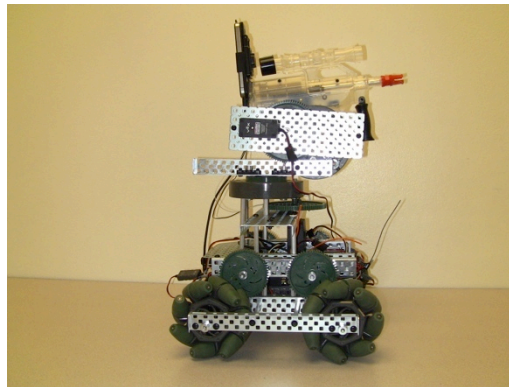
Figure 7.b) show the side view of GunBot. On this image the side of the gunmount design could be seen. Under the horizontal table gear a 12-tooth to 84-tooth gear system is arranged along with the Turntable gear to reduce speed and increase torque in the gun's movement.

Figure 7.c) shows the top view of GunBot's prototype. On this image we can see a vertical view of the 12-tooth to 84-tooth gear system connected to the vertical Turntable gear.

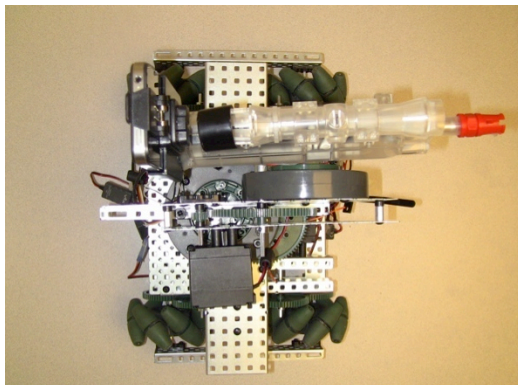
Figure 7.d) shows the bottom view of GunBot's prototype. On this image we can take an in depth look at the microcontroller and wiring.



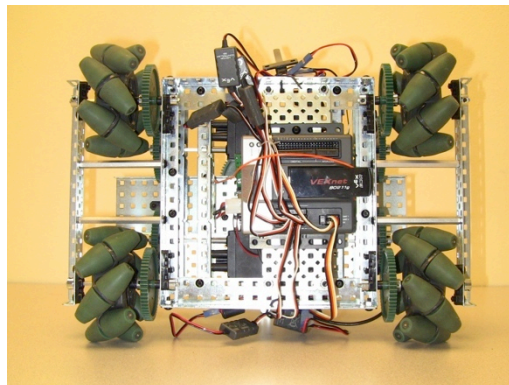
a) Front view



b) Side view



c) Top view



d) Bottom view

Figure 7. Multiple Views of GunBot

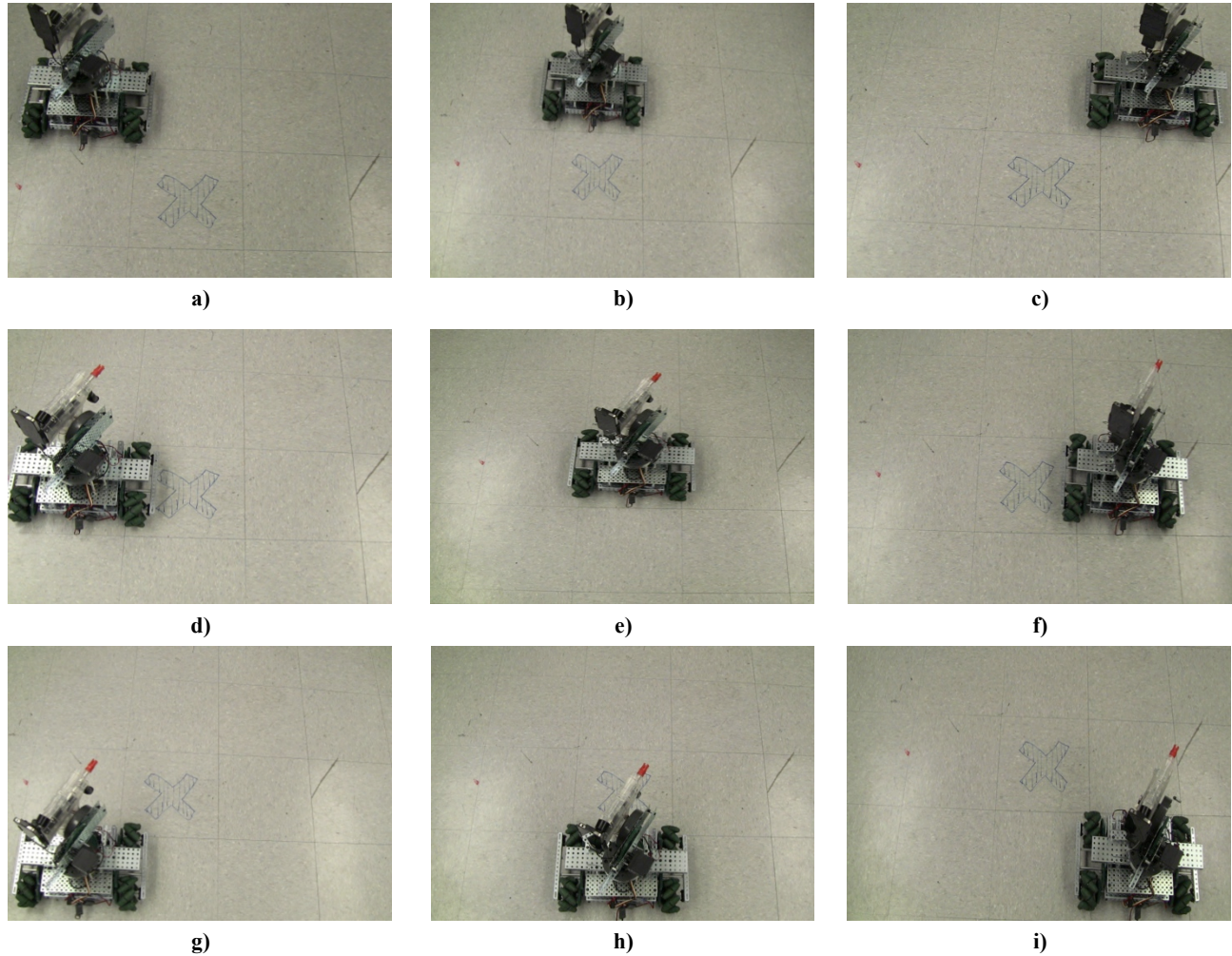


Figure 8. GunBots Omnidirectional Movement

Movement	Velocity	Percentage/Power
Forward/Backwards	1 foot/6.40 sec	100%
Horizontal	1 foot/7.30 sec	88%
Diagonal - 45 Degree	1 foot/11.55 sec	55%

Table 1.

Figure 8. shows GunBot's omnidirectional movement. Figure 8.e) shows the starting point marked by an "x". GunBot can move at a 45 degree angle forward as shown by figure a) and figure c). It can also move forward and backwards as show by figures b) and h), and side-to-side as shown by figure d) and f).

Table 1. shows GunBot's ground velocity on a smooth surface. 100% of GunBot's velocity is achieved throughout forward movement. During horizontal movement, with the same amount of power,

GunBot achieves 88% of its maximum velocity. While moving diagonally, GunBot achieves only 55% of its velocity.

Because of the mecanum wheel mechanism, which only allows the usage of all four-wheel motors for forward and reverse movement, and only the usage of two wheel motors for diagonal movement, there is almost a 50% drop from GunBot's maximum velocity during diagonal movement. This drop in velocity is inevitable to achieve omnidirectional movement.

Movement	Velocity
Vertical	90 degrees /9 sec.
Horizontal	90 degrees/7 sec.

Table 2.

Table 2. Displays the average velocity achieved by GunBot's gun mount movement.

GunBot's iPhone application allows GunBot to track down a target's face and lock into it. Figure 9a) displays GunBot's application logo. Once the icon is pressed the start up screen of the GunBot's application is displayed, as shown in Figure 9b)

After a quick glance at the start up screen, GunBot's auto target tracking function powers on. Figure 9c) displays GunBot's fully functional iPhone application.

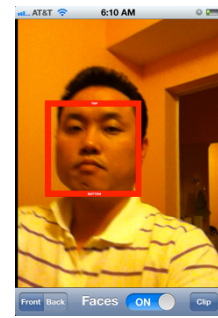
The application locks onto the target's face and places a red square around it. The far left button on the application's screen allows the use of the iPhone's front or back camera, the middle button is used to turn the auto target tracking function on and off, meaning disabling or starting serial communication between the iPhone and the microcontroller, which allows GunBot to move its gun until it locks into the target.



a) iPhone App Logo



b) Application Start up Screen



c) Auto-target Tracking Function ON

Figure 9. GunBot's Auto Target Tracking System

6. Discussion

The alpha type bot had a caterpillar drive system and had a gun mount with movement only in the vertical position. The two-motor drive robot lacked adequate mobility in that it could not strafe in multiple directions. The main problem was of the lack of mobility of the gun mount. To solve this we proceeded

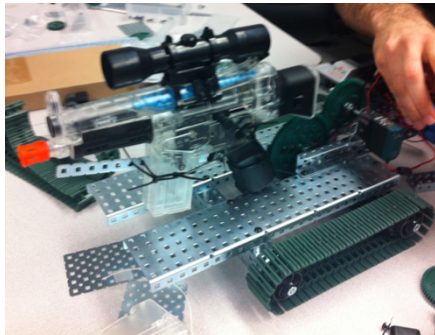


Figure 10. Alpha Type GunBot

to the beta type Gunbot

The beta type bot was very similar to the prototype Gunbot. To increase the mobility we switched out the two-wheel drive and changed it to four-wheel mecanum drives. We also used two Turntable gears to give 120-degree horizontal and 90-degree vertical movement. We then created our iPhone face detection software that allowed us to have our first semiautonomous Gunbot. Figure 11 shows the beta type GunBot.

There were also many improvements on the microcontroller software side of Gunbot, which allowed the microcontroller to utilize the improvements to the gun mount and make use of the iPhone application.

At the time there was also a critical problem which was the lag caused by the slow processing speed of the iPhone, which prevented the Gunbot from zooming in on its target.

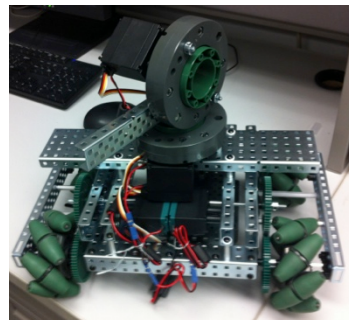


Figure 11. Beta Type GunBot

To correct these challenges we updated the Gunbot to its present version, the prototype. The prototype attempted to solve the problems by improving the software through designing a more efficient algorithm.

We also tried to solve this problem by greatly improving the gun mount. We lowered the gear ratio of the mounts to improve the accuracy. In the end the improvement to the gun mount maximized its movement, giving it 360-degree horizontal movement and 120 degree vertical movement.

6.1 Limitations

We decided to limit our Gunbot by focusing our Gunbot as a strictly anti-personnel vehicle. Due to size and our desire to maintain agility we will not equip our Gunbot with anti-armor weaponry nor equip it with vehicle detection and identification technology. We will not equip Gunbot with anti-ship weaponry. We will also not equip our

Gunbot with anti-air weaponry; however, the user could always attempt to shoot at those targets.

In order to maintain mobility we will not design GunBot to have a heavy load capacity. We will also not greatly increase the size of Gunbot to enable it to have a heavy load capacity, as this will make Gunbot to easy of a target to be worth using. We will not optimize Gunbot's carrying ability nor will we give Gunbot multifunctional tools like arms.

Gunbot will not be designed for advanced human interaction. While Gunbot will be equipped with a wide array of sensor technologies we will not implement technologies that will allow Gunbot to communicate and interact with immediate humans. In other words, the only way to send commands to Gunbot will be through Gunbots command console.

Gunbot will not be designed for aquatic movement. The definition of aquatic movement in this case is any movement that requires moving through water of a depth greater than 1 inch or moving under water. Gunbot will also not be designed for flight capabilities. The purpose of Gunbot is to accurately obtain target information and track them. If Gunbot were flying such accuracy would not be possible and the target tracking would be less effective.

6.2 Future Works

Our next goal is to prove the concept of an advanced auto target tracking system using image processing and depth perception technology base on the XBOX Kinect sensor. Utilizing the Kinect we will be able to take advantage of the built in camera and depth perception ability. Using the Microsoft's Kinect SDK we will build upon our knowledge of image processing and development a smarter and more flexible face detector. To process the Kinect and interpret the data we will use a fast computer to run our software, which will greatly reduce the runtime of the image processing. Our software will be designed to allow for smooth transition between multiple targets and a Graphical User Interface (GUI) that will simplify and improve user experience. We will also work on developing an entirely original frame for GunBot. All of our parts will be designed with the idea of optimizing GunBot's ground movement, gun movement, and auto-target tracking system.

In our final design through continuously improving upon Gunbot we will develop a truly avant-garde machine. In an effort to optimize the already highly mobile mecanum wheel, we utilize encoders to align the power output of each of the motors for the four-wheel drive. In recreating our design we will also improve the quality of our parts i.e. wheels, motors, and frame.

These improvements will provide immediate and impressive results, including massive improvements in agility and coordinated directional movement. With the continuous development of the GunBot AI, we will develop our own software that will improve user experience and reliability when handling GunBot.

The software will also take care of sensor inputs. Our sensors will consist of multiple high definition cameras and lasers to provide 3d mapping and 360 degree monitoring of all situations. GunBot's facial

detection and image detection abilities will enable it to differentiate between friend, foe, and civilian targets, turning GunBot into the ultimate soldier.

7. Conclusion

In this paper a design of a semi-autonomous UGV with omnidirectional movement and an auto target tracking system has been presented. Our prototype has showed that this is indeed feasible. The omnidirectional movement has been implemented with the mecanum wheels and the auto target tracking has been implemented via apple face detection software. Our inexpensive design of an UGV will provide the military with the capabilities to accomplish critical missions more rapidly and successfully. This UGV will also be applicable in many other fields such as mapping out disaster territories and supporting police officers. There are however limitations with our current prototype. The lack of coordination with the mecanum wheels and the delay from the face tracking will be solved by later models of our Gunbot. Future Gunbots will use higher quality motors to balance the wheels and more advanced face-tracking technology, which will greatly reduce any lag in target auto-tracking.

8. Reference

- [1] Block, Ryan. "Metal Storm's Talon UGV GrenadeLauncher." *Engadget*. AOL Tech, 30 Mar. 2005. Web. 29 Apr. 2012. <<http://www.engadget.com/2005/03/30/metal-storms-talon-ugv-grenade-launcher/>>.
- [2] Defense Advanced Research Projects Agency, Strategic Computing Program Second Annual Report, Arlington VA, February 1986.
- [3] Flynn, A.M. "Redundant Sensors for Mobile Robot Navigation", MIT AI Lab Technical Report 859, 1985.
- [4] Fong, Terrence and Charles Thorpe. "Vehicle Teleoperation Interface." *Kluwer Academic Publishers*. 2001 Autonomous Robots, 30 April 2012.
- [5] "GlobalSecurity.org - Reliable Security Information." *GlobalSecurity.org*. Web. 29 Apr. 2012. <<http://www.globalsecurity.org>>.
- [6] Harmon, S.Y. "Autonomous Vehicles", Encyclopedia of Artificial Intelligence, Wiley and Sons, NY, 1986, pp 39-45.
- [7] H.R. Everett. "Sensors for Mobile Robot Systems: Theory and Application", A.K. Peters, Wellesley MA, 1995.
- [8] Karl Iagnemma, Undengaad, Ishigami, Spenko, Oncu, Khan, Overholt, Hudas. "Design and Development Of An Agile, Man Portable Unmanned Ground Vehicle" MIT, 2008.
- [9] Khan, Imad, and Mathews Spenko. *Dynamic and Control of an Omnidirectional Unmanned Ground Vehicle. Intelligent Robots and Systems*. IEE, 11 Oct. 2009. Web. 30 Apr. 2012. <<http://ieeexplore.ieee.org/stamp/stamp.jsp?arnumber=05354251>>.

[10] Klafter, R.D. "Mobile Robots, Research and Development", *International Encyclopedia of Robotics: Applications and Automation*, Wiley and Sons, NY, 1988, pp 920-943.

[11] Meystel, A. *Autonomous Mobile Robots -- Vehicles with Cognitive Control*, World Scientific Publishing Co, Singapore, 1991, chapter 2.

[12] Mikhalchuk, Andrey. "UGV | RoboStuff." *Everything about Robots and Robotics*. 19 Feb. 2009. Web. 29 Apr. 2012. <<http://robostuff.com/http://robostuff.com/tag/ugv/>>.

[13] "Military." *Remote Ordnance Neutralization System (RONS)*. Web. 29 Apr. 2012. <<http://www.globalsecurity.org/military/systems/ground/rons.htm>>.

[14] "SRI Technology: Shakey the Robot." *SRI International*. SRI. Web. 31 Apr. 2012. <<http://www.sri.com/about/timeline/shakey.html>>

ScouterBot: Design of a Low Cost Autonomous Ball-boy Robot

Daniela Chavez Guevara, Jong-Hoon Kim

Discovery Lab, School of Computing and Information Science
Florida International University, 11200 SW 8th St, Miami, Florida 33199
dchav016@fiu.edu, kimj@cis.fiu.edu

Abstract

In 2011, 25 million amateur and professional people played tennis in the U.S alone[9]. People enjoy the game so much that they are willing to pay an instructor approximately \$20 - \$80 per hour[1][7][14] just to learn the tricks of the game. But as they don't want to pick up tennis balls after their training, so some of them end up paying an extra fee for the service or hire a personal ball-boy to do the work for them.

However, many tennis players don't want to spend the money for hiring a ball-boy to pick up all the tennis balls they used even though they don't like to do this tiresome task because they feel the job is trivial but the cost is expensive. So the solution proposed is the creation of a fully autonomous ball-boy robot that would automatically pick up tennis balls while the user is playing a tennis game or during training hours.

This solution was reached by building a robot called ScouterBot, which as its name implies, performs the task of "scouting" by using a robot sensing strategy based on ultrasonic sensors, being its principal objective to pick up tennis balls in an open environment without depending on human control. Prototyping and issues of implementation of the ScouterBot are discussed and explored on the paper.

Keywords: Autonomous, sensing strategy, robot, tennis balls.

1. Introduction

Nowadays we find different kinds of machines that make human lives easier. New inventions and technology keep being developed, allowing society to step each day closer to an era where machines are going to form a more important part of human lives as well as economy impact on society. However, it is people's desire on having more advanced machines to work with, what makes actual inventors explore further and deeper, always looking for a way to create a robot that works at human service.

Service Robot

Since the year of 1836 [8] we have had complex machines working with us. The industrial revolution [8] brought us the definition of "machine", starting the era in which humans and machines work together. But, what about service robots: robots that work for humans instead of working along humans. That was the next step: "The first electronic autonomous robots were created by William Grey Walter in Bristol, England, in 1948. The first digital and programmable robot was invented by George Devol in 1954 and was ultimately called the Unimate. Devol sold the first Unimate to General Motors in 1961 where it was used to lift pieces of hot metal from die casting machines at the Inland Fisher Guide Plant in the West Trenton section of Ewing Township, New Jersey. Since then we have seen robots finally reach a more true assimilation of all technologies to produce robots such as ASIMO, which can walk, and move like a human. Robots have replaced humans in the assistance of performing those repetitive and dangerous tasks which humans prefer not to do, or are unable to do due to size limitations, or even those such as in outer space or at the bottom of the sea where humans could not survive the extreme environments." [16] But in the field of sports, people still has machines not robots working for them.

Tennis Field Robot

In tennis courts we find ball-throwing machines, as well as in baseball fields. People own them because they make possible to train individually, and also because the features of a ball-throwing machine allow the player to change how often the machine throws balls so the player can practice at his own pace and it has a random oscillator that automatically throws balls in a sweeping pattern from side to side so the player gets a complete workout while hitting balls on the run [19]. Hence, it is easier and more comfortable for the player or amateur to play his favorite sport. But, what about when the training time ends, there is no robot to help the tennis player to collect the balls. Of course, there are robots such as: the playmate and gamma ball mower [25][26] that have retractable arms and a spring loaded arms mechanism that allows the machine to collect tennis balls while the user is pushing it around the field, but

those are controlled by humans, it is not the same as having a fully autonomous robot that picks up balls by its own. Having one of those robots on a tennis court would be the best complement for a tennis player or amateur's equipment. Thinking of this, ScouterBot project was started, so people would have a ball-boy robot working for them.



Picture 1. The Ball Picker [24]

Previous projects such as “The Ball picker” and “Mobile Robot Navigation and target tracking System” have shown that ScouterBot idea is not recent but comes in different packages that need to be put together.

Both projects present deficiencies. “The Ball picker” project picks up tennis balls successfully but its design is rudimentary and very unreliable, it lacks kinetics, and speed in its motion. On the other hand, the “Mobile Robot Navigation and target tracking System” is more than successful avoiding obstacles by using sensors from Xbox's [28] and Kinect's [10] devices, which not only increases costs but also requires a more powerful system than a microcontroller to support the data collection.



Picture 2. Mobile Robot Navigation and target tracking System [13,17,18]

2. State of the Art

A ball-boy robot should have a mixture of features that will allow the robot to be fully autonomous and that would

make the robot efficient when collecting balls. In order to make this possible, three important aspects need to be considered:

- The type of tennis courts surfaces on which the robot will move,
- The robot's hardware
- The robot's programming code.

A ball-boy robot should be able to move on the three different types of tennis courts surfaces [22], which are: grass courts, clay courts, hard courts and carpet courts.

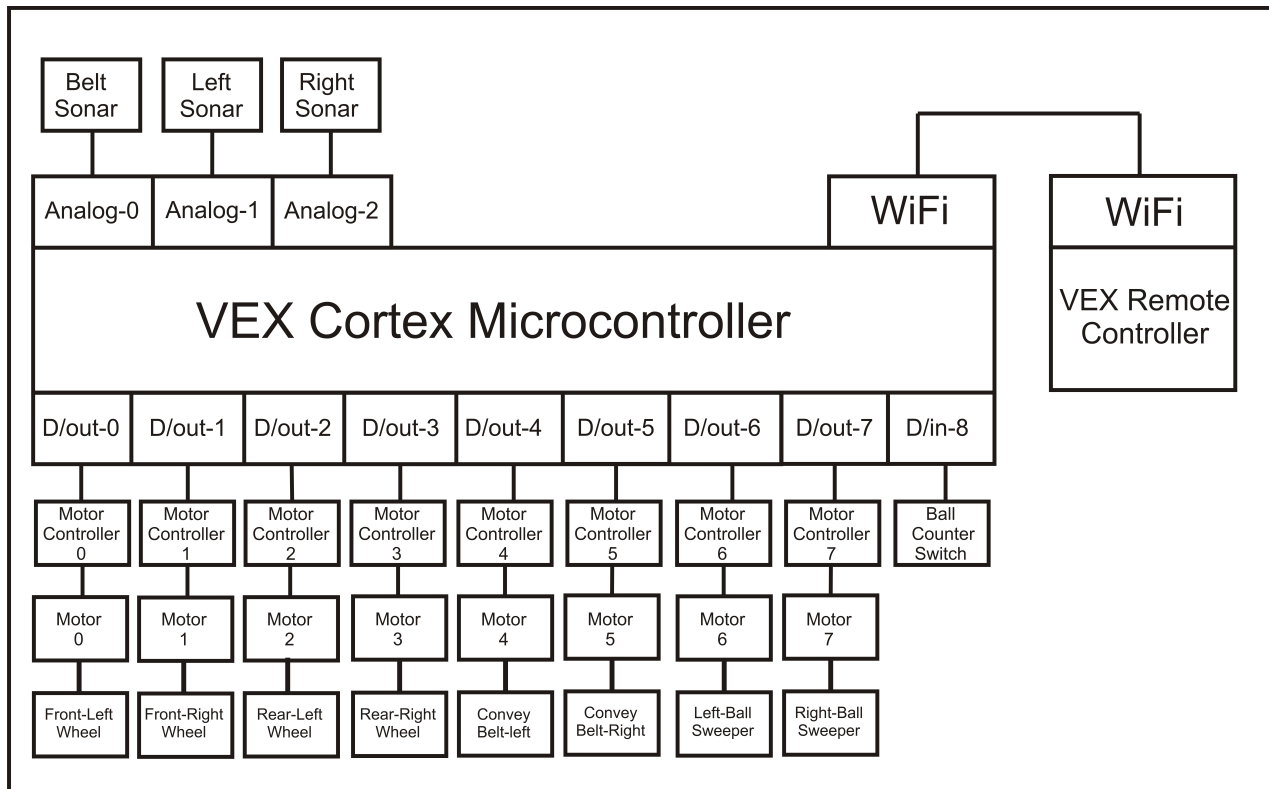
A ball-boy robot's design should not be easily breakable since it is going to be wandering around the tennis court for long intervals of time, depending on the amount of balls that it has to collect. Also, it has to resist erosion and changes in humidity and temperature. Its design has to show a solid structure but it should be simple for a faster and easier maintenance and it should allow the robot to have smoothness during its motion.

A ball-boy robot's programming code has to make the robot able to recognize the difference between the balls that it should pick up, the obstacles that it has to avoid, and other different objects. Including the features of speed and sensing techniques, the first one would help the robot to control its speed depending on the surface on which it is working, and the second one would improve the robot's recognition and understanding of its surroundings as well as the robot's productivity and effectiveness.

Overview of ScouterBot

ScouterBot was built following these three aspects as mentioned; consisting of two pairs of Omni-wheels that allow ScouterBot to move on clay courts, hard courts and carpet courts. Its structure is not easily breakable and durable, and can be carried around without problems as well as it has no difficulties on maintenance. ScouterBot has three ultrasonic sensors, two at its sides for detecting obstacles, and one at the center for detecting the balls to be picked up making ScouterBot a fully autonomous robot whose programming code is programmable so it can be programmed to pick up balls of different sizes.

3. ScouterBot Architecture

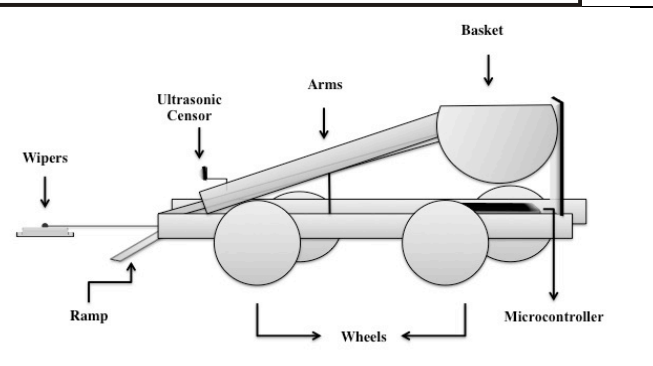


Picture 3. ScouterBot Architecture

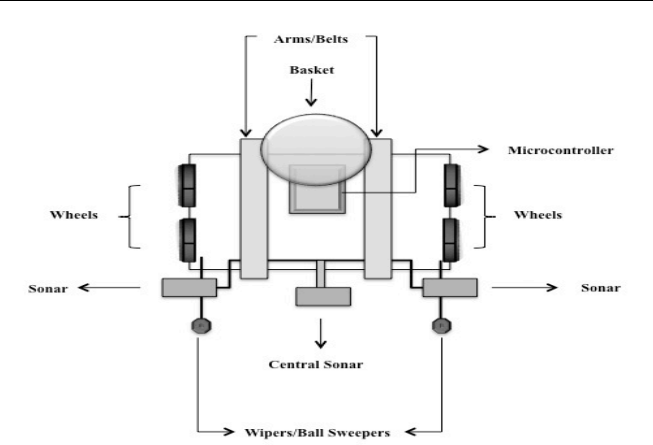
ScouterBot's system consists of two parts, one main system controller and a remote controller. The main system controller consists on the VEX Cortex microcontroller and uses eight digital outputs and one digital input. Eight motor controllers are connected to each digital output and to eight motors respectively. The first pair links the motors of the front wheels to the microcontroller as well as the second pair links the motors of the rear left and right wheels. The fourth and fifth motor controllers link the convey belt's motors to the VEX cortex and so do the sixth and seventh motor controllers by linking the ball sweeper's motors to the cortex. The only one digital input is linked to the ball counter switch and the belt sonar, left sonar and right sonar sensors are connected to the three analog ports respectively. Finally, the VEX remote controller is connected to the VEX cortex using Wi-Fi.

4. Mechanical Design

In the paper, we propose efficient ball picking mechanism which consists of the belt system and two sweepers for conveying balls to the basket as well as guiding balls to the gate of the belt.



Picture 4. Side View of ScouterBot Design



Picture 5. Front View of ScouterBot Design

As shown in Figure 4, ScouterBot's body structure consists of two pairs of wheels and the Vex cortex microcontroller attached to its base frame. The basket is supported by a thin piece of metal and also attached to the arms.

The ramp and wipers are held by the base frame and the ultrasonic sensor is located on one of the arms.

Figure 2 shows a better diagram of where the ultrasonic sensors or sonars are located.

5. Implementation

Since we are aiming for a low-cost autonomous picking up balls robot it was decided to use the VEX kit for robotics classroom [5]. The metal pieces that come with this kit allowed us to make a solid hardware structure for ScouterBot, easy to maintain and easy to carry.

Structure Subsystem

* Basket: At the superior extreme of both arms is attached the basket, which is the one that retains a certain number of tennis balls (between 8 and 9). It was carefully designed so the balls would stay inside without rolling down or obstructing other balls' path.

* Body Frame Dimensions :

- Height: 28cm
- Base's length: 37cm
- Base's width: 33cm

Motion Subsystem

* Wheels: Considering the clay courts, hard courts and carpet courts it was decided to use the Omni wheels [30], since they reduce the friction during its motion and make the turning much faster and smoother.

* Motors [31]: In total ScouterBot uses 8 motors with one microcontroller each one. (VEX website link)

* Arms or conveyers: The arms or conveyers are on the base, attached by one pair of thin cylindrical columns located at their sides and two metal plates. Both have a length of 31.5cm and the motors installed on their superior extremes when activated make the conveyers rotate so the ball is pushed up towards the basket.

* Wipers: A pair of wipers is also located at the lateral sides of ScouterBot. They are almost horizontally parallel with the front wheels, and have the task of pushing any ball outside the central sonar range into its range. So the cycle of collecting the ball and guiding it inside the basket is repeated.

Sensing Subsystem

* Ultrasonic Sensors [29] : One central sensor is attached half way of the arms, almost at the end of the bottom extreme. This ultrasonic sensor has a range of 8 inches within which it detects the ball to be collected. To then, immediately activate the motors installed on the arms, so the conveyers will take the ball inside the basket. Two sensors are at each side of the arms. They have the function of detecting the obstacles allocated within their respective ranges so then the robot proceeds to avoid crashing with the obstacle.

Power Subsystem [4]

* Battery: 7.2V Rechargeable Battery(NiMH)

* Capacity : 2000 mAh

Manual Control Subsystem [2]

* Joystick for manual control: ScouterBot can change from an autonomous mode to a manual control device like a joystick.

Programming Language

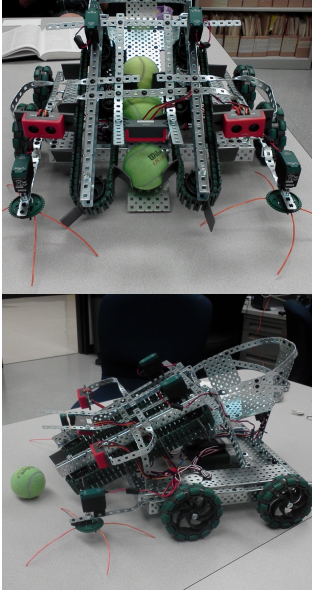
* Software: to make the sensors work along with the motors requires a programming language. The VEX cortex microcontroller [3] was used and the language to write the programming code is ROBOTC [15].

ScouterBot has been going through many improvements to reach its actual condition. A limit switch (Sensing Subsystem) was added and the programming code was modified so ScouterBot will know how many balls it was collecting.

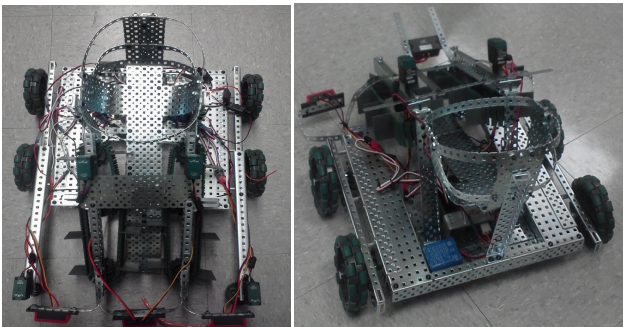
Another attempt to make of ScouterBot a suitable autonomous ball-boy robot was also made by changing the programming code in order to make ScouterBot stop completely once it collected a fixed amount of tennis balls.

6. Prototyping

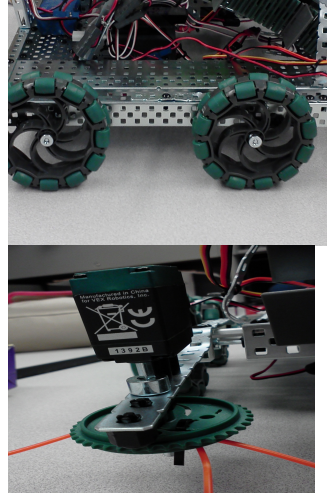
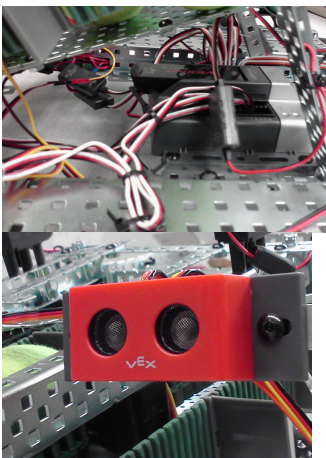
For the prototyping of ScouterBot, we used VEX robotics classroom Kit which allows us to build this design quickly and efficiently.



Picture 6. Front and Side View of Prototype ScouterBot
 In picture 6, the prototype of ScouterBot shows how to pick and convey tennis balls to its basket using a pair of belt system. Two sweepers guide the balls to the gate of the belt system so that ScouterBot can collect balls efficiently.



Picture 7. Top and Back View of Prototype ScouterBot



Picture 8. VEX Cortex Microcontroller, Sonar, Omni-wheel, and Sweeper.

In Picture 8, the VEX Cortex Microcontroller is attached to the base frame for an easy wiring. An image of the sonar is depicted to show its ultra sonic emitter and receiver. The Omni-wheels' structure help ScouterBot to have a smooth motion when going forward, backwards and turning to the sides. The ball weeper is attached on the motor as shown in the picture.

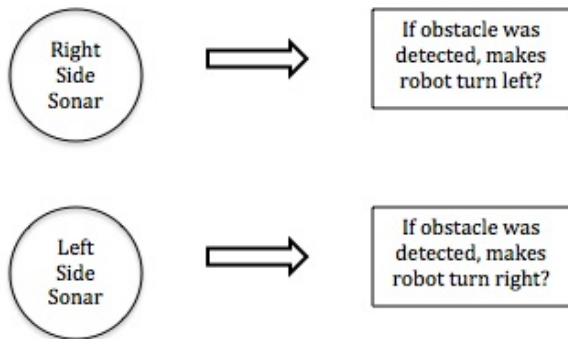
7. Discussion and Future Work

ScouterBot wasn't working well at the beginning of the project, there were some deficiencies on its design and on its programming code that wouldn't let ScouterBot have a good motion, nor detect obstacles. ScouterBot wasn't fully autonomous; we controlled it with a joystick and it did everything backwards. Although the wiring was correct we discovered that for some reason the motors were flipped, so we had to flip them again in order to make ScouterBot's motors go forward.

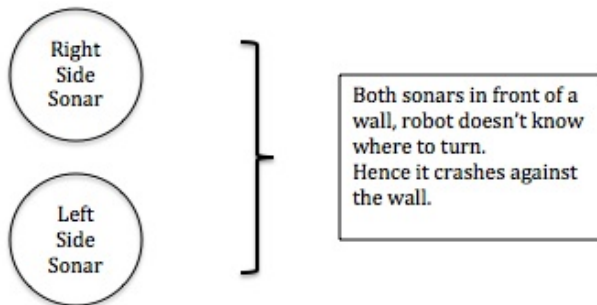
Understanding the RobotC programming language also took a while; we discovered that the perfect speed for the motors to either go forward or backwards was 50% of its maximum power due to stable mobility. The turning motion had the same speed, and the conveyer arms motors worked at a speed of 100 % of its maximum power.

However, once that we understood the programming language, coding the ultrasonic sensors didn't represent a challenge. The lateral sensors detected a wall or obstacle within a range of 15 inches. But when both sensors were in front of a wall, ScouterBot got confused and crashed into the wall. A brief explanation of the problem and the solution is shown below:

- Detailed functioning of each ultrasonic sensor:



- Problem:



Picture9. The problem and solution for obstacle avoidance

* Solution applied

Inside the code we allowed ScouterBot to go back and forth four times and then turn right to then resume its task of collecting balls.

Problems noticed while testing

Ball wouldn't be picked up because the central sonar couldn't detect it. Because we had assigned a value of 10 inches to the central sonar's range. The appropriate value for it to detect the ball ended up being 8 inches, after recalculating the tennis ball diameter.

The limit witch or touch sensor turned off the whole robot when one ball was picked up. After further testing we discovered that the touch sensor is extremely sensible so that when the ball touched it, the value read by the sensor was of 3 units. Thus, ScouterBot understood that he had collected three balls, and stopped functioning. Solution: multiply the actual number of balls to be collected by 2 and input that as the limiting value.

*Remaining Problem: The robot picks up seven tennis balls and it turns off, except the motors at ports 8 and 9, which belong to the wipers. We are still testing and trying to find a solution.

Future Implementations

Within our ideas of giving ScouterBot a better understanding of its surroundings, we plan to install more

ultrasonic sensors and a camera. These additional ultrasonic sensors will provide efficient obstacle avoidance while the camera would give ScouterBot the eyes that it needs to recognize the tennis-balls to be collected intelligently. Hence the programming code would be improved.

Because ScouterBot can move without any difficulties on tennis clay, hard and carpet courts, the idea of changing the model of the wheels is contemplated as well as changing the design of the wipers, in order to make ScouterBot work on tennis grass courts without presenting deficiencies in its motion.

Research on more efficient sensing techniques would also make ScouterBot's awareness of its surroundings sharper and more accurate. Our goal is to have a similar sensing strategy as the "Mobile Robot Navigation and target tracking System" project but it would take time since we have restrictions on our budget.

8. Conclusion

In this paper, we proposed a low-cost autonomous ball-boy robot called ScouterBot. ScouterBot is based on an ultrasonic sensor obstacle avoidance strategy combined with a conveyor belt mechanism being its main objective to pick up tennis balls autonomously. The prototype of this design demonstrates the feasibility of ScouterBot and its autonomous feature. More detailed examination on sensing techniques and improved programming algorithms remain as a future work.

Acknowledgments

* *PhD. Jong-HoonKim, provided constant advising and guidance that helped us to complete ScouterBot project.*

* *Michael Lazo, provided assistance building the robot and writing the programming code.*

* *Frank Hernandez, provided assistance debugging the original programming code and improving it.*

* *Ian Raisbeck, provided assistance on writing the code for the limit switch.*

References

- [1] [online]USTA High Performance Coaching Program | USTA. (n.d.). from http://www.usta.com/About-USTA/Player-Development/Coaching-Education/USTA_Coaching_Education_Department/
- [2] [online]Control - Robot Accessories - Products - VEX Robotics. (n.d.). <http://www.vexrobotics.com/products/accessories/control?ref=home>
- [3] [online]Logic - Robot Accessories - Products - VEX Robotics. (n.d.). <http://www.vexrobotics.com/products/accessories/logic>

- c?ref=home
- [4] [online]Power - Robot Accessories - Products - VEX Robotics. (n.d.).
<http://www.vexrobotics.com/products/accessories/power?ref=home>
- [5] [online]Structure - Robot Accessories - Products - VEX Robotics. (n.d.).
<http://www.vexrobotics.com/products/accessories/structure?ref=home>
- [6] [online]Bender, J. F. (n.d.). Tennis Ball Boy Salary | eHow.com.
http://www.ehow.com/info_12043703_tennis-ball-boy-salary.html
- [7] [online]Building your tennis career â€œ that's who we are. (n.d.)
<http://www.uspta.org/default.aspx?MenuItemID=1966&MenuGroup=New-USPTA&&AspxAutoDetectCookieSupport=1>
- [8] [online]Category. (n.d.). Industrial Revolution Inventors
<http://americanhistory.about.com/library/charts/blchartindrev.htm>
- [9] [online]History of Softball - Page 2 of 2 - SportsKnowHow.com. (n.d.).
<http://www.sportsknowhow.com/softball/history/softball-history-2.shtml>
- [10] [online]Kinect - Wikipedia, the free encyclopedia. (n.d.). <http://en.wikipedia.org/wiki/Kinect>
- [11] [online] A Man Among (Ball) Boys and (Ball) Girls - New York Times.
http://www.nytimes.com/2006/08/27/sports/tennis/27cheer.html?_r=1
- [12] [online]Miranda, K. (n.d.). The Average Salary of a Tennis Coach | eHow.com.
http://www.ehow.com/info_7747949_average-salary-tennis-coach.html
- [13] [online]Mobile Robot Navigation and Target Tracking System . (n.d.).www.eecs.ucf.edu/courses/cap6121/spr12/readings/mobile.pdf
- [14] [online]Month. (n.d.). Coaches and Scouts :U.S. Bureau of Labor Statistics.
<http://www.bls.gov/ooh/Entertainment-and-Sports/Coaches-and-scouts.htm>
- [15] [online]ROBOTC.net :: ROBOTC Natural Language. (n.d.). <http://www.robotc.net/NaturalLanguage/>
- [16] [online]Robot - Wikipedia, the free encyclopedia. (n.d.). <http://en.wikipedia.org/wiki/Robot>
- [17] [online]Robotics Club and Laboratory at UCF. Retrieved May 3, 2012, from
<http://robotics.ucf.edu/gallery/view.php?gallery=ground&dir=ground04022011&title=First%20Autonomous%20Testing&date=Apr%202,%202011>
- [18] [online]Robotics Club and Laboratory at UCF. Retrieved May 3, 2012, from
<http://robotics.ucf.edu/gallery/view.php?gallery=surface&dir=boat06092011&title=First%20Day%20of%20Practice&date=Jun%209,%202011>
- [19] [online]TENNIS CUBE from Sports Tutor. (n.d.). SportsTutor.com,
<http://www.sportstutor.com/tennis/cube/>
- [20] [online]THE PLAYMATE MOWER. (n.d.).
<http://www.playmatetennismachines.com/mower.htm>
- [21] [online]Tennis Instructor Salary | Glassdoor. (n.d.)
http://www.glassdoor.com/Salaries/tennis-instructor-salary-SRCH_KO0,17.htm
- [22] [online]Tennis court - Wikipedia, the free encyclopedia. (n.d.).
http://en.wikipedia.org/wiki/Tennis_court
- [23] [online]The Ball Picker. (n.d.).
people.ece.cornell.edu/land/courses/ece4760/FinalProjects/s2009/peterfkung/BallPicker.htm
- [24] [online]Type, E. (n.d.). PayScale - Tennis Coach Salary, Average Salaries .
http://www.payscale.com/research/US/Job=Tennis_Coach/Salary
- [25] [online]Tennis Ball Machines Racquet Stringers Tennis Racquets and Bolle Sunglasses..
<http://www.tennisballmachinestore.com/TMOWER.htm>
- [26] [online]Tennis Ball Machines Racquet Stringers Tennis Racquets and Bolle Sunglasses..
<http://www.tennisballmachinestore.com/TMOWER.htm>
- [27] [online]Wimbledon - Ball Boys & Girls. (n.d.). Wimbledon -
<http://www.wimbledon.com/championships/behind-the-scenes/ball-boys-and-girls>
- [28] [online]Xbox 360 - Wikipedia, the free encyclopedia. (n.d.). http://en.wikipedia.org/wiki/Xbox_360
robot, m. t., robot, o. c., & travelled., m. i. (n.d.).
- [29] [online]Sensors - Robot Accessories - Products - VEX Robotics.
<http://www.vexrobotics.com/products/accessories/sensors?ref=home>
- [30] [online]Motion - Robot Accessories - Products - VEX Robotics. (n.d.).
<http://www.vexrobotics.com/products/accessories/motion/276-2185.html>
- [31] [online]Motors - Robot Accessories - Products - VEX Robotics. (n.d.).

Semi-Autonomous Crane Prototype with Payload Stabilization

Hershel Parmar

Student - University of North Florida
6168 Whitsbury Court
Jacksonville, FL, 32258
1-904-521-1709

HershelParmar@gmail.com

John Williams

Student - University of North Florida
443 14th Avenue South
Jacksonville, FL, 32250
1-904-610-1988

John.B.Williams@comcast.net

Brandon Smith

Student - University of North Florida
13850 Thomasville Court
Jacksonville, FL 32223
1-904-945-1088

bts.smith85@gmail.com

Rachel Vasquez

Student - University of North Florida
1711 Canopy Oaks Drive
Orange Park, FL, 32065
1-904-612-6477

vasgrs@gmail.com

Daniel Cox

Professor - University of North Florida
1 UNF Drive
Jacksonville, FL, 32224
1-904-620-1845

dcox@unf.edu

ABSTRACT

Among the various crane systems in existence for load transportation, a standard reach-stacker crane scale prototype is developed. The approach is to create a hybrid truck-mounted crane with payload stability features. The implemented prototype is designed to a 1/20th scale model crane system, which would effectively lift a proportionally scaled intermodal container while stabilizing its roll and pitch motions. Development of the prototype requires coupling electrical engineering principles to ensure the task would meet power, mobility, and user adaptability objectives. Incorporating these guidelines, a field operator would be able to transfer a given load with ease from one location to another while the developed stability mechanism allows for smooth and safe transportation. The motivation is guided by the development of advanced technologies for the Northeast Florida region which is evolving into a major national transportation logistical hub. Development of the integrated mechanical and electrical subsystems are described, including various unexpected changes as well as aberrant solutions from the initial design plans. Changes in the mechanical structure were reflected in the design evolution of the electronic systems. This led to numerous explorations creating many alternative solutions for torque, stability, power consumption, and drive system issues encompassed in the generation of the final prototype design. Ultimately, the design plan separated into two facets; creating a robust system which would remain stable during load transportation, and the design of a stability mechanism which would continuously correct any erratic behavior of the payload motion. These two facets guided the creation of the crane system into a final prototype with minimal mechanical errors, many of which the electrical system was able to, either compensate for, or eliminate through the implementation of coded logic. This allows for the operator to focus solely on the task of transferring a load between two points with the ease of using a single intuitive input device, remotely or onsite.

Keywords

Hybrid Crane, Payload Stability, Intermodal-Container Transport, Autonomous Stability Mechanism, Remote Operation

1. INTRODUCTION

Currently consisting of three public marine terminals and a single passenger cruise terminal, JAXPORT is continuing to grow and improve in an effort to boost the economic power of the Northeast Florida region [1]. Cargo flows through this port system daily with new trade lanes established continuously, increasing the port's necessity of speed and overall payload transportation output. Considering operator restraints and reduction of man power in zones where crates weigh approximately 80,000 pounds, the need for a crane system with an autonomous stabilizing mechanism becomes vital to prevent injury in the workplace, while reducing the transportation time in transferring a payload from ship to dock or vice versa. Standard cranes known as reach-stackers are generally utilized to perform these tasks, requiring two or more operators for safer transportation. This often requires an operator to control the crane from an onboard cab while the other operator in the vicinity of the payload guides the motions to ensure the crane is lifted correctly.

In an effort to design a system which would reduce requirements for operators, a crane prototype has been built to a 1/20th scale. This prototype performs all the tasks of a standard reach-stacker crane with the addition of a stabilizing platform. A control box encloses all the electronic systems and allows remote input from an offsite operator via some type of intuitive controller. This controller enables the operator to lift and lower a payload using the clamping system, subsequently transporting it to a destination with the assistance of an onboard camera, real-time stabilizer platform, and powerful drive system. The camera provides the operator with a view of the payload site, allowing a safe distance to be kept from the crate itself. This allows a single operator to focus on the whole transportation process either using the provided display or watching the crane itself from a distance. Creating a scaled prototype demonstrates similarities with many real crane systems [2]. In addition to the stability mechanism, the creation of the crane requires focusing on weight distribution and material selection, while optimizing the logic and electronics necessary to run the entire crane system remotely with minimal error. These concepts will further be explained within this paper.

2. CRANE REQUIREMENTS AND SPECIFICATIONS

2.1 Electrical Requirements

For the purpose of scaled prototyping, the entire system is fully wired from the controller to the components aboard the crane. Having a fully wired system implies that everything would be hard-wired to each component from a single central processing unit (CPU). The wires from the components follow a bus line to a central control box, protecting all the electrical components from the elements and detrimental effects from motion vibration. Minimal components are placed on the crane. The payload stabilizer platform requires keeping the gyroscope external to the control box. The gyroscope and the camera system are the only two electrical components placed on the crane itself.

As for the movement of the crane, a front wheel drive vehicle that would be fully balanced during motion and performing zero radius turns is needed. The crane is designed to turn and drive with a geared motor system that could handle the payload weight and any natural swaying tendencies. Taking into consideration the limited number of ports and power available on the CPU, the optimization of coded logic speed and component integration with physical filters to prevent and eliminate any electrical noise is also required.

2.2 Mechanical Requirements

The crane prototype requires an efficiently maneuverable structure, with or without a loaded payload crate, using a single input device. The final size of the mechanical system requires scaling a standard reach-stacker with hybrid aspects of a truck-mounted crane. Effectively scaling the previously mentioned crane systems down to a testable size for a laboratory environment requires selecting appropriately sized actuators and sensors. Limiting the size of these parts also places constraints on the power produced by these subsystems which leads to generating a significant mechanical advantage for lifting the payload and operating the drive mechanism. The platform of the crate clamping device requires full stability in at least the pitch (X-axis) and roll (Y-axis) directions. This requires either a fully mechanical gravity-propelled weight system which would react to the tilting motion or an electromechanical system with motors that actively assist in the weight balancing process with a motion sensing feature. Creating this autonomous stability system improves payload transportation time and reduces the operator's need to wait for the platform to stabilize. In addition to the stability device, a camera would assist in visual alignment of the payload crate before coupling.

In lifting the crate, the boom of the crane must be well balanced about the pivot point on the base of the crane. This requires adding counterweights to the rear of the boom, closer to the base. Once these weights are added, the base must be weighted proportionally to eliminate any backward directional tipping when the crate is not present. This leads to creating a robust drive system which prevents cambering of the wheels while supporting the weight fluctuations from the time the crate is lifted, lowered, released, and the crane recedes from the crate's destination. As for the lifting system of the crate, motors are used with the combination of speed and torque to provide a stable lift process.

2.3 Electrical Specifications

For the purpose of effectively performing calculations and minimizing space, a microcontroller (MCU) was chosen for

central data processing. The prototype system requires 5V for operation since many of the peripherals also require the same logic level. Implementing 5V logic allows for easier integration with 3.3V peripherals when regulating the main bus power. Considering the power constraints associated with the sizing of the parts when scaling the crane, 12V peripherals became necessary to generate the lifting power needed for lifting the proportionally voluminous crate. In an effort to include a 12V system, low-to-high level logic was implemented using various transistor circuits in combination with relay logic.

The MCU is used to read user input and translate the data to control numerous DC motors, a stepper motor, a linear actuator, and the gyroscope aboard the stability platform. In order to optimize the processes and eliminate user interface lag, a minimum 4MHz system clock is needed to effectively provide a 2MHz bus clock. This clock also has to be configurable for other processes such as pulse width modulation (PWM) and analog-to-digital conversion (ADC). Allowing the MCU to sample data quickly from the gyroscope and the controller, the crane can operate smoothly and eliminate unnecessary motions. This directly translates to an elimination of noise in the stabilizer system when the system exhibits jerking tendencies during payload transportation.

The user interface device for the prototype is a Sony PlayStation 2 controller. This controller provides the joysticks for lifting and driving with precision speed. It also includes a number of switches and buttons for the user to select various modes of operation. This type of system represents a good choice for an operator to control the crane remotely as it incorporates all the controls in a single handheld device.

2.4 Mechanical Specifications

In determining the scaling method for the physical structure of the crane prototype, it quickly became evident that scaling a real crane's weight using a 1/20th scale is nearly impossible with the available materials in the region. This led to the realization that scaling would be done based on volume which also ensures that weight dimensions of the final product were to scale. At 1/20th scale, a 70,000 pound crate becomes 8.4 pounds and an 80-foot boom is reduced to 48 inches. The base assembly with the wheels and pilot and controls becomes a 15-inch by 7.5-inch cart holding the boom and all of the drive mechanisms necessary for operation. The final assembly had to be fully balanced, with the weight distributed and supported properly. This is checked by using basic static calculations. During any maneuvering operations, keeping the weight centrally located is important in increasing mobility, so the boom was designed with a high lift angle as the goal.

The lifting mechanism needs to be operated for two distinct methods. For fast and sweeping motions, the boom is designed to move up and down using a linear actuator. The base of the actuator is positioned at the base of the turret mounts, and the top of the actuator attached to the boom some distance away from the pivot point. This generates a moment to quickly lift and lower the boom and crate assembly while the positioning optimizes the range of motion for the boom. The force required from the actuator is estimated from the static load.

The mounting points and stroke of the actuator are determined using Equation 1 and Equation 2. Any fine movements, such as lowering the lifting mechanism onto the crate, are handled by a stepper motor pulling on a braided chord. This chord would be wrapped around a spindle connected to the stepper motor,

following the boom up to a redirecting pulley, ultimately attached at a swivel joint with four corner points to the stability platform. The torque is calculated with Equation 3, leading to a 220 oz.-in stepper motor torque value. A transmission with a gearing ratio of 6-to-1 has been implemented to increase its mechanical advantage.

$$\frac{a}{\sin A} = \frac{b}{\sin B} = \frac{c}{\sin C} \quad (1)$$

$$c^2 = a^2 + b^2 - 2(ab)\cos\gamma \quad (2)$$

$$T = F \times r \quad (3)$$

The remaining systems needed for a fully functional prototype are the drive mechanism and the crate clamping system. It is determined that the target weight of the crane far exceeds the axle strength of the small DC drive motors available. In order to keep a full range of motion by controlling two drive wheels independently, an independent axle system driven by DC motors and gears needed to be designed and utilized. The clamping mechanism needed to be compact and lightweight in order to maximize the space and effectiveness of any balancing system on the lifting mechanism. A physical clamp utilizing springs and a DC motor are used for gripping the corners of the crate, providing a very compact and fail close method for holding the crate during transportation. Equation 3 and Equation 4 were used to determine the appropriate DC motors for the drive system, while only Equation 3 was needed for the clamping mechanism motor.

$$\Sigma F = MA \quad (4)$$

The primary material chosen for the crane assembly is mild steel. The reason for this is the ease of welding and machining of the material. Also, the strength of the steel will greatly exceed the maximum stresses seen from the load. This will eliminate the need for any stress/fatigue calculations. The deflection of the boom is also minimized by the over sizing of the boom material. This reduces the need for any bending or deflection calculations.

3. DESIGNS AND ALTERNATIVES

With the overall system requirements and specifications for the crane's drive system and payload balancing necessities, many design alternatives have been evaluated and some of them are described below.

3.1 Alternative Base Design 1

The first design, as seen in Figure 1, uses a single tower to support the boom and four driving wheels. The base moves and rotates while the boom raises and lowers the crate using a chord attached to a motor. This design limits the stability of the boom since there is only one turret. Also, the level of maneuverability of the base creates substantial complexity, resulting in an estimated failure and an extended design time.

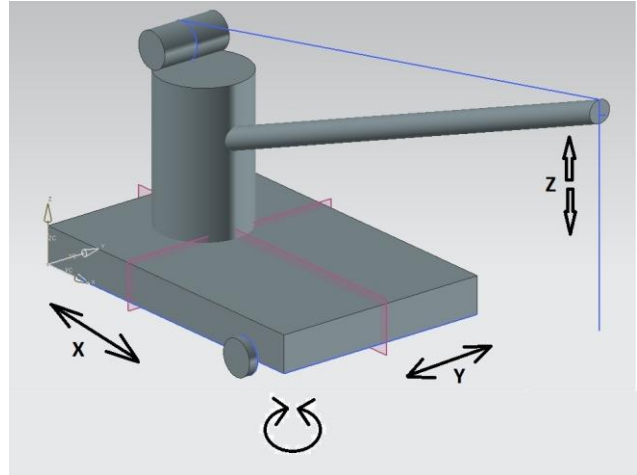


Figure 1. Alternative Design #1

3.2 Alternative Base Design 2

The second design (Figure 2) distributes some of the movement of the crane's drive mechanism to the turret. With a rotating turret, the drive mechanism requires less maneuverability. The longer boom design also widens the range of motion. The boom length is approximately 48 inches, so a rotating turret allows for an 8 foot radius in a stationary loading and unloading area. However, any rotating turret design raises two concerns; the stability of the system as the turret rotates and the strength of the rotating mechanism. Any rotation plate must be very secure to handle the torque and the downward force sustained by the bearings at any given moment, while also minimizing any friction to allow for a motor to turn the plate easily and efficiently.

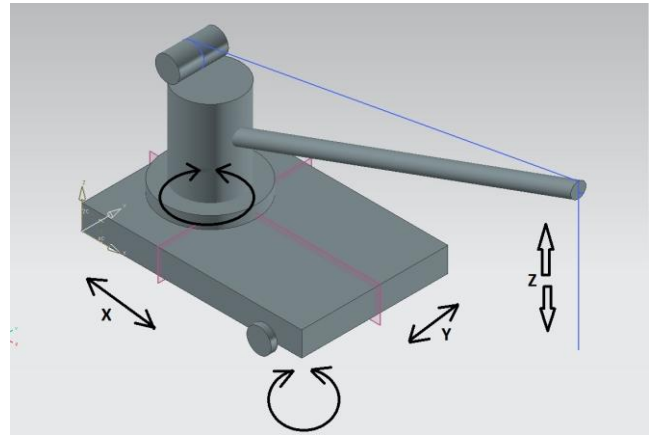


Figure 2. Alternative Design #2

3.3 Alternative Base Design 3

The final alternative incorporates three key features lacking in the first two alternatives. The whole assembly, shown in Figure 3, has a lower profile than the other two, with a wider turret and the counter weight to relieve torque on the boom. The counter weight also allows for a longer boom while being more stable. The drive mechanism for this design is very simple with two independently driven front wheels and ball bearings under the rear of the base plate. This alternative requires a fixed turret assembly, with a pivoting boom to pick up the crate and help with maneuverability while driving.

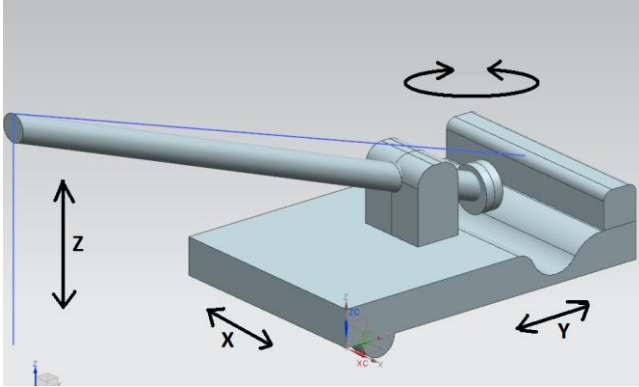


Figure 3. Alternative Design #3

3.4 Stabilizer Platform and Clamp Mechanism

Creating a stability mechanism that continuously corrects any erratic behavior of the crate due to swaying and transportation motion is a demanding task. There were a number of design alternatives which led to two primary designs.

3.4.1 Stabilizer Platform Design 1

The first lifting mechanism alternative, suggested in Figure 4, utilizes electromagnets for grasping a crate. The crate is fabricated with magnets on the top to match the electro-magnets on the clamping mechanism. However, any design that utilizes electromagnets for this scaled model would be very heavy. With a target weight of 8.4 pounds for the entire crate holding cargo, a large amount of the allowable payload would have been consumed by just the magnets instead of space for the cargo. Also, the balancing mechanism on this design allows space for only a single weight moving across the platform for stability in only one direction.

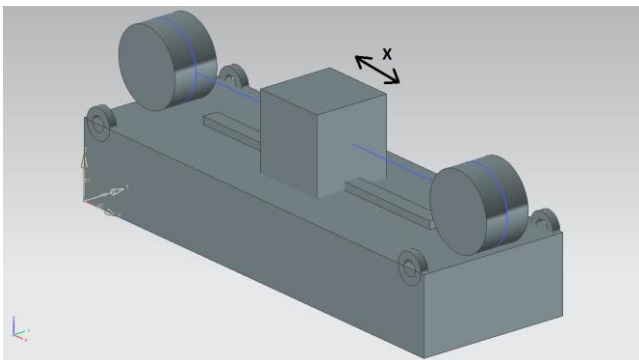


Figure 4. Stability Platform Design #1

3.4.2 Stabilizer Platform Design 2

The selected idea for the lifting mechanism (Figure 5) equips spring-loaded clamps to hold onto the crate as it is lifted. This saves a great deal of weight on the lifting mechanism by having only small metal hooks and a motor for the clamping motion. The crate has much less weight due to the holes required for the arms of the clamp mechanism to grasp. Also, there is minimal electrical signal interference, since the motors have much less current transmitted along the cables to lift the crate, allowing the balancing mechanism to work much more effectively. With the weight savings, reduction of complexity, and lower power consumption, this design proves to be the best choice of the alternatives considered.

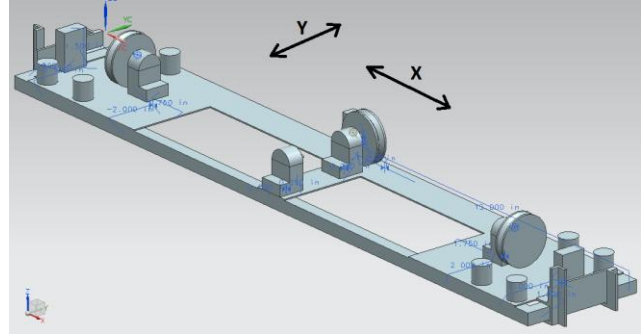


Figure 5. Stability Platform Design #2

3.5 Electronics, Peripherals, and Power Issues

Choosing a microcontroller for the purpose of controlling the entire mechanical system using electrical components is a critical task. In addition to size restrictions there were also speed necessities. While laying out the various features of the two main MCU choices under consideration, it became obvious to sacrifice size for the benefit of pure processing power.

3.5.1 TI MSP430

The Texas Instruments MSP430 (Figure 6) series microcontroller was considered for use in data processing since it is very small and perfect for space requirements. However this MCU is not powerful enough to handle the various signals from the gyroscope, the controller, and other peripherals and it simply lacks the ports necessary for outputting signals to the peripherals as well. The MCU also runs on a 3.3V logic level which essentially requires creating or purchasing numerous logic shifter circuits for integrating 5V logic components. This introduces error to the system when a sampling rate for the controller and gyroscope is high and the shifter circuit simply cannot keep up with the changes.



Figure 6. Texas Instruments MSP430 MCU [3]

3.5.2 Freescale MC9S12C128

Reviewing the necessary requirements to run the mechanical system, the Freescale HCS12C128 microcontroller (Figure 7) has been chosen for processing all the signals. All the specifications were met with this MCU. It hosts 60 available ports, containing six PWM ports, seven ADC ports, and 41 general-purpose input/output (GPIO) ports. It also meets the speed criteria with a 4MHz system clock and is configurable to utilize the phase-lock loop feature which would virtually increase the speed to 32MHz if necessary.



Figure 7. Freescale MC9S12C128 MCU [4]

3.5.3 Power Issues

When determining the source of power for the prototype crane system, a number of power supplies were designed, built, and tested. Initially, an AC voltage rectifier was considered to power at least the peripherals but the circuitry required a transformer to step down the voltage from a standard wall outlet. Also, the integrated circuit rectifier chips only provide current up to 1.5 amps. Although these chips were readily available, they would not produce the required 6 amps to run the entire system.

Another idea required numerous 9V batteries that would be put in series to generate 18V. This would work but would be expensive since power would be consumed faster. It became clear that the battery approach would only be reasonable if high quality batteries were used; however, this adds unnecessary cost.

The selected solution for this issue was to buy a computer power supply which is capable of producing a peak value of 20 amps. Routing the wires to a simple terminal strip allowed for 12V, 5V, and 3.3V power rails. This method was beneficial in many ways, especially for its ability to produce enough power for all the peripherals and shut down automatically in cases of short circuitry.

3.5.3 LPR550AL Dual Axis Gyroscope

In order to stabilize a payload, a motion sensing device is used. Initially an accelerometer was considered but the gyroscope seemed to be the perfect choice for real-time angular motion sensing. The LPR550AL (Figure 8) measured pitch (X-axis) and roll (Y-axis) rotations as was shown in Figure 5. The gyroscope was more precise than the accelerometer and the one selected below had an analog output, measuring $\pm 500^\circ/\text{s}$ in its default configuration. This is far greater than the accuracy necessary for platform tilt sensing, although there is a configurable option of $\pm 2000^\circ/\text{s}$ for greater precision needs.



Figure 8. LPR550AL Dual Axis Gyroscope [5]

4. SOLUTIONS

4.1 System Assembly

Following the 1/20th scale assigned for the most practical modeling, steel was the best material available to create a realistic weight and keep the model rigid. The drawings in Figure 9 and Figure 10 demonstrate the final design of the crane prototype and stabilizing mechanism.

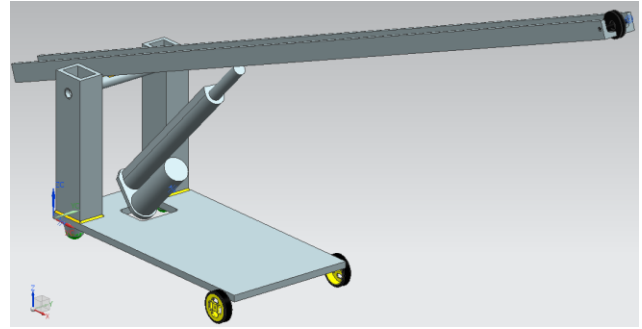


Figure 9. Final Design of Structure

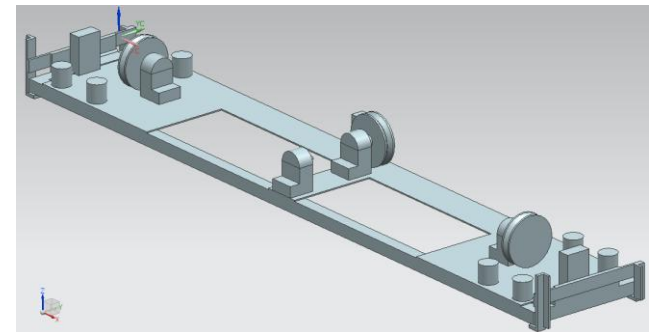


Figure 10. Final Design of Stability Platform

A 3/8 inch steel plate operated as the base for the crane, and 1/4 inch steel sections have been welded together to create the turrets. The turrets have been placed at the base plate's rear extrema to maximize the ability of the crane to efficiently balance with a payload. The base is driven with two wheels, placed on axles resting on pillow block bearings fixed to the bottom of the base. The drive motors are placed on top of the base allowing for quick modifications of the system in order to keep the timing belts in tension. Underneath the turrets at the back of the base, two roller balls with ball bearings have been welded in place to allow maximum maneuverability of the base.

The next main subsystem is the boom. Four holes are drilled through the two turrets (two holes for each turret) to place a bar used as the pivot point of the boom. A piece of pipe, with a larger inner diameter than the pivot bar's diameter, is welded to the boom as a fixed point of rotation. The short section of the boom hanging off the back end of the crane is utilized as counterweight and for mounting the winching device. Ten pounds of steel counterweight is added to the back of the boom for balance and to create a solid mounting point for the stepper motor. The stepper motor is fixed to the weights with a gearing harness and the harness supports the motor and an axle with the 6-to-1 gear ratio. This axle holds the braided chord for lifting the crate and a separate section is used to wind the cables leading to the balancing mechanism.

The boom is fitted with two more integral pieces. The lifting end of the boom is cut to make room for mounting a wheel. This wheel is extended above and out from the end of the boom, and guides the chord from the axle to the lifting mechanism with minimal friction. Finally, a linear actuator is fitted to the boom and the base plate for quickly lifting the boom and decreasing the overall length of the cart when in the upright position thereby increasing maneuverability. The bottom end of the actuator is lined up with the turrets, directly beneath the pivot point. The top of the actuator is mounted to the boom at 9.5 inches from the pivot point. This gives the actuator plenty of mechanical advantage to create the moment needed to lift the boom under full load. The distance also allows the boom to be parallel to the ground when the actuator is fully retracted, resulting in an angle of 71 degrees from horizontal when the actuator is fully extended. This places the weight approximately above the drive wheels, maximizing the driving and turning capability of the crane. The assembled prototype is shown in Figure 11.



Figure 11. Final Crane Assembly

The last mechanical section of the crane is the balancing mechanism for the crate (Figure 12). The clamping mechanism promotes a failsafe design. If the crane loses power with a magnetic system, the crate would immediately fall without this device. The clamping mechanism allows for the crate to stay attached under any power conditions, creating a safer design. The mechanism consists of four arms, two on each side, with each end connected together as shown in Figure 12. A spring on each side holds the clamps closed, and the motor pulls on two strings to pull the arms towards the center of the platform which opens the clamps. A geared DC motor provides the force to open the clamp. Once the crate is aligned with the clamp mechanism, the operator releases the DC motor signal, allowing the arms to retract to the closed position with the force of the springs.



Figure 12. Final Stabilizer Platform

The platform above consists of three weights, one in the long direction and two in the short direction, each controlled by a DC motor. The motors pull each weight based on the signal from a gyroscope placed on the platform. The MCU processes this signal continuously, forcing a motor reaction to allow the weights to

counter the undesired motion of the crate. Upon observation of the final design, there are a few changes that would improve any future designs. The long direction for the weight to travel could utilize an all-thread bar spun by a high speed DC motor. The all-thread would move a very heavy nut across the length of the lifting mechanism, keeping the weight on a single track and controlled more precisely. The balancing mechanisms on each end of the platform could utilize a system of gears to swing a weight further than the short distance they travel now. A mechanical connection along with the longer travel distance would most likely increase the effectiveness of these side weights.

4.2 Control Console and Logic

A number of components are added to assist the operation of the crane. As these components were identified and specified, the programming was fine tuned for each component with errors corrected through this process. The logic coded for this system follows the simple high-level flowchart seen in Figure 13.

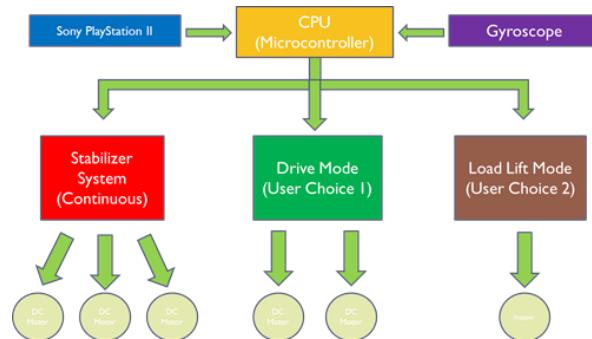


Figure 13. Software Flow Chart

The control box is shown in Figure 14. The operator will be able to turn on the system and begin interacting with the crane using the attached controller. The controller hosts two analog joysticks and momentary toggle switches used for performing different operations in two isolated modes. The joysticks demonstrate a linear sensitivity as demonstrated in Figure 15 and Figure 16



Figure 14. Control Box and Operator Console

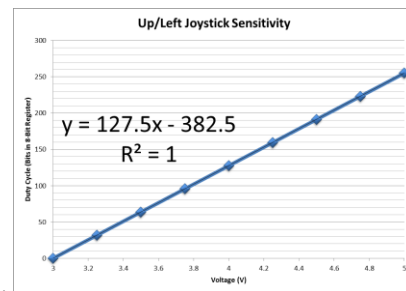


Figure 15. Up/Left Sensitivity - Voltage vs. Duty Cycle

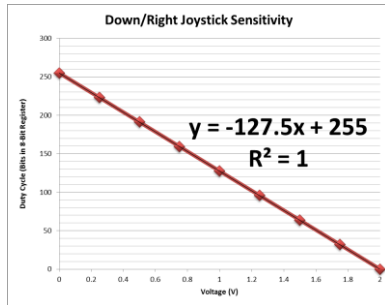


Figure 16. Down/Right Sensitivity - Voltage vs. Duty Cycle

The equations seen in Figure 15 and Figure 16 are used for coding the motor velocity depending on the intensity and direction the operator may push the joystick on the controller. These values are processed to output to various motor controllers in the form of PWM. The PWM signal is configured according to the bus clock of the microcontroller which is half the value of the system clock frequency. This MCU has a 2MHz bus clock frequency of which the inverse (period) results in a refresh rate of 5.0×10^{-7} seconds. This is too fast for certain applications, especially for the stepper motor driver. For this reason, a significantly lower frequency of 50Hz is chosen. In order to achieve this frequency, a few calculations are performed to slow the signal speed using prescaler values. Equation 5 shows the clock prescaler equation which assists in outputting a 50Hz PWM signal.

$$\text{Prescaled Clock} = \frac{(\text{Bus Clock})}{(\text{Prescaler}) \times (\text{PWMSCLB}) \times 2} \quad (5)$$

This equation leads to numerous calculations and iterations which help setup the MCU PWM register for a 50Hz output signal. Once the registers are setup, indicated by two consecutive tones from the console, the user is free to operate the crane.

Initially the system is in “Drive Mode” as seen in Figure 14. This allows the user to control the two drive wheels with the left and right joysticks. In this mode, the lifting abilities are disabled to prevent mishandling of the crate while in motion. For the operator to lift a payload crate using the clamp mechanism, the “Load Lift Mode” must be toggled by pressing down the two joysticks. This enables the operator to reel the line, clamp onto a crate, and lift or lower the boom. Meanwhile, the MCU continuously reads the gyroscope for angular velocity measurements. The MCU processes this information, continuously supplying a signal to the platform motor network to adjust the weight positions in an effort to stabilize the crate’s motion during transport.

5. CONCLUSION AND FUTURE WORK

Creating a scaled prototype of a real crane system has been a challenge in many ways. While the concept of transporting a load is fairly simple, there are solid engineering principles incorporated in every aspect of the design and assembly to bring the prototype to fruition. Issues concerning material selections seem to strain the progression of the build the most, mainly because it becomes difficult to find a strong material, within a given budget, and meet all the expected criteria. The idea of a steel-based crane seems fairly robust and heavy; however, it is not necessarily a sufficient counterweight to prevent the crane from tipping. This issue is resolved by using a different material which takes up less space but has a greater density and weighs more. Apart from the material selection, the concept of platform stability when a load is

being transported requires a further developed control system. While shifting a set of weights based on tilt sensing methods achieves platform stability, increasing the precision of the correction method would allow the system to stabilize faster. Developing a control system to stabilize the platform requires focusing on reducing the settling time of the stability mechanism. Adding a set of infrared sensors along the track of the weights would enhance the current gyroscope feedback information. By using position sensors, a specific position becomes attributed to the weight itself. Introducing this type of feedback for the weights crosschecks the gyroscope data, improving its accuracy. In experimenting with the current prototype, it is noticeable that the crate does not always sway to the left or right with equal displacement from the neutral position. This results in a weight distribution bias since the weight continues to move to one side of the platform, temporarily erring the stability feature. If the weight was too far to one side and kept sliding in that direction, a position sensor would notice the biased displacement of the weight. At this point, the system would monitor the gyroscope for further information. Depending on the angular velocity, the MCU could halt the motion of the weight temporarily or shift it to the opposite side of the platform to better improve the stability.

Regardless, there are many ways to improve this prototype design. However, creating this prototype has combined two powerful traits of two different crane systems. Focusing on the maneuverability of the reach-stacker crane and the reach of a truck-mounted crane and rope system, the prototype can successfully accomplish the following two tasks; remotely moving payloads from a ship to the dock and directly placing it in the cargo area or truck bed with the use of a single machine, which normally requires two machines with two crews of operators.

6. ACKNOWLEDGMENTS

This project was performed in the EML 4804 Mechatronics course and partially funded through the UNF School of Engineering. Other contributions were kindly made available by the Jacksonville Machine and Repair shop.

7. REFERENCES

- [1] Jacksonville Port Authority. *About JAXPORT*, Jacksonville Port Authority, April 2012, Internet: <http://www.jaxport.com/about-jaxport>
- [2] Linde Material Handling. *Reach Stackers from Linde Material Handling ensure speedy goods handling at Baltic harbours*, Linde Material Handling, Aschaffenburg, Germany, February 2008, Internet: http://www.linde-mh.com/en/main_page/company/company_1.jsp
- [3] Mouser Electronics Product Knowledge Center, *Texas Instruments MSP430 Ultra-Low Power Microcontrollers*, Mouser Electronics, Mansfield, TX, 2006, Internet: <http://www.mouser.com/timsp430/>
- [4] Axiom Manufacturing Inc, *NEW!! CSMB-12C128*, Axiom Manufacturing Inc, Richardson, TX, 2006, Internet: <http://www.axman.com/?q=node/325>
- [5] Pololu Robotics and Electronics, *LPR550AL Dual-Axis (Pitch and Roll or XY) Gyro with ±500°/s and ±2000°/s Ranges*, Pololu Corporation, Las Vegas, NV, July 2009, Internet: <http://www.pololu.com/catalog/product/1270>

Mobile Autonomous Robotic Sentry (MARS) with Facial Detection and Recognition

Tyler M. Lovelly
University of Florida, Dept. of
Electrical & Computer Engineering
12315 Clarendon Ct
Spring Hill, FL 34609
+1 727.808.4376
tyler727@ufl.edu

Dr. A. Antonio Arroyo
University of Florida
Machine Intelligence Lab (MIL)
338 MAE-B, UF
Gainesville, FL 32611
+1 352.392.2639
arroyo@mil.ufl.edu

Dr. Eric M. Schwartz
University of Florida
Machine Intelligence Lab (MIL)
321 MAE-B, UF
Gainesville, FL 32611
+1 352.392.2541
ems@mil.ufl.edu

ABSTRACT

This paper outlines the design and implementation of the Mobile Autonomous Robotic Sentry (MARS) unit with facial detection and recognition capabilities. MARS patrols its surrounding area, performing obstacle avoidance and searching for human threats using facial detection. Once a threat has been identified, MARS will aim at its target and fire projectiles. In addition to facial detection, MARS can be trained to recognize specific faces and identify them as threats or non-threats.

Keywords

Mobile, Autonomous, Robotic, Sentry, Facial Detection, Facial Recognition, Eigenface, Principle Component Analysis

1. INTRODUCTION

MARS was designed and built for the Intelligent Machines Design Laboratory (IMDL) at the University of Florida. It was developed using various custom and commercial parts, some modified to fit the needs of the design. MARS uses infrared (IR) proximity sensors and DC motors connected to wheels to perform driving and obstacle avoidance. An Internet Protocol (IP) network camera and wireless router allow MARS to continually send images to a nearby laptop computer where image processing can be performed to detect and recognize faces. The laptop sends information back to MARS via wireless RF modules. MARS will receive information about the location of its target and commands to fire, at which point it will turn towards its target if necessary and trigger firing of an automatic dart shooter. The design, layout, parts, and behaviors of MARS are outlined in the following sections.

2. INTEGRATED SYSTEM & PLATFORM

The control board used for MARS is the Epiphany DIY robotics board from Out of the Box, LLC, shown in Figure 1, which uses an Atmel ATxmega64A1 microcontroller.

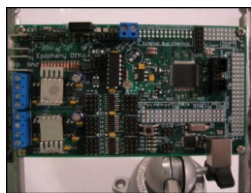


Figure 1. Epiphany DIY microcontroller board

The robot platform consists of two circular pieces of wood, approximately 30cm in diameter. These pieces are attached flat and parallel to each other, forming a two-piece platform onto which parts can be mounted. MARS is shown fully assembled in Figure 2.



Figure 2. Mobile Autonomous Robotic Sentry (MARS)

The parts and layout of the bottom piece of the platform are shown in Figure 3. The control board, which runs the C program that forms the basis of the robot's behavior, is mounted in the center. Three IR proximity sensors are mounted to the front of the platform, with the right and left sensors facing outwards to broaden the range which can be observed. Two DC motors are mounted to the upper sides of the platform, with a ball caster at the back for support. This allows for simple driving and turning movements. The main power supply is mounted behind the control board, and connected to a power routing board in order to simplify wiring and layout. Power is then routed thru an on/off switch and to the control board's power supply, motor drivers, and to the top platform. The control board also contains an Xbee wireless RF chip which allows for communication with a nearby laptop.

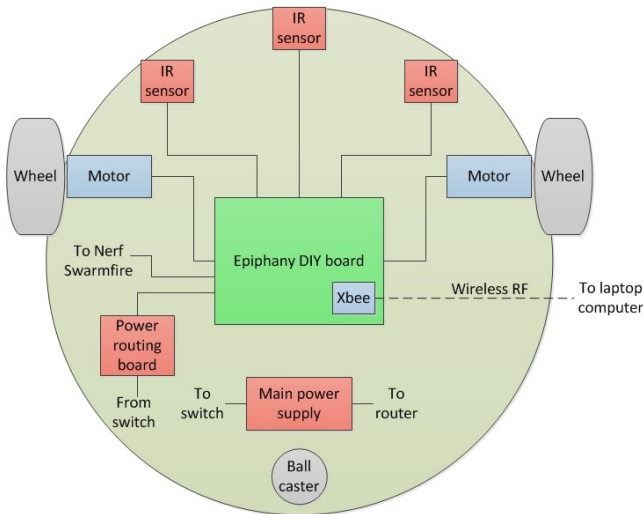


Figure 3. MARS platform bottom piece layout

The parts and layout of the top piece of the platform are shown in Figure 4. An IP camera is mounted front and center and tilted upward in order to maximize its field of view to include faces of people standing upright and several meters away. It uses its own power source and is connected via Ethernet to a wireless router which allows transmission of images to a nearby laptop computer. The router is powered by the main power supply on the platform below. A Nerf Swarmfire automatic dart shooter is mounted in the center facing forward and on an upward angle in order to best target any threats it must fire upon. The top platform also contains the on/off switch for the robot.

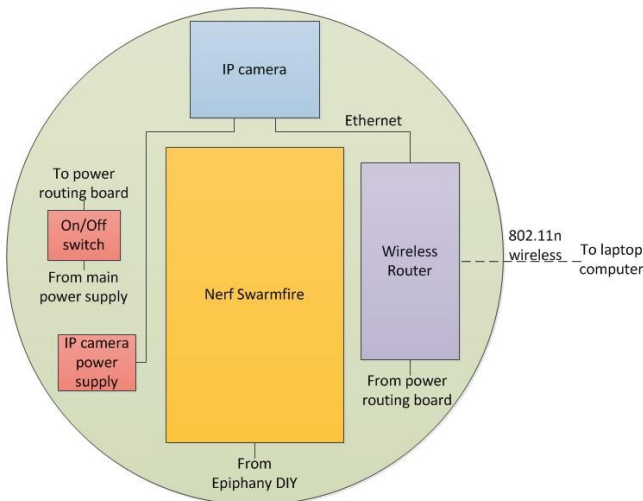


Figure 4. MARS platform top piece layout

A nearby laptop computer, which runs the C++ program used for image capturing and processing in order to detect and recognize faces, is shown in Figure 5. It captures images from MARS thru its connection with the wireless router and sends commands and targeting information back using an Xbee wireless RF chip, connected via an Xbee USB dongle.

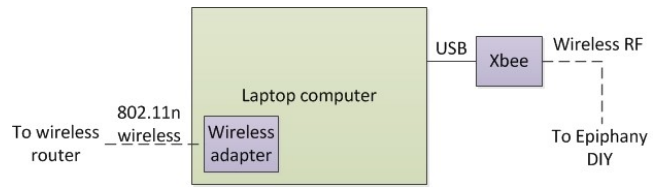


Figure 5. Laptop computer connectivity

The main power supply consists of eight rechargeable AA batteries, shown in Figure 6 with rechargeable battery packs, connected in series in an 8-AA battery holder. These were chosen because of adequate battery life and because their combined voltage suited power requirements for the control board, DC motors, wireless router, and Nerf Swarmfire. The battery holder is mounted to the platform using Velcro which allows easy removal and reattachment when recharging batteries.



Figure 6. ReVive Refresh Pro series AA smart chargers with truCELL 2700 series rechargeable AA batteries

3. DRIVING & OBSTACLE AVOIDANCE

MARS drives using two DC motors attached to wheels and mounted to the bottom piece of the robotic platform, with a ball caster at the back for support. The motors and metal mounting brackets are shown in Figure 7. Motors were selected based on relatively small current draw, adequate torque to support and move the weight of the robot, and appropriate RPM for driving speed requirements.

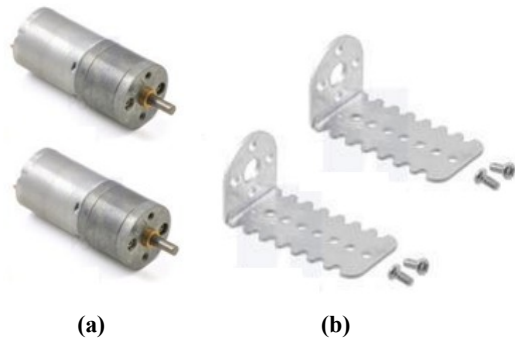


Figure 7. (a) 75:1 metal gearmotors, 75 RPM, 80mA free-run, 2.2A stall, 85 oz-in (6.1 kg-cm); (b) 25D mm metal gearmotor brackets

The wheels were chosen based on their size and ability to be mounted to the motors with mounting hubs, shown in Figure 8.



Figure 8. (a) 70x8mm wheels; (b) Universal Aluminum mounting hubs for 4mm shaft, 4-40 holes

The motors are connected to the motor drivers on the control board, where driving can easily be controlled using Pulse Width Modulation (PWM). Turning can be done by simply running one motor backwards. The longer one motor runs backwards, the farther MARS turns in its respective direction. Therefore, variable turning behavior can be accomplished.

Obstacle avoidance can be performed using the three IR proximity sensors mounted to the front of the bottom piece of the robotic platform. The IR sensors are attached to small pieces of wood which are mounted to the platform using Velcro, allowing the sensors to be easily adjusted to suit different driving environments. The sensors chosen, shown in Figure 9, were selected due to their appropriate range of detection for the robot's obstacle avoidance purposes.



Figure 9. Sharp GP2D120XJ00F IR proximity sensors, 3-30cm range

The IR sensors are connected to analogue-to-digital converters (ADCs) on the control board. While MARS is driving, it is constantly reading values from these sensors. If the reading shows an obstacle is in the way, there is a slight 50ms delay and the reading is checked again. This removes false positives due to random spikes in readings from the sensors.

Once an obstacle has been detected, MARS will turn to avoid it and continue driving. The direction and length of its turn are determined by the combination of readings from the three sensors, shown in Table 1. This gives MARS dynamic obstacle avoidance behavior in order to safely navigate and patrol its surroundings.

Table 1. Obstacle avoidance turning behavior

Left obstacle	Center obstacle	Right obstacle	Direction	Time (ms)	Rotation (°)
No	No	No	Forward	∞	0
Yes	X	Yes	Right	3500	180
X	Yes	No	Right	1750	90
No	Yes	Yes	Left	1750	90
No	No	Yes	Left	500	25
Yes	No	Yes	Right	500	25

4. IMAGE CAPTURING & PROCESSING

MARS captures images using an IP network camera, which is modified to be powered by four AAA batteries connected in series in a 4-AAA battery holder, mounted with Velcro for easy battery replacement. The IP camera is connected via Ethernet to a wireless router. The router is modified to be powered by the main power supply. The IP camera and wireless router are shown in Figure 10.



Figure 10. (a) Cisco-Linksys WVC80N IP camera; (b) Belkin N150 Wireless-N router

This allows images from the IP camera to be captured by any device which is on the same secured wireless network. A nearby laptop computer connected to the network continually captures images in order for facial detection and recognition to be performed.

The IP camera is configured to continually take low quality 320x240 MJPEG video at 4 frames per second. This setting is adequate for facial detection and recognition purposes and allows image frames to be captured from the video stream and processed at a steady rate with minimal lag. Due to a short initialization delay when first establishing the connection to the network video stream, the first 150 frames captured are not processed in order to remove any initial lag.

To prevent against false positives, a face must be detected in three consecutive frames in order to be valid. With facial recognition operating, only every third frame in which a face is detected is analyzed and compared to known faces in order to remove extra lag caused by facial recognition processing.

These configurations allow for an effective and rapid image capturing and processing system.

5. FACIAL DETECTION

The facial detection system uses the OpenCV library's cascade classifiers for facial and eye detection. These classifiers are trained and encoded with information about contrasts between regions in the image relating to features of the class being detected, in this case faces and eyes [1] [2].

When a frame is captured, it is first converted to grayscale and its histogram is equalized in order to normalize brightness and increase contrast in the image. A cascade classifier for faces is used to detect faces in the frame. A cascade classifier for eyes is then used with the segments of the images containing faces to detect eyes within faces.

Faces can be detected at both close up and far standing range in normal indoor lighting environments. It was found that detection of eyes was unreliable at far range and therefore only facial detection is used to determine robot behavior. Faces and eyes in

each frame are circled and displayed in real time, shown in Figure 11.

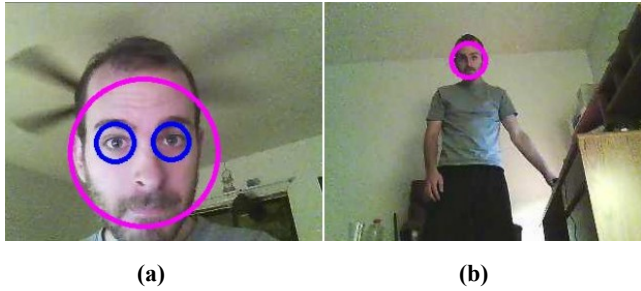


Figure 11. (a) Facial and eye detection at close range; (b) Facial detection at far standing range

6. FACIAL RECOGNITION

The facial recognition system is based on an OpenCV implementation of the eigenface technique, based on Principle Component Analysis (PCA) dimensionality reduction [3] [4].

In the eigenface technique for facial recognition, faces are projected in a PCA subspace that is more easily analyzed than the original image space due to reduction of dimensionality. Eigenvalues are generated which represent the “distance” between two faces in the PCA subspace. If this distance is below a certain threshold, the faces are said to match.

Offline training is used to process a large set of training images of a known person’s face. It is best to use training images taken from varying ranges and lighting conditions and to take a large sample from the same lighting environment in which MARS will be operating. Several examples are shown in Figure 12. The PCA subspace information for each of the training faces is stored in an XML file to be referenced later.



Figure 12. Training faces in 40x40 format, taken from varying ranges and lighting conditions

When a face is detected in a frame, the segment of the image that contains the face is resized to 40x40 and saved. This resizing has several advantages. It causes image segments from faces detected at varying ranges to scale in size and quality, allows the eigenface algorithm to work with consistently sized images, and reduces processing time and image dimensionality by working with a small image size.

Once the resized face image segment is saved, the eigenface algorithm tries to recognize the face by comparing it to all known faces saved during training. An eigenvalue is returned which represents the “distance” between the face and the known face for which it matches best. If this value is below a certain threshold, the faces are considered a match and the person has been recognized.

MARS can classify known faces as threats or non-threats and use this information to determine firing behavior.

7. TARGETING & FIRING

The laptop computer sends commands to fire back to MARS via Xbee wireless RF modules, shown in Figure 13.

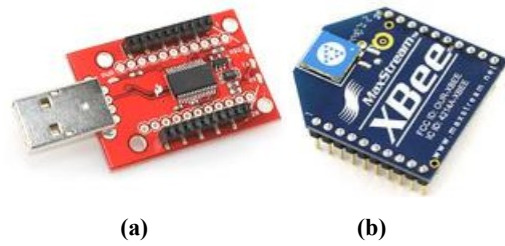


Figure 13. (a) Xbee Explorer USB dongle; (b) Xbee wireless RF chip

A minimum delay of 10 seconds is required between sending commands in order to prevent MARS from going into a constant firing loop while operating in large crowds.

When a face is detected, its horizontal location in the frame is used to determine the location of the threat for targeting purposes. This information is sent back to MARS along with the firing command. When MARS is told that its target is on the left or right side of its field of view, it will turn in the correct direction to aim at its target before firing.

MARS fires foam darts at its targets with a Nerf Swarmfire dart shooter, shown in Figure 14. This dart shooter was chosen due to its automatic firing mechanism and its ability to hold up to 20 darts.



Figure 14. Nerf Swarmfire dart shooter

The dart shooter is modified in order to reduce size and weight. The entire back segment is removed and much of the casing is stripped. This also allows access to the internal electronics, which is necessary in order to interface it with the control board.

The automatic firing mechanism of the dart shooter is operated by a DC motor which rotates the barrel and activates a spring plunger to fire darts. The trigger and safety simply switch power to this motor to trigger firing. These switches are removed and the motor is connected directly to a motor driver on the control board, powered by the main power supply. This gives MARS the ability to start and stop automatic firing as needed.

8. CONCLUSION

MARS accomplishes all of its original design goals, producing a mobile autonomous sentry unit with facial detection and recognition capabilities.

MARS provides a proof of concept for any mobile autonomous machine that has behaviors based on image processing, in particular facial detection and recognition. This can expand beyond sentry units to functions ranging from criminal identification to search and rescue.

Future development of MARS will focus on several key areas. Range of obstacle detection sensors should be improved and more

sophisticated driving behavior developed, incorporating fuzzy logic to produce smooth navigation and turning. A permanent light source should be mounted to MARS, providing consistent light towards its field of view in order to more reliably detect and recognize faces in varying lighting environments. Accuracy of targeting behavior should be increased by mapping threat locations in image frames into more detailed targeting commands.

More information about MARS, including source code, can be found online [5].

9. ACKNOWLEDGMENTS

My thanks to Dr. Arroyo and Dr. Schwartz for offering students an exciting and interactive learning environment.

10. REFERENCES

- [1] *Face Detection using OpenCV*, OpenCV Wiki, Aug. 25, 2011, opencv.willowgarage.com/wiki/FaceDetection
- [2] *Cascade Classifier*, OpenCV 2.4.0 documentation, opencv.itseez.com/doc/tutorials/objdetect/cascade_classifier/cascade_classifier.html
- [3] Hewitt, R., *Seeing With OpenCV – A Five Part Series*, SERVO Magazine, Jan. - May 2007, T & L Publications, Inc, www.cognotics.com/opencv/servo_2007_series/
- [4] *Simple face recognition using OpenCV*, The Pebibyte, Jan. 21, 2011, pebibyte.wordpress.com/2011/01/21/simple-face-recognition-using-opencv/
- [5] *Mobile Autonomous Robotic Sentry (MARS)*, plaza.ufl.edu/tyler727/imdl/

Survey of Rechargeable Batteries for Robotic Applications

Melissa Morris and Sabri Tosunoglu

Florida International University
Department of Mechanical and Materials Engineering
Miami, Florida, USA
305-348-6841, 305-348-1091
morrism2@asme.org, tosun@fiu.edu

ABSTRACT

Electronic devices require increasing amounts of power as processors and sensors improve. Unfortunately, battery capacities are increasing at a much slower rate. This is especially an issue in mobile robotics where there is not only an assortment of sensors and processors, but also higher-current actuators that demand a significant amount of power. The required battery weight and size is a bottleneck when attempting to achieve miniaturization or longer operational range. Traditional commercial batteries can quickly become depleted, thus severely limiting the functionality of mobile robots. This paper will explore common commercial as well as several investigational rechargeable battery types. Each battery type will be evaluated for use in robotic applications in order to provide some insight into current and emerging choices for various applications.

Keywords

Robotics, Power, Rechargeable Battery, Mobile Robots.

INTRODUCTION

Batteries are devices that convert chemical energy to electrical energy. This allows for both energy storage as well as a direct method of producing of direct current (DC) electricity. The electrical energy is created through an electrochemical oxidation reduction (redox) reaction within the battery [1]. When connected to a load, batteries will produce electrical energy until the reactants are depleted. Batteries can be classified into four groups:

1. *Primary Cells*: These can be discharged only once and are then discarded or recycled after this single use. Primary batteries are commonly used in consumer electronics such as cameras and toys.
2. *Secondary Cells*: These can be easily recharged. Secondary batteries be used as back-up or temporary augmentation for another power source, such as in vehicles or laptop computers. They can also be used as the sole energy source instead of primary cells in order to reduce waste or to avoid physically changing the battery when depleted. In addition to replacement of primary cells in many applications, these batteries are commonly the primary energy source for cell phones and tablet computers.
3. *Reserve Batteries*: Unlike the “active” batteries above, these have one component, such as the electrolyte, separated to avoid chemical deterioration. These

batteries can be stored for long periods and then activated as needed. These are typically seen in weapon systems.

4. *Fuel Cells*: These are considered a battery by some sources (such as [1]) but not by others (such as [2]). Either way, they differ in that a fuel cell is supplied fuel from outside of the reaction chamber and will continue to function as long as fuel is supplied. They do however function through a redox reaction like batteries and unlike most capacitors [3].

The rest of this report will focus primarily on secondary cells, as these are the most useful for robotic applications. Secondary cells (also referred to as rechargeable batteries) can be used both for augmentation or emergency loads and as the main source of power in robotic applications.

All batteries consist of a positive electrode (anode), a negative electrode (cathode) and an ionic conductor (electrolyte). Many cells also have a separator that physically keeps the electrodes from shorting, but allows ions to flow [3]. Most batteries can be classified as a wet cell, when the electrolyte is liquid, or a dry cell if the electrolyte is a gel or solid. These components together form a cell. Multiple cells may be stacked together and packaged to form a battery [4], though this term is also commonly used when referring to a single cell packaged for consumer use [1].

Batteries function by converting ionic transfer into electron transfer. When a battery is discharged through a load, negative ions (anions) flow through the electrolyte to the anode. Here, electrons become loose through the oxidation of the anode. The electrons then flow through the load and back to the cathode. The cathode experiences a reduction reaction as the electrons are gained and positive ions (cations) flow to the cathode through the electrolyte [1]. Charging of the cell involves simply reversing this process by connecting a power source instead of the load. This power source must be DC in order to be compatible and leave a net charge within the cell. These processes are depicted in Figure 1.

BATTERY TYPES

There are many types of batteries. The section will focus only on secondary or rechargeable batteries since these are of interest in robotics both for environmental reasons and for ease of repowering the system. Plugging in a robot can be made autonomous with minimal trouble while changing battery packs involves more power usage and eventual human involvement unless the depleted batteries are recharged upon swap [5].

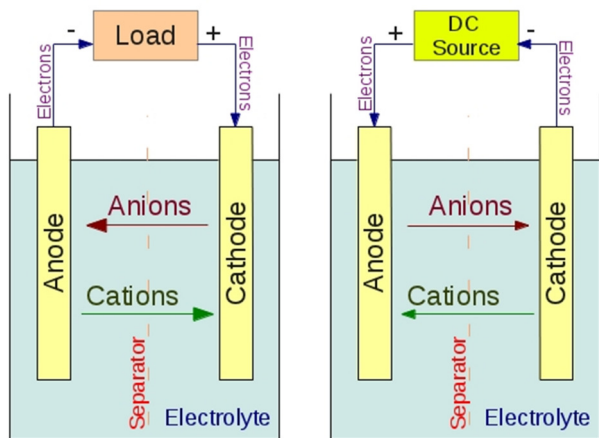


Figure 1: Battery discharging (left) and charging (right)

Lead-Acid Batteries

The lead-acid battery was developed by Raymond Louis Gaston Planté in 1860 [6]. This became the basis of the first type of usable rechargeable battery. Despite other forms of rechargeable batteries, the lead-acid battery is still very common in a wide range of applications [7].

Lead-acid batteries are either flooded or valve-regulated [8]. Flooded lead-acid batteries are composed of lead plates serving as electrodes that are immersed in water and sulphuric acid. These batteries require some maintenance due to the loss of hydrogen over time. Valve-regulated lead-acid batteries, on the other hand, are sealed and have a pressure-regulating valve to keep air from getting into the cells. However, sealed lead-acid batteries are more expensive and have a shorter life than flooded batteries [8]. These batteries can have a liquid or gel electrolyte.

Full power can be delivered by this type of battery extremely quickly. This makes them ideal for uses where a large amount of power may suddenly be needed – which is why they are used for electrically starting internal combustion engines in most vehicles.

The cost of lead-acid batteries is the lowest of all rechargeable battery types for the amount of power delivered. Problems with these batteries include sensitivities to temperature that affect both the life of the battery and cycle life [8]. The depth of discharge of lead acid batteries can vary from around 20% for 'starting' batteries to 80% for 'deep cycle' batteries. They have an open circuit voltage of up to 2.1 V [9]. Both power and energy of a lead-acid battery is increased by increasing the surface area of the electrode. These batteries are candidates for large and medium-scale robots, but their short cycle life may outweigh their low cost when used constantly [4].

The battery shape and size is usually dictated and cubic, but some types of lead acid batteries can have more customized shapes. They also have a rapid self-discharge rate of 3-20% per month [4], making them unsuitable for applications where a robot may sit for lengths of time before use.

Table 1: Properties of a Lead-Acid Battery

Specific energy	35-50 Wh/kg [10] [9]
Specific power	150-400 W/kg [10]
Cell voltage	2.1 V [1]
Cycles	250-1,000 [8]; 2000+ [7]
Life	5 years [8]
Efficiency	75-85% [8]
Max depth of discharge	20-80% [1]
Self-discharge rate	2-8%/month, some 20-30%/month [1]

Alkaline Batteries

Rechargeable alkaline batteries come in several types. The first type has a nickel oxide cation electrode and an iron anode and are commonly referred to as nickel-iron batteries. The second type also has a nickel oxide cation electrode, but the anode is composed of cadmium so that these batteries are commonly called nickel-cadmium (NiCd or NiCad) batteries [10]. More recently, nickel-hydrogen and the commercially successful nickel-metal-hydride (NiMH) batteries have found favor for many applications.

Thomas Edison developed a useful version of a nickel-iron battery in 1901 [11]. Nickel-iron batteries have double the specific energy of lead-acid cells, are rugged, have a long life cycle at deep discharges (80% depth of discharge) and can handle fairly high discharge rates [10], [12]. However, they do not perform as well as lead-acid batteries at low temperatures and they can be damaged by high temperatures [4]. In addition, nickel-iron cells have a relatively high self-discharge rate due to high corrosion and gassing on the leads causing poor efficiency [10]. These batteries are therefore not widely used anymore, though they used to be preferred for large vehicles due to their robustness [11]. Some research is being done on this type of battery to make them maintenance-free, provide better performance, and be more attractive through the use of a starved-electrolyte and sealed package [12].

Table 2: Properties of a Nickel-Iron Alkaline Battery

Specific energy	50-60 Wh/kg [10]
Specific power	80-150 W/kg [10]
Cell voltage	1.5 V [10]
Cycles	2,000 [11]
Life	20 years [12]
Max depth of discharge	80% [11]
Self-discharge rate	20-40%/month [1]

Unlike nickel-iron batteries, nickel-cadmium batteries are widely used and still widely researched. They were invented by Waldemar Jungner in 1899 [11]. NiCd batteries have a lower specific energy than nickel-iron, but otherwise perform better and do not suffer from the other problems of nickel-iron cells. In addition, they have a constant discharge voltage, can be continuously overcharged (especially if vented), and are very reliable [10]. They can also be made into many shapes and sizes through different manufacturing techniques [10]. They are acceptable for use in high-temperature applications [8]. These are not used more often because they cost ten times as a lead-acid battery and because of environmental concerns when disposing of cadmium [10]. They also have memory effects which cause gradual reduction in capacity if they are not fully discharged and charged during every cycle [8]. Like lead-acid batteries, NiCd batteries are available vented or sealed [8]. Vented batteries allow oxygen and hydrogen gases to be released in the case of overcharging or rapid discharging in order to make the battery safer and less expensive [8]. However, sealed batteries can be used in any orientation [10].

Table 3: Properties of a Nickel-Cadmium Alkaline Battery

Specific energy	30-60 Wh/kg [10] [11]
Specific power	80-150 W/kg [10]
Cell voltage	1.2 V [10]
Cycles	1,000 to 50,000 [8]
Life	10-15 years [8]
Efficiency	60-70% [8]
Max depth of discharge	60-80% [1]
Self-discharge rate	5-15%/month [1]

Nickel-hydrogen batteries were designed as a replacement for nickel-cadmium batteries. However, due to the high cost of obtaining and storing the hydrogen, these batteries are only used in space applications. They are of interest because they have a very high specific energy (50 Wh/kg) and very long life cycle even under deep discharging [10]. They are also not susceptible to cadmium whisker development, which has caused numerous system failures in government systems including ones in space [13]. They are also tolerant to overcharging and reversal [1].

Table 4: Properties of a Nickel-Hydrogen Alkaline Battery

Specific energy	50 Wh/kg [10]
Cell voltage	1.4 V [1]
Cycles	1500-6000 [1]
Life	15 years [1]
Self-discharge rate	Very high except at low temperatures [1]

To overcome the cost and storage problems with hydrogen, nickel-metal-hydride cells were developed. They are in some ways similar to nickel-cadmium batteries, but they have some additional advantageous such as more power. Hydrides store hydrogen within their physical structure. These can later be extracted for use in the battery. A common hydride is an alloy based on nickel, aluminum, and rare earth metals though there is another based on titanium and zirconium [11]. NiMH cells show the most promise for an aqueous electrolyte cell [14] [15].

Table 5: Properties of a Nickel-Metal Hydride Alkaline Battery

Specific energy	60-80 Wh/kg [10]
Specific power	200-300 W/kg [10]
Cell voltage	1.2 V [10]
Cycles	300-600 [1]
Life	2-5 years [1]
Self-discharge rate	15-25%/month [1]

Nickel-zinc is another type of rechargeable battery under investigation. Though it outperforms both lead-acid as well as the other alkaline batteries in many ways, it is not in production due to the solubility of zinc in potassium hydroxide [11]. It simply can not sustain enough cycles for commercial success.

Table 6: Properties of a Nickel-Zinc Alkaline Battery

Specific energy	70 -100 Wh/kg [10] [11]
Specific power	170-260 W/kg [10]
Cell voltage	1.6 V [11]
Cycles	up to 500 [11]
Life	Currently unknown [1]
Max depth of discharge	100% [1]
Self-discharge rate	<20%/month [1]

Nickel-iron and nickel-hydrogen cells have an open circuit voltage of about 1.5 V when fully charged [10]. NiCd and NiMH on the other hand have an open circuit voltage of about 1.2 to 1.3 V, though this stays relatively constant through most of the discharge [10]. This means that most commercially used alkaline rechargeable batteries have voltages less than the primary alkaline counterparts. For this reason, more batteries may be needed in series if a rechargeable alkaline replaces a primary alkaline in any application. Nickel-zinc would be an excellent substitute with an open circuit voltage of 1.6 V [11].

All alkaline-based batteries are sensitive to temperature. They typically perform best in the range of -20 to 40 °C. Another

feature of the alkaline batteries is that using the batteries at a lower depth of discharge leads to increased cycle life.

There are other alkaline-electrolyte batteries, such as silver oxides. These include silver-zinc batteries and silver-cadmium batteries [1]. Though their high energy density is attractive, they are very expensive and have short life cycles so that they are not currently of interest for robotics. There is also the zinc-alkaline-manganese dioxide battery. This battery proved to have a short cycle life and be difficult to recharge, so these are also not of current interest [1].

Lithium Batteries

Lithium is attractive because it is the lightest metal, and thus produces lighter batteries. It also has a high specific capacity and specific energy [10]. Lithium is not used with an aqueous electrolyte to avoid undesired chemical reactions [10]. Lithium in metal form is not used in rechargeable batteries because it forms dendrites that tear through the separator and cause the electrodes to short [10]. Instead, rechargeable lithium batteries use lithium ions spread within a carbon anode (when charged) or oxide cathode (when discharged) [10]. This technology holds a lot of promise, but does not completely replace alkaline batteries due to its higher cost.

The lithium-ion cell was invented in 1979 and provided an open circuit voltage of up to 4 V [16]. Using lithium as an ion rather than a metal solved the recharging problems of dendrite growth. Still, the battery does not do well if overcharged or heated and can lose capacity if either of these events occur [10]. Advantages include a relatively low self-discharge rate, no memory effect, and high energy [4]. Reducing the depth of discharge increases the cycle life of the batter. For example, at 100% depth of discharge (DOD), 3,000 cycles are expected while at 40% DOD over 20,000 cycles are possible [1]. Due to cost and safety considerations, lithium-ion technology is used primarily for small consumer electronics [17] and has only slowly and recently been debuting in vehicles and other high-power applications [18]. Even in consumer electronics, the use of this battery technology is sometimes limited by the high cell voltage, which is more than double the typical alkaline primary cell voltage [19].

Table 7: Properties of a Lithium-Ion Battery

Specific energy	80-180 Wh/kg [10]
Peak power	200-1000 W/kg [10]
Cell voltage	3.05 V [10]; 4.2V [1]
Cycles	3,000 [1]
Life	5+ years [1]
Max depth of discharge	100% [1]
Self-discharge rate	2-10%/month [1]

Since lithium-ion batteries are expensive due to the use of cobalt and nickel, other options are being considered. The use of manganese is being investigated, but so far it is not proving to be

extremely stable [10]. Loss of charge capacity and chemical issues were reported in early work [20]. More recent work is showing improvements, but mostly at room temperature since performance quickly decreases as the temperature increases [18]. In addition, research is being done on other altered chemistries such as using aluminum-silicon-graphite anodes in place of carbon for increased safety and energy density [21]. This study showed that silicon was useful in improving the energy capacity with some reduction in cell degradation caused by the battery reacting by itself.

Lithium-sulfur was heralded as the next trend in batteries both for energy density and safety [20], however it did require a control circuit and does not seem to have advanced as quickly as hoped. Recently there were still reports of trouble in achieving the expected power, maintaining the charge, and maintaining chemical stability [22]. Work was done on the electrolyte [23] as well as adding a coating to the electrodes [24], but the capacity decreased with time. The later paper did show that carbon was helpful in slowing the reaction, however. More recent work suggests that wrapping the cathodes in graphene has proven effective in slowing or even stopping the loss of capacity [25].

The use of nanostructures is also a trend in the research of lithium-ion technology. One paper describes work using nanospheres of titanium-dioxide-carbon to produce a lithium-ion cell of only 1.5 V [19]. This would allow lithium-ion rechargeable batteries to be used in nearly all consumer electronics. It also provides a rechargeable option superior in voltage and possibly energy density than both NiCd and NiMH technology. Nanocomposite spheres of sulfur-carbon are being investigated to improve lithium-sulfur technology mentioned above in an by optimizing surface area contact [26]. These spheres could also be used to buffer internal mechanical strains and improve cycle life against this type of failure [27]. Silicon nanowires, not spheres, are suggested as the best way to incorporate silicon in a lithium-sulfur cell by another group of researchers [28].

Other lithium-ion technology utilizes iron-phosphate. Early work didn't report huge success. In fact, the carbon seemed to have a negative effect [29]. However, a more recent paper describes the manufacture of a foam that becomes a three-dimensional substrate for this battery technology [30]. The use of this foam and a copper-tin anode showed significant stabilization of the lithium-sulfur cell.

Lithium polymer batteries hold some promise as well. These work acceptably if the polymer is thin enough and the cell is made large enough to account for the limited current density [10]. The polymer acts as a solid electrolyte when it is embedded with liquid electrolyte [9]. It allows for almost solid-electrolyte performance while maintaining the cell at room temperature [31]. Electroactive polymers such as Nafion can be used with a lithium compound to create a rechargeable battery. An early one was reported in literature, but it suffered severely from self-discharge as does other similar technology [32]. Metals other than lithium can be used as well, but even after investigating numerous substances, it seemed to be favored for investigation despite the self-discharge and cell degradation drawbacks [33].

Sodium Batteries

Sodium batteries are of interest because of a low mass, non-toxicity, low-cost and abundance of sodium [10]. These batteries have a potential for high specific energy. They are also capable of explosion, so care in their use must be taken such as not using an aqueous electrolyte [10]. Because of their size and high operational temperatures, they are not suited for on-board mobile robotic applications. However, a brief overview is included for completeness and because they have interesting features and properties when used as back-up power or for a stationary supply.

One of the most promising sodium batteries is the sodium-sulfur (NaS) battery. It has a very high energy density, a long life, low maintenance, and high efficiency [34] [35]. The electrolyte must be kept above 270°C, however, which can take energy and create thermal management issues [34].

Table 8: Properties of a Sodium-Sulfur Battery

Specific energy	150-240 Wh/kg [10]
Specific power	230 W/kg [10]
Cell voltage	2.71 V [10]
Cycles	2,500 to 40,000 [8]
Efficiency	86-89% [8]
Max depth of discharge	100% [8]
Operating temperature	270°C [8]

Another type is a sodium-nickel-chloride battery. It was developed in Africa and was dubbed the ZEBRA battery [10]. It is able to operate at slightly lower temperatures than the NaS battery, but still quite high at 175 to 400 °C. The battery is cell-failure tolerant, which makes it more robust. This is a beneficial feature to make this battery feasible since the electrolyte is ceramic and may be prone to cracking [36]. This battery type is being proposed for electric vehicle use, but no actual tests were found.

Table 9: Properties of a ZEBRA Battery

Specific energy	90-120 Wh/kg [10]
Specific power	130-160 W/kg [10]
Cell voltage	2.58 V [10]
Operating temperature	175-400 °C [10]

Flow Batteries

Flow batteries can also be considered as a type of fuel cell or a battery-fuel cell hybrid [10]. Though they run on an external fuel source, they are charged and discharged like a battery. They are described below for completeness, but like sodium batteries, they are not currently of much interest for on-board power for mobile robotics.

Vanadium Redox flow batteries are the most common flow batteries found in literature. These are composed of vanadium ions in sulphuric acid. A pump controls the flow from each of two tanks – one with the positive vanadium ion electrolyte and another from the negative vanadium ion electrolyte. Vanadium redox flow batteries offer a fast response and high overload capacity. They can also be fully discharged without decreasing the life of the battery. These batteries have low power densities, but are not suited for small-scale energy [8]. Therefore, their use in robotics would be restricted to large-scale power applications or back-up power. There are working batteries of this type in use. As with other battery technology, some improvement is achievable with respect to capacity losses, though the battery does well at producing electrical energy [37].

Table 10: Properties of a Vanadium Redox Flow Battery

Specific energy	20-30 Wh/kg [10]
Specific power	100 W/kg [10]
Cell voltage	1.2 V [8]
Cycles	10,000 [8]
Life	7-15 years (estimated) [8]
Efficiency	85% [8]
Max depth of discharge	100% [8]

Another popular flow battery in literature is the zinc-bromine (ZnBr) flow battery. This battery is basically a fuel cell with bromine stored in an external tank within the battery [10]. It works much like the flow battery above. Like the vanadium battery, the ZnBr battery can be fully discharged without a reduction to the life of the battery. It also does not have any memory effect and has a large energy density [8]. This battery can be made smaller than a vanadium battery, but it is still only suitable for larger-scale mobile robotics. It was successfully tested in a Chrysler vehicle, but there were concerns about safety and system complexity [38].

Table 11: Properties of a Zinc-Bromine Flow Battery

Specific energy	65-85 Wh/kg [10]
Specific power	90-110 W/kg [10]
Cell voltage	1.8 V [8]
Cycles	2,000 [8]
Efficiency	75-80% [8]
Max depth of discharge	100% [8]

A third type of flow battery that will be explored is the polysulphide-bromide (PSB) flow battery. This battery has an

open circuit voltage of 1.5 V. It has a wider range of operating temperatures as well [8].

Table 12: Properties of a PSB Flow Battery

Cell voltage	1.5 V [8]
Cycles	2,000 (estimated) [8]
Efficiency	75% [8] [39]
Operating temperature	20-40°C [8]

A newer type of flow battery is an alkaline single flow zinc-oxide battery. This battery depends upon composite electrodes with nanostructures. This battery is not fully functional as of the last reported research [40]. Another battery is the single zinc-nickel battery [41]. This particular configuration shows a lot of chemical instability and so isn't at all promising in its current state.

Other Batteries

Some batteries do not fit into any of the categories above. One class of batteries is metal-air batteries. These are of interest because they are not expensive and are environmentally friendly, but recharging is difficult [39]. A specific example is the zinc-air battery. A rechargeable version was developed that uses mechanical charging rather than electrical. In this process, the battery is disassembled and rebuilt. Recharging can therefore occur in a few minutes, but involves some technical ability [10]. These cells have high specific energy, but relatively low specific power.

Table 13: Properties of a Zinc-Air Battery

Specific energy	200 Wh/kg [10]
Specific power	100 W/kg at 80% discharge [10]
Cell voltage	1.6 V [1]
Cycles	300 [39]
Efficiency	50% [39]

Another metal-air battery is the aluminum-air battery. It has an theoretical voltage of 2.7 V and an very high energy density (8.1 kWh/kg for the metal) [1;42]. The authors making the theoretical calculations determine that this type of battery can provide the same range in an electric vehicle as cars get with internal combustion engines. Like the zinc-air battery, cost for materials is relatively low making this an interesting area for research. Iron-air is another battery type with a cell voltage of 1.3 V, but this one does not hold much favor as iron tends to rust in this environment and stability is an issue [1]. Other possible metals include lithium (3.4 V), cadmium (3.4 V), and Magnesium (3.1 V).

Although a fuel cell is technically not the same as a rechargeable battery, some brief comments will be noted here since recent

research shows some promising developments for robotics. Most current fuel cells must be kept in an upright position and are also rather large when considering the fuel cell, fuel tanks and control system. This is to maintain the proper pressures of fuel and water being pumped throughout. However, miniaturizing the fuel cell allows passive flow systems such as capillary action to control the fuel cell and it can be used in any orientation [43]. These tiny fuel cells expand the use of fuel cells to smaller robotics including MEMS technology.

Though not a battery, ultra capacitors can sometimes be beneficial when used in conjunction with batteries. Ultra capacitors function like other capacitors with charges stored on two parallel plates. They have a very long life cycle, high efficiency and a high power density (they can quickly respond to supply energy as well as quickly recharge). The problem is that they have a lower energy density than batteries and so they can not provide as much power for a given size [44]. They can be very useful in providing additional power during short bursts for for low power applications. They have been proven for use in powering robots during battery hot-swapping as well [5].

DISCUSSION

Rechargeable battery selection in general depends upon several factors. These include mechanical and chemical stability, storage capability, operation temperature, self-discharge rate, discharge curve features, cost, safety, recharge capability, cycle life, charge time and overcharge/overdischarge protection [3]. Within these considerations are factors such as the maximum voltage, maximum current, running time, charging time, and depth of discharge. Some battery properties are interrelated. For instance, increasing the depth of discharge (the amount the battery is drained of power) will decrease the number of cycles that most batteries can last [8].

If a battery is to be used on a mobile robotic platform, the size and weight are critical factors to consider. The battery is typically the limiting factor in size reduction of robotic systems. In addition, the weight of the battery often adds a significant weight to the system and thus increases power usage. Larger or medium-sized robots may do best with lead-acid batteries because of their lower cost and wide availability. However, smaller robots cannot operate under such a heavy load and would benefit from an alkaline battery. A lithium-ion battery provides even more power at a reduced weight for even smaller devices; however, it has at a larger cost.

If the application will be upgrading or swapping with primary batteries or cells, then battery voltage becomes an issue. Since commercially available secondary alkaline cells have significantly lower voltages than their primary cell counterparts, modified lithium-ion batteries or other emerging technology will best serve this need. Otherwise, provisions need to be made for including extra cells in series and parallel to obtain the desired voltage and current.

Many ground-based mobile robots may expect to remain in an upright position, but other ground-based systems as well as nearly all aerial and underwater robots do change their orientation. These robots require batteries that work in all orientations. Therefore, they may not be able to utilize most vented batteries, fuel cells and flow batteries. Sealed batteries are the best choice

here, but come at a higher cost and shorter life cycle than similar vented batteries.

One of the biggest advantages of both NiCd and lithium-ion batteries for smaller robots is that the battery shape can be adjusted when manufactured. This allows the battery to best fit the available space or desired area to maintain a good center of gravity. These batteries, particularly, lithium-ion also allow for multiple material options to best operate in a variety of locations including underwater [45].

As with any component of a robot system, factors such as availability, assembly and manufacturability, aesthetics, integration, and support infrastructure (for electrical charging and disposal/replacement procedures) are all important considerations as well. In addition to traditional manufacturing and economic considerations, the environmental and global impacts are also important considerations. For instance, if a robot needs to be RoHS compliant, then lead-acid batteries are not a suitable choice. Studies have been done investigating the environmental impact and recycle-ability of various battery types. One study in Europe [46] found that salt-based batteries tend to have the least amount of impact, however their size and temperature requirements do not work well with most (if not all) mobile robotic platforms. Lithium-ion technology is therefore the most promising battery for environmentally-conscious projects. This is especially true for smaller robots that need a customized battery shape to fit within the platform. Lead-acid, nickel-cadmium and nickel-metal-hydride all have a more significant environmental impact. Since not all countries have battery recycling infrastructure set-up for all battery types [47], this can mean lots of contaminants end up in landfill and thus water and food supplies. Still, recent work has improved the recycle-ability of lead-acid batteries by recovering more lead and sulphates [48]. In addition, investigations were performed in China [49] and India [50] to develop a method of recovering cadmium and other heavy metals from batteries. Advances such as this can equalize this aspect of battery selection.

Finally, it should be noted that optimizing control and operation planning can increase the performance of a robot without upgrading the battery technology. Mobile charging stations is one option. One interesting proposal even suggests the possibility of having a mobile robot change batteries in other mobile robots [51], but of course the additional robot may add additional energy costs in addition to complexity.

CONCLUSION

This paper has reviewed the major types of rechargeable batteries available. In addition, many investigational batteries were discussed. For the most part, battery selection involves a trade-up between cost, power and size. However, advances are making this technology more diverse and robust, so it can be expected that more choices will be available as work progresses. This may allow for batteries to be better suited for mobile robots.

REFERENCES

[1] Linden D. and Reddy T.B., *Handbook of Batteries*, McGraw-Hill, 2001.
[2] Hodge B.K., *Alternative Energy Systems and Applications*, Wiley, 2010.

[3] Winter M. and Brodd R.J., What Are Batteries, Fuel Cells, and Supercapacitors?, *Chemical Review*, **104**, pp. 4245-4269, 2004.
[4] Singamsetti N. and Tosunoglu S., A Review of Rechargeable Battery Technologies, *16th World Multi-Conference on Systemics, Cybernetics and Informatics*, July 17-20, 2012.
[5] Bonani M., Longchamp V., Magnenat S., Retornaz P., Burnier D., Roulet G., Vaussard F., Bleuler H. and Mondada F., The MarXbot, a Miniature Mobile Robot Opening New Perspectives for the Collective-robotic Research, *IEEE/RSJ International Conference on Intelligent Robots and Systems*, October, 2010.
[6] Kurzweil P., Gaston Plante and His Invention of the Lead-Acid Battery - The genesis of the first practical rechargeable battery, *Journal of Power Sources*, **195**, pp. 4424-4434, 2010.
[7] Takehara Z., On the Reaction in the Lead-Acid Battery (as a special review-article by the 2005' Gaston Plante Medal recipient), *Journal of Power Sources*, **156**, pp. 825-830, 2006.
[8] Connolly D., *A Review of Energy Storage Technologies*, University of Limerick, 2009.
[9] Palacin M.R., Recent Advances in Rechargeable Battery Materials: a chemist's perspective, *Chemical Society Reviews*, **38**, pp. 2565-2575, 2009.
[10] Dell R.M., Batteries: fifty years of materials development, *Solid State Ionics*, **134**, pp. 139-158, 2000.
[11] Sequeira C.A.C. and Pedro M.R., Battery Storage, *Ciencia & Tecnologia dos Materiais*, **20**, pp. 21-30, 2008.
[12] Hariprakash B., Martha S.K., Hedge M.S. and Shukla A.K., A Sealed, Starved-Electrolyte Nickel-Iron Battery, *Journal of Applied Electrochemistry*, **35**, pp. 27-32, 2005.
[13] Cyganowski A., Brusse J. and Leidecker H., *Nickel Cadmium Batteries: a medium for the study of metal whiskers and dendrites*, Notre Dame Preparatory School and NASA Goddard, 2006.
[14] Beck F. and Ruetschi P., Rechargeable Batteries With Aqueous Electrolytes, *Electrochimica Acta*, **45**, pp. 2467-2482, 2000.
[15] Ruetschi P., Meli F. and Desilvestro J., Nickel-metal Hydride Batteries. The Preferred Batteries of the Future?, *Journal of Power Sources*, **57**, pp. 85-91, 1995.
[16] Scrosati B., Recent Advances in Lithium Ion Battery Materials, *Electrochimica Acta*, **45**, pp. 2461-2466, 2000.
[17] Ritchie A. and Howard W., Recent Developments and Likely Advances in Lithium-Ion Batteries, *Journal of Power Sources*, **162**, pp. 809-812, 2006.
[18] Sun H., Chen Y., Xu C., Zhu D. and Huang L., Electrochemical Performance of Rare-Earth Doped LiMn2O4 Spinel Cathode Materials for Li-Ion Rechargeable Battery, *Journal of Solid State Electrochemistry*, **16**, pp. 1247-1254, 2012.
[19] Cao F., Wu X., Xin S., Guo Y. and Wan L., Facile Synthesis of Mesoporous TiO2-C Nanosphere as an Improved Anode Material for Superior High Rate 1.5 V Rechargeable Li Ion Batteries Containing LiFePO4-C Cathode, *Journal of Physical Chemistry*, **114**, pp. 10308-10313, 2010.
[20] Dudney N.J., Bates J.B. and Lubben D., Thin-Film Rechargeable Lithium Batteries, *Proceedings of the American*

Ceramic Society 97th Annual Meeting, Symposium on the Role of Ceramics in Advanced Electro-Chemical Devices, April-May, 1995.

[21] Zhou W., Upreti S. and Whittingham M.S., Electrochemical Performance of Al-Si-graphite Composite as Anode for Lithium-ion Batteries, *Electrochemistry Communications*, **13**, pp. 158-161, 2011.

[22] Kolosnitsyn V.S. and Karaseva E.V., Lithium-Sulfur Batteries: Problems and Solutions, *Russian Journal of Electrochemistry*, **44**, pp. 506-509, 2008.

[23] Zhu X., Wen Z., Gu Z. and Lin Z., Electrochemical Characterization and Performance Improvement of Lithium/Sulfur Polymer Batteries, *Journal of Power Sources*, **139**, pp. 269-273, 2005.

[24] Choi Y., Chung Y., Baek C., Kim K., Ahn Y. and Ahn J., Effects of Carbon Coating on the Electrochemical Properties of Sulfur Cathode for Lithium/Sulfur Cell, *Journal of Power Sources*, **184**, pp. 548-552, 2008.

[25] Wang H., Yang Y., Liang Y., Robinson J.T., Li Y., Jackson A., Cui Y. and Dai H., Graphene-Wrapped Sulfur Particles as a Rechargeable Lithium-Sulfur Battery Cathode Material with High Capacity and Cycling Stability, *Nano Letters*, **11**, pp. 2644-2647, 2011.

[26] Liang C., Dudney N.J. and Howe J.Y., Hierarchically Structured Sulfur/Carbon Nanocomposite Material for High-Energy Lithium Battery, *Chemistry of Materials*, **21**, pp. 4724-4730, 2009.

[27] Hwang S.S., Cho C.G. and Kim H., Polymer Microsphere Embedded Si/graphite Composite Anode Material for Lithium Rechargeable Battery, *Electrochimica Acta*, **55**, pp. 3236-3239, 2010.

[28] Yang Y., McDowell M.T., Jackson A., Cha J.J., Hong S.S. and Cui Y., New Nanostructured Li₂S/Silicon Rechargeable Battery with High Specific Energy, *Nano Letters*, **10**, pp. 1486-1491, 2010.

[29] Yang S., Song Y., Ngala K., Zavalij P.Y. and Whittingham M.S., Performance of LiFePO₄ as Lithium Battery Cathode and Comparison with Manganese and Vanadium Oxides, *Journal of Power Sources*, **119-121**, pp. 239-246, 2003.

[30] Yao M., Okuno K., Iwaki T., Awazu T. and Sakai T., Long Cycle-Life LiFePO₄/Cu-Sn Lithium Ion Battery Using Foam-Type Three-Dimensional Current Collector, *Journal of Power Sources*, **195**, pp. 2077-2081, 2010.

[31] Li G., Li Z., Zhang P., Zhang H. and Wu Y., Research on a Gel Polymer Electrolyte for Li-ion Batteries, *Pure Applied Chemistry*, **80**, pp. 2553-2563, 2008.

[32] Li N., Lee J.Y. and Ong L.H., A Polyaniline and Nafion Composite Film as a Rechargeable Battery, *Journal of Applied Electrochemistry*, **22**, pp. 512-516, 1992.

[33] Novak P., Mueller K., Santhanam K.S.V. and Haas O., Electrochemically Active Polymers for Rechargeable Batteries, *Chemistry Reviews*, **97**, pp. 207-281, 1997.

[34] Hussien Z.F., Cheung L.W., Siam M.F.M. and Ismail A.B., Modeling of Sodium Sulfur Battery for Power Systems Applications, *Elektrika*, **9**, pp. 66-72, 2007.

[35] Ryu H., Kim T., Kim K., Ahn J., Nam T., Wang G. and Ahn H., Discharge Reaction Mechanism of Room-Temperature Sodium-Sulfur Battery with Tetra Ethylene Glycol Dimethyl Ether Liquid Electrolyte, *Journal of Power Systems*, **196**, pp. 5186-5190, 2011.

[36] Dustmann C., Advances in ZEBRA Batteries, *Journal of Power Sources*, **127**, pp. 85-92, 2004.

[37] Fabjan C., Garche J., Harrer B., Joerissen L., Kolbeck C., Philippi F., Tomazic G. and Wagner F., The Vanadium Redox-Battery: an efficient storage unit for photovoltaic systems, *Electrochimica Acta*, **47**, pp. 825-831, 2001.

[38] Swan D.H., Dickinson B. and Arikara M., Demonstration of a Zinc Bromine Battery in an Electric Vehicle, *IEEE AES Systems Magazine*, **May**, pp. 20-23, 1994.

[39] Joseph A. and Shahidehpour M., Battery Storage Systems in Electric Power Systems, *IEEE Power Engineering Society General Meeting*, October, 2006.

[40] Pan J., Ji L., Sun Y., Wan P., Chen J., Yang Y. and Fan M., Preliminary Study of Alkaline Single Flowing Zn-O₂ Battery, *Electrochemistry Communications*, **11**, pp. 2191-2194, 2009.

[41] Cheng J., Zhang L., Yang Y., Wen Y., Cao G. and Wang X., Preliminary Study of Single Flow Zinc-Nickel Battery, *Electrochemistry Communications*, **9**, pp. 2639-2642, 2007.

[42] Yang S. and Knickle H., Design and Analysis of Aluminum/Air Battery System for Electric Vehicles, *Journal of Power Sources*, **112**, pp. 162-173, 2002.

[43] Swaminathan V.V., Zhu L., Gurau B., Masel R.I. and Shannon M.A., Integrated Micro Fuel Cell with On-Demand Hydrogen Production and Passive Control MEMS, *Microfluid Nanofluid*, **12**, pp. 735-749, 2012.

[44] Khaligh A. and Li Z., Battery, Ultracapacitor, Fuel Cell, and Hybrid Energy Storage Systems for Electric, Hybrid Electric, Fuel Cell, and Plug-in Hybrid Electric Vehicles: State of the Art, *IEEE Transactions on Vehicular Technology*, **50**, pp. 2806-2814, 2010.

[45] Hyakudome T., Yoshida H., Ishibashi S., Sawa T. and Nakamura M., Development of Advanced Lithium-Ion Battery for Underwater Vehicle, *2011 IEEE Symposium and Workshop on Scientific Use of Submarine Cables and Related Technologies*, April, 2011.

[46] Van den Bossche P., Vergels F., Van Mierlo J., Matheys J. and Van Autenboer W., SUBAT: An assessment of sustainable battery technology, *Journal of Power Sources*, **162**, pp. 913-919, 2006.

[47] David J., Nickel-Cadmium Battery Recycling Evolution in Europe, *Journal of Power Sources*, **57**, pp. 71-73, 1995.

[48] Soundarajan C., Sivasankar A., Maruthamuthu S. and Veluchamy A., Improved Lead Recovery and Sulphate Removal from Used Lead Acid Battery Through Electrokinetic Technique, *Journal of Hazardous Materials*, **217-218**, pp. 452-456, 2012.

[49] Huang K., Li J. and Xu Z., Characterization and Recycling of Cadmium from Waste Nickel-Cadmium Batteries, *Waste Management*, **30**, pp. 2292-2298, 2010.

[50] Agrawal A., Pathak P., Mishra D. and Sahu K.K., Recover of Metal Values from Spent Nickel-Cadmium Rechargeable Batteries by Solvent Extraction Route, *Proceedings of the XI*

International Seminar on Mineral Processing Technology, MPT-2010, pp. 1195-1201, 2010.

[51] Saito Y., Asai K., Choi Y., Iyota T., Watanabe K., Kubota Y., Watanabe K. and Kubota Y., Development of a Battery Support System for the Prolonged Activity of Mobile Robots, *Journal of*

Electronics and Communications in Japan, (translation of Transactions of the Institute of Electrical Engineers of Japan), **94**, pp. 60-71, 2011.

State of the Art in Inductive Charging for Electronic Appliances and its Future in Transportation

Neha Chawla

Department of Mechanical and Materials Engineering
Florida International University
Miami, Florida, USA
786-419-0915
nchaw002@fiu.edu

Sabri Tosunoglu

Department of Mechanical and Materials Engineering
Florida International University
Miami, Florida, USA
305-348-1091
tosun@fiu.edu

ABSTRACT

Inductive charging is a method of moving power wirelessly. A power generating source system is placed near a power storing or power transferring system. An electromagnetic field is generated between the two objects and power is moved from one system to the other. Inductive charging is a way of moving power from a main system to a subsystem such as moving the power from the power grid to a local transformer. It is applied to a wide variety of systems from small hand-held devices to robotic platforms and electric vehicles. In this study, the working principle, advantages, disadvantages and limitations of inductive charging mats/pads used for electronic devices are discussed. The new advancements in inductive charging for transportation are also reviewed in this study.

1. INTRODUCTION

Inductive charging works on the basic principle in which two power systems are placed very close to one another. They need not to be exposed or connected to each other. Each of these power systems contains an electrical coil that stores electricity for the device's use. The coils' proximity to each other results in the generation of a low power electrical field that connects them. This field allows the transfer of electricity between the two systems. The two systems share electricity until they both have exactly the same amount of power. In inductive charging, one of the devices, i.e., the sender, is constantly powered so that it can send power to the receiver continuously until the receiver is fully charged.

1.1 Advantages:

Induction charging has several advantages over standard power transfer. One major benefit is that it is wireless. There is no limitation on the number of devices that may be charged at once. Hence, a single inductive charging mat can charge several devices at the same time. Inductive charging carries a far lower risk of electrical shock when compared with conductive charging, because there are no exposed conductors.

The ability to fully enclose the charging connection also makes the approach attractive where water impermeability is required; for instance, inductive charging is used for implanted medical devices that require periodic or even constant external power, and for electric hygiene devices, such as toothbrushes and shavers, that are frequently used near or even in water. Due to encapsulation it can be used in harsh environments. High power is

allowed in the output of the system. Low maintenance required thus decreasing the cost of the system comparatively. Inductive charging makes charging mobile devices and electric vehicles more convenient; rather than having to connect a power cable, the unit can be placed on or close to a charge plate.

1.2 Limitations:

The main disadvantages of inductive charging are heat and power consumption. It takes more power to inductively charge an item than charge it through normal means. This is due to the power lost to the electric field used to connect the coils. The process has the potential to generate immense heat indicating the amount of electricity being lost in the process of charging. Inductive charging also requires drive electronics and coils, increasing the complexity and cost of manufacturing. Using high frequency switches in electronic converters may cause interference in nearby equipment. The system may not work or the losses may increase if there is any metallic object in the middle of the magnetic connection. Magnetic radiation is harmful for the user's health. At the frequencies of interest in IPT systems a maximum of 2.6 uT is allowed to be exposed to the body. This being an averaged exposure limit and it has been described by Australian Radiation Protection and Nuclear Safety Agency (ARPANSA). Newer approaches reduce transfer losses through the use of ultra-thin coils, higher frequencies, and optimized drive electronics resulting in more efficient and compact chargers and receivers, facilitating their integration into mobile devices or batteries with minimal changes required.

Table 1. Summary of Advantages and Disadvantages of Inductive Charging

Advantages	Limitations
<ul style="list-style-type: none">• Wireless• A number of devices can be charged at a time• Electrically safe• Can be used in harsh environments due to encapsulation• High power in output• Waterproof• Low maintenance• Charging is convenient	<ul style="list-style-type: none">• More power consumption• Low efficiency• Heat generation is more than traditional charging• Complex circuitry• High cost of manufacturing• Harmful magnetic radiations emitted

2. HISTORY

In 1901, Nikola Tesla used the principle of electrodynamic induction to transfer electromagnetic energy without the need of wires to construct the Wardencllyffe tower (Figure 1) to transmit power between America and Europe but was destroyed by US government in 1917.

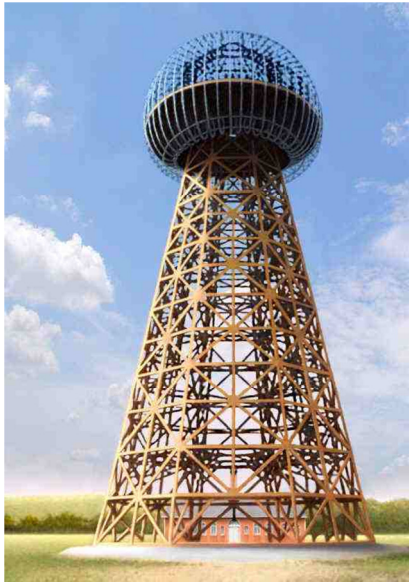


Figure 1. Wardencllyffe Tower

Andre Marie Ampere discovered 200 years ago that a magnetic field is created around the wire if electricity is transmitted down a wire. Then Michael Faraday developed the fundamental law of induction, a process that enables the transfer of power from one wire to another using magnetic field. Later the Maxwell equation was established, which is the basis of several everyday devices including electrical motors and generators. The basic technique used by Tesla earlier is now used in any situation where batteries are being charged without physical contacts. It is used in recharging electric toothbrushes or wet/dry electric shavers. Induction cooktops that transfer energy directly to a pot's metal bottom but remains cool to touch also uses the same principle.

In 2007, MIT researchers proposed the wireless power transmission based on strong coupled magnetic resonance and successfully lightened a 60 W bulb over 2 meters with a transfer efficiency of 30%. In 2008, Intel demonstrated an experiment setup to lighten a 60 W bulb over 1 meter with the transfer efficiency of 70 %.

3. INDUCTION CHARGING MATS/ PADS

Induction powers the charging mats that wirelessly transfer energy to the devices and allows them to be recharged by simply placing them on the top of the mat. Inside the mat there is an inductive coil through which the electricity runs and the power is transferred to a second coil attached to the device. Inductive charging uses an electromagnetic field to transfer energy between two objects. This is usually done with a charging station. Energy is sent through

inductive coupling to an electrical device, which then can use that energy to charge batteries.

There is a small gap between the two coils employed in each of the sender and receiver of the energy within the respective devices due to which inductive charging is considered a short-distance wireless energy transfer, despite the fact that there are typically more wires used with inductive charging than direct-contact charging, because it frees the user from having to deal with wires between the two devices.

Induction chargers typically use an induction coil to create an alternating electromagnetic field from within a charging base station, and a second induction coil in the portable device takes power from the electromagnetic field and converts it back into electrical current to charge the battery. The two induction coils in proximity combine to form an electrical transformer.

Wireless charging is an emerging trend for mobile and portable devices with various products appearing in the market by providing significant user convenience. Magnetic resonance based charging is a technique that provides support for charging multiple receivers with the same transmitter. Wireless charging has been popular since 2009 with products like Palm Pre., Dell Latitude, PowerMat and many other similar products.

The technologies for wireless charging can be either magnetic induction or radio frequency or optical or conduction. Magnetic induction converts electrical energy to magnetic energy. It allows transmission over an air gap and is typically short to midrange. For microwave or radio frequency, the parabolic dish focuses radio waves which are typically long range waves towards intended target. They can also include low power receivers for energy harvesting. For optical or infrared, the laser light is focused on photovoltaic cells that convert light energy to power. In conduction, the power transfer occurs due to metallic contact between transmitter and receiver. Compared to inductive coupling and RF radiation, wireless power transfer via strong coupled resonance is more suitable for wireless power transfer in a range from a few centimeters to a few meters for mobile consumer devices. Many researches have been conducted to investigate the principle and design of wireless power transfer via strong coupled resonance. A wireless charger prototype based on strong coupled magnetic resonance was presented and emphasis was put on design considerations and experiments for real wireless power transfer applications based on this technology.

Magnetic induction has two categories namely magnetic induction coupling and magnetic resonance coupling. In inductive coupling, the source drives a primary coil creating a sinusoidally varying magnetic field which induces a voltage across terminals of secondary coil, thus transferring power to load. This type of mechanism is used in transformer where the magnetic field is confined to high permeability core. Magnetic resonance coupling is more advantageous since it has an extended range, alignment insensitivity and potential to support multiple receivers. The gain is over a very small range implying that very accurate tuning is required for magnetic resonance coupling.

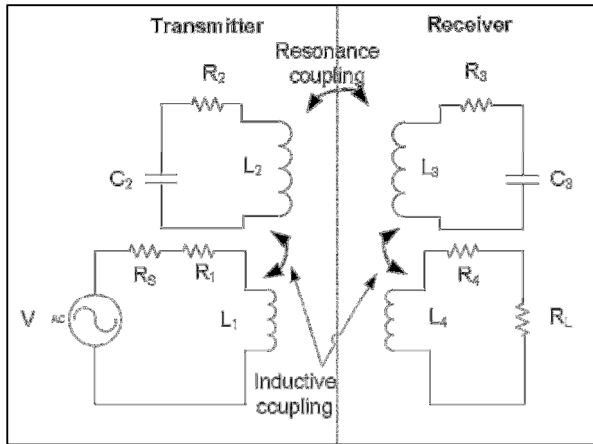


Figure 2. Magnetic Resonance Coupling Circuit Model [8]

Figure 2 shows the circuit model for magnetic resonance. The transmitter (source) is the charger and the receiver (load) is the device to be charged. The source and load are inductively coupled to the resonant circuits to remove the effect of loading (parallel impedances), which results in a high Q of the circuit.

4. SINGLE RECEIVER CHARGING

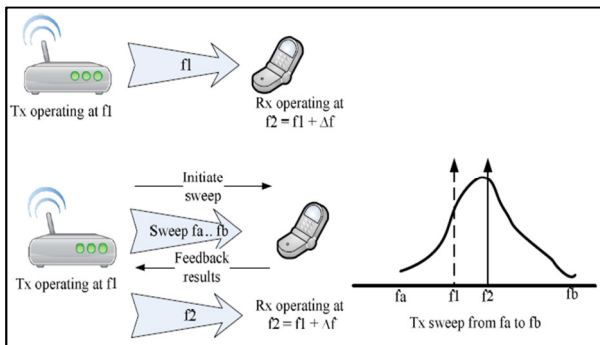


Figure 3. Single Receiver Charging [8]

The single receiver charging system consists of a transmitter and receiver designed to operate at a frequency for resonance power transfer as shown in Figure 3. The frequencies of transmitter (f_1) and receiver (f_2) may deviate due to process, voltage and temperature variations inside the components of a device or due to the presence of metallic elements in or near the device. The frequency tuning is done by changing the capacitance or inductance values via a shared communication interface between transmitter and receiver by frequency sweep which can be performed by finely adjusting the resonant circuit at transmitter over the desired range of operation. Assuming the mobile to be stationary, the maximum power transfer from transmitter to receiver occurs at frequency f_2 ; i.e., the operating frequency of receiver. Receiver keeps the record of the power level received for each of the sweep steps. The sweep step is then reported to the transmitter by the receiver where maximum power transfer occurs back to transmitter via communications interface. The transmitter then tunes its circuit to frequency f_2 and transmits at f_2 for maximum power transfer efficiency.

5. MULTIPLE RECEIVER CHARGING

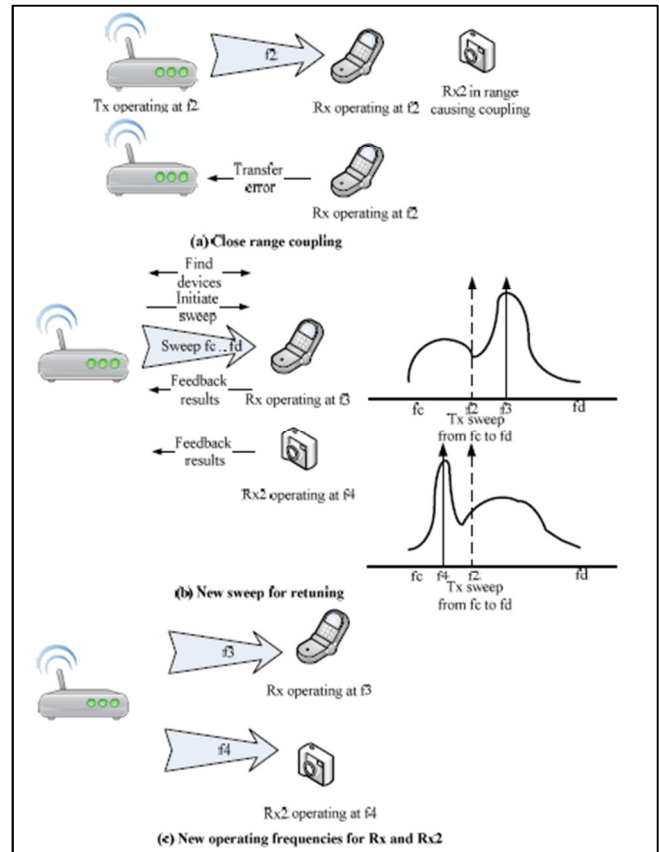


Figure 4. Multiple Receiver Charging [8]

Figure 4 shows the multiple receiver charging. A split resonant peak is caused by the coupling to the first receiver when a second receiver comes close to the transmitter. The receiver detects the loss in power transfer due to multiple receiver coupling which is reported to the transmitter by receiver. After the information of the loss is received, the transmitter estimates the reasoning behind power transfer loss. It first searches for alternate receivers in vicinity using its communications interface. It then sweeps from frequency f_c to f_d with stepsize $s = (f_d - f_c)/N$ where N is the number of steps in the sweep. If other receivers are detected then each receiver receives the sweep and notes the frequency sweep at which maximum power was transferred. Maximum power transfer occurs at different frequencies for each receiver. Results of the sweep are communicated back to the transmitter via communications interface.

The transmitter contains multiple resonance structure to communicate with multiple receivers. The number of simultaneous receivers supported by this method is dependent on the number of resonance structures available at the transmitter. The transmitters can time-multiplex between the multiple receivers and retune to operating frequency of each receiver which allows supporting charging a greater number of receivers than the number of resonance structures available at the transmitter. The time multiplexing is dependent on the current charging status for each receiver and the transmitter and allocates

more time to the receiver which is less charged. Time multiplexing helps reducing coupling between the receivers and is used when the coupling is very strong and the resonant peaks are outside the tuning range of the transmitter.

6. PRODUCTS AVAILABLE IN MARKET

Various products available in the market for inductive charging are discussed below.

6.1 PowerMat 3X



Figure 5. PowerMat 3X [9]

PowerMat 3X as shown in Figure 5 is a sleek, slim three position wireless charging mat for home and office. A magnetic attraction between every receiver and each access point on every Mat assures that alignment is precise and the most efficient charging occurs. Communication between the Mat and the Receiver allows the mat to deliver an exact amount of power for the proper length of time so that the transfer of power is safe and efficient and no energy is wasted. When the device reaches full charge, power is shut off to that device, which avoids overcharging of the device's battery as well as saves energy. Once full power is achieved and the Auto Shut Off has occurred to save energy, the system will monitor the status of the battery in the device. If the battery is used, the system will again initiate charging and return the battery to a full charge.

6.2 Duracell MyGrid



Figure 6. Duracell MyGrid [11]

The Duracell MyGrid Charging Pad as shown in Figure 6 is a flat square with a single raised edge. It measures 8 by 6.5 by 0.75 inches at its largest point and fits easily on a desk or bedside table. It consists primarily of 12 magnetic strips, which carry the actual charge to the devices. With a maximum power output of 15VDC/1A, it's a very efficient device, charging all four gadgets in more or less the same amount of time as by using their bespoke power adapters, all the while saving around 15% on energy consumption. The myGrid switches off once each device is fully

charged, saving on unnecessary power use or overcharging your batteries. Duracell have implemented touch sensitive safety procedures that power off the device when it comes into contact with your fingers or inappropriate metallic objects.

6.3 Energizer Inductive Charger



Figure 7. Energizer Inductive Charger [10]

Energizer Inductive Charger as shown in Figure 7 is based on Qi Technology and aims to be the next-generation charging solution for many devices. The *Energizer* Inductive Charger conveniently charges up to three of your devices at one time. Two inductive Qi charging zones are located on the top surface of the pad for simple, easy charging. For both Qi and non-Qi devices, the USB port on the back is ideal for charging additional phones, headsets, mp3 players, cameras, GPS devices, and any other device up to 5 watts. The charging pad offers two stations to charge devices. Additionally, the two LEDs above each station will illuminate in a neon blue color to indicate that it actively charges the device. Even though the charging pad slopes down at an angle, devices do not slide or move around. On the back, there is the proprietary charging port and a standard USB port, which allows the user to charge other devices.

6.4 WildCharge Pad



Figure 8. WildCharge Pad [12]

Pure Energy Solution's WildCharge Pad as shown in Figure 8 wireless phone charger offers comparable features and output capabilities. The WildCharge Pad provides 15 watts of output power, enough to charge multiple devices simultaneously. It works through the traditional contact-point transference principle where two conductive materials transfer electricity to charge the battery.

Table 2. Comparison of the Various Induction Charging Products Available in the Market

Comparison Points	PowerMat 3X	Duracell myGrid	Energizer Inductive Charger	Wild Charge Pad
Overall Rating				
Device compatibility: This section rates the wireless chargers on their compatibility with select mobile devices	Excellent	Good	Fair	Good
Specifications: This section rates each wireless charger on its output capacities including output watts and device features	Excellent	Fair	Good	Fair
Durability/Ability to endure damage	Excellent	Fair	Good	Fair
Help and support provided by the manufacturer	Excellent	Fair	Good	Good
Features				
Device compatibility	Compatible with iphone4, 3G/3GS, Ipod Touch, Blackberry Curve, Blackberry tour, Blackberry Bold, Blackberry Pearl, HTC EVO 4G, Motorola DROID X, Nintendo DS/DSi,	Compatible with iphone4, 3G/3GS, Ipod Touch, Blackberry Curve, Blackberry Tour, Blackberry Bold, Blackberry Pearl, Motorola DROID X	Compatible with Iphone 3G/3GS and Blackberry curve	Compatible with Iphone 3G/3GS, Ipod Touch, Blackberry Curve, Blackberry Bold, Blackberry Pearl, Nintendo DS/DSi,
Maximum no of devices the wireless charger can power at once	3	4	3	4
Power output (Watts): No of watts that the wireless charger produces	18	15	15	15
Internal battery: It allows the devices to charge mobile gadgets without the pad being plugged into the wall	Has internal battery	Does not have internal battery	Does not have internal battery	Does not have internal battery
Full charge shutoff: This feature stops sending power to devices once they reach full charge	This feature is available	This feature is not available	This feature is available	This feature is not available

7. INDUCTIVE CHARGING IN TRANSPORTATION

Transportation sector is the largest consumer of fossil fuel worldwide and thus important factor in reducing fossil fuel demand. Pollutant emissions and oil consumption are caused by transportation sector. Currently the transformation in automobiles from internal combustion engines (ICE) vehicles to hybrid fuel cells vehicles (FCV). The limited availability of fossil fuel and to reduce the emissions in transportation sector, the development of electric vehicles worldwide over the past decade has been initiated. The price of EV is nearly twice than that of ICE vehicles which is largely due to the limitation of battery technology. The charging time of EV is very long when compared to ICE car.

Currently, plugin connections are used in EVs for charging where the user inserts the plug into the receptacle of the car to charge the batteries. It has the following disadvantages. The major

disadvantage of using cable and connector type is the risk of electrocution especially in wet and hostile environments since it delivers 2- 3 times more power than standard plugs at home. Long wires also pose a tripping hazard and are also aesthetically poor. In harsh climate locations that have snow and ice, the plug-in charge point may become frozen onto the vehicle. Thus in order to eliminate the above disadvantages, the inductive charging has been developed which can charge the batteries wirelessly. Road electrification as shown in Figure 9 can be developed so that the power is transferred to the vehicle as it moves along the electrified section of the roadway. It would eliminate the problem of range with EVs as the required power by the vehicle travelling on freeways can be supplied by the grid directly through the roadway but the infrastructure cost is high.

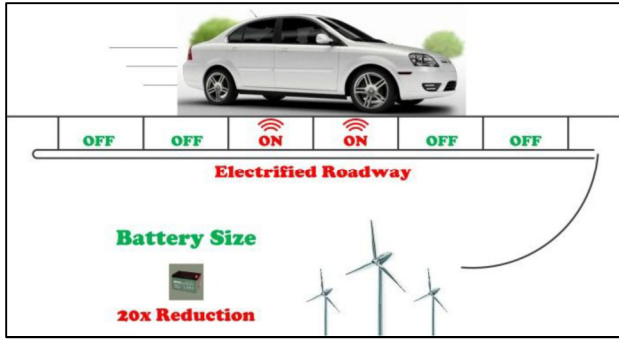


Figure 9. Electrified Road (Efficiency can be kept high if the magnetic field is only turned on at the instant the vehicle is travelling over it [5])

First, high frequency alternating currents are produced by the power supply in transmitter pad that inductively transfers power to receiver coil. The receiver electronics converts this high frequency power that was received via induction to DC which is suitable for charging. These systems are mostly loosely coupled; hence resonance and high frequency operation is required.

Adoption of an inductive power transfer system (IPT) as shown in Figure 10, to charge the batteries on board the electrical vehicle has been proposed by A. Neves et Al. It is known as wireless electrical charger for the inexistence of physical contact between the source and the load.

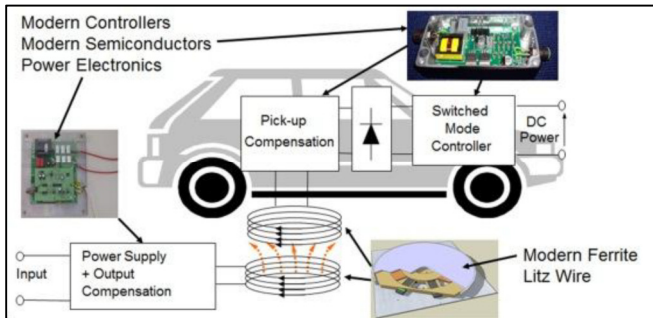


Figure 10. Inductive Charging System [5]

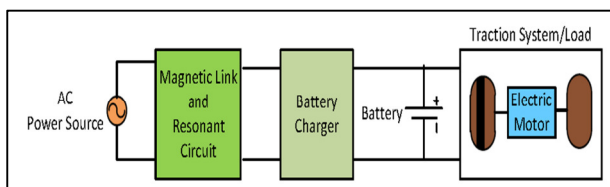


Figure 11. Main Blocks of an IPT Vehicle Charging System: (1) Power Source, (2) Magnetic Link, (3) Resonant Circuit, and (4) Battery Charger [5]

Basic circuit of an IPT vehicle as shown in Figure 11 constitutes of 4 major blocks namely a power source, a magnetic link, a resonant circuit and a battery charger. Power source is for connection between magnetic link and power grid and is composed by and rectifier followed by an inverter. The current amplitude and frequency can be controlled by allowing power flow of the system. The magnetic linkage transfers the power between battery charger and power source and is composed of 2 coils that have either an iron core or no core. The resonant circuit

compensates the reactive part of total impedance by increasing the power transfer efficiency. Battery charger controls the charging process and changing voltage to the levels accepted by each type of battery. The magnetic linkage and resonant circuit are the most important parts of the IPT system.

Charging of lithium battery for portable electronic products and concept of common charging applies contactless power transmission technique. Charging platform comprises of several pot type cores with array structure, allowing circuit to be charged within a permitted region of displacement on charging platform. Poor power transmission efficiency occurs since a larger air gap exists in contactless structure compared to other contact structures.

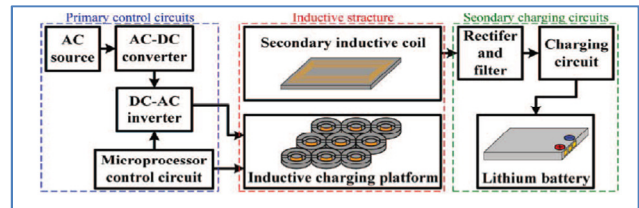


Figure 12. The Framework of Contactless Inductive Charging Platform [5]

Hung-Yu Shen et Al. aimed at providing convenient and uniform charging method for portable electronic products using contactless inductive charging. Figure 12 shows the framework of contactless inductive charging platform. Upon designing contactless inductive charging system, the analysis of magnetic allocation for inductive structure is the first consideration, relying on the result of analysis to obtain appropriate inductive structure and to consider the impact of current direction of array core on the allocation of magnetic fields. Next, closed-loop control structure is applied, enabling the system to work in the domain of high efficiency. The structure of contactless inductive charging platform proposed in this research is shown in Figure 12. It shows that the converter transforms AC into DC and then the inverter again transforms the DC into AC for driving inductive core of the primary. In the secondary, the inductive core picks up power from primary and the power is then rectified in order to charge the lithium battery. The charging scheme utilized in the research was constant current and constant voltage. Their research analyzed the magnetic field allocation of different core and considered the impact of induced magnetic field on other electronic equipment.

The charging platform was then designed by several pot type cores with magnetic enclosure due to the analysis results. The influence of current direction of the coil on allocation of magnetic field was investigated to choose appropriate induced structure and current direction of the coil. Microprocessor control circuit is utilized to adjust input power when the secondary is removed from the charging platform and reduces energy depletion. The coupling effect of each part of the charging platform was shown to provide the best position to place the secondary. Additionally, the induced structure was implemented leading to plane circuit. Result of experiment showed that the contactless inductive charging platform was able to charge a battery with charging current of 200mA under the condition of a gap 2.5mm between the secondary and the charging platform. The highest transfer efficiency was found to be 55% between primary and secondary was able to work normally within a large enough displacement.

Part of energy was lost in leakage inductance of induced structure. Transfer efficiency can be improved by overcoming the above weakness and by other type of induced structure and magnetic material added to increase the coupling coefficient.

8. STATE OF THE ART OF INDUCTIVE CHARGING FOR TRANSPORTATION

Magne Charge inductive charging was employed by several types of electric vehicles around 1998 but was discontinued after California Air Resources Board selected SAE J1772 in 2001 or Avcon conductive charging interface for electric vehicles in June 2001. In 2009, Evatran, began development of Plugless power for proximity charging system for electric vehicles. With the participation of the local municipality and several businesses, field trials were begun in March, 2010, on the system scheduled to be available in fourth quarter 2010.

Researchers at Korea Advanced Institute of Science and Technology have developed an electric transport system where vehicles get their power needs from cables underneath the surface of the road surface via non- contact magnetic charging where power source is placed underneath the road surface and power is wirelessly picked on the vehicle by itself. It will improve overall efficiency by minimizing air resistance and thus reduces energy consumption.

The major advantage of the inductive approach for vehicle charging is that there is no possibility of electric shock as there are no exposed conductors, although interlocks, special connectors and RCDs (ground fault detectors) can make conductive coupling nearly as safe. An inductive charging proponent from Toyota in 1998 contended that overall cost differences were minimal, while a conductive charging proponent from Ford contended that conductive charging was more cost efficient.

From 2010 onwards, car makers are signaling their interest in wireless charging as another piece of the digital cockpit. In May 2010, a group by the Consumer Electronics Association set a baseline for interoperability for chargers.

In November 2011, the Mayor of London, Boris Johnson, and Qualcomm announced a trial of 13 wireless charging points and 50 EVs in the Shoreditch area of London's Tech City, due to be rolled out in early 2012.

Halo Wireless Electric Vehicle Charging (WEVC) technology seeks to solve this problem with wireless inductive charging for electric vehicles. Qualcomm Halo WEVC has basically taken inductive charging--which you probably already see in devices such as your electric toothbrush--to the next level, by making it possible to send kilowatts "over an air gap of hundreds of millimeters while still maintaining high-energy transfer electricity."

Qualcomm Halo WEVC has developed an inductive charger that consists of two parts: a charging plate that attaches to the bottom of the vehicle and a charging mat that can be placed on or below the ground. Inductive charging uses magnetism to transfer power up to 3.5 kilowatts at greater than 90 percent efficiency. Their trial will be in London and will span over a period of 2 years and involve about 50 cars.

9. CONCLUSION

Wireless energy transmission technology has been developed in which electrical energy is transmitted from power source to an electrical device without using wires. The limited fossil fuel availability throughout the world has allowed the electric vehicles to develop over the past decade. The technology has improved sustainability but still consists of various drawbacks which need to be researched upon in order to commercialize it.

10. REFERENCES

- [1] Michael G. Egan, Dara L. O'Sullivan, John G. Hayes, Michael J. Willers, and Christopher P. Henze, "Power-Factor-Corrected Single-Stage Inductive Charger for Electric Vehicle Batteries," IEEE Transactions on Industrial Electronics, vol. 54, No. 2, pp. 1217-1226, April 2007.
- [2] Yun You, Boon Hee Soong, Selva Ramachandran and Wei Liu, "Palm Size Charging Platform with Uniform Wireless Power Transfer," 11th Int. Conf. Control, Automation, Robotics and Vision, Singapore, pp. 85-89, December 7-10, 2010.
- [3] Hung-Yu Shen, Jia-You Lee, Tsunug-Wen Chang, "Study of Contactless Inductive Charging Platform with Core Array Structure for Portable Products," CECNet, International Conference, pp. 756-759, April 2011.
- [4] A. Neves, D. M. Souza, A. Roque, J. M. Terras, "Analysis of an inductive charging system for a commercial electric vehicle," Proceedings of the 2011 - 14th European Conference on Power Electronics and Applications, pp. 1-10, Lisbon, Portugal, Aug. 30 - Sep. 1, 2011.
- [5] Hunter Hanzhuo Wu, Aaron Gilchrist, Ky Sealy, Paul Israelsen, Jeff Muhs, "A review on inductive charging for electric vehicles," IEEE International Electric Machines and Drives Conf., pp. 143-147, May 2011.
- [6] Yanping Yao, Hongyan Zhang, Zheng Geng, "Wireless charger prototype based on strong coupled magnetic resonance", International Conference on Electrical Engineering and Information Technology, pp. 2252-2254, August 2011.
- [7] Huiqing Zhai, Helen K. Pan and Mingyu Lu, "A practical wireless charging system based on Ultra-Wideband retro-reflective beamforming," IEEE Antennas and Propagation Society International Symposium (APSURSI), Arlington, Texas, July 1-17, 2010.
- [8] Sridhar Rajagopal and Farooq Khan, "Multiple receiver support for magnetic resonance based wireless charging," June 2011.
- [9] Review of PowerMat 3X, 2012.
- [10] Energizer official site for Energizer inductive charger, 2012.
- [11] Duracell MyGrid official site, 2012.
- [12] Review of Wild Charge Pad, 2012.

Robotic Art for STEM

Ravi Shankar
CEECs, FAU
777 Glades Road
Boca Raton, FL 33431
(561) 297-3470

shankar@fau.edu

Joseph Anthony Gundel
PhD Student, CEECS, FAU
777 Glades Road
Boca Raton, FL 33431
(561) 297-3470

jgundel@fau.edu

Agnes Nemeth
Henderson Univ. School, FAU
777 Glades Road
Boca Raton, FL 33431
(561) 297-3470

anemeth4@fau.edu

Don Ploger
Education, FAU
Bc-49, 217
Davie, FL 33314
ploger@fau.edu

Steven A Hecht
Program Professor, Education
Nova Southeastern University
North Miami Beach, FL
shecht@nova.edu

ABSTRACT

In this paper, we describe our experiences in using geometric art to develop robotic skills in both undergraduate and high school students. The intent was to use robots to enhance interest in STEM (science, technology, engineering, and mathematics) disciplines among high school students and in system level design and integration issues in the undergraduate student population.

Keywords: K-12, STEM, Autonomous Robot, Education, System Integration

1. INTRODUCTION

In this paper, we describe our experiences in using geometric art to develop robotic skills in both undergraduate and high school students. Our undergraduate students developed a low cost robotic prototype with the primary goal to make it affordable to K-12 students and schools. The robots, of necessity, are made of imprecise mass manufactured components. This allowed the undergraduate students to consider system issues, and optimize with regard to cost, battery drain, ease-of-use, and performance. This process helped us identify a low cost kit that high schools can afford to purchase, and an assembly process that high school students can easily follow. We chose robotic art as the primary vehicle to expose high school students to robotics because of the social context such a team project can provide. Further, we chose to use geometric robotic art in an effort to limit the options, but also to emphasize the STEM aspects of robotic use. This semester's pre-engineering course for 9th graders has led to an even lower cost kit and an improved curriculum. These are fully programmed autonomous robots that execute the geometric pattern without any remote control from the student teams.

2. METHODS

The robotic kit used comprises of a DF Robot 2WD mobile platform, 2 DF Robot wheel encoders, Parallax Ping Ultrasonic sensor, Robotics DMS IR (infrared) Distance sensor, Arduino Uno microcontroller board, Arduino Protoshield, 2 H-bridge motor drivers, and a few other miscellaneous items, all secured from the two suppliers [www.robotshop.com, www.sparkfun.com]. Arduino is an open source initiative that provides significant hardware and software support for embedded system designers [1]. Arduino's Sketch language and APIs

provide programming support for the underlying microcontroller without exposing the user to the extremely complex and confusing register level details of the ATmega 328 microcontroller from Atmel [2]. The Arduino platform was developed primarily to aid the artists (to control the stage props, applause, music, etc., for example) without overwhelming them with the underlying electronics. Extrapolating, it seemed like a good fit for both our engineering undergraduate students (from computer science, electrical engineering, and computer engineering), so they could focus on systems issues, and for high school students who have limited or no programming and electronics skills.

Students work in teams of three and use a large canvas (80 cm by 80 cm sheet with greeting card thickness) to draw their art on. They use a color pen that could be mounted in the center of the robotic platform when needed. The robots have three wheels, with two motors that are driven (through an H bridge and a power amplifier) from the PWM (pulse width modulation) outputs of the Arduino Uno microcontroller. The robot also has one ultrasound ping sensor mounted in the front and two infrared sensors mounted on the two sides. The sensors are used to ensure that the robot travels on a straight line; this is achieved with reflector walls placed to make a 1 m x 1 m square fence. The wheel encoders provide 10 positive going pulses per turn. Student teams use Sketch to program their robots. Undergraduate engineering students used interrupts and achieved intricate geometric patterns [3]. We have intentionally restricted our 9th grade high school students to draw simpler patterns, but repeating in some way, so we can show how an algorithm can be reused with changes in parameters. The goal then is to make sure the algorithm is rugged and that it leads to repeatable results, and use this algorithm in different contexts to create the pattern. For example, a triangle involves two algorithms repeatedly used: drawLine () and turnAngle (). The first one will need two parameters: distance and angle, while the latter one will need one parameter: angle, with the angles referring to a standard coordinate system. Our work from fall semester with undergraduate students is well documented at our robotics website, with links to their blogs and their demo videos [3]. We used this robotic platform in a course (Intro to Mechatronics) taught to 9th graders this semester. Their blogs also may be accessed from our robotics site [3]. Their demo videos are available at their blog sites. A survey and an interview were conducted by one of the co-authors who is a professor in

education to understand how effective our teaching was, from both Mathematics and Engineering perspectives.

3. RESULTS

3.1 Engineering pertinent experiences from our undergraduate level course:

This class, offered in fall 2011, had an equal number of students from computer science, computer engineering, and electrical engineering. Each team was typically comprised of one student member from each of these three disciplines. Such teaming helped them harness different strengths and also appreciate and accommodate different perspectives. Seven teams were formed. The students used a 1 m x 1m floor space with reflector walls encircling the space. The student blog sites and videos of their robotic art are available at our website [3]'s January 8, 2012 postings. Two teams focused on creating simple polygon patterns (a rectangle and a triangle); See videos of groups 1 and 6 [3]; this required effective use of the IR receivers and the ultrasound sensor for distance measurements, corrections for interference and potential avoidance of 'drunken sailor' behavior of the robot because of the IR receiver characteristic in near field (more on this later). A third team (group 3) created intricate polygon pattern that was repeated a large number of times [3]. This required effective use of optical encoders and interrupts. The former did not yield clean ten pulses per turn, as would be expected. The electromechanical bouncing was evident even here and led to thousands of pulses. The students used back-to-back NAND gates and software delays to overcome the problem. Prioritization of interrupts had to be carefully thought through. Finally, while some teams complained of loss of precision in robotic movement when the batteries were somewhat drained, this group managed to create intricate patterns without losing control. Group 7 specialized in building a pen holder and the reflector walls that were used by other teams. The pen we had chosen was too bulky and the pen holder with pen ended up being a drag on the performance of the robot. Further, the use of four wheels caused large circles when the robot turned. It appears that other teams suffered because of lack of communication and coordination. However, we also recognized the need to help them plan and strategize; and also address issues in a piece-meal fashion. Experiences, both positive and negative, helped us identify a better kit and a focused syllabus when this material was used to teach a mechatronics course to high school students this semester (spring 2012).

3.2 Engineering pertinent experiences from our high school level course.:

This course attracted 17 ninth graders at the Henderson School, FAU's University School on our Boca Raton campus. These students are in their pre-engineering program. This was the second engineering program that they had taken. The students comprised of 11 boys and 6 girls, with strong aptitude for mathematics and engineering. Five teams of 3 or 4 students were formed and were asked to choose a geometric pattern of medium complexity to draw with their robots. Each team built their own robot and developed algorithms for drawing lines and rotating by given angles. This required calibration of their robot's wheels for the distance traveled (at different PWM duty ratios) in a given time period, and the length of the PWM train to make a complete circle (at different PWM duty ratios). To make such a tight circle, the outer wheel was subject to this PWM train, while the inner wheel was held stationary. One could make fairly precise angular turns

by controlling the duration of the PWM train. Different groups needed angles of 45, 60, 72, or 90 degrees depending upon the mathematical shape they were creating. Our initial goal here was to have the student teams use the reflector walls along the fence as guideposts; but the IR receiver characteristic has a negative slope in the near field. So, any simple algorithm that checks for a large reading from the near side IR sensor to keep the robot away from that wall ended up making the robot end up at the wall. It was difficult to convey a more sophisticated algorithm to the student teams because of the time pressure to get a working prototype completed. Another way would have been to use ultrasound sensor to measure the distance from the front wall and use that to correct the robot's path. Time pressure precluded us from incorporating either. Thus the final student implementations ended up being 'deaf' to the surroundings that executed their motions purely based on control of the motors with PWM trains and different duty ratios. The five teams implemented four different patterns (Trinity force of courage, Butterfly, "FAU", and Star). Links to their blogs and demos are provided in the February 21, 2012 posting at our robotic site [3].

3.3 Other activities

One of the co-authors, with the college of education, interviewed five of the students who had signed the IRB form agreeing to the study. He interviewed them at the end of the semester in groups of 2 or 3 with the intent to see whether the course made any significant difference in the student's understanding of the underlying Mathematics and Engineering principles. Results from this study will be published at an ASEE conference to be held at the University of Texas, El Paso, TX.

4. DISCUSSION

(1) We have taught project oriented courses for a number of years. The emphasis, before this spring semester, had been to give lectures, and institute a few quizzes, but essentially allow the teams to develop the project on their own. However, unlike the robotics course, the earlier groups (in non-robotics oriented courses) had the benefit of projects completed by even earlier groups of students; that facilitated the thinking of that term's students. However, this was missing for the fall 2011 students taking our robotics course, and some of their projects suffered. We changed our approach to teaching such project oriented courses this semester. The first half of the semester is now focused on the theory during the lecture hours, while they build the robots during the lab hours. Several quizzes and a mid-term exam evaluated the students on the lecture and lab material. This ensured that the students had an acceptable minimum level of understanding and competence when they started the project in the second half of the semester. The students also had a clearer idea of how they were faring in the class. The younger high school students may also have needed reinforcement of the ideas. Either way, it appears that we were able to help them in successful completion of their projects. This was a significant improvement over the results from the fall 2011 semester with our undergraduate students from three different disciplines. (2) The high school students, under time pressure, discarded our recommended approach for use of infrared and ultrasound sensors and designed their algorithms merely based on control of distance traveled and angle turned. Successful completion of their projects is proof that high school projects can be undertaken with a simpler robotic kit. This brings down the cost from about \$160 per kit (currently) to about \$100, our targeted price point that should be

met for schools to afford the robots. (3) The high school students seem to have had problems with soldering, and thus had to use breadboards to connect wires from motors (and sensors) on to the Arduino Photo shield and the Arduino microcontroller board. It appears that we will use, in future course offerings, wire-wrap technology to make semi-permanent connections and avoid the potential for one of the bread-board wires to pop off and cause malfunctioning of the system. (4) Battery drainage was blamed by one student group for not drawing their star with proper angles, thus leading to a gap at the end. This group used 100% duty ratio and tried a large size star. Another team that drew a smaller sized star completed without any problems. (5) All these issues provide enough research material for an undergraduate robotics course in engineering at a later date. We expect to focus on building components or subsystems that can aid expansion of robot's role in STEM education for high school students. Possible examples of this are: robust sensor sub-systems for tracking; optical encoder-based interrupt driven sub-system for angular turns; and graceful slowdown based on battery voltage fall—off characteristics.

5. CONCLUSIONS

NSF (National Science Foundation) has launched a new initiative entitled CE21 (Computing Education for the 21st Century) [4]. Researchers at other institutions have explored the use of Java, Processing, and Python to expose K-12 students to computer education. We provide here yet another programming paradigm based on robotics and the Sketch language that has the potential to provide a social context and attract non-STEM oriented students to the STEM fold. Learning programming with robots has the advantage (relative to the above cited programming languages) of providing a social context and a hands-on experience. However, commercialization of robotics has priced the robots too far beyond the point of affordability for K-12 schools. We believe we can

build low cost robots that schools can afford. We have presented our experiences in that regard here.

6. ACKNOWLEDGMENTS

Our thanks are due to Dr. Hanqi Zhuang, Professor, CEECS, FAU, who provided initial funds to purchase a few robotic kits and support of an engineering student. We leveraged these to submit a well researched proposal to FAU who funded us with \$2,800 to obtain robots used in the undergraduate class. Funds for the robotic kits used in this semester's course for 9th graders came from the office of Dr. Tammy Ferguson, Principal of FAU's Henderson School. We thank them and Dr. Ail Zilouchian, Associate Dean, Engineering and Computer Science, who facilitated the offering of this course to high school students, and provided significant logistics support and leadership to make it all happen.

7. REFERENCES

- [1] Arduino Open Source site, , <http://www.arduino.cc/> , retrieved on May 8, 2012.
- [2] Atmel Microcontroller site, <http://www.atmel.com/Images/doc8161.pdf> , retrieved on May 8, 2012.
- [3] Our Robotics site at FAU: <http://robotics.fau.edu/> , retrieved on May 8, 2012.
- [4] CE21, NSF's recent initiative on computing education: http://www.nsf.gov/funding/pgm_summ.jsp?pims_id=503582 , retrieved on May 8, 2012

PANTERA: Lunar Mining Excavator

Narine Kelvin Harrylall, Ramon Garo, Janet F. Reyes, Sabri Tosunoglu

Florida International University
Department of Mechanical and Materials Engineering
10555 West Flagler Street
Miami, Florida, USA

954-547-1184, 786-263-3680, 954-240-3301, 305-348-1091
kharrylall@gmail.com, rgaro001@fiu.edu, jreye031@fiu.edu, tosun@fiu.edu

ABSTRACT

In this paper, we describe the development of a lunar robotic excavator named Pantera. Currently, no technologies are available that would enable a manned bases on the moon, or any other celestial body, to mine local resources for the production of vitals such as oxygen, water, or fuel. In order to be viable, a lunar colony would need to be able to live off the land as much as possible. The design of such a robot is challenging for multiple reasons. Some of these reasons include the abrasive characteristics of lunar soil, lack of air or water in space and the ability to tele-robotically communicate with the robot. For these reasons, extensive research was undertaken and an efficient lunar mining excavator concept was created.

Keywords

Robot, robotic platform, lunar mining excavator, NASA

1. INTRODUCTION

Lunar mining opens a new door of opportunities and resources. Not only would excavating regolith provide the world with energy resource such as Helium-3, but it will also lead the way towards moon colonization.

According to Dr. Schmitt, a former NASA astronaut and geologist, the moon is capable of helping us with our future energy problems, as it would provide a source of Helium-3, which is rarely found on Earth. This isotope is available in the lunar surface due to the exposure of the solar winds and would be used with deuterium to produce nuclear fusion [1]. This was proven by the abundant amount found in some of the rock specimens obtained after the Apollo mission [2]. Along with the Helium-3 found on the moon, various by-products of the excavation would be produced; thus, providing a source to fuel possible Earth-Moon transportation and lunar manned stations [1].

Not only has the United States looked at such possibilities of mining the moon, but China has also looked into the manner by launching exploratory probes and crafts to further exploration and research [3]. With the drive for exploration and the desire to secure energy resources, human colonies would be required. For this application, it has been suggested that moon mining is essential for lunar colonization to occur in order to facilitate its workers by providing them with refuge, facilities and a place to grow their food [4].

Lunar mining, besides opening a door towards the exploration and usage of new energy resources, is also leading towards a new road for entrepreneurs and businesses. For example, some companies are starting to launch space funeral services. The space funeral company, Celestis, promises to deliver and deposit about 100 sets of ashes in lunar soil [5]. Even though this company has not yet successfully buried its contractors, the company continues to grow and gain more popularity. This is a prime example of the increased human activity being proposed on the moon.

Currently there is a NASA competition that inspires students to create a lunar mining robot in order to compete against other universities. Since 2007, NASA has been sponsoring annual regolith excavation challenges, continually revising the rules and modifying conditions. Initially, these challenges had few participants but they kept attracting an increasing number of universities. In total, 62 universities registered and 36 actually competed in the 2011 competition [6]. The Black Point 1 Simulant—also known as BP-1—is the lunar regolith simulant that will be used in the NASA Lunabotics competition. The BP-1 was made from the basal flow in the Black Point Volcanic Field in northern Arizona [7]. This same simulant is to be used to test the effectiveness of the lunar mining excavator described in this report.

This paper presents the design and development of a lunar mining excavator. After extensive research, the evolution of conceptual designs and finite element analysis simulations, the model was then fabricated. Several past, current and future technologies that could be used as an application for lunar excavators were examined. These included surface mining technologies, the design of previous lunar simulant excavators and robotic rovers that successfully operated on the Moon and Mars. Based on the knowledge gained from this research, ideas were formed and 3D models were created on SolidWorks. Stress, strain and maximum displacements of different sections of the robot were then created and analyzed to ensure a sturdy, reliable and efficient robot.

The paper is organized as follows: An outline of the robot is demonstrated in Section 2. Conceptual models and the final design are presented in Section 3. The development and fabrication of the different sections of the robot are described in Section 4. In Section 5, the results of the stress, strain and

displacement studies are shown and analyzed. Finally, Section 6 summarizes conclusions and outlines plans for future work.

2. Outline and Design Specifications

The design of Pantera primarily focused on three different systems. These systems included:

- Mobility system
- Dumping system
- Collection system

The team set out to build a robot that was compact and efficient. With that in mind, the maximum dimensions of the robot were limited to 1.5 m in length, 0.75 m in width and 0.75 m in height. The weight limit created was 80 kg (~176lbs), which was found by comparing the weights of different prototype lunar mining excavators. The robot also needed to have a rapid collection and dumping rate. Based on research undertaken, a collection and dumping rate of 15.8 kg of simulant per minute was set out to be achieved.

2.1 Mobility System

The wheels of Pantera needed to be able to overcome the craters and small to medium sized rocks that would be seen on the lunar surface. Another challenge involved with the wheel selection was the use of pneumatic tires. Because the robot was aimed to simulate lunar conditions, the pneumatic tires that most vehicles incorporate, could not be used. This is because of the lack of atmospheric pressure in space. It was decided that the wheel system needed to deform to objects and also keep traction in order to move Pantera.

2.2 Dumping System

In order for the dumping of the simulant to be achieved, the bottom edge of the hopper needed to be able to reach a height of 2cm above the analysis bin. The analysis bin stood 1.93 feet above a level surface with a 1.7 foot length and a 1.97 foot width. There were three bins put together with the same dimensions giving the total inside width of the analysis bin to be 5.5 feet.

2.3 Collection System

The collection mechanism utilized a horizontal auger which rotated at high speeds to draw in and throw the soil through a chute. The blades of the auger were housed in a shroud to help direct the flow of the soil to the chute. This housing needed to be able to fit within the frame of the chassis, both in length and in width. The housing of the collection mechanism also needed to be raised and lowered in order to keep the blades of the auger from dragging through the simulant as the robot moved through the lunar surface. For this to be achieved, the design needed to incorporate mechanisms to attach actuators, pulleys and other mechanical systems.

3. Pantera Designs

3.1 Conceptual Model I

The first proposed excavation robot was based around a four-wheeled platform that incorporated elements from current designs of snow blowers and surface mining equipment. The wheels were relatively large and had appropriate treading to allow the excavator to maneuver well in the loose lunar soil and around

small obstacles that would be witnessed on a lunar surface. The mining method used to collect the lunar soil was a two-stage collection system similar to that found in snow blowers. The first stage was a centrally divided spreading auger mounted horizontally at the front of the platform. This spreading auger was run such that it would move the lunar soil towards the center of the auger. At this point the wedge or flat plate created by the joining of the two opposing auger threads would scoop up the soil and throw it with sufficient velocity to reach the nearby second stage. The second stage was composed of a rotating impeller that launched the soil into a guide chute, depositing the soil into an on-board collection bin.

In order for the excavator to be able to drive along the surface effectively, the front auger needed to be raised and out of the way such that it did not collide with any obstacles or create unnecessary drag while the excavator is en-route to or from the mining area. This created the need to be able to lower or rotate the auger assembly into the mining position with either a single degree of freedom prismatic joint, such as an actuator, or a single degree of freedom revolute joint like a high-torque servo motor. In addition to the mechanism necessary to raise or lower the auger, the on-board collection bin will also require another single degree of freedom revolute joint in order to tilt the bin and deposit the collected soil into a collection bin to be analyzed. Combined this makes for two degrees of freedom.

The excavator and operator utilized an IEEE 802.11 b/g in order to simulate wireless control and transmission to and from a mission control center, to the robot. There was at least one camera facing forward that was oriented downrange and another mounted in the front that was to be angled downward to give the operator a view of the simulant immediately in front of the auger during mining. Finally, a third camera was pointing backwards to give the operator a view for depositing the collected simulant into the analysis bin. The specific control interface was likely to be a USB gamepad or a USB joystick along with additional inputs provided by way of a standard keyboard, if necessary. When returning from the mining area to deposit the collected lunar soil, the excavator was placed into reverse control mode where inputs from the control interface produced the opposite output from the driving motors. This will enable the operator to control the excavator normally while driving it in reverse, thus focusing on the rear display.

In surveying both previous conceptual lunar mining excavators and currently used surface mining equipment, the two stage mining system similar to snow blowers was chosen as it would provide several advantages over the mining systems that are typical of previous conceptual lunar mining excavators.

The most significant of these advantages is speed of collection. Even small snow-blowers meant for clearing sidewalks and driveways are capable of removing several hundred pounds of snow per minute. The same technology is used with sand for rapid beach restoration operations which is similar to the mining conditions of a lunar surface.

Another second advantage of the two stage system is that it can be a very robust mining mechanism. This design makes use of only a few moving parts that rotate at high speed. In previous conceptual designs— chains, pulleys, and conveyor belts— were all noted to have been common. While these components have certainly been made to work, installation and maintenance are more difficult.

This combination of high reliability and high speed mining should make for an extremely efficient excavator. Figure 1 illustrates a SolidWorks model of the first proposed design.

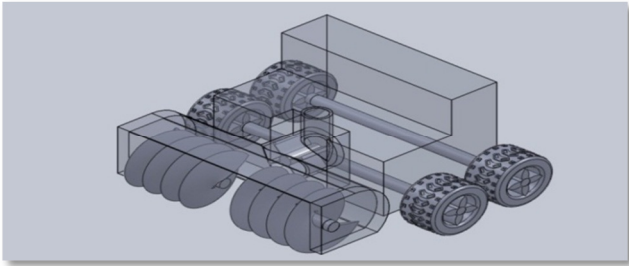


Figure 1. Conceptual design I

3.2 Conceptual Model II

Following the previous design consideration, the Ariel AMP 24 snow blower auger and impeller mechanism was used and the design was built around it. For this case, instead of having a solid body, it was decided for the chassis to be built from the 80/20 aluminum extrusion to reduce the weight of the overall robot. This would allow the robot to be built with less machining time and would be easier for troubleshooting.

The auger's housing would have an extended shoot for the lunar soil to travel after the impeller hits it. This will allow a smooth transition into the hopper.

This design would have a 6-wheeled platform instead of 4-wheels because of the terrain and load analysis. Since the batteries, hopper, collected lunar soil and auger will be in the middle of the robot, the 6-wheeled design would allow for better driving conditions and weight distribution. The front of the chassis would be different than the rest of the robot as it would be smaller on width to reduce the surrounding material needed to enclose the front motors. The hopper will be mainly made out of thin aluminum sheets which would be supported by linear actuators to assist in the dumping mechanism.

A SolidWorks rendering of the second proposed design is shown in Figure 2.

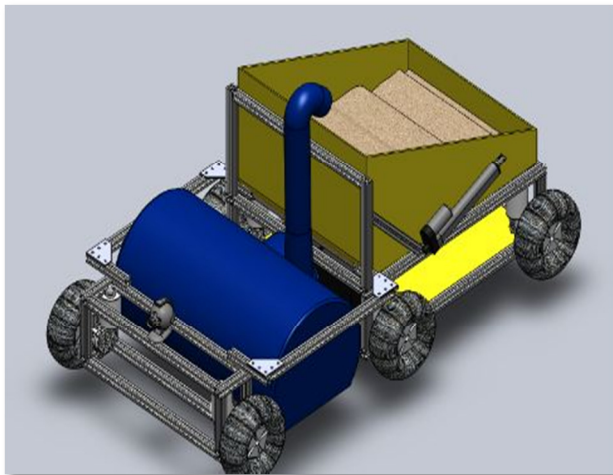


Figure 2. Conceptual design II

3.3 Final Design

For the final design, the Snow Joe SJ620 auger was chosen. The Snow Joe is a more compact and smaller auger than the Ariel AMP 24 auger since the assembly does not have an impeller mechanism and it is a one stage auger. A special housing was made to cover the majority of the auger from the back and the front to reduce dust while mining.



Figure 3. Final design of Pantera

The design would still contain the two pan and tilt camera design, 80/20 chassis and the 6 wheeled platform. The hopper will be made out of a light plastic and re-designed to contain more regolith since the lunar soil characteristics are magnetic and light in weight. Figure 3 illustrates the final design of Pantera.

4. Fabrication of Pantera

4.1 Collection System

In order to create the collection system associated with Pantera, the process was split into five different phases:

- Phase I: Creation of three dimensional model and engineering drawings
- Phase II: Cutting of plastic to reduce weight
- Phase III: Pulley selection
- Phase IV: Mounting of raising/lowering plates

4.1.1 Phase I: Creation of three dimensional model and engineering drawings

In order to aid in the creation of the housing, three dimensional models were created. These models ensured that the housing would fit securely in the chassis with space for linear actuators and linear bearing mounts. The dimensions of the auger blade and how the blade would be mounted was also a crucial factor to the design of the housing. From previous testing, "Clouthing," of soil was a major issue and was also taken into account with the model. Figure 4 shows the engineering drawing of the housing that was used in the creation of Pantera.

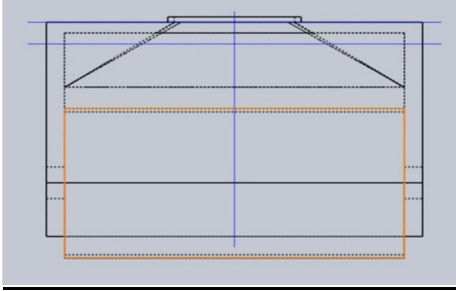


Figure 4. Engineering drawing of housing

4.1.2 Phase II: Cutting of plastic to reduce weight

The housing that came with the SnowJoe SJ620 incorporated many contours and excess material that was not needed for the creation of our robot. These excess materials and contours needed to be trimmed down to help reduce the weight of the overall housing, ensure the housing would fit in the required space and to be able to mount plates to the housing so that it could be raised and lowered. To remove the excess material, a Dremel rotary tool was used. By carefully moving the Dremel through any unnecessary areas, the housing would become more efficient and practical for the use of our robot. Figure 5 and Figure 6 show the before and after pictures of the housing as the Dremel was passed through the excess material.



Figure 5. Before removal of excess material



Figure 6. After removal of excess material

4.1.3 Phase III Pulley Selection

Once the housing was shaved and ready to be used, the next step was to select the pulleys that would give the appropriate

rotations per minute needed to collect the soil. Based on previous testing, it was noted that the SnowJoe's blades originally rotated at 2390 rpm. Due to the large weight related to the motor that came with the SnowJoe, a replacement motor was selected. The specifications of the new motor gave a max rotational speed of 2650 rpm. From here it was decided that the pulley system would have to reduce the rpm's from 2650 down to within 75% of 2390 rpm.

Two pulleys needed to be selected in order to have this reduction, one for the motor and one for the auger. The initial reasoning was to replace both pulleys, but due to how the original pulley on the auger was mounted, that pulley had to be re-used. That pulley had an outside diameter of 5.5". From the given information, the size of the second pulley and belt lengths were calculated from a RPM/Pulley calculator created by the team at www.temecularodrun.com. The pulleys also needed to match bore sizes and availability. With these restrictions applied Table 1 represents the pulley system configuration:

Table 1. Pulley calculations

<u>Name</u>	<u>Dimension</u>	<u>Unit</u>
RPM of Drive Motor	2650	RPM
Drive Pulley Size	4	Inches
Driven Pulley Size	5.5	Inches
Calculated Driven RPM	1927.27	RPM

4.1.4 Phase IV: Mounting of motor and raising and lowering plates

With the pulleys selected, it was then time to mount the motor. The placement of the motor was a crucial portion of the collection mechanism because the motor placement had to be far enough away from the auger pulley to keep a constant tension on the pulley belt. With constant tension, the reduction of slippage is maximized and overall efficiency of the auger motor is increased. Once the location was decided, it was mounted and secured by using two U-clamps.

In order to attach the raising and lowering system to the housing, plates needed to be selected and positioned so that the overall weight of the auger could be evenly distributed when being lifted or lowered. The plate was selected to be in the center of the back of the housing. This position allowed a leveled surface to mount the plate and also provided an even weight distribution on the overall system.

4.2 Dumping System

The hopper construction was made by a series of prototypes. At first, a cardboard mock hopper was made using the dimensions and sketches made in SolidWorks. The cardboard box hopper was fitted with the hardware on the chassis. Since the hardware was modified and not simulated in the simulations, the cardboard box aided with the true width dimensions which included the mounting hardware, nuts and screws. The linear

actuators were attached to the hopper according to the simulations to verify the movements of the hopper to ensure no obstructions were faced.

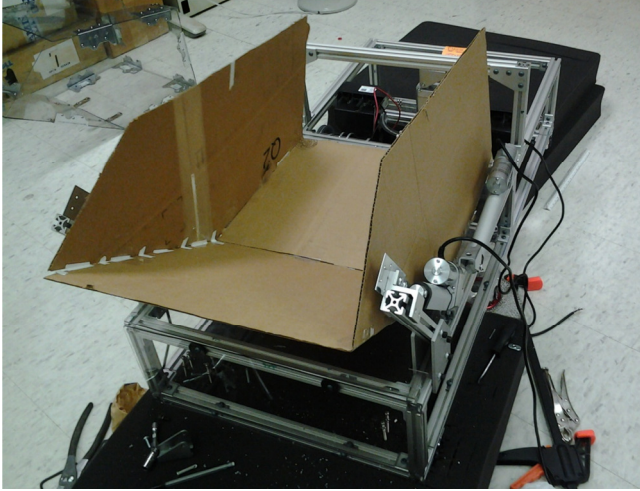


Figure 7. Cardboard hopper mockup

The final hopper prototype was made out of clear polycarbonate plastic with steel angle brackets. The angles in the hopper aid the dumping of the simulant. In the front of the hopper, a specialized box-like opening was cut to aid the soil as it allowed the design to work with the shroud design. The top plastic that was added aided with the sturdiness of the overall hopper and it was able to reduce the clouding caused by the lunar soil. Different steel plates were added in the connecting points of the linear actuators to increase the contact area and to reduce shear. The plastic was cut using an electric saw for the long pieces and a jig saw for the more complicated and smaller cuts required. The holes for the bolts were cut using an electric drill with masonry bits. To ensure the prevention of leaking of the soil, a polycarbonate sealant was used aside from the brackets on the edges of the hopper where more than one side would mate. When the adhesive would dry, a small covering layer of hot glue was added to ensure no leaking.



Figure 8. Final hopper design

4.3 Mobility System

The wheels of Pantera were created using a mixture of chainmail, floral wire, polypropylene balls and a hub in which they can all be wrapped around. The hub used was the Assassin II 4" aluminum bead lock wheel, which is depicted in Figure 9. This wheel was the center of the wheel system and offered good structural support for the tires that were to be created.



Figure 9. Assassin II beadlock rim

Once the wheels were selected, approximately 3 inches were cut from the long side of a sheet of chainmail. The ends of this newly cut sheet of chainmail were weaved together using the European 4 in 1 method. Floral wire was run along the circumference of the sheet on both ends and then the rim was placed in the center of the sheets. The floral wire was then pulled towards the center of the rim while giving enough slack to allow the circumference rings to align with the screw holes of the rim. The rings of the tire were carefully put into place and the screws were lightly tightened. By applying equal pressure to all the screws, the half-made tire was flipped and the chainmail was pulled upwards and filled with the polypropylene balls. The same procedure was followed as before and the bead lock ring was screwed onto the opposite side of the wheel. With this completed, one tire was completely assembled. Figure 10 represents a completed Pantera tire.



Figure 10. Final wheel assembly

The goal was to select a wheel size that was not too big and would produce a ground contact pressure that would be safe for lunar conditions, less than 7 to 10 kPa.

Equation 1. Maximum Lunar weight of robot

$$W_{max,Lunar} = m_{max} \times A_{g,lunar} = 115.9 \text{ kg} \times 1.63 \frac{m}{s^2} = 118.917 \text{ N}$$

Equation 2. Maximum Earth weight of robot

$$W_{max} = m_{max} \times A_g = 115.9 \text{ kg} \times 9.81 \frac{m}{s^2} = 1136.965 \text{ N}$$

Equation 3. Individual wheel ground contact patch area

$$\text{Individual Wheel Contact Patch Area} = \frac{\text{Area}_{contact}}{\text{Wheel Width}} = \frac{\text{Contact Patch Length}}{\text{Contact Patch Length}}$$

Equation 4. Total ground contact patch area

$$\text{Total Contact Patch Area} = \frac{\Sigma \text{Area}_{contact}}{\text{Wheel Width}} = \frac{\text{Contact Patch Length}}{\text{Contact Patch Length}} \times \text{Number of Wheels}$$

Equation 5. Lunar ground contact pressure

$$P_{Lunar} = \frac{W_{max,Lunar}}{\Sigma A_{contact}}$$

Equation 6. Earth ground contact pressure

$$P_{earth} = \frac{W_{max}}{\Sigma A_{contact}}$$

Table 2. Ground contact pressures for various patch areas

Wheel Width (cm)	Contact Patch Length (cm)	Contact patch Area (cm ²)	Total Contact patch Area (cm ²)	Lunar Ground Contact Pressure (kPa)	Earth Ground Contact Pressure (kPa)
5.08	10.16	51.61	309.68	6.10	36.72
5.08	12.7	64.52	387.10	4.88	29.37
5.08	15.24	77.42	464.52	4.07	24.48
5.08	17.78	90.32	541.93	3.49	20.98
7.62	10.16	77.42	464.52	4.07	24.48
7.62	12.7	96.77	580.64	3.25	19.58
7.62	15.24	116.13	696.77	2.71	16.32
7.62	17.78	135.48	812.90	2.32	13.99
7.62	20.32	154.84	929.03	2.03	12.24
10.16	10.16	103.23	619.35	3.05	18.36
10.16	12.7	129.03	774.19	2.44	14.69
10.16	15.24	154.84	929.03	2.03	12.24
10.16	17.78	180.64	1083.87	1.74	10.49
10.16	20.32	206.45	1238.71	1.53	9.18
10.16	10.16	103.23	619.35	3.05	18.36

4.4 Electronic System

4.4.1 Electrical System Analysis

In order for Pantera to be successful and safe the electrical system had to be designed with four main goals. These were: having sufficiently high voltage, current, and capacity ratings to power all devices onboard, using components capable of handling the power they would be transmitting, and keeping the weight as low as possible.

For the drive motors, the current drawn was calculated by dividing the required torque per motor by the torque constant. When surveying available gear motors it was commonplace for torque constants and gearbox efficiencies not to be published by the manufacturers of gear motors. When the torque constants were not available, estimations on the current drawn had to be made using the common peak efficiency/peak power ratings. When gearbox efficiencies were not published, the very high reduction ratio required justified estimating a low efficiency of 65%. A gear ratio of 256:1 was found to be common for planetary gearboxes and was thus used for the majority of torque calculations.

Equation 7. Torque at the motors

$$T_m = \frac{T_w}{\eta \times n} = \frac{9.417 \text{ Nm}}{.65 \times 256} = 0.0566 \text{ N} \cdot \text{m}$$

Equation 8. Current drawn by drive motors

$$I = \frac{T_m}{k_t} = \frac{0.0566 \text{ N} \cdot \text{m}}{5.7 \frac{\text{mN} \cdot \text{m}}{\text{A}}} = 9.93 \text{ A}$$

Table 3. Electrical components of Pantera specifications

Component	Quantity	Voltage Range (VDC)	Maximum Current Drawn (A)
Drive motors	6	6.0 – 14.4	10
Auger motor	1	12	70
Mining system linear actuator	1	12	5
Dumping system linear actuator	4	12	5
Camera	2	5	2
Microcontroller	1	7-12	1

4.4.2 Battery Analysis

The battery system for Pantera would need to be of sufficient voltage to adequately power all the onboard components. Early on this requirement was seen as easy to achieve since no voltage greater than 12 V was required by any single component.

In order to calculate the maximum continuous discharge the various phases of the mining competition were analyzed to determine which would require the most continuous current. Considering that the motor driving the auger far alone exceed the current requirement of any other system, the mining portion of the

competition was focused on to determine the continuous current requirement. The main components drawing current are: six drive motors, auger's motor, microcontroller, and a single camera.

To simplify calculations and introduce another layer of safety the maximum expected current drawn by each of the following components was rounded up and summed for the battery calculations. The values of current drawn for the motors was rounded up to the nearest ten and the current drawn for the camera and microcontroller was rounded up to the nearest whole number.

Table 4. Maximum current drawn by components running simultaneously during excavation

Component	Quantity	Current drawn (A)	Total current drawn
Drive motors	6	10	60
Auger motor	1	70	70
Camera	1	2	2
Microcontroller	1	1	1
Total			133

As seen in Table 4. Maximum current drawn by components running simultaneously during excavation **4Error! Reference source not found.**, the auger's motor alone accounts for more than half of the current drawn during mining and the total continuous current required during mining could be as high as 133 Amps. Such a high continuous current requirement could not be met by single lightweight battery packs and would likely require two or more battery packs to be installed in parallel.

Equation

9. Continuous current requirement during mining

$$I_{battery,continuous} \geq I_{mining} \therefore I_{battery,continuous} \geq 133 A$$

Similar to the calculations for continuous current, the required battery capacity and runtime were calculated using the most power intensive phase, mining. It was impossible to accurately estimate the power requirements, however, the mining phase would require far more current than any other portion of the robot and would very likely take up less than a quarter of the total mining time. Because of this the team decided to select battery pack/s that would allow for more than five minutes of continuous mining.

Equation 10. Required battery capacity for sustained mining

$$Cap_{battery} \geq I_{mining} \times T_{req,mining} \\ = 133 A \times \left(5 \text{ min} \times \frac{1h}{60 \text{ min}} \right) \cong 11.1 Ah$$

Initial searches through online battery retailers did not yield any results for lightweight battery packs with capacities of at least 11.1 Ah. The proposed solution was to install two or more lightweight lithium polymer (LiPo) battery packs with capacities of 8000 mAh and continuous discharge rates of 128 A in parallel. As long as these battery packs were rated for at least 12 V, the capacity and continuous current ratings for the whole system

could be adjusted by simply adding more in parallel. It was not necessary to install more than two in parallel though, as the following calculations show that two have more than enough capacity and continuous current capacity.

Equation 11. Continuous discharge rating for candidate battery packs if installed in parallel

$$2 \times I_{battery,continuous} \geq I_{mining} \therefore 256 A \geq 133 A$$

Equation 12. Mining runtime with candidate battery packs in parallel

$$T_{mining} = \frac{(2 \times Cap_{battery})}{I_{mining}} = \frac{(2 \times 8000mAh)}{133 A} \\ \cong 0.12 h \times \frac{60 \text{ min}}{1 h} = 7.2 \text{ min}$$

4.4.3 Wiring Analysis

The wiring for Pantera was split into two main categories. These were signal wires and power transmission wires. The signal wires were only for control and feedback signals from the various motor controllers and the potentiometers built into the potentiometers. These signals were low voltage and very low current, less than 40 mA and thus, narrow AWG 24 wiring was used for signals.

As the name suggests, the power transmission wires were used to transmit power to the various motors and cameras on Pantera. These wires had to carry considerably more current at higher voltages than the signal wires. The auger motor's power transmission wires had to be especially robust, as that motor could potentially stall at 133 A. Therefore, the power wires would temporarily have to deal with a great deal of current before a fuse was blown. Since all of the wire lengths in Pantera would be fairly short, generally two feet or less, the required gauges of wire could be the same or only slightly bigger than what came on the battery and auger motor. These gauges are AWG 13 and AWG 14 respectively.

5. Finite Element Analysis

The program SolidWorks 2010 was used to run the Finite Element Analysis (FEA) for the main components of Pantera. This software allows us to analyze the main critical points subjected to the most stress, strain and deformation according to the materials properties and applied forces.

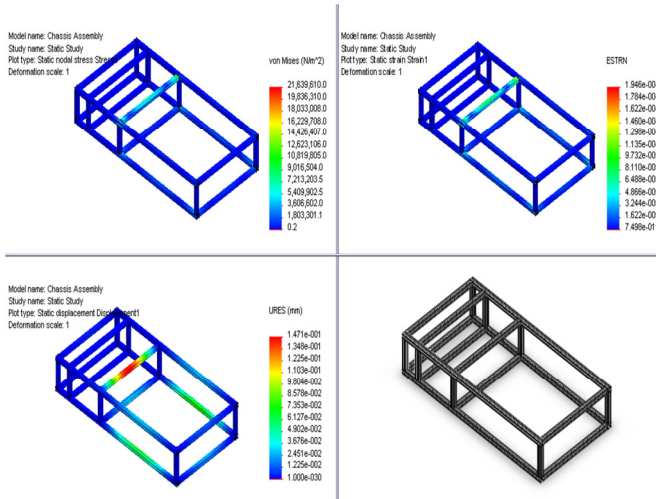


Figure 11. FEA analysis of chassis

Table 5. FEA results for chassis

Name	Type	Min	Location	Max	Location
Stress1	VON: von Mises Stress	0.218	(-0.368	2.16396e +007 N/m^2	(14.62 51 in, 6.539 82 in, Node: 10.00 59 in)
		214 N/m^2	13 in, 3.492 13 in, Node: 62852 0		
Displacement1	URES: Resultant Displacement	0 mm	(-0.407	0.147056 mm	(15.49 21 in, 7.148 54 in, Node: 0.624 922 in)
		Node: 41946 2	0.251 846 in, -10 in)		
Strain1	ESTRN: Equivalent Strain	7.498 2e- 011	(3.590 21 in, 3.483 35 in, Element: - 37164 5	0.000194 646 Element: 231859	(15.41 89 in, 6.503 3 in, 10.06 93 in)

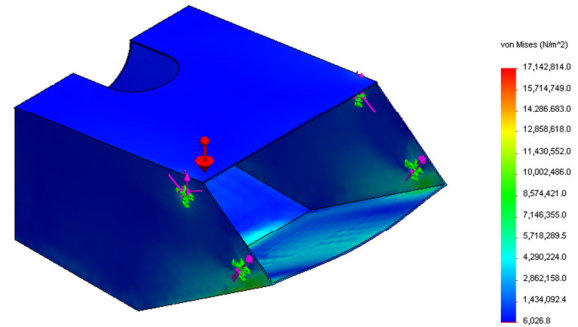


Figure 12. Stress analysis of hopper

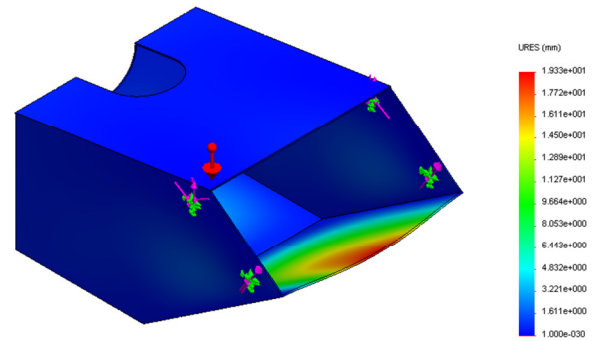


Figure 13. Displacement analysis of hopper

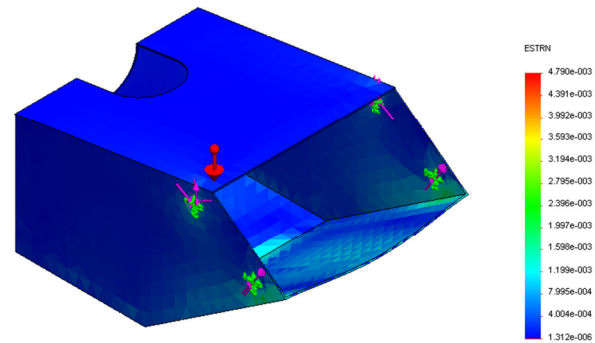


Figure 14. Strain analysis of hopper

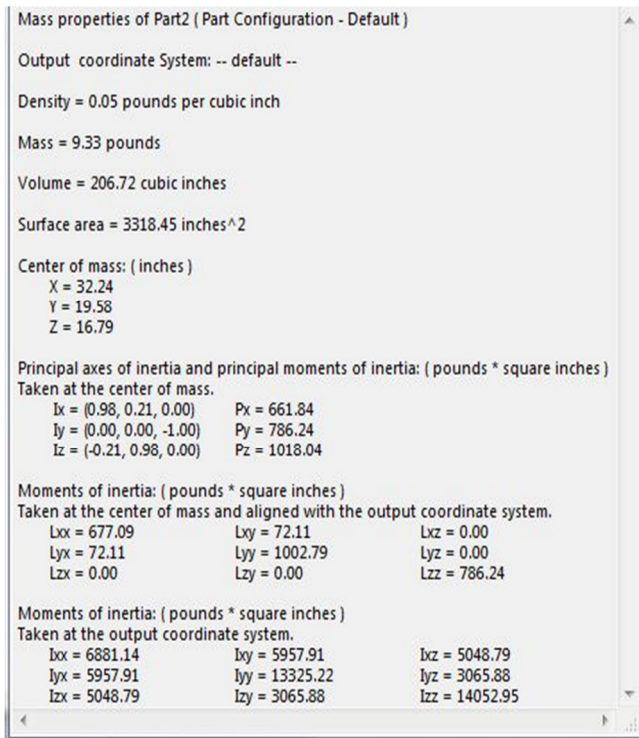


Figure 15. Hopper mass properties analysis

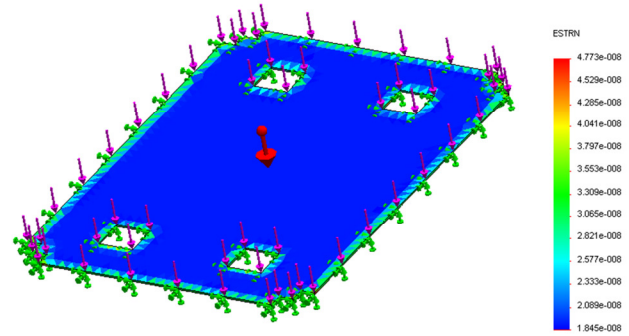


Figure 18. Bottom plate strain analysis

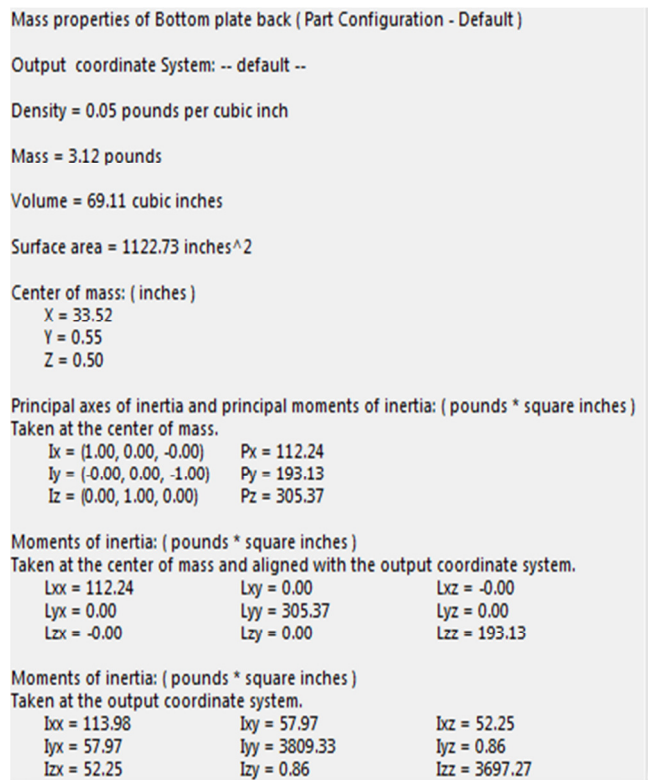


Figure 19. Bottom plate mass properties analysis

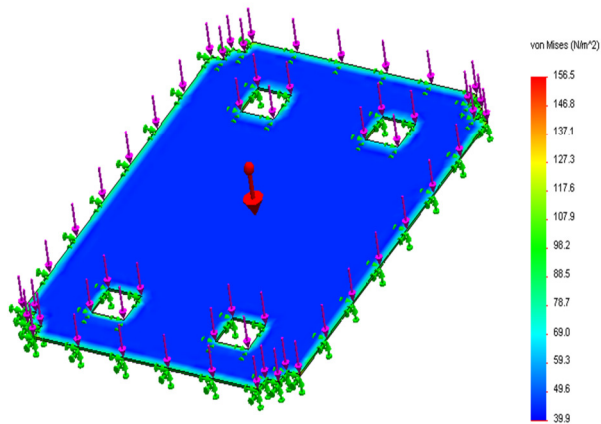


Figure 16. Bottom plate stress analysis

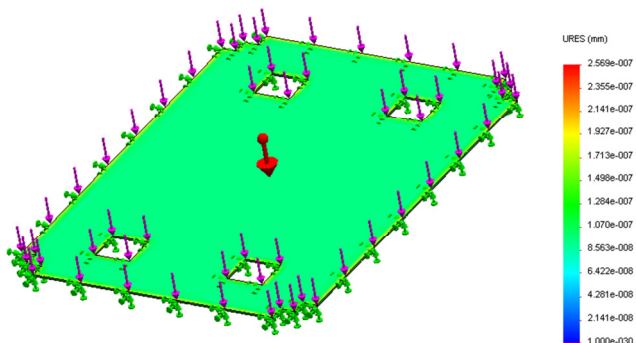


Figure 17. Bottom plate displacement analysis

Even if the simulations did show that the polycarbonate would withstand the forces applied with 100 lbs. of lunar simulant, it does not include the bolts, screws and plates that are used in the actual hopper, which was made with human error. The bottom plate also does not display the bolts added nor the shear or strains caused by them; instead they are shown as a uniform force.

6. CONCLUSIONS AND FUTURE WORK

Development of a lunar mining excavator offered a great experience to the entire design team. However, one lesson learned is that the scale of the project is one that demands many resources in labor, money and time. This project could not have been accomplished without the recruitment of other team members of different disciplines. These members include Jonathan Broche, Alberto Chestaro, Kristopher Rosado and the assistance of Mr. Richard Zicarelli, Director of Engineering

Manufacturing Center. Without the assistance of these team members, the electronic wiring, programming and many of the machining tasks could not have been completed in time. Therefore, as part of future recommendations, we suggest that the appropriate size in team members be at minimum five fully available and involved persons.

When designing a lunar excavator, it is important to have firm conceptual designs and the pros and cons of every aspect of the robot design must be carefully evaluated. Successful evaluation of the options and team consensus on the final design selection definitely provides the team an edge.

Based on the task definition at hand, it is almost impossible to create a fully functional, efficient robot at low cost. Many of the elements needed to power, move and communicate with the robot are relatively expensive. It is advised that any team willing to attempt such a rigorous project must search and obtain a substantial amount of funding from various resources. With sufficient funding, component selection can be carried out with respect to efficiency, and cost sacrifices can be kept to a minimum; thus, creating an efficient robot.

7. References

- [1] P. D. Spudis, "Mining the moon," *American Scientist*, vol. 94, no. 3, p. 280+, 2006.
- [2] New Scientist, "Lunar to-do List," *New Scientist*, vol. 182, no. 2442, p. 5, April 2004.
- [3] New Scientist, "China's moon plan. (Dispatches)," *New Scientist*, p. 8, 2003.
- [4] Design News, "Moondust's potential sparks lunar designs," *Design News*, p. 35, 1992.
- [5] A. a. G. L. Boyle, "Rocks to riches: Once it was all about exploration. Now exploitation is the name of the game.," *New Scientist*, p. 28+, 2002.
- [6] NASA Lunabotics, "NASA: Education @ Kennedy," 27 October 2011. [Online]. Available: http://www.nasa.gov/pdf/485336main_LunaboticsFAQ.pdf. [Accessed 29 October 2011].
- [7] R. P. Mueller and P. J. Van Susante, "A Review of Lunar Regolith Excavation Robotic Device Prototypes," in *Space 2011 Conference*, Long Beach, 2011.

Robotic Tennis Ball Collector

Neha Chawla, Wuqayan Alwuqayan, Ahmed Faizan, Sabri Tosunoglu

Department of Mechanical and Materials Engineering
Florida International University
Miami, Florida, USA

305-903-8455, 786-419-0915, 786-972-7523, 305-348-1091

walwu001@fiu.edu, nchaw002@fiu.edu, afnu001@fiu.edu, tosun@fiu.edu

ABSTRACT

This paper describes a robot to collect tennis balls in a driving range and is called as Robotic Tennis Ball Collector (R.T.B.C). This system avoids stopping the players for ball collection permitting a higher use rate of the field. The purpose of this prototype is to avoid any object found on its way and pick up tennis balls by detecting and then collecting them. R.T.B.C will reduce the time and effort required in collecting the tennis balls from around the tennis court.

1. INTRODUCTION

Robots have always been an object of fascination in our society. They have been portrayed as humble servants of man as well as evil creations that rise to overthrow their masters. All robots share one thing in common at the root of their design and purpose - they can perform tasks in place of humans. Life is filled with many repetitive tasks, and if robots are able to perform those tasks, they can help to ease an overarching burden. With that said, robots are optimal replacements for humans in a multitude of scenarios. As simple as it may seem, the primary action in many repetitive tasks is picking up objects and moving them to other locations. Be it picking up garbage from the floor, moving parts along an assembly line or removing fallen debris, robots that can pick up and move objects will always be useful.

Tennis players develop their skills by repetition, in order to achieve that goal they practice with several balls one after the other. After the balls are finished, the player and the instructor have to pick up the balls to continue the training, wasting money and valuable time. Nowadays, the balls pick up and its delivery to the balls dispensing machine is carried out with human intervention, by using some machines with trolleys but always driven by humans. In order to improve this task, the need for dedicated and specialized vehicles is becoming a must, not only to speed up the task but also to reduce the maintenance costs of the whole system. The main goal of this project is to design and build a prototype of a tennis ball collector which will be useful indoors and outdoors. The prototype is able to walk freely on the floor avoiding obstacles. The prototype is able to locate tennis balls and pick them up

2. HISTORY OF TENNIS

Some people believe that that the ancient Egyptians, Greeks, and Romans played different versions of tennis. Drawings and descriptions of any tennis-like games have not been discovered, but a few Arabic words dating from ancient Egyptian times are

cited as evidence. The theory goes that the name tennis derives from the Egyptian town of Tinnis alongside the Nile and the word racquet evolved from the Arabic word for palm of the hand, rahat.

Tennis was first created by European monks to be played during religious ceremonies for entertainment. When it began, the player hit the ball with the hand. Soon after that leather glove came into existence which was later replaced with a handle for effective hitting and service of the ball and thus a racquet. Tennis balls underwent frequent alterations due to the evolution of racket from the first wooden ball to leather ball filled with cellulose material.

The game was cherished by the monasteries across Europe during the 14th century. The royal family of France adopted this game during 16th and 18th centuries and was called 'Jeu de paumme' and was regarded highly by kings and noblemen as the game of palm. The French players would shout 'Tenez' which meant 'Play' when the game would begin and later the game was called 'Tennis'.

In 1480, Louis XI of France forbade the filling of tennis balls with leather, sand and sawdust but instead be made with good leather and filled with wool. Scottish craftsmen made tennis balls from a wool-wrapped stomach of sheep or goat and tied with rope. Some that were recovered from hammer beam roof of Westminster Hall during restoration were found to be manufactured from a combination of putty and human hair.

In 1874, Major Walter Wingfield acquired the patent rights for equipment and rules for the game which bore close resemblance to modern tennis. Charles Goodyear invented vulcanized rubber and since then Germans have been most successful in developing vulcanized air filled rubber balls.

The first tennis court emerged in US in 1874. The original court devised by Wingfield was in the shape of an hourglass which tapered at the net. It was shorter than the modern court which we have today.

Wingfield's design of tennis court and rules underwent several changes since then till the game gave to the modernized version which is played today. Later the game spread to different parts of the world like India, Russia, China and Canada.

In 1877, the All England Club held the first Wimbledon tournament, and its tournament committee came up with a rectangular court and a set of rules that are essentially the game we know today.

The net was still five feet high at the sides, a carryover from the game's indoor ancestor, and the service boxes were 26 feet deep, but by 1882, the specifications had evolved to their current form.



Figure 1: Early field-tennis

Tennis balls must conform to certain criteria for weight, size, deformation and bounce criteria to be approved for regulation play. According to the International Tennis federation (ITF) the official diameter of the tennis ball is approximately 6.7 cm (2.63 in.) and weight is around 57 gms. It is generally bright green in color. To modify their aerodynamic properties they are covered in a fluffy fibrous felt. A ball is tested for bounce by dropping it from a height of 100 inches (2.54 m) onto concrete; a bounce between 53 and 58 inches (1.3462 - 1.4732 m) is acceptable (if taking place at sea-level and 20°C / 68°F; high-altitude balls have different characteristics when tested at sea-level). Modern regulation tennis balls are kept under pressure (approximately two atmospheres) until initially used.

Professional tennis matches can generally last for more than 3 hours with a rest period of little more than 10 minutes between sets. Training for such endurance matches becomes difficult without a partner of adequate skills hence tennis players use automatic ball launching machines to train without a partner. An automatic ball launching machine that holds 100 balls will launch balls at an average rate of 10 balls every 29 seconds. Therefore, the total time the machine can last without the need to refill would be

$$\frac{29s}{10\text{Balls}} \times 100\text{balls} = 290 s \quad (1)$$

Hence the maximum time that a tennis player can play with an automatic ball machine is around 4minutes and 50 seconds. After this, the player will have to stop to collect around the tennis court using a bottom loading basket. This is a stressful and time consuming procedure which is generally despised by avid players. By experimenting it was shown that it would take in an area of

2:15 to manually pick up 85 balls. It was thus determined that the player would take 2 minutes to pick up all the balls after using the full capacity of tennis ball machine.

$$\frac{135s}{85\text{Balls}} \times 100\text{balls} = 158 s \approx 2:38\text{min} \quad (2)$$

Hence, it shows that according to the available technology, a player will spend approximately 35% of time collecting tennis balls instead of playing. The delay also leads to long annoying and tiring breaks and increases the match time considerably making the players more tired.

3. CONCEPTUAL DESIGNS

Employing humans to collect balls from around the tennis court is generally done while playing a professional match but is not feasible for players while training because it will be costly. Various projects have been performed by students in colleges to find a solution for collecting balls around the tennis court. They have used the knowledge of Robotics to build robots which could perform the required tasks. Listed below are a few examples of the projects that were done for collecting the tennis balls.

3.1 Vacuum Cleaner Type Collector

A tennis ball collector was designed on the principle of a vacuum cleaner. The handling is simple for any person. The capacity of the collector is up to 200 balls.



Figure 2: Conceptual design 1

3.2 Eagnas Roller Ball Collector

Eagnas roller ball collector is a simple and effective way of quickly and easily gathering up tennis balls from the tennis court. As it is rolled along the balls pop up through the bars and get into the barrel section.

Once all the balls are collected the collector is up-ended and sits upon the handle. A locking pin can then be used to prevent the barrel from turning and a section of the barrel hinges opens as a door.



Figure 3: Conceptual design 2

3.3 Bear Claw Collector

There have been several products which are introduced in the market in order to collect the tennis balls. Robots have been designed to collect balls from around the tennis court. Bear claw tennis ball collector has been designed by students at Berkeley University which uses a camera with color tracking that navigates to tennis ball and uses the mechanical claw to grab the ball, lift it and put in the onboard basket.

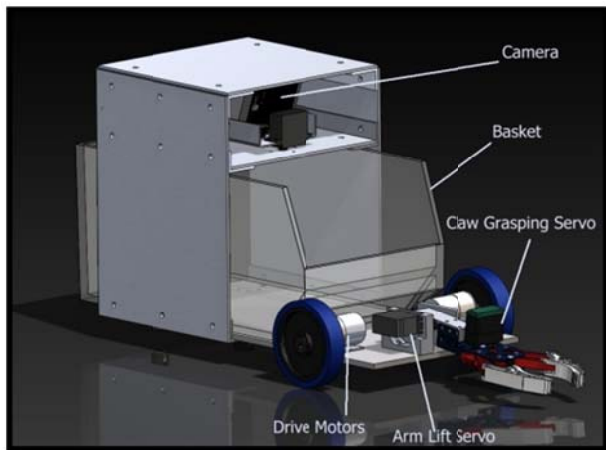


Figure 4: Conceptual design 3

3.4 Ballbot Project

BallBot Project by Dominic Ford consists of a microcontroller which captures frames from camera on board the robot, analyses them, locates objects which look like tennis balls, navigates to them and collects them. After collecting all the balls around the court, it dumps all the balls in the assigned location.



Figure 5: Conceptual design 4

4. PROPOSED DESIGN

When we decided that our final project would be a robotic tennis ball collector we had several ideas on the concept and the design. After trying to incorporate every important aspect of the different designs we considered we came up with our ideal design. The ideal design would be something as described here on. It would have an RC platform with the cavity or enclosure for storing the tennis balls underneath it.

The enclosure would have a one way valve which would act as a restriction offering motion of the balls only in one direction hence not allowing the balls to fall out once they were forced into the cavity or enclosure. The enclosure would have RC controlled gates in front of it which would open and close forcing the balls that are in its reach into the cavity. The RC platform would be able to charge using a charging pad which works on the principle of inductive charging. Due to the constraints of time and fiscal inputs we had to modify the design to something that would be more feasible. The final design had the enclosure in front of it in the form of a box made out of Styrofoam backed with very thin plywood layer to add strength.

The RC controller for the gates had to be different than the remote for the RC platform. In the ideal design it would be replaced with just a button on the controller for the platform since that is what its essential function is, to act as a switch. Also we had to scale the whole design down to be used for smaller sized Nerf balls instead of tennis balls. At the end of the day as a team we were satisfied with the prototype for the project as it showed our potential design and validated its feasibility.

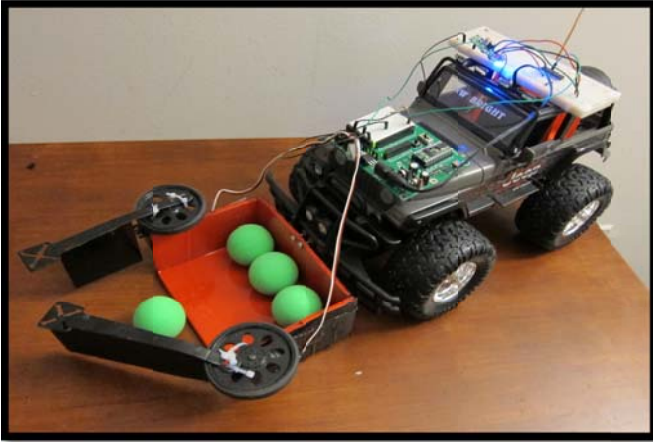


Figure 6: Prototype of the proposed design

5. BUILDING THE PROTOTYPE

A miniature scale prototype was built, assembled, and tested. For demonstration purposes the prototype utilizes an RC platform. The building process was divided into four major steps:

- Remote control circuit
- Gate controlling circuit
- Ball cavity enclosure
- Actuators operated gate

5.1 Remote Control Circuit

To build a remote control circuit, a microcontroller out of a broken helicopter was used (Figure 01). The microcontroller outputs were identified. There were two sets of outputs, the left trigger uses a common ground (IO2) with one node that goes from 0 to 5 VDC (IO1) and the other goes from 0 to -5 VDC (IO3). As the remote control throttle is increase from the lowered position to the top position the voltage from IO1 and IO3 increase from 0, being the lowest position, to 5 VDC and -5 VDC respectively. IO2 and IO1 are then connected to a relay in our transition phase. The relay named K2 uses 5 VDC to activate a contact that connects the two lower legs. When activated our Vss is then allowed to ground out the center of the two resistors, giving us a low value.

The right trigger uses a different circuit due to the changes in the circuit in the helicopter micro controller. The controller has two pins, IO4 and IO5, for the right stick. When in the neutral position (middle position) both IO4 and IO5 will give 0 VDC. When the controller is moved into the lower position we will get IO4 at 0 VDC and IO5 at 5 VDC. Finally when the controller is moved in the upward position we get IO4 at 5 VDC while IO5 is at 0 VDC.

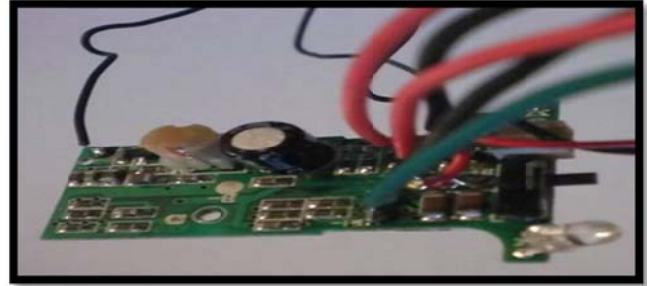


Figure 7: RC microcontroller

5.2 Gate Controlling Circuit

In order to build a circuit that would control the open/close gate, a Boe-Bot circuit board was used. The Boe-Bot circuit board must receive and interpret signals that would be coming from the RC circuit. Since the Boe-Bot does not interpret negative voltage a ULN2030A transistor array had to be used. This chip uses 5 VDC to power it, same as Boe-Bot circuit board. When the node on the left is given 5 VDC the node directly to its right will drop to 0 volts and when the node is grounded to 0 VDC the respective node will produce 5 VDC. The nodes are paired off horizontally 2 to 17, 3 to 16 and 4 to 15 continuing in this order. Using our 0 VDC ground as VSS we can produce a drop in the Boe-Bot's circuit board Pine #1 and #2 by grounding the node between the resistors to VSS.

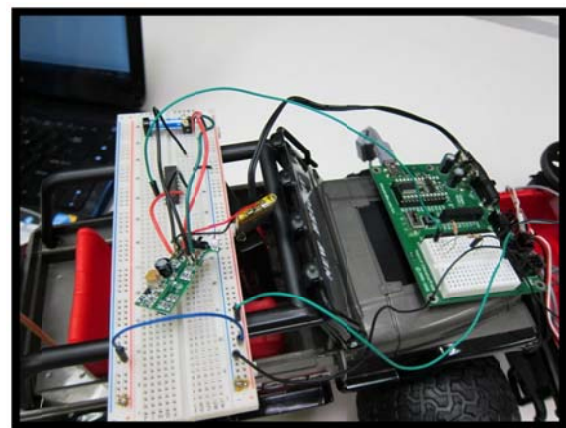
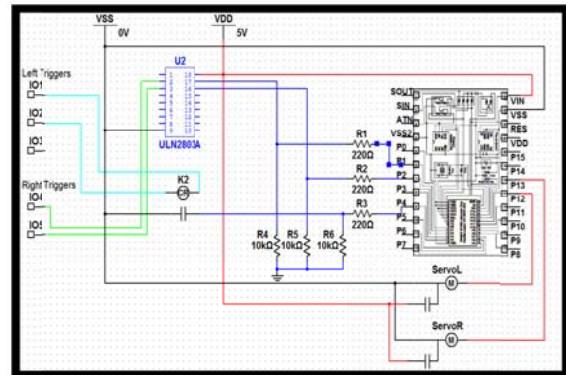


Figure 8: Gate circuit and circuit diagram

5.3 Ball-Cavity Enclosure

A rectangular shape box was designed and built to resemble the ball-collecting enclosure. The box has an open frontend and its dimensions were carefully considered such that it will not restrict the front wheels motion of the RC vehicle (Table 01). The weight of the box was also taken into consideration. IT has to be adequate, light enough to be moved around by the RC vehicle, yet rigid enough to withstand mounted actuators and prevent any possible collapse. The box interior was made out of foam board and the exterior was made out of lightwood board for reinforcement. The ball-collecting enclosure was double coated for surface protection and mounted to the frontend of the RC vehicle with 5mm ground clearance to ensure smooth maneuver and operation. Width length height dimension inches

Table 1: Ball-cavity dimensions

Ball-Cavity Enclosure	
Dimension	cm
Length	11.5
Width	16.5
Height	7



Figure 9: Balls cavity enclosure

5.4 Actuators-Operated Gate

Servo- actuator gate was designed and built. The gate consists of two open/close claws that would push the ball inside the cavity via remote control. Claws dimensions were carefully selected (Table 02); one claw is longer than the other to insure necessary force required to push the ball all the way in. The shorter claw acts as a bull-guide to prevent balls from slipping away upon collection. The claw frame was made out of aluminum to minimize the weight without compromising the needed rigidity and strength (Figure 10). The claw body was made out of Styrofoam for easy mold and mount. The claws were double coated for proper protection and functionality. The assembly was connected to the actuator servos and mounted on the ball-cavity walls.

Table 2: Claws dimensions

Gate-Claws Dimensions "cm"		
	Left Claw	Right Claw
Length	14	7
Height	7	7
Thickness	0.5	0.5



Figure 10: Gate-claws assembly

6. PROGRAM ALGORITHM

Two circuits were built to operate the open/close claws via remote control. The first circuit (RC-circuit) receives analog signal from the remote control unit and convert them into binaries via microcontroller and ULN2030A transistor array. The output binaries are transferred to the second circuit (Gate-circuit) inputs through ULN2030A transistor. The RC circuit receives continues 5 VDC thus its output remains 1 unless the circuit is tripped which leads to 0 VSS. A very high resistor was used in order to trip the RC circuit when the stick of the remote control unit is pushed UP. Gate-circuit input (P1) controls the status of the left and right actuators (P14 and P15). When the input is 1 (5 VDC) the gate remain close, and when the circuit is tripped the input would be 0 (VSS) thus the gate would open for 3 seconds enabling the user to position the RC platform in the proper place to collect the ball.

A short and simple program code was made using PBASIC. To control the RC output two conditional statements were made and each would run certain subroutines.

- 1- If the input port is activated, the gate claws remain still.
- 2- If the input port is deactivated, the gate claws open for three seconds and then close.

The code details are as follows:

Table 3: Sample Code

```
R.T.B.C.
' {$STAMP BS2}
' {$PBASIC 2.5}

counter VAR Word
DEBUG ? IN1

IF IN1= 0 THEN Open
IF IN1= 1 THEN still

END

                                'Subroutines'
Open:

FOR counter = 1 TO 5                ' Number of pulses.
PULSOUT 14, 750                    ' Right servo stand still.
PULSOUT 15, 850                    ' Left servo full speed ccw.
PAUSE 100
NEXT

FOR counter = 1 TO 40
PULSOUT 14, 750
PULSOUT 15, 750
PAUSE 100
NEXT

FOR counter = 1 TO 6

PULSOUT 14,750
PULSOUT 15,650
PAUSE 75
NEXT
RETURN
```

still:

```
FOR counter = 1 TO 5                ' Number of pulses.
PULSOUT 14, 750                    ' Reight Stand still.
PULSOUT 15, 750                    ' Left servo full speed ccw.
PAUSE 100
NEXT
RETURN
```

7. CONCLUSION

A prototype of the proposed Robotic Tennis Ball Collector was successfully built. The design utilizes a remote control platform and integrates it with two other circuits. The first circuit receives analog signal from the remote control unit and transfer it to a binary through microcontroller and transistor. The second circuit receives the binary signal to control the open/close claws of the balls cavity enclosure. The prototype demonstrates the ability to maneuver easily and avoid obstacles along the way.

The prototype displays minimum human intervention with the task on hand. However, there is still room for further improvements. The objective of the proposed design is to have a fully autonomous robotic platform to execute the task of tennis-ball-collecting. With more time and more available resources, the objective will be met. Furthermore, the model may incorporates some extra high-tech features such as ball weight and/or pressure check that will enable the R.T.B.C to distinguish between valid and invalid tennis balls.

8. REFERENCES

- [1] Heiner Gillmeister, "Tennis: A Cultural History," Leicester University Press, London, England, 1998.
- [2] Luís Fernando Costa Pacheco, André Joaquim Barbosa de Oliveira, António Fernando Macedo Ribeiro, "Mobile Robot for Autonomous Golf Balls Picking," University of Minho, Guimaraes, Portugal, 2008.
- [3] Justin Ellis , Tony Morelli, Amandeep Sohal, "Autonomous Mobile Robots ," University of Nevada, Reno, 2005.
- [4] Johnathon Schultz, Peter Clain, Jesse Miner, "Wall-E Robot," Final Report, Cornell University, Ithaca, New York, 2010.
- [5] Ryan Collier, Mohammed Adham, Perry Haldenby, Kevin Smith, "Autonomous Tennis Ball Collector," Design Report, University of Waterloo, Ontario, Canada, 2009.
- [6] Kevin Dluzen, Jonathan Hall, Diyang Qiu, "PV Autonomous Golf Ball Retriever, University of Illinois at Urbana – Champaign, 2012.
- [7] Rodrigo Andres Barbosa, Karina Chang, ,Luxon Laborieux , Juan Zuluaga, "Self-Piloted Tennis Ball Collector," Final Report, Florida International University, Miami, Florida, 2008.

Viability of Indoor Robotic Air Aquariums

Lazaro Herrera, Francisco Peleato, Jong-Hoon Kim
Discovery Lab, School of Computing and Information Science
Florida International University, 11200 SW 8th St, Miami, Florida 33199
lherr012@fiu.edu, fpele001@fiu.edu, kimj@cis.fiu.edu

ABSTRACT

Zoos and aquariums are visited by 700 million people every year; they are popular tourist locations all around the world and generate billions of dollars of revenue yearly. More than nine million people in the US own a small household fish tank, which indicates a desire to bring some of the aquarium features into their homes.

We considered the viability of real-life indoor aquariums. We found that the deficiencies that lead to the problem are closely related to costs of operation (maintenance), spacing (for housing) and personnel (for upkeep). In this paper, we analyze the problem, provide our current solution to the issue, and discuss future uses of the solution developed in order to tackle this problem.

Our solution is to bring smart robotics and smart algorithms in the form of autonomous robotic fish aquariums into the every-day home in order to deliver awe-inspiring simulated aquariums. The solution tackles the cost of spacing (by moving the aquarium into the air), the personnel (by removing the humans and replacing the fish with robots) and the costs of operation (by requiring just air space and helium).

For this solution, we created environment-aware fish simulators that were capable of replicating basic fish functions (such as swimming) along with full usage of avoidance maneuvering, ultrasonic sensing systems, and Bluetooth wireless networking. A key part of our solution is attempting to improve the existing user interaction between the current generation of robotics and humans from our current rudimentary simple button control to more sophisticated algorithms such as Fast Fourier Transform for voice.

Keywords

Keywords: Autonomous Robot, Aerial Robot, Bluetooth

INTRODUCTION

This paper focuses on the development of test platforms, algorithms and wireless Bluetooth control required for an indoor robotic air aquarium. Because of the inherent cost with water-based home aquarium systems that cannot rival the bigger aquariums, normal home aquariums are both smaller and less impressive. We approached the problem from a biological sense, using robotics to replicate the functions of fish. Implementation of basic swimming motions and obstacle avoidance were a key element to imitating the look and feel of our robotic air aquarium. This paper gives an overview of how we accomplished our solution, challenges, test data and viability assessment.

BACKGROUND

As seen before, millions of people just in the US are willing to spend the money to bring the aquarium experience into their home. For the reasons of cost detailed previously, many companies and people around the world have resorted to robotics in order to make this a reality. At an average \$20 cost per person, current aquariums around the world are capable of making 1.4 billion dollars every year just from the desire of people to see amazing sea creatures in front of their eyes. The average home setup runs between \$100 and \$1000+ for a small home aquarium system and does not fully utilize the space within the home to maximize the user enjoyment of their “aquarium”.

Robotics to simulate marine creatures is not a new concept. In the past, many companies and individuals have used robotics with marine-life-like form in order to simulate realistic marine behaviors. In the past, a German company, Festo and Essex University have used robotics to simulate sea-creatures with their AquaPenguin[3], AquaJelly[4] and AquaRay[5] prototypes, Essex Robotic Fish[12] and expanding it to air sea creatures as well.

The AquaPenguin[3] is a completely autonomous running on an AVR Mega 128 capable of moving through water at 5km/hr. The AquaRay[4] is a wirelessly-controlled robotic manta ray with a maximum speed of 1.8km/hr with a 40Mhz processing unit. The AquaJelly[5] is a light-controlled underwater jelly fish robot running on 2 ATmega168 chips at 8Mhz each with a ZigBit module for radio communication. It has a temperature and pressure sensors along with a 2-way infrared communication system. The Essex Robotic Fish[12] is a \$42,000 robotic fish equipped with chemical sensors in order to detect water pollution.



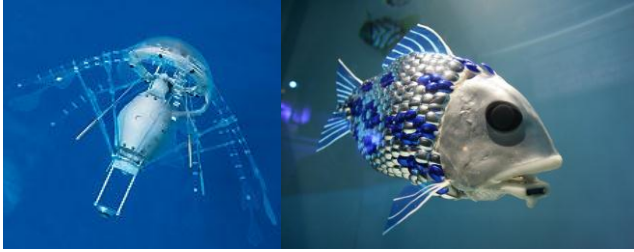


Figure 1. Festo Water Prototypes and Essex Robotic Fish

The AirJelly[1] is a remote-controlled jelly fish robot based on a 3V coreless motor. The AirPenguin[2] is a flying helium filled balloon powered by a 32-bit microcontroller, with a 3-axis compass/accelerometer and wireless 2.4Ghz Zigbee network developed by the German engineering company Festo. It includes other sensors such as a temperature sensor.

We will compare these aerial robots to ours in order to compare viability, cost and features.



Figure 2. Festo Air Prototypes.

STATE OF THE ART

Although the previous robots are great marvels of modern technology, we are going to compare them against our own system in order to show that our system is simply better than theirs in many aspects.

The AirPenguin[1] design is rather innovative and much like ours but is not as cost effective as our expected final design. It also does not implement microphone localization as our finalized product will.

The AirJelly[2] design is only remote controlled and has no autonomous capabilities unlike ours, making it highly unviable for the home entertainment sector.

Our design combines the best of both worlds, implementing an autonomous system along with a direct control system with Bluetooth and the Air Aquarium (AA) Serial communications system. Also, with the advent of the Roomba robotic vacuum cleaning system being used by millions of homes, it is no longer unusual to have robotics within the home.

APPROACH

Our approach to this project first attempted to replicate the basic fish capabilities in order to create a realistic model of the marine life we are attempting to replicate. On this idea, we modeled our robots and our algorithms to accomplish the task.

Robot

Our basic robot prototype is based on the Megafliers™ flying helium fish [9]. The fish is a helium balloon with a guide-rail running down the bottom that allows for altitude changes and a tail to provide propulsion, each one powered by a 1.5v DC motor. Changing the position of the ballast on the guide rail significantly alters the flight dynamics through changing the center of mass causing the fish to pitch up or down; moving the tail while doing this causes the fish to gain or lose altitude. We replaced the stock wireless RF radio control system with our own electronics system powered by an Arduino Nano running at 8MHz powered by a 3.7v 110mah portable battery. Our first stage involved using the microcontroller along with a TB6612FNG Dual Pololu Motor Driver Carrier in order to begin basic movement simulation [10]. The second stage was to interface our sonar sensors to the board as outlined below.



Figure 3. Tail propulsion system

Sensors

For this design, we used two LV-Maxsonar®-EZ1™ MB1010 sonar modules[11]. The modules have an effective range from 6 to 254 inches giving us total environment-awareness capability for our robot models. One of the two devices was attached on the built-in rail for forward range detection as to fulfill one of our primary simulation objectives (basic obstacle detection). The second of the devices was attached as to range the distance to the floor giving us effective height readout of our current position. Our approach was a classic logical approach for the forward sensor, we would monitor if the distance to an obstacle was smaller than our algorithm would allow and if it was, we would trigger an avoidance maneuver. The height sonar was more complex, instead opting for a range of about 70in of “acceptable height” so that the fish was at eye-height; if the fish drifted from that height, it would perform a “dive” or “climb” maneuver.

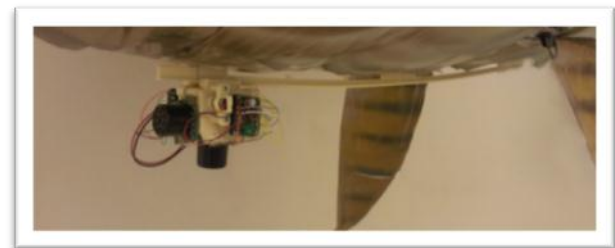


Figure 4. Assembled Sensor Suite on Guide Rail

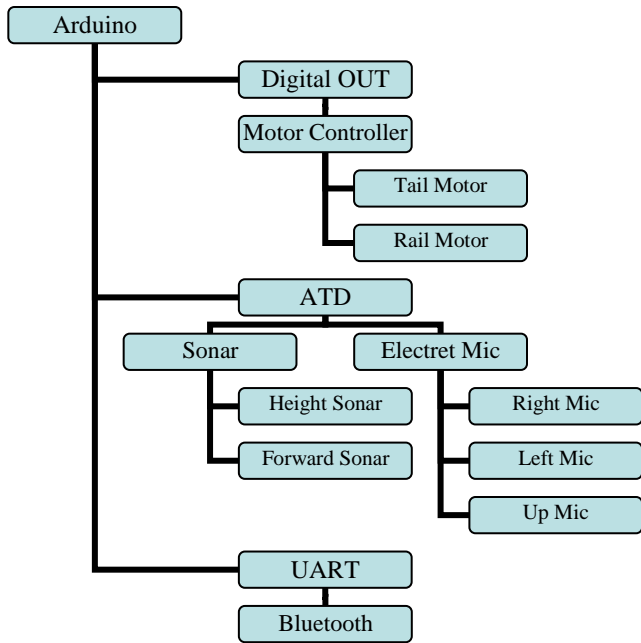


Figure 5. Architecture for final product.

Based on the previous architecture, we built the test platforms in order to test our solution’s effectiveness. The main Arduino board

uses Digital Out (to control the motor controller), Analog To Digital (for sonars and microphones) and UART (for Bluetooth functionality).

Communications

For the communication stage, we interfaced our Arduino board to a BlueSMIRF Gold Bluetooth device and created code to receive, process and execute serial commands using the FLK serial communication protocol we implemented. The Bluetooth standard is a proprietary open wireless technology for exchanging data over short distances (usually less than 30ft.)

The protocol is designed to be reusable and remappable for any Bluetooth project while having the capability of being extensible through the seventh and eighth bit for data length. With that, one can simply add extra hardware such as a LED screen on the side for advertising, or sensors for a data gathering platform; modify the Arduino code to fit the new hardware and it should work with the existing protocol.

The protocol’s specification is detailed below. As can be seen, communication begins with “{“ and concludes with “}”. All data is sent as characters and is delimited by “|” in between each parameter for different commands. A sample command such as requesting a readout of the forward sensor will be sent as follows “{0|1|0|00}” and would return “{2|1|1|2|50}” corresponding to a 50in. readout from the sonar.

Byte #	Description	Function	Value	0	1	2	3	4	5	6	7	8	9	10 thru n	n + 1
0	Message Delimiter	Separate Messages													
0	Beginning of message		{												
1	Operation type	Get	0												
		Set	1												
		Report	2												
3	Operation to perform	Height sensor	0												
		Forward sensor	1												
		Altitude up	2	0 for OFF / 1 for ON											
		Altitude down	3	0 for OFF / 1 for ON											
		Tail right	4	0 for OFF / 1 for ON											
		Tail left	5	0 for OFF / 1 for ON											
		Forward speed	6	0 for STOP / 1 for SLOW / 2 for MEDIUM / 3 for HIGH / 4 for FULL											
		Auto	7	0 for OFF / 1 for ON											
5	Unused		0												
7 & 8	Length of data		00 thru 99												
10 thru n	Data														

Figure 6. Architecture for final product.

For user control, we devised a Java-based Bluetooth control system. Java's capability for cross-platform work makes it capable of being run on any 32-bit Macintosh, Linux or Windows machine. Our main focus was to make easy to understand and allow the user to have control of every basic shark function that the built-in avoidance algorithm had access to. In the end, this was our final iteration of the control system.

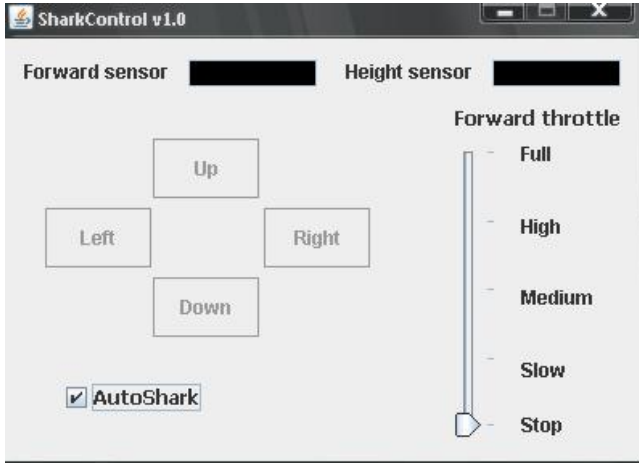


Figure 7. Shark Control GUI

One of the key features is the ability for a user to switch back to autonomous control on-the-fly for any reason as detailed on the following diagram. A simplified logic for our autonomous algorithm is laid out below.

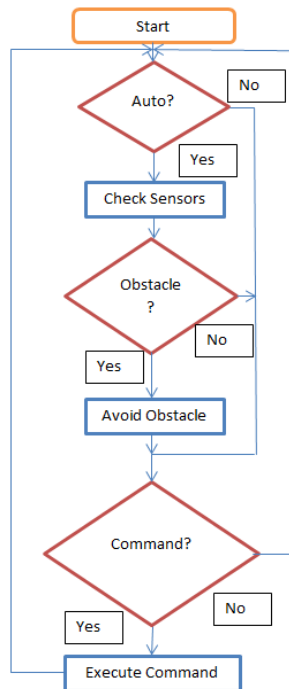


Figure 8. Programming Logic

PROTOTYPING AND EVALUATION

Our test results for the four fish that we created were within the preset test parameters (must avoid obstacles, must replicate fish

functionality, and must be controllable). We created three obstacle-avoiding robots that would fly in “pseudo-formation” and avoided obstacles including each other. The fish would stay within 50in. of any obstacles and would fly between 120in. and 160in. off the ground. Our fourth fish, a “shark model” was equipped with a short-range camera and the Bluetooth control system; the system was tested and worked within acceptable limits. Some issues did exist during the building and testing of these robotic sea creatures and as such, they are detailed below. Figure 8 shows our 3 prototypes, bass, nemo, and shark; the bass has basic obstacle avoidance, the nemo has the microphone localization system and basic obstacle avoidance and the shark has the Bluetooth control system, a camera and basic obstacle avoidance.



Figure 9. Our Prototypes

DISCUSSION

Solutions

During the preliminary integration of the sensors with the motor, we noticed that during the motor power phases all sensor data would be lost. We later on attributed this phenomenon to a critical voltage drop causing the Arduino to reset due to an inability to provide the necessary 2.5V to the sonars and 3.3V to the motor controller system. The problem was solved by separating the power supply for the Arduino and sensors, and the motor controller with one battery each. The extra weight added by the previous solution to the aforementioned motor controller issue caused the test platform to over the planned weight limit of 28 grams worth of electronics. Our solution to this was to puncture the plastic casing that acted as ballast with a drill until we reached our desired weight. The solution exceeded our expectations and allowed every one of our models to be lighter and capable of carrying more equipment for future test runs.

Issues

During the sensor integration stage, it became apparent that the sensors had an issue when the distance was less than 6in. When this situation presented itself, it would return a maximum 254in, unlike what the datasheet listed; causing some issues for our obstacle and height maneuvering logic [7]. Our second problem came from the Sparkfun Electret Microphones, which required a full Fast Fourier Transform pass in order to become usable for our project[8]. The Arduino's 8Mhz processor could not handle the amount of data even with the Arduino FFT library doing the work. As it stands, this is an unresolved issue. During the final stages, our last set of issues appeared. The first issue was simply a Bluetooth range issue when the device went beyond 25ft. and would instantly disconnect [6]. The disconnection would cause the Java GUI to lock up and become irresponsive. The second issue was with the analog wireless camera we installed on the shark; due to interference, the range was simply cut down to about 20ft. leading to severely minimized usable camera range (after 10ft., the picture would be too grainy to be usable for navigation). The solution to this issue will be to move to Wi-Fi Adhoc networking and having a digital camera use the same networking system.

FUTURE WORK

Our tests with this system are far from done. In the near future, we will implement the full "Follow me" functionality to allow users to interact with the aquarium via the electret microphone array detailed in the wiring diagram above. We also expect to expand into the advertising field by creating larger versions of our existing marine creatures and bringing them to life. We expect this to have real-life use as this sort of advertising medium has not been fully explored in the past or used by any commercial entity. We expect these to be done soon in order to be fully commercialized.

CONCLUSION

In this paper we presented our idea about a cost-effective air aquarium to rival the more expensive prototypes around the world.

We built our three prototype models, tested them for viability in the real world and evaluated the true usefulness and capabilities of our current prototypes, and contrasted them with other systems such as the AirPenguin and AirJelly.

We then located issues such as sonar issues, microphone issues, motor controller issues and others. We tackled issues and fixed as many as possible within our current system in order to improve our system for the future. The remaining issues have to be fixed in the future in order to achieve full commercialization.

REFERENCES

- [1] "AirJelly." *Festo Corporation*. Festo Corporation, n.d. Web. 1 May 2012. <http://www.festo.com/rep/en_corp/assets/pdf/AirJelly_en.pdf>.
- [2] "AirPenguin." *Festo Corporation*. Festo Corporation, n.d. Web. 1 May 2012. <http://www.festo.com/rep/en_corp/assets/pdf/airpenguin_en.pdf>.
- [3] "AquaPenguin." *Festo Corporation*. Festo Corporation, n.d. Web. 1 May 2012. <http://www.festo.com/cms/en_corp/9777.htm>
- [4] "AquaJelly." *Festo Corporation*. Festo Corporation, n.d. Web. 1 May 2012. <http://www.festo.com/cms/en_corp/9772.htm>.
- [5] "AquaRay." *Festo Corporation*. Festo Corporation, n.d. Web. 1 May 2012. <http://www.festo.com/cms/en_corp/9786.htm>.
- [6] Bhagwat, P.; , "Bluetooth: technology for short-range wireless apps," *Internet Computing, IEEE* , vol.5, no.3, pp.96-103, May/Jun 2001.
- [7] Drumheller, Michael; , "Mobile Robot Localization Using Sonar," *Pattern Analysis and Machine Intelligence, IEEE Transactions on* , vol.PAMI-9, no.2, pp.325-332, March 1987.
- [8] McDowell, P.; Bourgeois, B.; Iyengar, S.S.; , "Formation maneuvering using passive acoustic communications," *Robotics and Automation, 2004. Proceedings. ICRA '04. 2004 IEEE International Conference on* , vol.4, no., pp. 3843- 3848 Vol.4, April 26-May 1, 2004.
- [9] "Mega Fliers." *Mega Fliers*. WOW Products, n.d. Web. 1 May 2012. <<http://66.215.26.25/products.html>>.
- [10] "TB6612FNG.pdf." *Pololulu*. Pololulu, n.d. Web. 1 May 2012. <<http://www.pololu.com/file/0J86/TB6612FNG.pdf>>.
- [11] "MB1010_Datasheet.pdf." *Matrixbot*. Matrixbot, n.d. Web. 1 May 2012. <http://www.maxbotix.com/documents/MB1010_Datasheet.pdf>.
- [12] "Essex University." *Essex University*. Essex University, n.d. Web. 1 May 2012. <<http://dces.essex.ac.uk/staff/hhu/HCR-Group.html>>

DriMix 4ics – Mobile Autonomous Bartending

Robert Hartwell
University of Florida, Electrical &
Computer Engineering 12315
Clarendon Ct Spring Hill, FL 34609
+1 850 499 0019
peppercrunch@gmail.com

Dr. A Antonio Arroyo
University of Florida
Machine Intelligence Lab (MIL)
Gainesville, FL 32611
+1 352 392 2639
arroyo@mil.ufl.edu

Dr. Eric M. Schwartz
University of Florida
Machine Intelligence Lab (MIL)
Gainesville, FL 32611
+1 352 392 2541
ems@mil.ufl.edu

ABSTRACT

This paper outlines the design methodology, sensor configuration and final implementation of the DriMix 4ics robot. The DriMix 4ics is an automated bartending robot whose gross motor functions can be controlled via color segmentation and recognition, while menu driven drink mixing commands are driven by Quick Response Code. The aim of the robot is simplify the ordeal of what at times can be complicated, mixing of cocktails. Then once the mixing is complete return the cocktail to the appropriate order location

Keywords

QR Code, Color Recognition, Drink Mixing, Bartending, DriMix 4ics, Atmel, Android

1. INTRODUCTION

Drimix 4ics, the Drink Mixer for Alcoholics, was constructed for the Intelligent Machines Design Lab course at the University of Florida. The goal of the robot was to combine two things, creating an autonomous robot and making a drink mixing machine. The main objective of the project was to create a mobile robot that could go to a drink station, mix drinks, and then return to a user with the mixed drink.

This paper will cover: the overall system interaction of the DriMix 4ics, the movement and actuation of the robot, the sensors and their testing conditions, software design principle of the robot, the rudimentary power distribution system, the behavior of the robot, the experimental changes, and the lessons learned. An image of the complete set up can be seen in the Appendix.

2. DRIMIX 4ICS SYSTEMS

The systems of the DriMix 4ics can be divided into three main interaction areas; coding, the mobile platform, and the stationary platform. Coding can further be broken down into three main areas, Android, Matlab, and C on the Atmel. The mobile platform is the robot and the stationary platform is the drink mixing station.

2.1 Integrated systems

The DriMix 4ics uses the Epiphany DIY board [1]. This board is based on the ATXMega64A1 Microcontroller. The platform consists of several sensors, servos, DC motors, wireless communication, batteries, and a drink mixing station. The block diagram shown in Figure 1 describes the basic interactions of the platform as a whole.

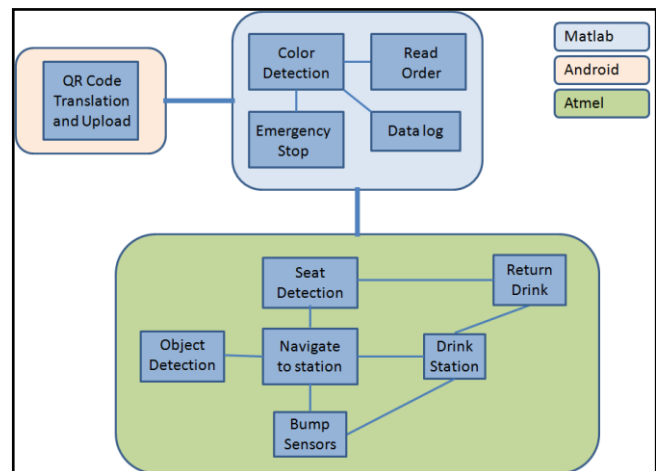


Figure 1. DriMix 4ics systems block diagram

The code in the pink box is controlled by the Android OS on a mobile phone. The communication link between Android and Matlab is either a WiFi, cellular, or LAN connection. The code in the blue box is handled by Matlab on a computer. Matlab would be considered the main “traffic conductor” as it handles the decoded QR orders, the color recognition, data logging, and issuing wireless commands to the robot. The link between Matlab and the Atmel chip on the robot is a simulated RS232 link sent over RF between two XBee modules. The coding in the green box is handled by the Atmel chip on the robot and controls the basic navigation and mixing routines on the robot.

2.2 Mobile platform – the robot

The mobile platform is composed of several layers. Each layer hosts a different sensors, motors, or actuators. The top two layers hold the adjustable servo array. The layer beneath that hosts the infrared rangars. Attached to this layer is the channel for the sliding drink return cart. The layer under this holds the microcontroller, bump switches, and guide rails. The very bottom of the robot hosts the battery packs, switches, DC motors, wheels, and an infrared array. The overall setup can be seen in Figure 2.

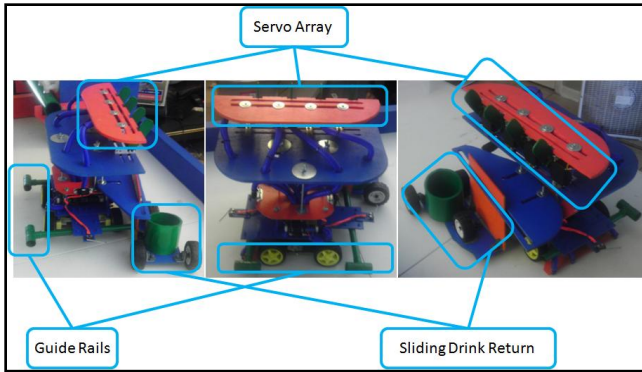


Figure 2. Mobile platform principle components

2.3 Stationary platform – the drink station

The stationary drink mixing station hosts plastic containers that hold various mixable drinks. On top of the levers of each of the spigots are lever guides that ensure the cams from the servo motors do not slip off while pressing down. The down spouts from the spigots are channeled into a larger collector that is angled and open at one end. This allows all of the liquid to be collected in the cup on the return cart. The mixing station can be seen in Figure 3.

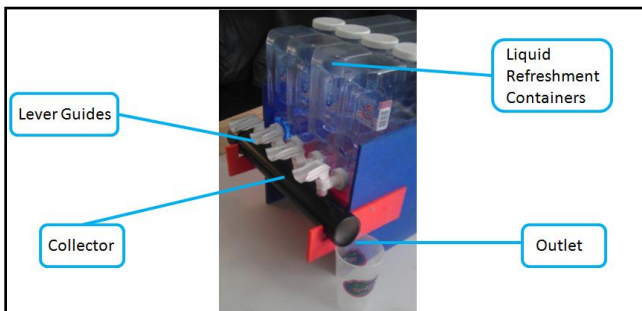


Figure 3. Mixing station principle components

3. MOVEMENT, ACTUATION, DRINK RETURN CART

This section covers the gross movement controls of the mobile platform. Covered first is the movement control of the platform, then the actuation system of the cam lobed servos, and finally the drink return cart.

3.1 Movement

The movement of the DriMix 4ics is controlled by four DC motors, movement is also guided by two guide bars that slide over a larger guide bar running the length of the table top. The guide rails can be seen in Figure 2. The mounting of the DC motors, as well as the specifications of the motors, can be seen in Figure 4. The four DC motors easily have the power to move the platform.

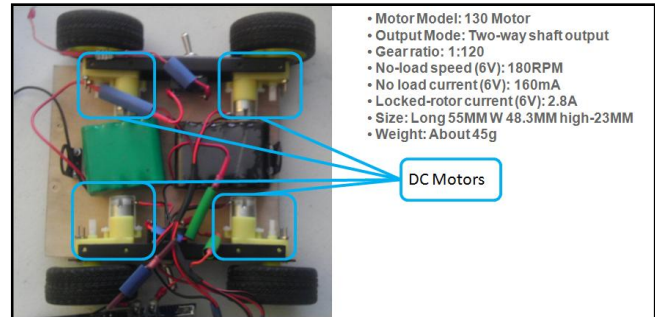


Figure 4. DC motors

Testing revealed that at only a fraction of the rated power was required for movement. In order to avoid the main guide rail becoming actuated, solid bar stock was run through its center.

3.2 Actuation

When docked next to the mixing station, the servo array mounted atop the mobile platform is brought into alignment with the levers of the spigots of the plastic liquid containers. Four Hitec servos [2] mounted in an adjustable servo array were fitted with cam lobes. The cam lobes were profiled to allow easy lever actuation when actuating the spigots of the drink station. The arrangement of the servos as well as the cam lobes can be seen in Figure 5.

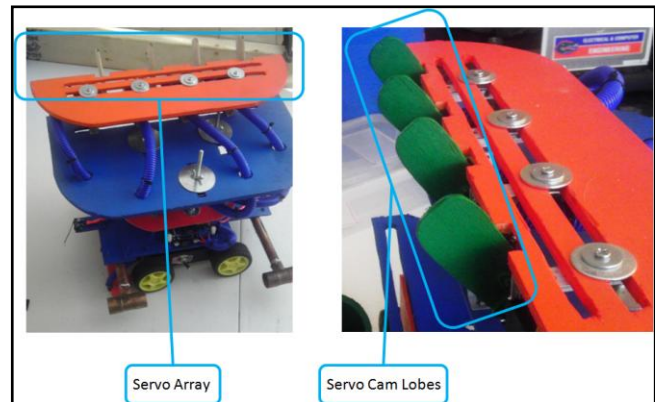


Figure 5. Servo array and cam lobes

3.2.1 Servo Alignment

In addition to cam lobes on the servos and lever guides on the spigots of the drink containers, the servo array is adjustable along the X, Y, and Z axis. This allows for overall and individual adjustment of servos to ensure proper alignment. Figure 6 shows the servo array and cam lobes in alignment with the spigot levers. Figure 6 also shows how the cams can be individually moved allowing for 3 degrees of freedom.

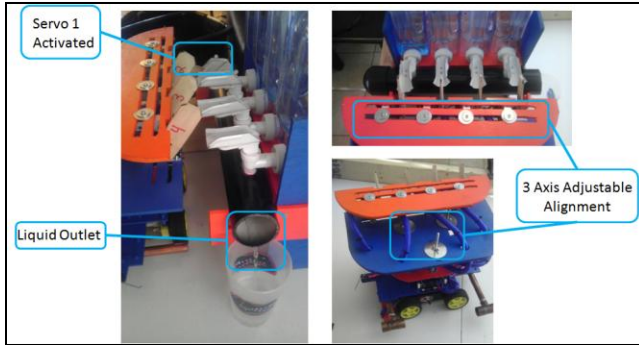


Figure 6. Cam alignment and adjustability

3.3 Drink return cart

A drink return cart needed to be fabricated due to the size and location of the drink mixing station, the ends of the bar, and the robot itself. The return cart and its attachment to the mobile platform were designed to allow extra clearance to compensate for the aforementioned size and placement issues. The design was achieved by creating an adjustable platform with a guide channel. The drink cart has a rigid guide wall that slide into the guide channel attached to the robot. This allowed for linear motion on 1 axis. This can be seen in Figure 7.

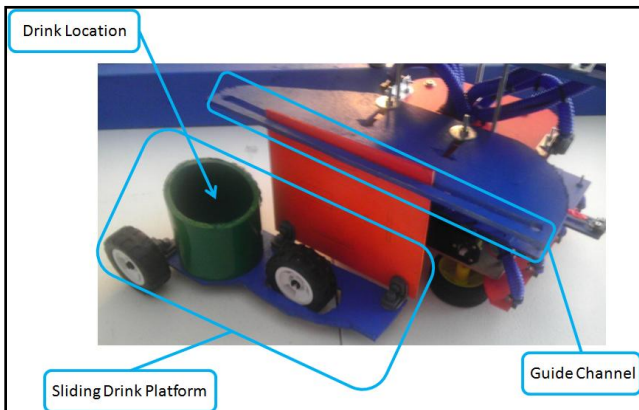


Figure 7. Drink return cart and platform mount

4. SENSORS AND POWER

The sensors of the DriMix 4ics consist of five main sensors groups along with Radio Frequency communication for updating the mobile platform with a variety of information. All sensors were tested under multiple conditions to ensure operation in most lighting conditions. The sensors used for the DriMix 4ics are detailed and explained in this section.

All of the sensors are summarized and described in Table 1. The table describes the function of each sensor and how the values of the sensors are used.

Table 1: Sensors descriptions

	EVO 3D	Ranging IR	IR Array	Switch	RF	Webcam
General Purpose	QR Code Decoding	IR Distance Sensor	Location Under Array	Physical Contact Detection	Radio Comm	Streams Video
How it Performs Function	Decoded MSG Sent to Dropbox	Return Alters Voltage Signal	Return Toggles High/Low	Allows Voltage Signal	Receive and Transmit	Video Streams to Matlab
What it Controls	Order Choice	Avoid Collisions	Line Following	Docking	Comm with laptop	Robot Control

4.1 Android phone

Cellular phones are very quickly becoming laptop replacements. As technology increases the computing power and battery life of these devices, they can quickly take on more and more roles. The average smart phone now has GPS, WiFi, video capturing, accelerometers, gyroscopes, and magnetometers, all functioning together in a very small package. In an effort to leverage some of these features that already exist, sitting in most everyone's pocket; the video capture and WiFi functions were used. The particular phone used with this platform is the EVO 3D. However the model is not terribly important as most smart phones can access and use the two applications that are needed to interface with the DriMix 4ics. This is true for both Android and iOS operating systems. The two applications used were Dropbox and any of the numbers of Quick Reaction code readers available on the Android market.

4.1.1 Quick Reaction code

Creating QR code can be accomplished from literally thousands of locations on the web or with Android or iOS applications. The same is true for decoding QR code. The only caveat for use with the DriMix 4ics is the application must be able to output the decoded QR message via ASCII text file. Again, this is available via multiple applications in the marketplace.

With four drink containers at the mixing station there were theoretically 24 combinations of mixable drinks. However, there realistically aren't too many people that mix vodka and whiskey in the same drink. By limiting the mixing combinations to actual drinks or combinations that would potentially taste good, the number dropped to 11.

QR codes were created to correspond with an ASCII representation of the drink name. These were then printed and tested to ensure accuracy. The generated QR codes can be seen in the Appendix.

4.1.2 Dropbox

Dropbox is a service that allows file backup and sharing across multiple platforms. What makes it ideal is that when one platform updates a file, the changes are immediately pushed out to all the other platforms. The disadvantage of this system is that a WiFi, LAN, or cellular network connection is required.

When a QR code is translated into an ASCII text file on the phone and put in the phone's Dropbox application, the results can be seen nearly instantly in the Dropbox application running on a computer or other cell phones.

This functionality allows Matlab to continually monitor the status of a file used as a drink order repository.

4.2 Webcam

A Gigaware webcam [3] was used to feed video of colored control cards to Matlab for processing. These control cards determined the overall functioning of the mobile platform. A green card indicated an order being placed while a red card indicated a need for emergency stop. The color detection was done via multiple filtering techniques of the video stream. The results of this process can be seen in Figure 8.

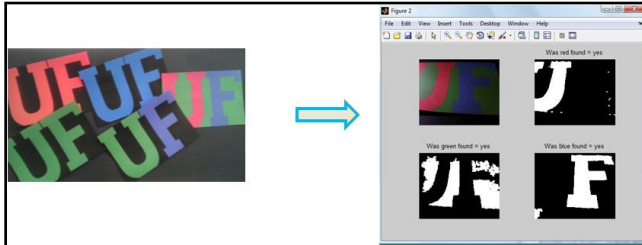


Figure 8. Control cards and filtering of an RGB example

4.2.1 Filtering operations

After pulling the video stream from the webcam into Matlab, it was split into the three principle color components of the RGB color space. Each color layer was then weighted and subtracted from the original stream, giving channels of just pure components. Each of these was then thresholded, allowing for variations of lighting conditions. With the separate RGB streams weighted and thresholded, multiple morphological operations were performed to reduce noise and increase fidelity.

First a morphological opening operation was run to remove any “salt” type noise in each channel. Then a dilation filter was used to connect adjoining pixels and emphasize remaining groups. Of the remaining groups after the filtering, contiguous pixels were counted. If the total number of pixels of a group were above a certain threshold, then it was counted as being a detection of that color group.

The result is that each color channel was effectively filtered of noise and only registered a detection if contiguous pixels of like color groupings comprised a large enough size.

Under poor lighting conditions this still allowed for adequate color detection. An example of this can be seen in Figure 7, where even with poor, uneven lighting the three color objects were still detected and classified.

4.3 Infrared rangers

Two Sharp IR range finders [4] were mounted on both ends of the mobile platform. The IR sensors allowed obstacles to be detected in the path of travel of the robot. They are set to activate over a set threshold value which can be altered according to ambient conditions or wanted activation range. Typically this range was set to be about a foot. The mounting of the sensors can be seen in Figure 9.

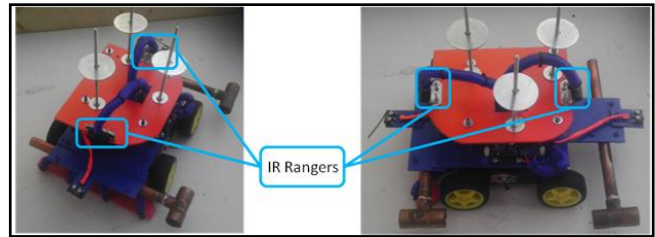


Figure 9. IR range finder mounting locations

The testing conditions of the IR rangers were focused on finding an acceptable range at which an object could be detected under most lighting conditions yet still be a safe distance from the mobile platform.

The test conditions of the IR Range finders can be seen in Table 2. Of note about the table, there was no lumen count measurement for the lighting conditions. The lighting was very much a subjective test as to “it’s bright in here” or “it’s dark in here,” as values from sensor returns were read over an X-CTU terminal window.

Table 2. IR ranging sensor test conditions and results

Metric	Lights Off	Lights On	Blinds Open	Outside
Baseline	250-290	260-290	260-290	260-290
Δ500 Distance	~17 in	~17 in	~17 in	~17 in
Break 1200	~ 12 in	~12 in	~ 12 in	~ 12 in
FoV @ 12 in	~3 in	~ 3 in	~ 3 in	~ 3 in

4.4 Infrared array

The IR reflectance sensor array originally tested was a QTR-8A [5] array. The conditions of testing can be seen in Table 3. However the QTR-8A was not used in the project. A custom spaced array was constructed. The individual IR transmit/receive pairs of this custom array are the same as those used in the QTR-8A, so retesting was not needed and the sensor test conditions would remain the same for the custom array. Testing for the IR Array was much like the testing conditions of the IR Rangers. The focus was to find the ideal range for accurate sensor measurement. The lighting conditions did not have a particularly large effect on the sensors. However there is a very small range for which the sensors are reliable, less than an inch of workable area. The table showing the testing conditions of the IR transmit and receive pairs can be seen in Table 3.

Table 3. IR array sensor test conditions and results

Metric	Lights Off	Lights On	Blinds Open	Outside
Min Range	1/8 in	1/8 in	1/8 in	1/8 in
Max Range	1 in	1 in	1 in	1 in

The custom array that was constructed using four pairs of individual IR transmit/receive pairs. The array can be seen in Figure 10. As can be seen the array is much wider than a standard QTR-8A.

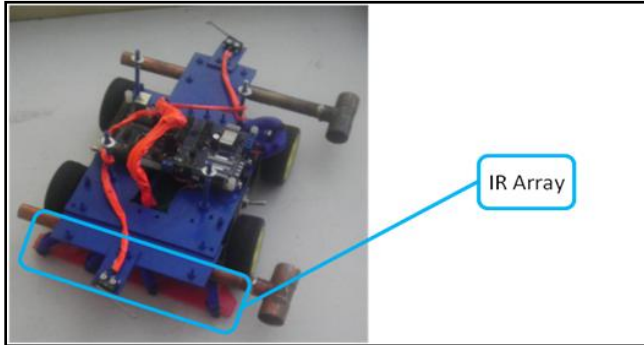


Figure 10. IR Array

4.5 Bump switches

Two bump switches were used on the DriMix 4ics, one on each end. These switches extended out past the main body of the mobile robot. The switches were used both in docking and in navigation. When an order is present and the front switch is activated the robot knows that it is at the mixing station end of the bar. When the rear switch is activated the robot knows that it is at the rear of the bar. Activating the switches either changes direction of travel, during drink polling operation. Or activating the front switch with an order in the system will activate the drink mixing sequence. The mounting locations of the bump switches can be seen in Figure 11.

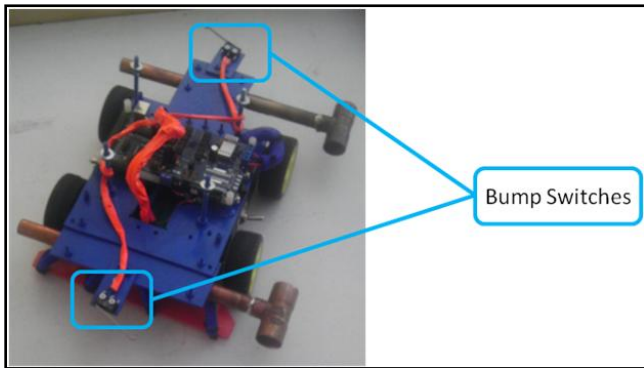


Figure 11. Bump Switches

Testing the bump switches was a simple matter of checking continuity under open and closed conditions.

4.6 Power

Power to the entire platform could have easily been supplied by a single battery pack, however two battery packs allowed for very long term testing and tuning without having to recharge. One battery pack supplied power to the Microcontroller main board while another supplied power to the motors. Each was independently controlled by a switch. This allowed for easily

turning off the motors when movement was not needed. The layout can be seen in Figure 12.

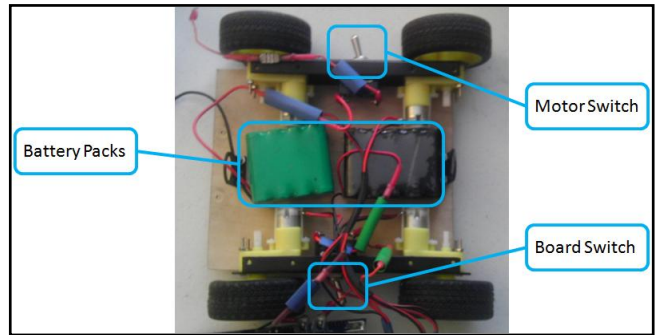


Figure 12. Battery packs and power switches

5. PLATFORM BEHAVIORS, EVOLUTION

The logic of the DriMix 4ics can be overall separated into five main behaviors. Matlab with the color recognizing control cards represent overriding controls of placing an order or stopping the mobile platform, but should not be considered behaviors.

5.1 Navigation

The DriMix 4ics essentially cycles back and forth on the bar top, stopping at each seating location, waiting for an order. Different seating locations on the counter top are marked by black bars of different lengths. The DriMix 4ics uses the IR array to determine the length of the array and thus order location. This is how the robot knows where a drink was ordered and where to take a drink after it is mixed.

5.2 Docking

Based on the direction of travel and activation of bump sensors, the robot knows which end of the bar it is located. Prior to activation the adjustable servo array is properly aligned with the mixing station. This way when the robot reaches the end of the bar with a drink order, activation of the drink levers will be aligned with the drink container spigots.

5.3 Mixing

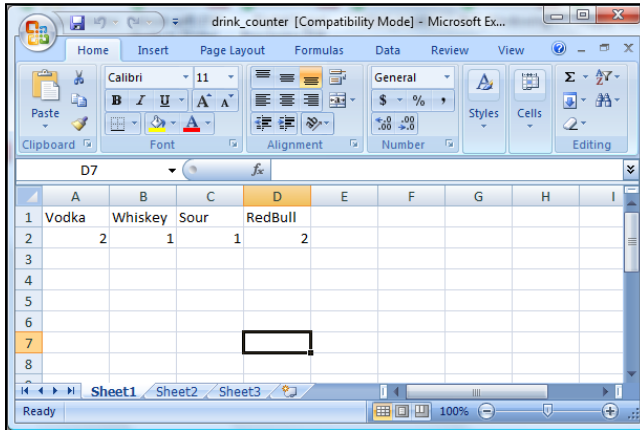
After the process involved with transmitting the order and tracking the order location and docking at the drink station, mixing can begin. After docking the proper servos will be activated based on the order received. The servos correspond to the drinks in the mixing station. The activation angle of the cam as well as the amount of time the cam remains in that position has been measured to ensure pouring a double shot. After activation of the servo and pressing of the spigot, fluids pour into the collector then into the cup on the drink return cart.

5.4 Object avoidance

There are three forms of object avoidance on the DriMix 4ics. IR rangers, bump sensors, and the emergency stop triggered by the webcam and “red” card. The IR rangers will cause the mobile platform to stop if they detect any object a foot in front of the path of travel. The red card causes a stop in motion, no matter the direction of motion. The bump switches will cause a reverse in direction of travel.

5.5 Updating drink orders

An order can be scanned and sent to Dropbox at any time. It is only after a green order card is detected, that the value of the order is scanned in and sent to the mobile platform. The Matlab control is what processes this. On the robot, unless the “waitfororder” value is 1 (indicating a green card was detected) any order value received is disregarded. Data logging occurs after the drink order has been processed and delivered, and the green card withdrawn. The format of the data logging in excel can be seen in Figure 13.



	A	B	C	D	E	F	G	H	I
1	Vodka	Whiskey	Sour	RedBull					
2		2	1	1	2				
3									
4									
5									
6									
7									
8									

Figure 13. Data logging in Excel

5.6 Platform evolution

The original chassis used for the DriMix 4ics was the DFRobot 4WD Arduino Mobile Platform [6]. The platform was chosen because it is light weight, inexpensive and has a four wheel drive system with four DC Motors. It was only during the course of the project that the platform was discovered to be inadequate for the required tasks. The DC Motors, wheels, and motor mounts were the only things that were kept from the platform. The base chassis was about expanded three inches wider and two inches longer than the original DFRobot. The chassis also had multiple tiers added to accommodate all of the sensors and servos used. Figure 14 shows an early iteration of the DriMix 4ics as well as the original DFRobot chassis.

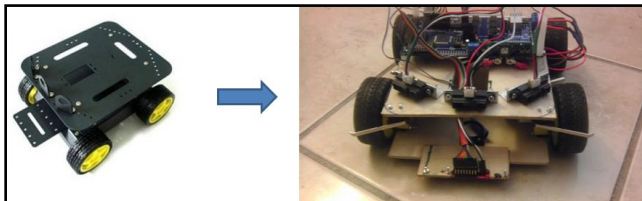


Figure 14. DFRobot chassis and early DriMix 4ics model

The original platform ended up have little in common with the finished product. Seen in Figure 14 is the original set up of the DriMix 4ics. In this configuration the DriMix 4ics was a much more mobile platform. The code at the time allowed the platform to “dodge and weave” as well as line follow. This was done with the intention of having the platform deliver the drink in a crowded room. However, none of those functions were required on a bar top serving drinks

6. CONCLUSIONS

The DriMix 4ics is able to take drink orders, accurately mix them, and return the drinks to the location they were ordered from.

6.1 Lessons learned

There were multiple lessons learned of the course of building the DriMix 4ics. Some of them will be listed below in no particular order.

- Gainesville humidity will warp thin wood. Mount everything to either sturdy wood or metal.
- Order backups of all sensors. You don’t have time to wait for a sensor in the mail.
- Work with HSV, not RGB. HSV is much more lighting invariant than RGB. Thus more robust.
- Make sure that sensors and moving part mounts are adjustable. Easy tweaking is the key to rapidly fixing problems.

6.2 Enhancements

One of the best ways to improve this project for the future would be to create a sturdier base chassis (see comments above about thin wood) and mount motors with metal shafts. Not only would a sturdier base fix the issues encountered with the wheels canting toward the center, but it would also aide in accurate sensor readings. The base that is starting to warp also affects the mounting of the IR array, causing one end of the array to be 1-2 mm lower than the other end. This does not affect sensor readings currently, because it is still within the sensor envelope.

Changing to the HSV color map would also be a much more robust implementation of color detection. The HSV map is much less sensitive to changes in lighting. Whereas the RGB color map is very sensitive to lighting conditions. I am sure that the general code could be improved as well, coding can always be improved.

7. AKNOWLEDGEMENTS

Without the use of the Android marketplace the robot’s ordering system would have been much less “slick.” Multiple QR applications were tested and used to ensure a wide variety of sources could be used to send an order.

Also, without the help of the TA in the IMDL class I’m certain development would not have been finished within the single semester time frame. Or the robot would not have been as complex as it is now.

8. REFERENCES

- [1] T. Martin. "Epiphany DIY board" Available: <https://sites.google.com/site/epiphanydiy/> [Accessed: 30-Apr-2012].
- [2] "HS-422 Servo Motor" Available: <http://www.robotshop.com/hitec-hs422-servo-motor.html> [Accessed: 30-Apr-2012]
- [3] "Gigaware webcam" Available: <http://www.radioshack.com/product/index.jsp?productId=11344037> [Accessed: 30-Apr-2012]
- [4] "Sharp GP2Y0A21YK0F Analog Distance Sensor 10-80cm" Available: <http://www.pololu.com/catalog/product/136> [Accessed: 30-Apr-2012]
- [5] "QTR-8A Reflectance Sensor Array" Available: <http://www.pololu.com/catalog/product/960> [Accessed: 30-Apr-2012]
- [6] "DFRobot 4WD Arduino Mobile Platform" Available: <http://www.robotshop.com/dfrobot-4wd-arduino-mobile-platform-3.html> [Accessed: 30-Apr-2012]

9. APPENDIX

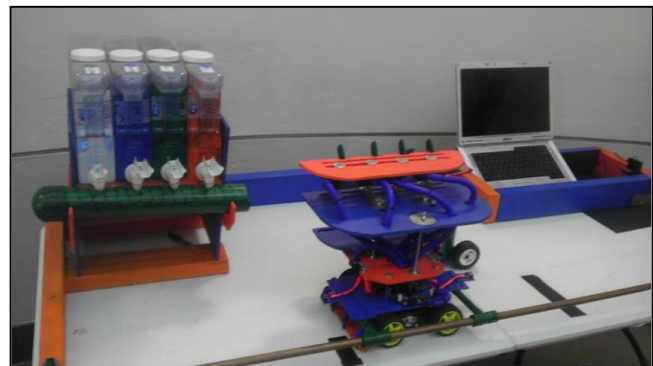
The appendix contains the QR codes created for the menu and a picture of the complete set up.



Appendix Figure 1. Menu items



Appendix Figure 2. Menu items



Appendix Figure 3. The DriMix 4ics

Throughput Specifications for Upstream Biotechnology Process Automation to Meet the Needs of Automated Drug Discovery Campaigns

Aura-Maria Cardona

Dept. of Computer & Electrical Eng. & Computer Sci.
Florida Atlantic University
777 Glades Road, Boca Raton, FL 33431
(1) 561 922 8886
acardon5@fau.edu

Zvi S. Roth

Dept. of Computer & Electrical Eng. & Computer Sci.
Florida Atlantic University
777 Glades Road, Boca Raton, FL 33431
(1) 561 297 3471
rothz@fau.edu

ABSTRACT

The paper presents an overview of the Drug Discovery process with emphasis on related process automation issues. It discusses what specific tasks within the drug discovery process can be automated, and why some of the components of the process cannot be automated. In the context of Biotechnology Automation, Drug Discovery is one of several possible “downstream” processes. Prior to starting a drug discovery campaign, certain “upstream” Biotechnology automation processes must conclude. Such processes involve samples preparation (such as a quantity of specific DNA segments or certain purified proteins), followed assay preparation. The paper explores possible throughput specifications for the upstream processes, as dictated by the needs of Drug Discovery.

Keywords

Biotechnology, Drug Discovery, Automation, Robotics.

1. INTRODUCTION

Automation plays an increasingly important role in many aspects of Life Sciences and especially in Biotechnology. With advances in automation, the human genome and other genomes have been sequenced. Modern Molecular Biology and Biotechnology have created new assays that, when automated, provide larger, more accurate and rapid amounts of information. Similarly, the pharmaceutical industry is heavily dependent on automation, especially as it shifts from products that treat diseases, to analytical methods that detect and classify diseases. Automation for the Life Sciences is therefore broad in scope and includes fluid handling and assay processing, high-throughput screening and drug discovery, high-throughput production and analysis of protein and DNA microarrays, devices for analyzing living cells, lab-on-a-chip analysis tools, and numerous detection methods.

We have paid special attention in the past to upstream protocols concentrating on RNA and DNA purification [1] [2]. Automation for this family of protocols is very important because as newer techniques are developed downstream, upstream protocols should also be improved to eliminate some of the bottlenecks existing today. This paper will give an insight of the targets’ requirements needed for a specific downstream protocol like Drug Discovery, which in turns become the goals for upstream protocols automation.

This paper discusses throughput specifications for upstream biotechnology process automation to meet the needs of automated

drug discovery campaigns. Section 2 describes the drug discovery process with its different steps. Section 3 describes the essential components of a drug discovery system. Section 4 centers specifically on the high-throughput screening component of drug discovery. Section 5 presents an example platform developed at Scripps Florida for high-throughput screening for drug discovery. Finally section 6 presents the specification that upstream biotechnology processes need to meet for drug discovery campaigns.

2. THE DRUG DISCOVERY PROCESS

In the past, most drugs have been discovered either by identifying the active ingredient in traditional remedies or serendipitously. In recent years drug discovery approaches relying heavily on automation emerged, allowing users to better understand how diseases and infections are controlled at the molecular and physiological levels and how to better target specific biochemical entities based on such knowledge.

Drug Discovery is a sub-area of Biotechnology involving research, design and development of new therapeutic drugs to treat known diseases. In Drug Discovery the focus is to understand how diseases (including infections) work at the molecular and physiological levels in order to be able treat such diseases at the root of the problem.

In general, Drug Discovery involves the following multiple aspects: the identification of possible molecular substance candidates that need to be targeted in order to effectively treat the disease; the synthesis of plausible candidate targets; the characterization of the candidate targets and of the disease mechanism that needs to be treated; the screening of each candidate target against a large number of compounds to find plausible therapeutic results; and the development of assays to identify therapeutic efficacy. Once all the above steps are performed and a compound has shown that it has a possible desired effect on the target being evaluated, the process of Drug Development begins which includes among other factors determining the proper dosage of the drug and exploration of its possible side effects.

The complete block diagram description of a pharmaceutical research and development process is shown in Figure 1. Following the exploration of the interaction of the disease with the organism at the molecular level, the target discovery process identifies target molecules that may be suitable for disease

treatment. These targets may be proteins such as receptors, enzymes or ion channels [7], or specific RNA or DNA segments [13] that interact with the disease to enable or inhibit the progress of the illness. As the ultimate goal of the human genome project is that as we may gain full understanding of all gene functions, all targets in future Drug Discovery processes would eventually become DNA and RNA sequences that express or inhibit diseases, totally replacing all other kinds of protein targets [5].

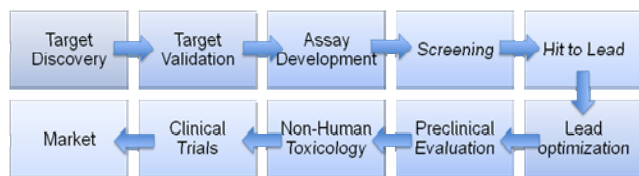


Figure 1. A conceptual block diagram of a complete pharmaceutical research and discovery process

Once an appropriate target is identified, it has to be verified. A level of confidence has to be determined to ensure that a given target is relevant to the disease under study, and that its manipulation will with high enough probability allow treatment of the disease. Depending on the type of target found, its manipulation (called modulation) is caused by means of different chemical compounds effectors (modulators). For instance, if the target were a receptor, the chemical substances used to manipulate such a target would be either agonist, substances which combine with the receptor on the cell membrane surface to produce a desired reaction, or antagonist, substances that combine with the receptor to prevent a physiological action. If the target found is an enzyme, the modulator used in such a case will be an activator or an inhibitor depending if the enzyme's chemical reaction needs to be enabled and stimulated or stopped and retarded. Finally, if the target found is an ion channel, opener or blocker compounds are used to affect an opening or a closure of certain ion channels.

Once the target is validated, the next step is an Assay Development where the goal is to identify the modulators mentioned above for a specific target. Assays are designed to monitor the target's interaction with different chemical substances or compounds during the screening in order to find out which substance interaction draws the desired chemical result for the target in hand.

Screening for drug discovery is a highly automated process. Since the goal is to expose the candidate target to a very large number of different chemical compounds, this process is performed using a high-speed parallel method known as High-Throughput Screening (HTS). The target has to be exposed to all those compounds in a hope of finding the desired interaction between target-and-compound to treat the disease. The screening process may give more than one compound that has the desired interaction. These possible compounds are called "hits". Further screening needs to be run in order to find the appropriate dosage to obtain the desired result. After the right dosage for each "hit" compound is found, trials are conducted in animal models. The compound that gets the best result from the animal models is then considered the "lead" compound.

Lead compounds are optimized in terms of strength and selectivity. The best compound is a one that affects only the desirable target with the desirable action, and its safety is assessed

before it becomes a candidate for drug development. Some compounds might be toxic even lethal to humans if the right dosage is not administrated.

After the lead compounds are identified and approved as candidates for drug development, Drug Discovery enters a process where preclinical evaluation and non-human toxicology tests are performed, followed by the clinical trials [9].

Information on the human genome, its sequence and what it encodes has been thought to be a new source for "drugable" targets, but still much work needs to be done to speed up the process of identifying possible targets and for the development of new drugs.

3. ESSENTIAL COMPONENTS OF A DRUG DISCOVERY SYSTEM

The drug discovery process system has four main components. The essential core components are Compound Collections (or Libraries), Assay Designs, HTS Technology Platforms, and Data Capture/Analysis Systems.

Compound collections are stored in custom-designed, fully automated warehouses where the compounds are formatted and made available to be instantly retrieved for testing. These compound libraries are under constant quality control. Compound libraries are constructed from a variety of different sources. These could be natural product samples, acquired from external sources, or it could be developed from combining different compounds to form "combinatory libraries", or these could have been developed and/or discovered in-house (i.e., by the HTS facility itself during various target discovery campaigns). Compound libraries are considered major assets within a company's set of discoveries, as these require a significant time and effort to assemble and a big financial investment [4]. The compounds discovered in-house have a particularly special value.

The second essential component of the drug discovery process is the collection of assay designs. It is vital for the process to design arrays that are chemically relevant and pharmacologically accurate to have a successful outcome from a target screening campaign. The small molecule domain is thought to have somewhere between 10^{40} to 10^{100} possible compounds, more than there ever be made [10]. Usually a screening campaign will test from 10^5 to 10^7 compounds [7]. The development of the assays requires expert scientific knowledge to make good judgment decisions as to how to choose a sensible screening sample of compounds (i.e., make an initial estimate of what compounds or family of compounds are relevant to the target in hand). This helps to enhance the quality and diversity of the collection being screened, and improve the success rate of the HTS campaign [17].

Designing a bioassay for a given target that is appropriate for HTS is very time consuming and is considered to be one of the bottlenecks in the drug discovery process [4]. Some of the parameters that have to be taken into consideration in the design of an assay can include choice of assay mode (agonistic or antagonistic), availability of standard protocols (readily available assays), reagent availability, and obviously, when talking about HTS, scalability. Biotechnology Automation, in general, is divided into upstream and downstream processes. For instance, upstream protocols govern the production quantity and quality of the targets required for the development of the assays for an HTS campaign. The design of such assays appears to be one of the

central challenges of upstream processing and it involves no automation.

HTS is the third essential, and considered by some scientists to be the most important, component of the drug discovery process [4]. Over the last 20 years companies have spent billions of dollars developing automated equipment for HTS. Today, there is a full range of automated equipment available for HTS from the comparatively simpler like modular workstations that can perform plate-to-plate transfer (see Figure 2), to the more complex involving integration of equipment and robotic manipulators like the Scripps Research uHTS platform described in a later section. In a later subsection HTS will also be discussed in more detail.



Figure 2. LabSystem MultiDrop 384 from Beckman Coulter [15]

The last major component of the drug discovery process is the data management operation. There are diverse software packages that have been developed; some of them are commercially available and others are customized solutions. These software packages help to capture millions of individual data points that are produced in each screening run to their visual interfaces, performs detailed analysis, and interpret the information acquired.

4. HIGH-THROUGHPUT SCREENING

The Drug Discovery industry is moving towards heavily automated processes that allow the screening of millions of compounds against different biological targets.

HTS is defined to be a process where hundreds of thousands to millions of compounds are tested for activity against disease targets of interest with the goal of identifying truly active evolutionary “hits” [4].

The evolution of HT platforms integrated into the drug discovery process is broken into five phases.

The first phase is the evolution of instruments and screening formats. The drug discovery community had to come to a consensus as to which formats to use in order for assays, consumables, and equipment to be somehow compatible and integrated. Modular semi-automated and automated workstations have been developed in accordance with those formats. Plate-to-plate transfer, reagent dispensing, centrifuging, and detection capabilities (see Figure 3) are among the operations that have been automated to use HT formats.



Figure 3. FlexStation 3: High efficiency dual monochromator-based optical system for all read modes from Cisbio [11]

A second evolution group involves miniaturization. Standard format 96-well plates (see Figure 4) and 384-well plates were developed in 1996, which can handle volumes of 50 μ l per well. Later on 1536-well plates were developed with volumes of 5 to 10 μ l per well. This last screening format is sometimes referred to as Ultra (or micro) High-Throughput Screening or uHTS. Some companies have developed customized formats like the 864-well plates from Affymax, 9600-well plates from Dupont Pharmaceutical, and 3456-well plates from Aurora Bioscience. These last one has become standard format for uHTS as miniaturization continues to evolve.

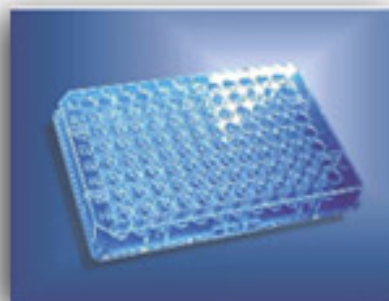


Figure 4. 96-well plate, Immulux™ microplate form Dynex [14]

A third group is the development of cellular HTS assays. The assays have to be compatible to the format used in HTS. The developments on these three groups are closely related. If for example, the format is miniaturized, the instrumentation and assays have to be miniaturized as well, which translates into, for example, new dispensing techniques involving lower volumes and greater resolution accuracy.

A fourth group is the actual development of the HTS technologies. Compound selection and quality control are big issues, but also in the screening campaign tests have to be included to examine drug-to-drug interaction problems, drug metabolism, and absorption or permeability issues that the target could present.

The fifth group is the quality control in HTS processes. The information collected from a screening run is very closely related

to the supply of robust reagents, and this is becoming an integrated part of the process. Assay quality, compound quality, and target quality are constantly monitored. The success of the campaign depends, in part, on the quality of the products used. As a result some of the process issues are how to get the compounds into the assays, how to store components, how to guarantee the purity and stability of the compounds, development of detection devices to measure assay products, and capture and analysis of the data.

5. EXAMPLE: HTS FOR DRUG DISCOVERY AT SCRIPPS FLORIDA

The Scripps Research Institute – Florida, has developed a High-Throughput Screening platform [13] that enables drug-target lead identification via ultra-high-throughput screening (uHTS) technology (see Figure 5). Using state-of-the-art instrumentation Scripps scientists develop and execute HTS Assay Development, HTS Target “Profiling” Assays, and Full-Scale HTS Screening, all well-known techniques used for Drug Discovery. HTS assays are performed in microtiter plates with 96, 384, and 1536 well formats.



Figure 5. The Scripps Research uHTS platform. a) Industrial anthropomorphic robotic arm, b) pin tool, c) liquid handlers, d) incubators, e) multimode plate reader, and f) kinetic imaging plate reader [13].

The main component of the Scripps uHTS platform, a HT robotic system from Kalypsys, is an anthropomorphic robotic arm (Item A in Figure 5) that moves assays and compound microtiter plates from one laboratory instrument to the next for processing. The remaining equipment is laid out around the robotic arm within its reachable workspace to allow convenient transfer and manipulation. A pin tool is one of the devices that are set around the robotic arm (Item B in Figure 5), and it is used to transfer compounds from the compounds plates to the assay plates. The pin tool has the same amount of pins as the number of wells in the plate; i.e., if the plates that are being used are of a 384-well format then the pin tool will have 384 pins, one for each well to allow transfer of the complete plate contents at once. The uHTS platform also utilizes an integrated liquid handler capable of dispensing up to 32 different reagents as well as of washing the plates as needed (Item C in Figure 5). Incubators are also laid out around the arm (Item D in Figure 5). These have a capacity of storing up to 700,000 samples in 1536-well format at different temperature and gas concentration levels. A multimode plate reader performs measurement operations (Item E in Figure 5). It records absorbance, luminescence, fluorescence, or fluorescence resonance energy transfer (with time resolution) information from microtiter plates. Another measuring device is a kinetic imaging plate reader that allows measurement of second-messenger or ion channel activity in live cells (Item F in Figure 5). The uHTS system is completed with another robotic platform that is used to manage and distribute the more than 600,000 compounds used for Drug Discovery Scripps Research. The Scripps automation HT

robotic system has a throughput of over 1 million assay wells per day and an on-line storage capacity of over a million compounds for both biochemical and cell-based drug screens.

6. HTS FOR DRUG DISCOVERY: SPECIFICATIONS FOR UPSTREAM BIOTECHNOLOGY AUTOMATION PROCESSES

Many recent drug discovery campaigns have revealed that for each drug that goes to market, approximately one million compounds have to be screened [7]. The current “rule of thumb” rates followed by drug discovery practitioners are that for every 500 compounds screened, one “hit” is typically found. For every two hits found, one will likely become an “active hit”. For every 20 active hits that are screened, one “lead” will eventually be found. For every five leads found, one will become a “candidate”. Finally, for every 10 possible candidates, only one could become a marketable drug.

The HTS campaign involves more stages and procedures than just the screening of the targets against the Compound Library. The HTS facility is the one in charge of developing the appropriate assays for the HTS campaign. Assay development is done first in 96-well format plates, and once the right volumetric ratio between substrate, target and measurement reagent is found, the assay is miniaturized to the desired HTS formats. To ensure that the assay works properly, 15 copies of the plates are typically run. This means that if the assay is developed successfully in the first try at least, just for the assay development the amount of target needed would be:

$$V_p = V_{TW} \times N_w \quad (1)$$

Where V_p is the volume of target needed for each plate, V_{TW} is the volume of target needed per well, and N_w is the number of wells used in a plate. Therefore the volume needed for the initial assay development in the 96-well plate format would be $50\mu\text{l} \times 96 = 4.80\text{ml}$ per plate. As 15 plates are run to validate the results the actual volume needed for the initial assay development is $4.80\text{ml} \times 15 \text{ plates} = 72.00\text{ml}$.

For the 384-well format only columns 3 - 22 are used, using only 320 wells. Columns 1 and 24 are not used to avoid edge effects and 2 through 23 are used for control/quality control purposes. This means that the volume needed for assay development at the 384-well format is $24\mu\text{l} \times 320 = 7.68\text{ml}$ per plate. The volume needed for 15 plates would be $7.68\text{ml} \times 15\text{plates} = 115.00\text{ml}$.

For the 1536-well format 1280 wells are used in columns 5 - 44. The volume needed per plate is $1\mu\text{l} \times 1280 = 1.28\text{ml}$ and for 15 plates the volume needed is 19.20ml .

For the 3456-well format 2880 wells are used in columns 7 - 66. The volume needed for this format per plate is $0.7\mu\text{l} \times 2880 = 2.02\text{ml}$ and for 15 plates 30.02ml .

The total volume needed for assay development is calculated by adding the different volumes calculated above needed for assay development. Thus 237ml of target is needed for the assay development process. This is only an amount calculated for the volumes used in [8], the total volume needed for any other assay development is expected to be in the same order of magnitude. Practitioners often recommend doubling the above calculated amount for assay development. Sometimes the target assays are

not needed to be miniaturized to all into HTS formats. At other times it simply cannot be miniaturized due to its molecular and biological properties, but the volume should be kept the same for any unexpected complications.

Following the development of the screening assay, target screening against the compound libraries is performed. Primary hits (active compounds) are typically confirmed using 384-well format and targets are counter-screened to eliminate false-positive from the primary hits. This cycle is repeated three times to produce three replicate results. The compound library screening and counter-screening can be performed using either 1536-well format or 3456 well format; yielding a total screening capability of 300,000 or 600,000 compound libraries, or even 1 million compound library.

Table 1. Volumes needed for target screening against the Compound Libraries.

<i>Format</i>	<i>Library size (number of screened compounds)</i>	<i>Volume per well</i>	<i>Total volume in liters (l)</i>
1536-wells	1,000,000	10 μ l	10.00
1536-wells	600,000	10 μ l	6.00
1536-wells	300,000	10 μ l	3.00
3456-wells	1,000,000	0.5 μ l	0.50
3456-wells	600,000	0.5 μ l	0.30
3456-wells	300,000	0.5 μ l	0.15

The Total volume shown in Table 1 in liters reveals what is needed for a single run. Often as mentioned in [8] at least three replicate results are obtained to assure good results, and this is done for the screening and the counter-screening. Therefore at least twice the total volume shown in Table 1 is needed in this stage for each campaign, but as much as six times the volume shown in Table 1 can be used for this stage. The total volumes in Table 1 were calculated by multiplying the volume of target needed for each well times the number of compounds that the target will be run against.

$$V_{SC} = V_{TW} \times N_{SC} \quad (2)$$

Where V_{SC} in the volume of target needed to screen the number of compounds in the chosen library, V_{TW} is the volume of target needed per well, and N_{SC} is the number of compounds that are screened. To run a HTS campaign of one million compounds with no replicated results, the target's volume needed could be as much as 20l (see Table 1). When a HTS laboratory is approached to run a HTS campaign, the user is typically asked for the amount needed by the screening multiplied by 1.5 of the target as a comfortable safety margin to develop the assays for the screening campaign. The concentration needed for the assays are in the 0.1 to 0.05mM range [9].

The quantity and concentration are the requirements taken into consideration for the purification of the starting target. The user has the liberty of choosing the appropriate protocol used for the upstream (sample preparation) process taking into account at least these two parameters, the volume needed and the concentration. The targets shelf time has its limits depending on its biological and molecular properties. These might have a longer shelf time than what a HTS campaign may last, but as the HTS facility

prepares fresh reagents for the campaign every 8 hours [8] fresh reagents to guarantee a successful campaign are expected as well. To ensure the quality and freshness of the targets, the targets are prepared in at least two batches, one that should be provided at the beginning of the campaign and the other one concluded towards the middle of it.

The target needs to be purified at the highest concentration specified, even though a higher concentration is often recommended so that no problems arise later on with the dilutions. It is a common practice to try to prepare samples at a concentration of 1mM but this is not always possible with the samples at hand.

Normally the total amount is not prepared straight from a biological source. Usually amplification methods are used on those samples obtained from the biological sources to meet the quantity requirements. If those quantity requirements were to be prepared only from biological sources it could take many months to prepare. Amplification methods duplicate copies of the samples. Depending the type of target, RNA, DNA or Protein, the user has different options with different duplication rates. It is up to the user to use the appropriate amplification methods. For example, if the target sample is a DNA segment, Polymerase Chain Reaction (PCR) is used.

PCR consists on three main steps: denaturing, annealing and elongation, and these are carried out at different temperatures [6]. Using a PCR machine (thermo-cycler), the sample goes through the different temperature changes. First at a temperature usually between 94 $^{\circ}$ – 98 $^{\circ}$ C, DNA is denatured, temperature is then lowered to 50 $^{\circ}$ – 65 $^{\circ}$ C where the primers attach to the DNA templates, and last, the temperature is increased to 75 $^{\circ}$ – 80 $^{\circ}$ C where elongation takes place. In this stage DNA polymerase synthesizes the complementary DNA strand to the DNA template by adding dNTPs to the strand. DNA target is doubled, hence leading to exponential amplification. Finally, the cycle starts again, and there are as many cycles as required or for as long as there are enough reagents to synthesize the new strands. Each cycle could take up to 5 minutes but this depends on the size of the DNA segment that is been copied. There is also an initializing step and a final hold step that can take up to 10 minutes each. Common PCR methods can only amplify DNA segments of up to 10 kilo-base-pairs. After the first exponential amplification stage, PCR enters a levelling off stage where the reaction slows down as the enzyme loses activity and the reagents are consumed, and at the end the reaction stops altogether due to the exhaustion of reagents and enzyme. It is a common practice to run no more than 40 cycles, meaning that one original DNA segment could be amplified in 14 hours to 1.0995 $\times 10^{12}$ copies. PCR reduces drastically the time taken to prepare the required samples for drug discovery and can increase the sample's concentration given a better outcome.

Protein Misfolding Cyclic Amplification (PMCA) is a protein amplification technique, one of many that exist, that is conceptually similar to PCR, and for this reason it has the same exponential growth of amplifying segments as that of PCR. In the case of protein amplification reagents become inactive more rapidly and therefore whenever running the protocol it is a common practice to run no more than 20 cycles, meaning that one original protein molecule could be amplified in 8 hours to 1.0485 $\times 10^6$ copies [3] [18]. RNA Amplification is a technique that has been recently developed [16] that is faster than other

techniques used up till now. The protocol can be performed in a day and it also has an exponential growth.

Finally, it is important to mention that depending on the size of the laboratory, the number of campaigns runs per HTS unit is between 10 to 30 runs per year; each takes about 12 to 36 days. At the end only five to 15 will end being good compound leads for further development.

7. REFERENCES

- [1] A.M. Cardona, Z. Roth. *Design Considerations in High-Throughput Automation for Biotechnology*. 2008 Florida Conference on Recent Advances in Robotics, FCRAR 2008.
- [2] A.M. Cardona, C. Han, Z. Roth. *Optimization of Multi-Centrifuge Steps in Biotechnology Automation*. 2009 Florida Conference on Recent Advances in Robotics, FCRAR 2009.
- [3] Amersham Pharmacia Biotech. *The Recombinant Protein Handbook: Protein Amplification and Simple Purification*. Amersham Pharmacia Biotech.
- [4] Banks, M. N., Cacace, A. M., O'Connell, J. et al. *High-Throughput Screening: Evolution of Technologies and Methods*. Drug Discovery Handbook, Wiley, 2007 p. 559 - 602.
- [5] Bartfai, T. & G. V. Lees. *Drug Discovery from bedside to Wall Street*. Elsevier Academic Press. 2006 Burlington, MA.
- [6] *Biotechnology Laboratory I Manual*. Biotechnology Laboratory I, Biological Science, Florida Atlantic University, Fall 2006.
- [7] Carnero, Amancio. *High throughput screening in drug discovery*. Clinical and Translational Oncology 8.7 (July 2006): 482(9). Academic OneFile. Gale. Florida Atlantic University. 13 Sept. 2009.
- [8] Chung, C.C., Ohwaki, K., Scheneeweis, J.E., et al. *A Fluorescence-Based Thiol Quantification Assay for Ultra-High-Throughput Screening for Inhibitors of Coenzyme A Production*. ASSAY and Drug Development Technologies, Volume 6, Number 3, 2008, p. 361-374, DOI: 10.1089/adt.2007.105.
- [9] Drews J. et al. Drug discovery: a historical perspective. Science 287, 1960 (2000), DOI:10.1126/science.287.5460.1960.
- [10] Eckstein, J. *ISOA/ARF Drug Development Tutorial*. Institute for the Study of Aging, Alzheimer Research Forum.
- [11] FlexStation 3, CISBIO – Bioassays, <http://www.htrf.com/splash.asp>
- [12] Gwynne, P. & G. Heebner. *Drug Discovery and Biotechnology Trends, Laboratory Automation: Scientists' Little Helper*. Science, January 2004.
- [13] Hodder, P., Baillargeon, P., Chase, P., et al. Spicer, T., Subramaniam, P., and Sullivan, L. *Probe and Drug Discovery: The Lead Identification Department*. Translational Research Institute, Scientific Report 2007.
- [14] Immulux™, DYNEX, <http://www.dynextechnologies.com/>
- [15] LabSystems MultiDrop 384, Beckman Coulter, <https://www.beckmancoulter.com/>
- [16] NuGEN. *System Uses Simple, Same-day Process to Give Researchers Global Gene Expression View Directly From Cell Lysate*. NuGEN, <http://www.nugeninc.com/>
- [17] Seethala, R. *Signal Detection Platforms for High-Throughput Screening*. Drug Discovery, Bristol-Myers Squibb, 2008.
- [18] Soto, C., Saborio, G., Anderes, L. *Cyclic amplification of protein misfolding: application to prion-related disorders and beyond*. Trends in Neurosciences, Volume 25, Issue 8, 390-394, 1 August 2002.

Learning Macros for Multi-Robot Manipulation Tasks

Bennie Lewis

Department of EECS
University of Central Florida
Orlando, FL 32816-2362
bennielewis@knights.ucf.edu

Gita Sukthankar

Department of EECS
University of Central Florida
Orlando, FL 32816-2362
gitars@eecs.ucf.edu

ABSTRACT

In this paper, we present a paradigm for allowing subjects to configure a user interface for multi-robot manipulation tasks. Multi-robot manipulation tasks can be complicated, due to the need for tight temporal coupling between the robots. However, this is an ideal scenario for human-agent-robot teams, since performing all of the manipulation aspects of the task autonomously is not feasible without additional sensors. In the best case, humans perform the delicate manipulation sections of the task, robots autonomously execute the repetitive driving, and the agents supporting the coordination through shared information propagation. Though the task itself is complicated, it is imperative that the user interface not be unreasonably complex. To ameliorate this problem, we introduce a macro acquisition system for learning combined manipulation/driving tasks. Learning takes place within this social setting; the human demonstrates the task to the single robot, but the robot uses an internal teamwork model to modify the macro to account for the actions of the second robot during execution. This allows the same macro to be useful in a variety of cooperative situations. In this paper, we show that our system is highly effective at empowering human-agent-robot teams within a household multi-robot manipulation setting and is rated favorably over a non-configurable user interface by a significant portion of the users.

Keywords: human-robot interaction, multi-robot manipulation, learning by demonstration

1. Introduction

Human-agent-robot teams [15] fill an important niche in robotics since they can accomplish tasks that robots cannot complete autonomously, forming a team unit that is greater than the sum of the parts. Ideally the human users focus on the difficult cognitive and perceptual tasks, the robots manage the planning and execution of repetitive physical tasks, while the agents handle the most cumbersome information processing tasks. At the core of designing an effective social system that includes human, agent, and robot teammates is the question of communication between the biological and synthetic entities—how to create a user interface that empowers rather than hinders teamwork and social learning?

Here we focus on the problem of multi-robot manipulation; the human user guides a team of robots to lift and clear clutter in a household environment. Since some of the objects are too large to be raised by a single robot, the



Figure 1. Two HU-IE robots cooperating together to clear the environment of objects and deposit them in the goal location.

robots must work together in tight temporal coordination to lift and transport the clutter to the goal area. Coordination failure leads to dropped objects and slow task completion times. The users must also effectively control the multiple degrees of freedom that the robot offers (wheelbase, arm, and claw). The human user brings the critical capabilities of perception and grasp planning to the system. With only limited sensor information, the humans are able to identify the objects (which can be hard, soft, or irregularly shaped) and rapidly determine where the robot should grasp an object. Figure 1 shows our robots manipulating different objects in close proximity, clearing obstacles in parallel.

In this paper, we address the general question of structuring the human-agent-robot interactions—how to design an interface that utilizes the humans’ perceptual and cognitive abilities without frustrating the user? Our belief is that the system must respect the humans’ individual differences, and give the users the flexibility to identify which task components should be performed autonomously. To do this, we introduce a macro acquisition paradigm for learning combined manipulation/driving tasks in a team setting.

In our multi-robot manipulation task, the user directs a team of two mobile robots to lift objects using an arm and gripper for transport to a goal location. The environment contains a selection of two different objects, some of which can be transported by a single robot and others that require both robots to lift. Figure 2 shows a picture of the team



Figure 2. Two HU-IE robots cooperate for bimanual manipulation. One robot is teleoperated while the other moves autonomously to mirror the user's intentions. The user can seamlessly switch robots during such maneuvers.

of robots cooperatively moving an object that cannot be carried by a single robot.

The paper is structured as follows. Section 2 discusses the related work on human-robot interaction. Section 3 describes the design and implementation of our robot platform. Section 4 outlines the configurable user interface. Section 5 discusses the macro acquisition method. Section 6 describes the methodology employed in our user study. Section 7 presents a selection of results from our experiments. We described related work on robot manipulation in Section 8, and Section 9 concludes the paper.

2. Human-Robot Interaction

Much of the work in human-robot interaction has centered on having the robots do more when the operator is unavailable using approaches such as cognitive workload modeling [8, 11] or adjustable autonomy [17, 16]. Yet fundamentally, synthetic and biological entities have very different capabilities that need to be respected during task division. Collaborative control [9] intelligently utilizes these differences by leveraging the user to perform perception and cognition tasks, rather than merely involving the user in the planning and command.

An alternative approach, espoused in this paper, is to view creating human-agent-robot teams as a process of coactive design, which was first introduced by Johnson et al. [10]. Coactive design concentrates on understanding the interdependence of joint activity and carries the expectation that human and robot will function in close and continuous interaction. Often how this interaction occurs is pre-determined by the designer; however, in our system the user interface is configurable, allowing the user's understanding of the task guide the periods of interdependence. To do this we allow the user to identify common subtasks before the actual task execution. Our intelligent user interface analyzes these sections of the task and creates a task abstraction for these activities. This task abstraction is then used 1) to build macros using a simple programming by example

method and 2) to inform the system's understanding of the user's autonomy preferences.

In a sense, this can be seen as a simple form of social learning between humans and robots [6]; the human teaches a single robot what to do, but during execution, the robot must account for the actions of the second robot and the user when performing the macro. To do this, the robot maintains a mental model of its robot teammates and modifies the macro to be useful in a team setting. Socially-guided exploration has been utilized in robot learning systems, but in that case the human partner provides social scaffolding during the learning process to guide the robot's actions during the learning of a non-cooperative task [5].

Programming by example has been incorporated into a variety of demonstrational user interface systems (see [12] for an overview). In the simplest instantiation, macros (sets of instructions) are recorded and replayed at the user's command without modification. To generalize the macros to alternate situations, machine learning methods such as supervised or inverse reinforcement learning can be used to learn an abstraction over features or rewards. Within robotics systems, learning by demonstration [3] or apprenticeship learning [1] has been principally used as a method to learn robotic controllers for high dimensional action spaces or to bootstrap reinforcement learning. Our work differs from conventional learning by demonstration this in that the user remains continually involved in system control during macro execution. The taskwork is learned by the user through demonstration, and the teamwork coordination model is preprogrammed. The users can express their autonomy preferences through designating sections of the taskwork to be automated and can opt to either accept or reject the learned macro if the initial demonstration does not match their expectations of the learned system.

3. HU-IE Robot Platform

Our robot, the Home and Urban Intelligent Explorer (HU-IE), features a mobile base attached to a robotic arm and gripper. It is designed to be able to retrieve light objects in a household environment with either carpets or hard floors. Our robot contains the following components: iRobot Create, Charmed Labs' Qwerk board, the arm from the NXT 2.0 Robotics Kit, a Logitech Communicate STX Webcam, and Tetrax Robotics parts. The total cost per robot is around US \$900. Figure 3 shows the interactions between the hardware components.

The HU-IE robot base consists of the following components:

Actuator: The iRobot Create has a differential drive that allows left and right wheel speeds to be independently specified.

IR Sensor: There is one IR sensor on the front left of the robot that can be used to detect walls and other robots. Objects do not always register on the IR sensor and can only be reliably detected by the operator using the camera.

Bump Sensor: The Create has a left and right bump sensor that trigger during physical collisions.

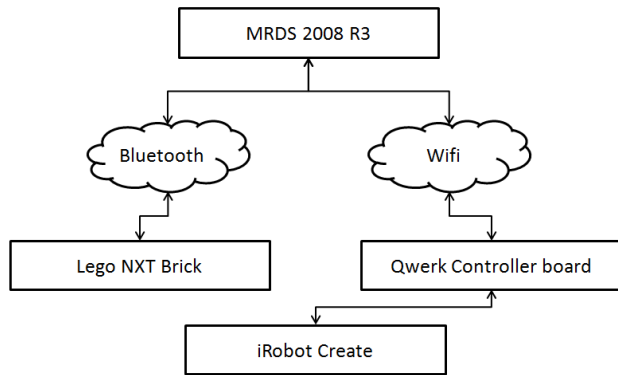


Figure 3. Overview of HU-IE hardware components

Cliff Sensor: The cliff sensor under the base of the robot is used to detect whether the robot has been lifted up and moved (e.g., between trials). In a household environment, it would be used to detect proximity to staircases.

Ultrasonic Sensor: We use an ultrasonic sensor that is mounted on the claw of the robot for grasp planning to determine whether an object grip is likely to be successful and to detect objects already grasped in the claw.

Accelerometer Sensor: The accelerometer sensor is mounted on the arm of the HU-IE robot and is used to measure the arm angle.

Wheel Encoders: We rely on the Create's high resolution wheel encoders for all localization in the small enclosed environment.

Webcam: A camera mounted on the robot arm presents a first-person perspective to the user during teleoperation. The user can also access the feed from a ceiling camera to obtain an overhead view of the workspace and both robots.

Qwerk: The Qwerk board contains a 200 MHz ARM9 RISC processor with MMU and hardware floating point units running Linux 2.6. For our purposes it functions a relay, forwarding sensor information from the Create sensors and webcam to the user interface.

The arm on the HU-IE robot was created using the LEGO NXT Robotic Kit. It is 1.2 feet long and extends 8 inches in front of the robot. The arm is actuated using three motors, can rotate 180° around the robot base and has an operating range of -45° to 90° in elevation. At the end of the arm is a four tong claw with rubber grips capable of grasping objects sized for a human hand. Tetrax Robotic Metal parts are used to bolt the arm to the iRobot Create. An NXT intelligent brick, containing a 32-bit ARM7 microprocessor, functions as the brain of the robotic arm. The NXT intelligent brick connects all the sensors and actuators together. Commands from the user interface are sent directly to the arm via Bluetooth, bypassing the Qwerk board. The webcam is mounted on the base of the HU-IE robot to enable the operator to view the object from the arm's perspective. It is important to note that, due to the relatively limited camera

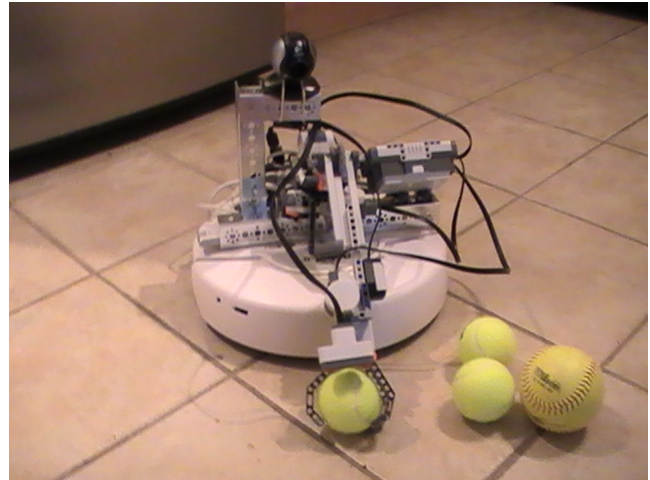


Figure 4. HU-IE combines a mobile base (3 DOF) with a robot arm (2 DOF) equipped with a gripper. This enables HU-IE to navigate indoor environments and pick up small objects.

and distance sensors on the robot, the human plays a critical role in system operation at identifying where and how to grasp objects. Without the human in the human-agent-robot team, it would be difficult to perform these operations entirely autonomously due to the lack of a detailed depth map. Figure 4 shows the complete robot system.

4. USER INTERFACE

The user views the environment and interacts with the HU-IE robot team through our configurable user interface (IAI: Intelligent Agent Interface). A rudimentary agent is embedded within the user interface to support teamwork by managing information propagation between the team members; it governs the information that gets sent to the robots and displayed on the user interface (Figure 5). Additionally it contains a macro acquisition system that allows the user to identify four key subtasks which are abstracted and used to create robot behaviors which the user can deploy during task execution. All commands to the robots are issued through an Xbox 360 gamepad, using a button to switch between robots.

In this paper, we present and evaluate the configurable section of the user interface. The basic user interface provides the user with two explicitly cooperative functions: 1) autonomous positioning of the second robot (**locate ally**), and 2) a **mirror** mode in which the second robot simultaneously executes a modified version of the commands that the user has issued to the actively controlled robot. When the user requests help to move a large object, these cooperative functions enable the robot to autonomously move to the appropriate location, cooperatively lift the object, and drive in tandem to the goal. Robots have the following built-in modes of operation:

Search: the robots wander the area searching for objects.

Help: a robot enters this mode if the human operator calls for help using the gamepad or when the teleoperated robot is near an object too large to be moved by an individual robot.

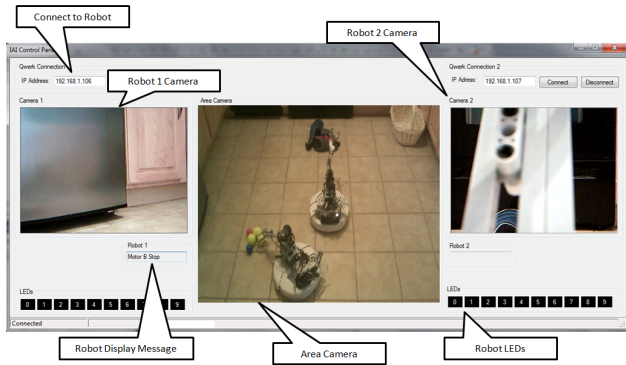


Figure 5. The user interface is designed to enable the user to seamlessly switch teleoperation between multiple robots. The IAI supports a cooperative mode where the agent supports the user's active robot by mirroring its planned actions. The user views the environment through an overhead camera and the robots' webcams.

Pickup: the robot detects an object and requests that the human teleoperate the arm.

Transport: the robot transports an object held by the gripper to the goal. Path planning is performed using A^* .

Locate Ally: the unmanaged robot autonomously moves to a position near the teleoperated robot.

Mirror: the robot mimics the commands executed by the teleoperated robot. This is used to simultaneously lift an object and transport it to the goal location.

Macro: This allows the user to designate a section of the task to be logged for analysis.

Due to the ease of development and simulation, we opted to use Microsoft Robotics Developer Studio 2008 R3 (MSRDS) to develop our robot control software. MSRDS runs on the .NET framework which allows the use of Microsoft Visual Studio 2010 to design and develop robot applications. The developer can use any of the programming languages that are supported by the .NET framework; our system was implemented in Visual C#.

The operator controls the robots using an Xbox 360 Gamepad controller (Figure 6) as follows. The trigger buttons on the Xbox 360 controller are used to toggle between the two robots and to activate the **mirror** mode in the unmanaged robot. The **A,B,X,Y** buttons are used to drive the mobile base. The right button halts the actively managed robot. The left and right analog sticks control the elevation and azimuth, respectively, of the robot arm. The claw grip is controlled by the D-pad on the Xbox 360 controller. To execute a previously acquired macro the user must press and hold the back button and then press one of the **A,B,X,Y** buttons.

5. Macro Acquisition

The most important aspect of the user interface is that it empowers the user to designate sections of the task for the robots to execute autonomously. The user might specify sections for multiple reasons: 1) they occur frequently 2) are

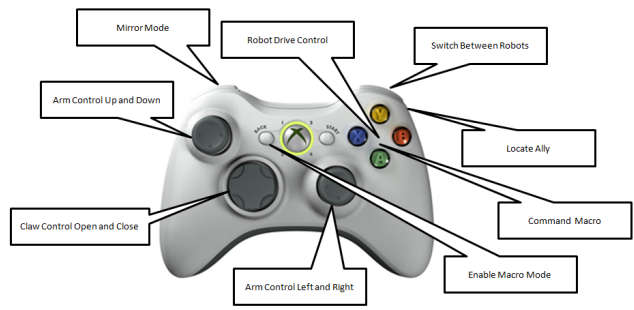


Figure 6. The physical interface to the IAI is through a Xbox 360 gamepad from which the operator can select a robot, send it explicit teleoperation commands, utilize built-in autonomous functions, and create macros.



Figure 7. Example of the execution of a recorded macro using mirror mode. Even though the macro was initially created using a single robot demonstration, it is generalized for coordinated action.



Figure 8. State representation of a recorded macro

tedious to perform 3) need to occur while the user is busy with other tasks, such as teleoperating the second robot. To make the process of macro acquisition simpler, the user initially performs a demonstration by teleoperating a single robot. However, during the task, the macro is automatically generalized to account for the execution state of the second robot. The macro can also be propagated across both robots by invoking the **Mirror** mode, without additional examples (Figure 7).

During the macro acquisition phase, the robot's state space trajectory is recorded, paying special attention to the initial and final states of the trajectory. The state includes the following features in absolute coordinates: drive start/end position, arm start/end, claw open/closed (Figure 8). Additionally, the status of all of the key sensor systems (cliff, wall, and bumper sensors) is logged. The agent also notes the current location of known movable objects in the environment and whether the user is teleoperating the second robot. The state space trajectory is then used to create an abstract workflow of the task which can be combined with the teamwork model and the path planner to generalize to new situations. To build the workflow, the state space trajectory is separated into drive, arm, and claw segments. Adjacent drive and arm segments are merged to form one long segment (Figure 9). The terminal position of the robot is retained in both absolute coordinates and also the relative position to the nearest object or robot.

After the macro acquisition phase, there is an acceptance phase during which the operator is given a chance to verify the macros' performance. When the human operator is satisfied that the macro was performed correctly then the macro is accepted and mapped to one of the Xbox 360

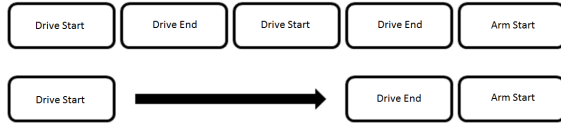


Figure 9. If the demonstration contains multiple short segments, the abstract task representation is created through merging superfluous segments.



Figure 10. Example abstract task representation for driving to the goal

A, B, X, Y buttons. During the acceptance phase, the macro is evaluated in multiple locations on the map and with the HU-IE robot arm at different angles.

If the macro representation was not accepted by the human operator, the system attempts to modify the macro using a set of taskwork rules. For instance, during the initial phase, it is assumed that the terminal positions are of key importance and that the robot should use the path planner to return to the same absolute position. In the second demonstration, the system used the recorded sensor data to identify the most salient object located near the terminal position and return the robot to that area. If an object is dropped during the acceptance phase, it is assumed that the drop is the principal reason for the macro non-acceptance and the macro is repeated using the same abstraction but with minor modifications to its positioning relative to the object using the ultrasonic sensor. For simplicity of user interaction, macro acquisition is done by teleoperating a single robot but during actual task execution many of the macros are actually executed in mirror mode, using the pre-programmed teamwork model. One of the most common macros developed by both expert and novice users was a macro for driving the robot to the goal (Figure 10).

6. EXPERIMENTS

Our experiments were designed to evaluate the performance and usability of the configurable interface on a variety of measures. The users were asked to clear objects from a cluttered household environment and transport them to a goal area using two robots guided by the configurable user interface. In total, the users interacted with the system for an hour and a half under the following conditions:

Training: Each participant was given a ten minute training session during which they were able to familiarize themselves with the teleoperation controls and the autonomous built-in modes. Subjects were encouraged to practice picking up objects and transporting them to a goal location.

Macro Acquisition: Each participant was allotted forty minutes to create four macros and map them to appropriate buttons. During the macro acquisition phase, the subjects principally interacted with a single robot. After creating each macro, they described the macro on a worksheet.

Scenario 1: For the first task, the participant had to use the two HU-IE robots to search the area and

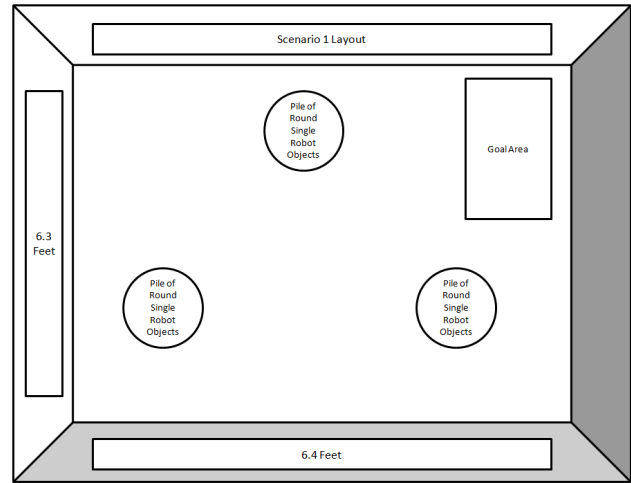


Figure 11. Scenario 1 Layout: the two robots operate in an area of $6.3' \times 6.4'$ and move small objects of different shapes from all piles to the goal area. This scenario is highly parallelizable if the users create the correct type of macros. Scenario 2 has a similar layout but with piles of large objects that require bimanual manipulation.

Table 1. Demographics and experience level of the user-study participants

Age	Gender		PC Game Skill Level		
	Male	Female	Expert	Mid	Beginner
20–28	10	10	4	6	10

transport small objects (movable by a single robot) to the appropriate goal. The environment contained three piles with five round shaped objects (shown in Figure 11).

Scenario 2: For the second task, the participants had to use the two HU-IE robots to search the area and transport awkward objects that required bimanual manipulation to the appropriate goal. This scenario contained three piles with large objects (boxes), arranged in a similar layout to Scenario 1. This was the hardest condition and was always presented last.

Detailed logs were collected of the user's entire interaction with the system, and the users were asked to complete pre and post test questionnaires. In total, twenty participants completed the user study, and Table 1 summarizes the demographics of the user group.

7. RESULTS

The main purpose was to evaluate the benefits of the configurable human-robot interface and answer the following questions:

1. what macros did users create and how were they used?
2. were there differences in the macro usage patterns in single vs. bimanual manipulation?
3. did the users prefer the macros to the build-in system functions? We also performed a post hoc within-user comparison of the configurable user interface vs. a

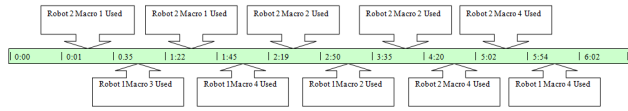


Figure 12. Timeline showing macro usage by an expert user in Scenario 1. Ten macros were used in total during the fifteen minute period. The set of macros included: 1) drive to pile, lift object, and deliver to goal 2) lift object and deliver to goal 3) lift object 4) deliver to goal.

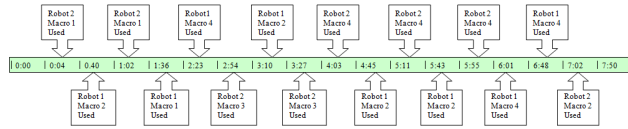


Figure 13. Timeline showing macro usage by a novice user in Scenario 1. Sixteen macros were used in total during the fifteen minute period. The set of macros included: 1) drive to pile and lift object 2) lift object and deliver to goal 3) lift object 4) deliver to goal.

non-configurable user interface designed for an earlier study [2].

The macros created by users varied in length and complexity, with a general trend that game skill correlated with shorter macros and longer periods of user teleoperation. Figure 12 shows an example of the macro usage pattern for an expert user performing Scenario 1. This can be contrasted with the pattern of novice macro usage (Figure 13) that shows a heavier reliance on macros. Overall, we found it encouraging that the configurable aspects of the user interface were more heavily used by novice users.

Pick up and delivery macros were very common, with the most frequently occurring macro being one for delivering objects to the goal. Interestingly, the execution of this macro was similar to the the built-in mode (**Transport**), but users consistently trusted their own macro and preferred to use it instead. It hints at the possibility that the process of creating their own macro made the system less opaque and more predictable to the user. From observation, we noted that the users created macros to help them with parts of the task that they struggled on during training; for instance, users who experienced more failed pickups would often focus on creating a good object pick up macro.

Many participants experienced some initial difficulty during the training period and first scenario in learning how to lift objects with the arm. By the second scenario, most users learned the knack of controlling the arm, resulting in fewer object drops. Users experienced more problems when using macros to pick up large objects that required bimanual manipulation and tightly synchronized action from both robots. This is reflected in the overall time required to complete both scenarios; unsurprisingly users require significantly more time to complete Scenario 2 than Scenario 1 (Figure 14).

During the experiments, we observed that users who used between 5-10 macro commands performed the task faster than the users who relied more on macros or were constantly teleoperating the robot. Overall macro usage for both scenarios is shown in Figure 15. In a post hoc comparison to users from a previous study who used a non-configurable version of the same user interface, macros appeared to

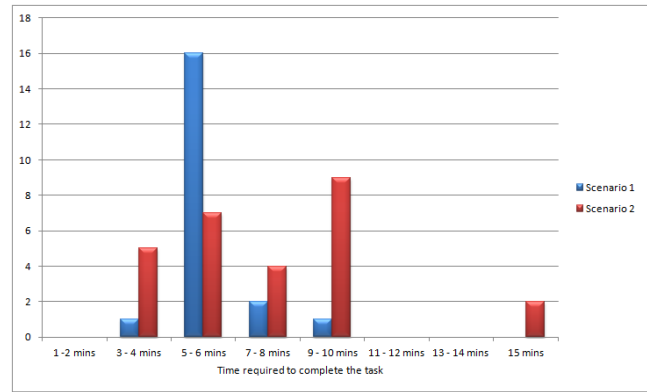


Figure 14. Histogram showing the time required the complete Scenario 1 and 2. Most users were able to complete the Scenario 1 task in one third of the allotted time. Note that there is more variance in the time required to complete the coordinated manipulation task (Scenario 2), and two users were not able to complete it in the allotted time.

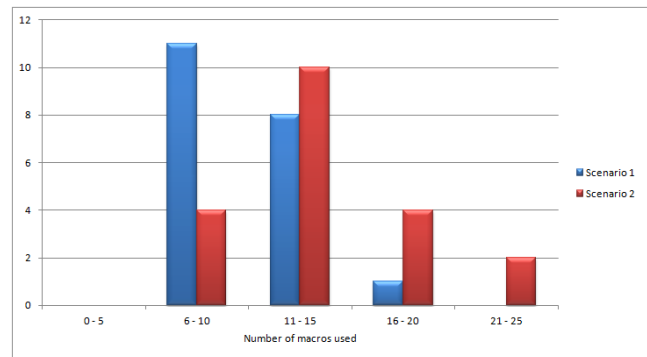


Figure 15. Histogram showing the macro usage by scenario. Bimanual manipulation (Scenario 2) was more macro intensive.

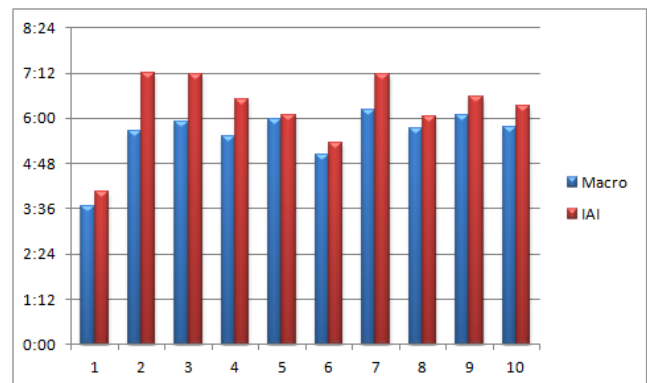


Figure 16. Post hoc analysis comparing the configurable and non-configurable user interface. The y axis shows time required to complete the scenario and the x axis the subject number. The configurable user interface appears to confer a slight time advantage.

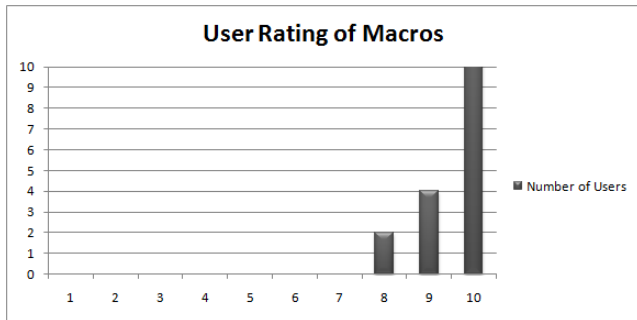


Figure 17. Histogram of user ratings of the configurable user interface on post-task questionnaires

confer a slight time advantage (Figure 16). The most significant results were in the user rankings of the interface which enthusiastically (70%) preferred the configurable user interface; overall, the interface scored high ratings in the post-questionnaire user ratings (Figure 17).

8. Related Work

Augmenting the robots with manipulation capabilities dramatically increases the number of potential usage cases for a human-agent-robot team. For instance, a number of USAR (Urban Search and Rescue) systems have been demonstrated that can map buildings and locate victims in areas of poor visibility and rough terrain [19]. Adding manipulation to the robots could enable them to move rubble, drop items, and provide rudimentary medical assistance to the victims. Effective human-robot interaction is an important part of the challenge of building urban rescue systems since full autonomy is often infeasible. The Robocup Rescue competition has recently been extended to award points for manipulation tasks.

Another Robocup competition, Robocup@Home [14] which aims to develop domestic service robots, also includes manipulation of household objects such as doors, kitchen utensils, and glasses. A set of standardized tests is utilized to evaluate the robot’s abilities and performance in a realistic home environment setting. Our scenarios are designed to simulate the problem of clearing clutter on the floor of a household environment and depositing it into a collection area. We only work with non-breakable items so the system is tolerant to failed pickups.

Srinivasa et al. [18] have developed HERB, an autonomous mobile manipulator that performs common household tasks. HERB can search for objects, navigate disorderly indoor scenes, perform vision-based object recognition, and execute grasp planning tasks in cluttered environments. Although lifting heavy objects is beyond the capabilities of several small robots due to center of gravity considerations, tasks such as clearing household clutter can benefit from the combined efforts of multiple robots. By giving every robot manipulation capabilities, small tasks such as flipping switches or opening doors can be performed in parallel.

Haptics can be a valuable tool for the human-robot interaction of manipulation tasks, allowing the operator a more immersive telepresence. Boompion and Sudsang [4] presented a distributed formation control algorithm for a robot team moving in a obstacle filled workspace. The

human operator used hand gestures to modify the group formation control parameter using a hand glove. Although haptics can reduce the overall information processing workload on the human user, we believe that they do not much to increase the human’s cognitive understanding of the taskwork and teamwork being performed by the human-agent-robot system. In our system, the act of teaching the robots appeared to imbue the users with increased confidence in the system and improved the mutual predictability between human and robot team members.

Our macro acquisition system extracts an abstract taskwork representation from a single robot demonstration which is then verified by the user during the macro evaluation phase. Dang and Allen [7] proposed a technique to decompose a demonstrated task into sequential manipulation tasks and construct a task descriptor. One goal of this research was to create a database of knowledge of how to manipulate every day objects. Our taskwork abstraction is similar, but can also be extended to the multi-robot manipulation problem.

There has been other work in learning team tasks by demonstration for urban search and rescue that relied on spatio-temporal clustering to segment robot behaviors [13]. Unlike our method, their system requires cooperative demonstrations to learn the team behaviors and no attention was paid to user acceptance aspects of the problem.

9. CONCLUSION AND FUTURE WORK

Adding a configurable user interface to a human-agent-robot team empowers the human operator to structure his/her user experience by expressing task-specific preferences for the amount of interdependence vs. autonomy between human and robot. This is consistent with the coactive design model for human-agent-robot systems. From a social learning perspective, teaching the system appears to improve the users’ understanding of the system, in addition to any actual improvements in overall task performance that result from improved cooperation between human-agent-robot team members. In this paper we demonstrate a macro acquisition system for learning autonomous robot behaviors by example; by separating taskwork (which is demonstrated by the user) and teamwork (which is modeled by the agent), we can generalize single robot macros to multi-robot macros. We plan to extend the teamwork model in the future by having the system learn user-specific teamwork preferences separately through demonstrations on a non-manipulation task.

Here, we address the problem of multi-robot manipulation in unstructured environments with limited sensors, which is a relatively new and challenging problem which utilizes the capabilities of all team members (human, agent, and robot) to achieve complicated bimanual pickups. Users expressed a significant preference for the configurable autonomy of macros over the built-in autonomous functions, and gave the user interface high overall ratings. In future work, we plan to improve the grasp planning aspect of the user interface by adding more visualization to aid the user in evaluating different possibilities for gripping the object. To do this requires better distance information about the object’s position which can be done by in a low-cost manner for small environments by augmenting the system with a Kinect sensor for the room.

10. ACKNOWLEDGMENTS

This research was supported in part by NSF award IIS-0845159.

References

- [1] P. Abbeel and A. Ng. Apprenticeship learning via inverse reinforcement learning. In *Proceedings of the International Conference on Machine Learning (ICML)*, 2004.
- [2] Anonymous, 2011.
- [3] B. D. Argall, S. Chernova, M. Veloso, and B. Browning. A Survey of Robot Learning from Demonstration. *Robotics and Autonomous Systems*, 57(5):469–483, 2009.
- [4] N. Boonpinon and A. Sudsang. Formation control for multi-robot teams using a data glove. In *RAM Robotics Automation and Mechatronics*, 2008.
- [5] C. Breazeal and A. Thomaz. Learning from human teachers with socially guided exploration. In *Proceedings of the IEEE International Conference on Robotics and Automation (ICRA)*, 2008.
- [6] J. J. Bryson. Representations underlying social learning and cultural evolution. *Interaction Studies*, 10(1):77–100, March 2009.
- [7] H. Dang and P. Allen. Robot learning of everyday object manipulations via human demonstration. In *IEEE International Conference on Intelligent Robots and Systems*, 2010.
- [8] X. Fan and J. Yen. Realistic cognitive load modeling for enhancing shared mental models in human-agent collaboration. In *Proceedings of the International Joint Conference on Autonomous Agents and Multiagent Systems*, 2007.
- [9] T. Fong. Collaborative control: A robot-centric model for vehicle teleoperation. Technical report, Robotics Institute, Carnegie Mellon, 2001.
- [10] M. Johnson, J. Bradshaw, P. Feltovich, C. Jonker, B. van Riemsdijk, and M. Sierhuis. The fundamental principle of coactive design: Interdependence must shape autonomy. In M. D. Vos, N. Fornara, J. Pitt, and G. Vouros, editors, *Coordination, Organizations, Institutions, and Norms in Agent Systems VI*, pages 172–191. Springer Berlin/Heidelberg, 2010.
- [11] B. Lewis, B. Tasthan, and G. Sukthankar. Improving multi-robot teleoperation by inferring operator distraction (extended abstract). In *Proceedings of International Conference on Autonomous Agents and Multi-agent Systems (AAMAS)*, 2010.
- [12] H. Lieberman. *Your Wish is My Command: Programming by Example*. Morgan Kaufmann, 2001.
- [13] M. Martins and Y. Demiris. Learning multirobot joint action plans from simultaneous task execution demonstrations. In *Proceedings of International Conference on Autonomous Agents and Multi-agent Systems (AAMAS)*, pages 931–938, 2010.
- [14] Robot at home. <http://www.ai.rug.nl>.
- [15] P. Scerri, L. Johnson, D. Pynadath, P. Rosenbloom, N. Schurr, M. Si, and M. Tambe. Getting robots, agents, and people to cooperate: An initial report. In *AAAI Spring Symposium on Human Interaction with Autonomous Systems in Complex Environments*, 2003.
- [16] P. Scerri, D. Pynadath, and M. Tambe. Adjustable autonomy for the real world. In *Agent Autonomy*, pages 163–190. Kluwer, 2003.
- [17] M. Sierhuis, J. M. Bradshaw, A. Acquisti, R. van Hoof, R. Jeffers, and A. Uszok. Human-agent teamwork and adjustable autonomy in practice. In *Proceedings of the International Symposium on Artificial Intelligence, Robotics and Automation in Space*, 2003.
- [18] S. Srinivasa, D. Ferguson, C. Helfrich, D. Berenson, A. Romea, R. Diankov, G. Gallagher, G. Hollinger, J. Kuffner, and J. Vandeweghe. Herb: a home exploring robotic butler. *Autonomous Robots*, 28(1):5–20, January 2010.
- [19] J. Wang, M. Lewis, and P. Scerri. Cooperating robots for search and rescue. In *Proceedings of AAMAS Workshop on Agent Technology for Disaster Management*, 2006.

Orchestration of Intelligent Ground Vehicles into a Homogeneous Swarm via the Google Cloud

Gautam Dash
University of Florida
gbdash@ufl.edu

Joshua N. Weaver
University of Florida
josh.n.weaver@ufl.edu

A. Antonio Arroyo
University of Florida
arroyo@mil.ufl.edu

Sean Wright
Yom Dom Corporation
sean.wright@yomdom.com

Eric M. Schwartz
University of Florida
ems@mil.ufl.edu

ABSTRACT

In this paper, we describe a Swarm of Robotic Ground Agents, which communicate with each other and collectively solve a myriad of tasks. The system deploys a Base Station, which communicates with all other Agents on the field. The Base Station also communicates with an Operations Center over the Internet. The Operations Center can arbitrate missions and monitor progress through a robust Cloud environment. The Base Station executes orchestration algorithms to achieve mission objectives. It distributes mission parameters to the Agents and relays gathered information back to the Operations Center through the Cloud. We elaborate on the development of our system in a cost effective and efficient manner.

Keywords

Swarm Ground Robots, Google Cloud

1. ROBOTIC PLATFORM

1.1 Initial Platform

1.1.1 Main Platform

The original platform was described in detail in our FCRAR 2011 paper [2]. For the current version of each individual robot agent, the XTM Rail 1/8-scale buggy (see Figure 2) was used [1]. The XTM Rail is a remote-controlled racing buggy with four wheel drive and a heavy-duty aluminum chassis and roll cage.

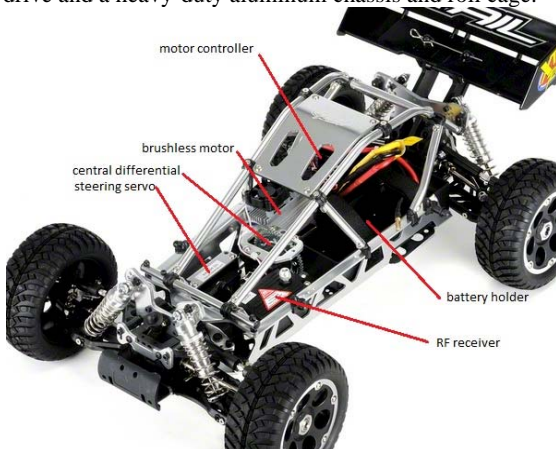


Figure 2. The XTM Rail.

The Rail uses a single brushless motor, which is cooled with a large heat sink and two cooling fans. The motor powers three differentials to allow for customization of the vehicle's movements and power output. The Rail is capable of reaching speeds up to 45 miles per hour. Each of the four off-road wheels is supported with threaded aluminum oil-filled shocks (see Figure 3), giving it enhanced stability and durability. The shocks can be adjusted depending on the payload of the vehicle.

The aluminum roll cage is attached to the chassis by six Phillips-head screws and a hinge joint, making it easy to open for access to the interior.

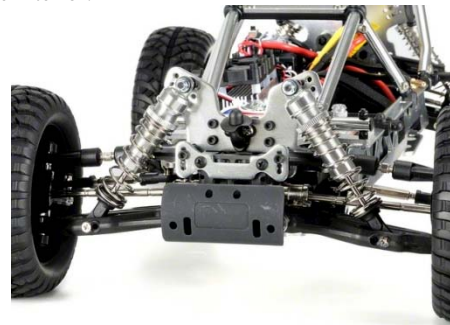


Figure 3. The front shocks.

The Rail has a radio frequency receiver to control both the brushless motor and the steering servo. Because of the way the receiver is connected, changing it to be controlled from a computer rather than an external radio signal is a trivial alteration.



Figure 4. The XTM Rail spoiler and rear shocks. The motor controller can be seen on the right.

The Rail is powered by a batter pack, and can use NiMH or LiPo packs with voltages ranging from 7.2 to 14.8V.

1.2 Updated Platform

1.2.1 Additional Equipment

Prototype 1:

The removal of the spoiler leaves four mounting points available on the top of the Rail. A computer case (see Figure 5) was constructed to hold a Linux installation to control the motor driver and steering servo in place of the RF receiver inside the vehicle.

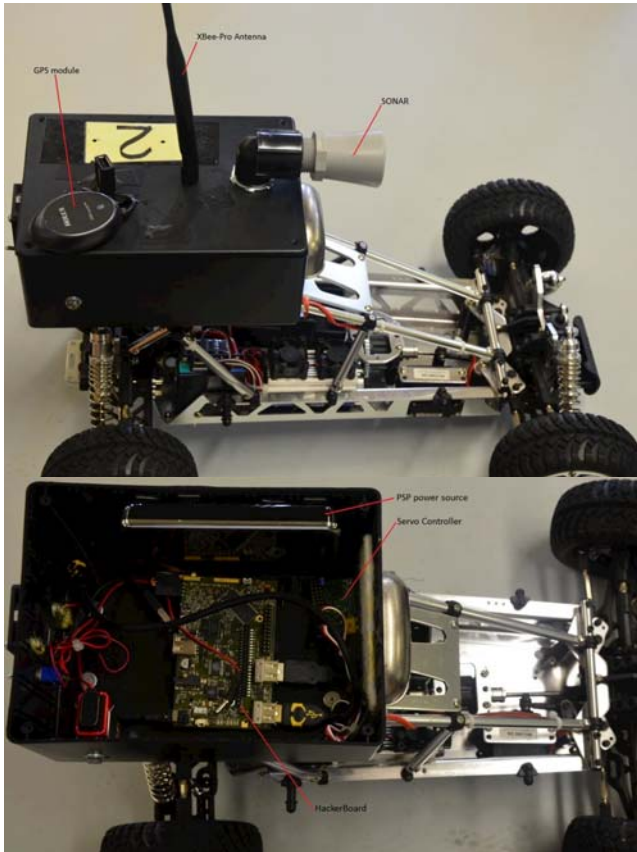


Figure 5. Prototype 1.

Inside the case is a Freescale iMX.233 processor board running at 454 MHZ called the HackerBoard [2], which has three USB ports, a standard serial port, and a micro-SD card. The case also contains a power source in the form of a PSP (PlayStation Portable) external power pack. A GPS module and a SONAR system were connected to the processor.

Prototype 2:

This version was designed to hold all the electronics inside the roll cage. The computer case has a Texas Instruments OMAP4460 mobile processor board called the PandaBoard [3]. It also has three USB ports, a standard serial port, and a SD card. A GPS module and a SONAR system were connected to the processor. An IMU was also connected to the processor for better estimation of position and orientation.

1.2.2 Operating System

Both the HackerBoard and the PandaBoard have a Linux installation for processing

1.2.3 Communications

One of the USB ports on the board is used to connect an XBee-Pro RF module for wireless communications. The XBee-Pro has a range of 24 kilometers and is used for communication between the robot agents and between each robot and the base station [4].

The PandaBoard also has on board WiFi which and be used to setup an ad hoc network for close range communication. This would enable each robot to communicate with all the others in the Swarm.

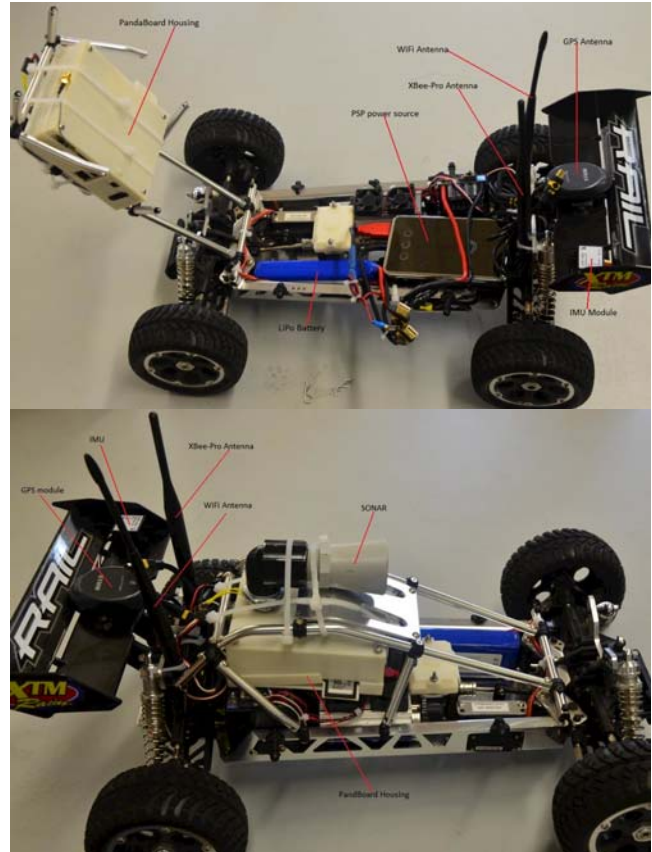


Figure 6. Prototype 2.

2. SWARM ROBOTS

2.1 Definition

The term swarm robotics is used to describe any coordinated multi-robot system made up of individuals which are relatively simple. By working together, a large number of simple robots are able to accomplish more complicated tasks. Swarm robots are often compared to similar swarms of animals, especially insects such as ants, which display similar behavior.

2.2 Uses

Swarm robots are notable in that an individual member is very inexpensive compared to a more complicated robot which is able to perform tasks on its own. Because of this, the loss of a single member of the swarm is not a setback in either operations or in cost. If a single multipurpose robot were to be lost while performing a task, it would mean a great loss in both performance and money and time investment. On the other hand, the loss of a single member of a swarm represents a minimal loss of both performance and investment. Individual swarm members can be

easily replaced at a cost which is relatively much less than a complicated single robot. In addition, because many of the members of a swarm are the same, the tasks that were being performed by the lost member can be easily done by any other member, resulting in a minimal loss of operational time.

These properties of swarm robots make them suitable for dangerous tasks. If the probability of the loss of a robot during a task is high, then swarm robots will still be able to perform the task without significant loss of time or monetary investment. Since the individual swarm members are relatively cheap and are all able to perform the same tasks as one another, it makes a single unit expendable.

3. SWARM IMPLEMENTATION

3.1 Implementation

3.1.1 Basic Implementation

The swarm is based on a mixture of placing orchestration algorithms on a base station, mission sets that come from a cloud environment and a robust command interpreter on the individual robot. The individual robots are flexible and programmable with a generic command interpreter that can handle multiple, disparate mission sets.

The mission sets are authorized from the Cloud. The Base Station receives these mission parameters and breaks them down into tasks for each Agent. It then sends them as commands to each Agent using communication packets. It monitors and processes any transmissions received from the Agents and relays analytics to the Cloud.

Each robotic agent has its own execution loop for low level control and self preservation. When it receives any commands, it executes the tasks associated with the command and sends any information processed from sensor data (like position of any obstacles, points of interest) to the Base Station.

3.1.2 Software Architecture

The swarm architecture consists of 3 platforms: Cloud, Swarm Lead, and Swarm Agent. The Cloud platform is a scalable web framework written in Java that communicates with the Swarm Lead using XML protocol. The Swarm Lead is a Java application that is executed on the base station and communicates with one or many Swarm Agents (robots) through communication packets. The Swarm Agent is a C++ application that is executed on each individual robot, which manages motors, sensors and reporting. Each of these platforms follows a Model-View-Controller (MVC) design pattern

3.1.3 Basic Execution Loop

1. A mission is created / authorized in the Cloud.
2. The Swarm Lead detects the authorized mission.
3. The Swarm Lead polls the network for available Swarm Agents.
4. Available Swarm Agents respond to the poll.
5. The Swarm Lead enlists the Swarm Agents.
6. The Swarm Lead spawns Swarm Agent threads and sends mission parameters.
7. The Swarm Agents execute the mission, providing feedback to the Swarm Lead.
8. When mission execution is complete, the Swarm Agents report their mission analytics to the Swarm Lead.
9. The Swarm Lead collects all mission analytics from Swarm Agents, and shuts down the threads.
10. The Swarm Lead reports mission analytics to the Cloud.
11. The Cloud displays mission analytics.

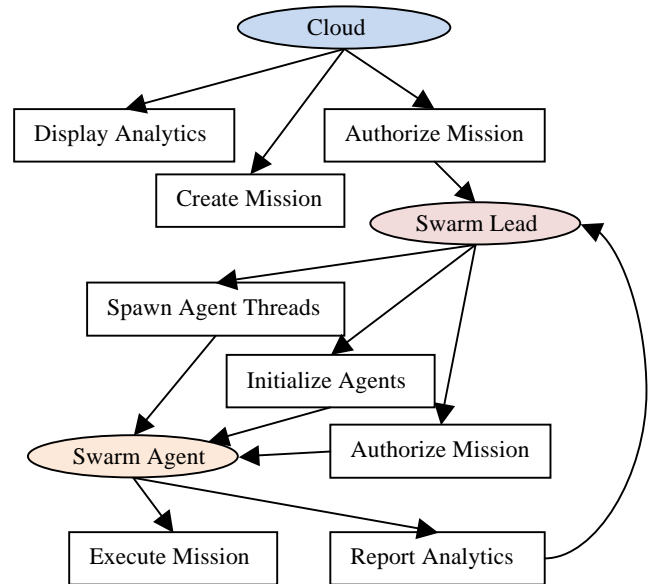


Figure 7. Process Flow in the Execution Loop.

3.1.4 Recent Changes

A few problems were identified with the first prototype of the robotic agents. Navigation based on only GPS updates resulted in the Agent overshooting its intended trajectory between GPS updates. To fix this, an Inertial Measurement Unit (IMU) was used to estimate the position and orientation between GPS readings.

The first prototype was slightly top heavy. The second prototype was designed to encase the electronics inside the roll cage.

The second prototype can also use WiFi to create an Ad-hoc network when in range for better bandwidth than serial communication over Xbee.

4. SWARM MISSIONS

4.1 Search and Rescue

Search and rescue is a basic task performed by the swarm. Like finding the proverbial needle in the haystack, Search and rescue involves finding a target in a comparatively large region.

Applications of search and rescue include searching for victims in rubble, finding a lost hiker, locating an escaped prisoner, and bomb detection. In many of these cases, the target has a beacon or some other method by which it can be detected. For some of them, such as a hiker's beacon, it may be detected at a distance. For other cases, such as searching for bombs or mines in a field, the detection may only occur at close range by way of a metal detector or chemical sensor. Regardless of the method of detection, the algorithm is similar.

The individual members of the swarm spread out and search for the target signal, whether it is an actual signal or a specific sensor reading. Once a single member is able to find the goal object, it transmits the location's coordinates to the rest of the swarm through the base station.

4.2 Area Survey

Area survey is a more specific task in which the swarm robots cover an area, identifying its makeup and creating a survey

report. The specifics of the survey can vary depending on the particular task. For example, the swarm robots might perform a geological survey of an area, dividing it into regions of sand, rock, and paved road. As the robots travel over the area, they store data about their current location and the coordinates, creating a map of the area in the process.

Other uses of the area survey task include identification of debris (FOD, or Foreign Object Debris) to determine suitability of a region for various purposes. This can find application in a variety of fields, including construction, cartography, and emergency aircraft landing site identification.

4.3 Area Setup

Similar to area survey, the area setup task prepares a surveyed area for use in a specific task. The specifics of area setup are determined by the application. For example, if a region had to be made level for construction work or some other purpose, then debris recognized in the area survey task can be disposed of during the area setup task. This can be accomplished by bringing a specialized robot to clear the debris, either by destroying it or by pushing, collecting, or otherwise relocating it to outside of the region.

The area setup task was successfully applied to a small scale setup of an emergency runway for aircraft. The swarm robots first surveyed the area to determine the most suitable region for a runway, using criteria such as flatness and lack of FOD. They then mapped out a region of the proper size for use as a runway and set up a landing zone. The robots themselves formed the landing zone boundaries and functioned as beacons to mark the region for the aircraft.

5. EXPERIMENTAL RESULTS

A Swarm of 5 robotic Agents was used to demonstrate the Area Setup at the Gainesville Raceway. The mission was created and authorized from the Command Center through the Cloud. The Base Station received the Mission parameters through the cloud and tasked individual Agents to various GPS points based on the parameters. Once the Agents were in position, the Base Station relayed the completion status to the Command Center through the Cloud. Figure 8 shows the Command Center Authorization - Arbitration page.

Mission Number	Name	Status	Action
686004	Area survey	Suspended	🟢 🟡 🔴
687007	Search and Rescue	Suspended	🟢 🟡 🔴
689003	Area Setup	Suspended	🟢 🟡 🔴
690003	Return to Base	Suspended	🟢 🟡 🔴
695001	Area Setup	Suspended	🟢 🟡 🔴
696004	Return to Base	Execute	🟢 🟡 🔴

Figure 8. Mission Authorization / Arbitration

Each Mission Number on the Mission Authorization page is a link to the Mission Details page which can be used to monitor the results of the Mission. Figure 9 shows a Mission Details page for a 'Return to Base' mission executed at the Reitz Union North

Lawn at University of Florida. The two robots used in this experiment acquired their GPS destinations marked '1' and '2' on the Google map. In the Mission shown, they were commanded to return to the base marker (blue '*').



Figure 9. Mission Details

6. FUTURE IMPROVEMENTS

The current Swarm implementation is based on a Star network topology with the Base Station as the central hub. The Agents are unaware of each other and there only exists a peer to peer communication between the Base Station and the Agents. In the next phase of development, we plan to create more of a mesh topology where in each Agent will be able to communicate with each other and the Base Station.

With a mesh topology, the focus would be to implement algorithms which ensure network connectivity between the Swarm Agents. The challenge here would be to generate trajectories or develop decentralized controllers for the non-holonomic, wheeled robots to transition from one configuration to another [5].

In the current implementation, if an Agent loses connectivity, it tries to return towards the last known location of the Base Station. In future, the Swarm could send another Agent in the last known direction of the lost Agent and the lost Agent could aim to return to the last known direction of the centroid of the Swarm, thus maintaining the efficiency of the Swarm.

7. REFERENCES

- [1] Team XTM. XTM Racing, 2011. <http://www.teamxtm.com>
- [2] <http://wiki.ladyada.net/chumbyhackerboard>
- [3] <http://omappedia.org/wiki/PandaBoard>
- [4] Emergent Collective Behavior in Autonomous Synergistic Swarm Robots; Sean Wright, Dr. A. Antonio Arroyo, Ian A. Arroyo, Joseph W. Simpkins, Brock Wright, Dr. Lavi M. Zamstein - Florida Conference on Recent Advances in Robotics, Gainesville, FL, 4-5 May 2011
- [5] Ensuring Network Connectivity for Nonholonomic Robots During Rendezvous; Z. Kan, A. P. Dani, J. M. Shea, and W. E. Dixon - IEEE Conference on Decision and Control and European Control Conference (CDC-ECC), Orlando, FL, December 12-15, 2011

Teleoperated Interface for the Staübli TX40 Robot

Arnold Cassell
University of North Florida
1 UNF Drive
Jacksonville, FL 32224
n00779662@ospreys.unf.edu

Thomas Trask
University of North Florida
1 UNF Drive
Jacksonville, FL 32224
n00017788@ospreys.unf.edu

Dang Huynh
University of North Florida
1 UNF Drive
Jacksonville, FL 32224
n00594953@ospreys.unf.edu

Daniel Cox
University of North Florida
Jacksonville, FL 32224
904-620-1845
dcox@unf.edu

ABSTRACT

User control of the robot motion is enabled through an internet-based communications system using two commercial user input devices for computers, the SpaceNavigator and the P5 Extended Reality Glove. The client software accepting the movements from the user by polling these input devices is described. The client software system allowing the user to control the data speed and motion sensitivity individually for the six motion axes has been developed. Commands are then sent via the internet to the Staübli controller, read through the communications features of the robot, and subsequently decoded and translated into motion commands using the VAL3 software of the robot. The interface also allows for control the robot's end-effector with simultaneous motion control. Algorithms developed to provide the motion control including input filtering, communications protocol, and motion calculations are described.

Keywords

Teleoperation, Staübli robot.

1. INTRODUCTION

The Staübli TX40 robotic arm is controlled by the Staübli model CS8C controller [1]. Forward and reverse kinematics are handled automatically by the robot controller and software from Staübli. The normal operational mode of the CS8C is to guide the arm through a preset or trained path, using a FIFO motion stack to queue movement commands.

While useful for predetermined tasks, this preprogrammed sequencing mode of operation is not desirable for teleoperation of the robot. A stack of queued commands awaiting execution will delay the immediate needs of a user. More importantly, the user intent is not necessarily predetermined under teleoperation conditions.

This paper describes a teleoperation interface using simple, off-the-shelf, user input devices. Section 2 of this paper describes an application to capture user commands and the introduction of the Staübli Control Panel. Section 3 describes the communication structure used to transmit the commands. Section 4 describes the architecture of the software written for the CS8C, including the working modes developed for teleoperation. Section 5 is a conclusion and discusses future work of this effort.

2. STAÜBLI CONTROL PANEL

A Graphical User Interface is created for use with the Windows Operating System in order control the stream of data being collected and sent. This developed interface, the Staübli Control Panel (SCP), is currently compatible with two off-the-shelf user input devices, the SpaceNavigator and the P5

Extended Reality Glove [3][4]. An SCP display is shown in Figure 1.

Positional data is captured from the input devices, as well as rotation about three axes. This data is displayed continuously to the user in the Motion Control section of the SCP.

The Server Control and Client Control sections of the SCP monitor the communications to and from the Staübli CS8C. Messages are displayed in the respective panels of the SCP.

The Diagnostics section of the SCP allows the operator to independently activate motion axes. The operator is also able to control the frequency that command messages are sent, as well as scaling the values of the movement commands being sent.

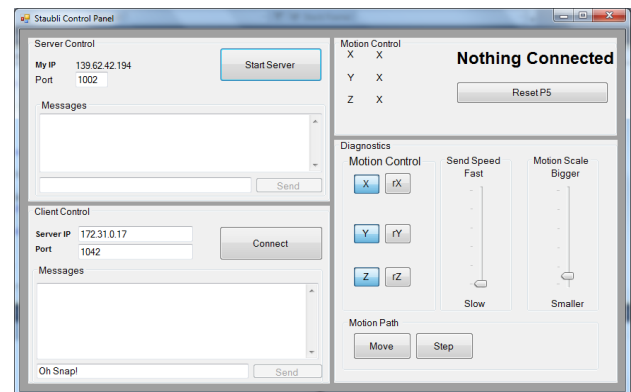


Figure 1. Staübli Control Panel (SCP)

As mentioned previously, the SCP currently accepts input from both the Essential Realities P5 extended reality glove ("P5") [2][5] and the 3DConnexion's SpaceNavigator 6 DOF mouse ("SpaceNavigator") [6]. The P5 consists of a plastic "glove" which the user slips onto their hand and a plastic "tower" that receives 6 DOF trajectory data from infrared LEDs mounted onto the aforementioned glove. Once the user ensures that the glove is on their hand securely, is powered on, and is within range of the tower, the user simply needs to move their gloved hand to have its motion mimicked by the TX40.

The SpaceNavigator is a puck-shaped motion controller that sits atop a base; it can be pressed left, right, forward, backwards, up, and down along with being able to be twisted/rotated about three axes. To operate the TX40 with this device, the user should move/rotate the SpaceNavigator in a desired direction to have the TX40 move in a similar manner. The more forceful that the SpaceNavigator is pressed, the faster the arm will move.

Both the P5 and SpaceNavigator communicate with the host PC via a standard USB connection. The SCP program flow is shown in Figure 2.

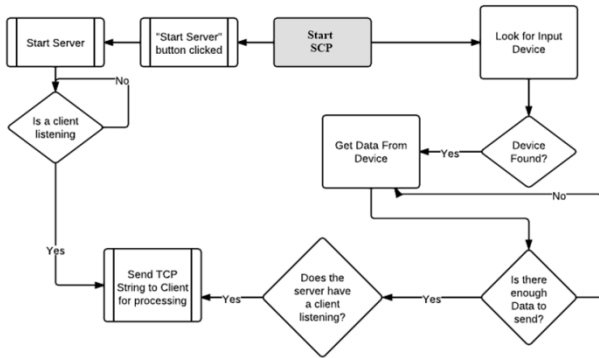


Figure 2. SCPOperational Flow Diagram

When the SCP starts, it begins looking for either the P5 or the SpaceNavigator. When found, motion commands from either connected device are collected and displayed in real time in the Motion Control section of the SCP (see Figure 1) [2] [3] [4] [7]. Once the TX40 has connected to the SCP's server, the SCP sends encoded versions of the motion commands to the CS8C via tcp/ip for processing (see Figure 2 and also the next section, Section 3) [9] [10].

The SCP's Diagnostics section can be used to meter how often and to what scale the collected motion commands are sent to the CS8 as well as enabling and disabling sending motion data for any of the 6 available axes (x, y, z, pitch, roll, yaw). The SCP also supports sending the CS8 Control commands directly, via the Client Control.

3. COMMAND STRUCTURE

Commands are broken down into two types, Control type and Motion type. Control commands are used to toggle working modes in the CS8C, or to activate the end effector. These command words are sent in plain text through tcp/ip communications.

The command to close the end effector is simply "grip," while the command to open the end effector is "release." Movement modes and also step modes may also be toggled with plain text command words. The movement and step modes are discussed in the next section.

Motion commands are sent as relative positional data, meaning each motion command is the change in position from the last motion command sent. These commands are formatted in a vector and resent in plain text, delineated by white-space. Motion along the X, Y, and Z axes are sent first, followed by respective rotations about the X, Y, and Z axes. A motion command may take on the following form, for example:

-1.3 7.12 0.01 2.1 0.0 0.101

This would be read in as "-1.3 along the X axis, +7.12 along the Y axis," and so on. The translational units are millimeters and angles are in degrees. Note these are relative motions.

Commands of all types are appended with a carriage return, which signifies the end of the message. This character is discarded before processing.

The CS8C also sends messages back to the Control Panel application, which contains the absolute position of the end effector relative to the origin of the workspace. Six values are sent in the same order and format as the motion commands shown above, for example:

210 15.1 -1.2 0.5 179.8 2.2

The X, Y, and Z values are millimeters of absolute displacement from the origin, whereas the Rx, Ry, and Rz values are measured in degrees.

4. VAL3 PROGRAM STRUCTURE

The CS8C program to accept commands from the SCP is written in the VAL3 programming language. This allows for easy creation of multiple threads or processes to handle asynchronous events simultaneously, one of the features of VAL3[11].

The main programs are the "tcpLink", which receives and reformats all incoming commands, "catch," which handles any events generated by those commands other than movement, "calculate," which processes the movement vectors, and "move" which constantly adjusts the position of the arm. The "user" program monitors the performance of the system and provides message feedback displayed on the SP1 Manual robot Control Pendant (MCP) of the TX40. The VAL3 program flow is shown in Figure 3.

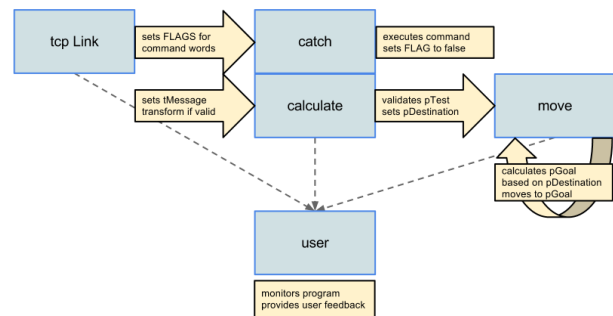


Figure 3. VAL3 Program Information Flow

In essence, the VAL3 program does the following:

- listens for relative motion command from tcp/ip
- verifies that the new command, when added to the current destination, will remain in the workspace,
- and adds that new command to the current destination.

In a separate, simultaneous thread the VAL3 program:

- compares the current position to the destination,
- and takes an incremental step towards the destination.

These are kept as separate threads so that they execute only when needed. The "move" program executes continuously during operation, and constantly checks the arm position against the destination. The others are always running, but wait for input before triggering any required calculations or actions.

4.1 Manual Control Pendant Feedback

The Staübli [1] SP1 Manual robot Control Pendant is shown in Figure 4.



Figure 4. SP1 Manual Control Pendant (MCP) [1]

By default in the design of the robot system, the MCP is the only device capable of operation the arm outside of the programming environment. It is used to load programs from within the CS8C, and control their execution. The MCP also provides maintenance and supervision functions. For this application, once the application has been started, only the screen is used to state message feedback to the user. An example is given below.

```
MOVEMENT MODE: TOOL TOGGLE
STEP MODE: BLEND TOGGLE
SYSTEM: TCP OK CALC OK CATCH OK MOVE OK
COMMAND #: 47
38.2 25.0 -7.2 0.15 0.0 0.0
GRIP RELEASE RESET EXIT
CURRENT DELTA GOAL
X: 235.1 X: 38.2 X: 241.7
Y: 117.2 Y: 25.0 Y: 141.8
Z: -15.1 Z: -7.2 Z: -31.0
Rx: 165 Rx: 0.15 Rx: 171.0
Ry: -0.2 Ry: 0.0 Ry: -0.2
Rz: 0.5 Rz: 0.0 Rz: 1.3
```

Figure 5. MCP Message Feedback Example

4.2 Movement Modes

The “calculate” function receives the transform from “tcpLink” and tests this new destination before any changes in actual motion are processed. There are three methods of applying the transform. The first is Tool mode, where rotation and motion are processed about the current position of the flange. Alternately, in Origin mode, rotation and displacement are relative to the origin of the workspace, which is located inside of the TX 40. These modes are inherent to the robot and VAL3 and adapted to teleoperation interface.

Lastly, Mixed mode allows displacement to be relative to the origin, but rotation to be measure relative to the tooling point. This last mode best matches user expectations of motion and thus is best suited to the teleoperation interface. This is a hybrid of modes inherent to the normal use of the robot and VAL3.

4.3 Workspace Boundaries

In order to limit the potential for the arm to overreach its own

limitations, an algorithm ensures the test destination (pTest) provided by the motion command exists within set boundaries. The boundaries of the workspace are shown in Figure 5.

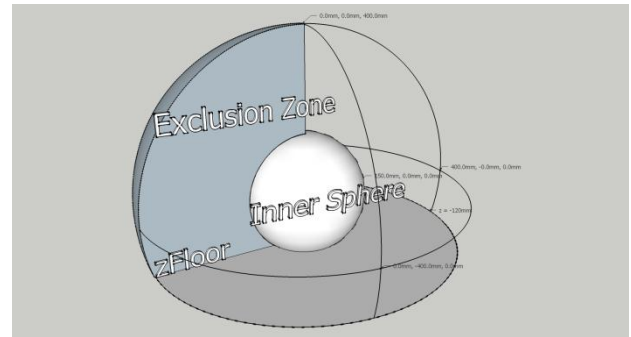


Figure 5. Workspace Boundaries

The program will not allow a destination point that is below the safe working floor (called zFloor). Neither will it allow a point that is outside the reach of the arm, or too close to the main body. Any such movement commands are instantly discarded.

4.4 Step Modes

The “move” program is responsible for bringing the arm’s current position closer to the destination provided by the “calculate” program. The standard method of controlling the arm position is asynchronous. Commands enter a stack, where they are executed sequentially, but they are not interruptible, nor are they responsive to the immediate needs of the operator.

Therefore motions in this program are segmented into smaller goals. The function of the “move” program is to compare the arm’s current position with the ultimate destination, and then calculate an intermediate small goal. That goal is sent to the arm and the “move” function waits until the arm is a certain distance away from that goal before calculating a new goal. That distance (known internally in VAL3 as the blendSize) is adjustable and is referred to as a Blend mode. When set to zero, the arm will make a full and complete stop at every goal along the way.

A graphical representation of the two Step mode and the Blend mode are illustrated in Figures 6 and 7.

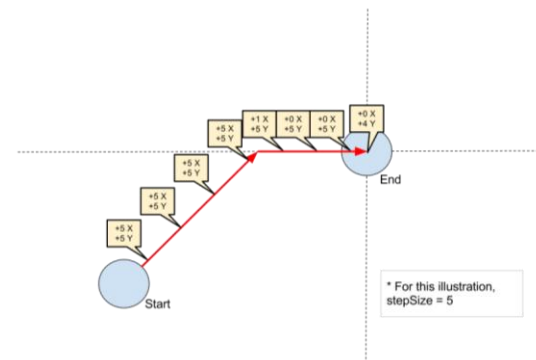


Figure 6. Step Mode

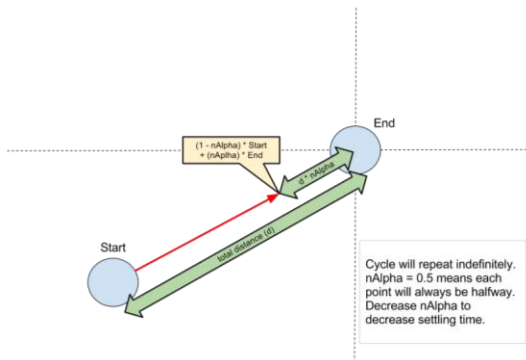


Figure 7. Blend Mode.

The parameters of these calculations are fully adjustable from within the program, and may be made available to the operator in the future. The total delay in the system can be up to nearly 350 milliseconds. Although this is beyond the expectation for real-time control, the system provides a reasonable teleoperated system using low-cost, off-the-shelf devices.

5. CONCLUSION

The TX 40 can be controlled in a relatively synchronous fashion by constantly monitoring where the arm is, and where the operator expects the arm to be, and sending intermediate adjustments at regular intervals. With this communication, simple but effective off-the-shelf devices are capable of use as teleoperated input devices. Several operating modes are made available for different tasks, and the ability to switch modes or isolate motion along a particular axis is provided and making use of VAL3 program features. A user interface includes the Staübli Control Panel (SCP) to aid the teleoperation user of the robot.

6. Future Work

Adjusting the parameters for blending to smooth some of the jitter in the arm's motion is likely to improve performance, although real-time issues with delay still exist in the current implementation. Also, motion commands which are purely rotational may present a problem due to kinematic closure as it is handled currently. As long as the destination is distant from the current position, meaning that the delay before adding another command to the stack does trigger, then this is less problematic. When that delay is not triggered, many commands fill the stack and delay responsiveness. A method for calculation of the arm motion needed to complete a move command, rather than the distance the end effector will travel, is also being developed to help overcome this issue.

Alternative input devices are being explored as well. Incorporation of additional alternative input devices, either to move the arm, or to provide insight into the operator's state, are being pursued. Several features of the arm control calculation could be modified based on user factors introduce many interesting and exciting prospects. Future releases of VAL3 and feature add-ons are also planned to be used to advance the teleoperation features of the system.

7. References

- [1] "Connectors, Robotics, and Textile machinery; Mechatronic Solutions bu Staübli," Staübli, 2012. [Online]. Available: <http://www.staubli.com>.
- [2] "Cyberworld Inc., Virtual Reality Solutions - P5 Glove - Virtual Reality Data Glove," Cyberworld Online, 2006. [Online]. Available: http://www.cwonline.com/store/view_product.asp?Product=1179.
- [3] P. Derrick Parkhurst, "Getting Data from the P5 data glove," [Online]. Available: <http://thirtysixthspan.com/P5/index.cgi>. [Accessed 2012].
- [4] "Robot Group - P5 Glove," [Online]. Available: <http://www.robotgroup.org/moin.cgi/P5Glove>.
- [5] "P5 Glove Community - Yahoo Groups," Yahoo, 2009. [Online]. Available: <http://tech.groups.yahoo.com/group/p5glove/>. [Accessed 2012].
- [6] "C# Marshalling Data with Platform Invoke," [Online]. Available: <http://msdn.microsoft.com/en-us/library/fzhhdwae.aspx>.
- [7] "3Dconnexions - Using TDxInput," 3DConnexions, 2012. [Online]. Available: <http://www.3dconnexion.com/forum/viewtopic.php?p=2213#2213>.
- [8] "Essential Realities P5 Glove," 2006. [Online]. Available: <http://www.vrealities.com/P5.html>. [Accessed 3/5/2012].
- [9] "3Dconnexions: SpaceNavigator," 3Dconnexions, 2012. [Online]. Available: <http://www.3dconnexion.com/products/spacenavigator.html>. [Accessed 2012].
- [10] "C# Tutorial - Simple Thread TCP Server," 2012. [Online]. Available: <http://www.switchonthecode.com/tutorials/csharp-tutorial-simple-threaded-tcp-server>. [Accessed 2012].
- [11] "VAL3 REFERENCE MANUAL Version 5.3," Staübli Faverges, Spartanburg, SC, 2009.

Design of 4C Mechanisms for Pick & Place Tasks

Pierre Larochelle

Florida Institute of Technology

Robotics & Spatial Systems Laboratory

pierrel@fit.edu

ABSTRACT

A novel dimensional synthesis technique for solving the mixed exact and approximate motion synthesis problem for spatial CC kinematic chains is presented. The methodology uses an analytic representation of the spatial CC dyad's rigid body constraint equation in combination with an algebraic geometry formulation of the perpendicular screw bisector to yield designs that exactly reach the prescribed pick & place locations while approximating an arbitrary number of guiding locations. The result is a dimensional synthesis technique for mixed exact and approximate motion generation that utilizes only algebraic geometry and does not require the use of any iterative optimization algorithms or a metric on spatial displacements. An example that demonstrates the synthesis technique is included.

Keywords: Spatial Mechanisms, 4C Mechanisms, CC Dyads

1. Introduction

As a product is assembled in an automated factory a common task that needs to be performed is the movement of parts or subassemblies from one location to another; this is commonly referred to as a *pick & place* task. For the assembly of a complex product the number of pick & place tasks that need to be performed could run into the thousands. Parts are picked out of bins and placed into subassemblies, subassemblies are picked up and placed into the final product, etc. One solution is to use devices with a high number of degrees of freedom such as industrial robots. Robots can perform these tasks but at penalties in costs, cycle time, and maintenance. A second solution is to use a cascading series of simple one degree of freedom devices; e.g. a series of servo motors. Creating such a manipulation pipelines takes a longer design time and is often more art than science.

Spatial robotic mechanisms offer another alternative. The synthesis algorithm presented here is part of ongoing efforts directed at realizing the capability to design two degree of freedom robotic spatial mechanisms capable of performing spatial pick & place tasks. These low degree of freedom devices are capable of producing the necessary spatial motion for accomplishing pick & place tasks. Hence, spatial robotic mechanisms provide an alternative for solving spatial assembly tasks that might otherwise require a robot or multiple single degree of freedom devices.

A well known result from screw theory [9, 1] is that moving an object from one spatial location to another doesn't

require six degrees of freedom. In fact, such motions can be accomplished with a single degree of freedom twist about a unique screw axis. However this solution is often impractical due to the location of the screw axis within the workspace and the collisions and interferences between objects that may result. Spatial robotic mechanisms are low degree of freedom machines that are a compromise between the 6 or more degree of freedom industrial robot and the series of single degree of freedom motion generators. Here, we focus on utilizing the spatial CC dyad as the motion generator for a class of spatial robotic mechanisms to achieve two desired locations exactly (i.e. pick & place) while approximating a set of guiding locations that take the workpiece from the pick location to the place location.

In a related work [12] presents the derivation of the constraint manifold for spherical RR dyads using the image space representation of displacements. This work was an extension of the ideas presented in [13]. In [11] the spatial generalization of the planar Burmester curves was presented from a geometric viewpoint. The focus of this work was the synthesis of CC and related dyads for exact motion generation through three and four locations. The synthesis of CC dyads for exact motion through 5 locations was presented in [10, 9]. In [3, 4, 5] the extension of Burmester theory, using Roth's line congruence approach [13], for the exact synthesis of 4C mechanisms for 4 locations is presented. The approximate motion synthesis of spatial 4C mechanisms for rigid body guidance was presented in [8]. Circuit and branch defects of the spatial 4C mechanism were investigated in [6] and the detection of self-collisions of the links was discussed in [2]. The methodology used here for performing the dimensional synthesis for mixed exact and approximate rigid body guidance is based upon the works of [14] and builds upon the spherical version presented in [7].

This paper proceeds as follows. First, the geometry and kinematics of the spatial CC dyad are reviewed. Next, the synthesis algorithm for solving the mixed exact and approximate motion generation problem for spatial CC dyads is presented. Finally, an example spatial robotic mechanism design is presented; the synthesis of a spatial 4C mechanism to accomplish a pick & place tasks exactly while approximating three guiding locations.

2. Synthesis Algorithm

A spatial 4C closed chain may be viewed as the combination of two CC dyads where each dyad consists of one link and

two C joints; one fixed and the other moving, see Fig. 1. The approach taken here is to synthesize two dyads separately and then join their floating links to yield a kinematic closed chain. Let the fixed axis be specified by the dual vector $\hat{\mathbf{u}}$ measured in the fixed reference frame F and let the moving axis be specified by $\hat{\mathbf{v}}$ measured in the moving frame M . Moreover, let $\hat{\mathbf{l}}$ define the moving axis $\hat{\mathbf{v}}$ in the fixed frame F so that, $\hat{\mathbf{l}} = [\hat{A}]\hat{\mathbf{v}}$ where $[\hat{A}]$ is the dual orthogonal matrix that defines M with respect to F [9]. Because the link is rigid, the dual angle between the two axes of the dyad remains constant. This geometric constraint may be expressed analytically as,

$$\hat{\mathbf{u}} \cdot \hat{\mathbf{l}} = \hat{\mathbf{u}} \cdot [\hat{A}]\hat{\mathbf{v}} = \cos \hat{\alpha}. \quad (1)$$

This constraint equation is the foundation of the synthesis algorithm presented below. In order to solve the mixed exact and approximate synthesis problem we first solve the exact synthesis problem for 3 prescribed locations.

2.1 Exact Synthesis for Three Locations

Here we select a moving axis $\hat{\mathbf{v}}$ of a CC dyad and solve for the corresponding fixed axis $\hat{\mathbf{u}}$ such that the dyad guides the moving body exactly through 3 prescribed locations [3]. To solve this synthesis problem we first work with the real or direction part of the CC constraint equations and then subsequently address the moment part. We write the real part of Eq. 1 for each of the desired locations, $[\hat{A}]_i, i = 1, 2, 3$. Next, we subtract the first equation from the remaining two to arrive at a linear system of equations,

$$[P]\mathbf{u} = \mathbf{k} \quad (2)$$

where,

$$[P] = \begin{bmatrix} (\mathbf{l}_2 - \mathbf{l}_1)^T \\ (\mathbf{l}_3 - \mathbf{l}_1)^T \\ 0 & 0 & 1 \end{bmatrix},$$

\mathbf{l}_i is the direction of the moving axis in the i^{th} location, $\mathbf{k} = [0 \ 0 \ 1]^T$, and \mathbf{u} is the desired direction of the fixed axis. Note that we must solve Eq. 2 for each moving axis direction to find its corresponding fixed axis direction. Moreover, note that since we are using 3-vectors to define the axes when in fact they are directions that only require 2 independent coordinates, the last row of $[P]$ is chosen to yield the vector \mathbf{u} that is the intersection of the fixed axis with the $z = 1$ plane. In the event that $[P]$ is rank deficient (i.e. when the fixed axis does not intersect the $z = 1$ plane) simply change the last row to any vector that does not lie in this plane (e.g. $[1 \ 0 \ 0]^T$). Next, we proceed to solve for the moment of the fixed axis.

We write the dual part of Eq. 1 for each of the desired locations, $[\hat{A}]_i, i = 1, 2, 3$ and then subtract the first equation from the remaining two to arrive at a linear system of equations,

$$[H]\mathbf{u}^0 = \mathbf{t} \quad (3)$$

where,

$$[H] = \begin{bmatrix} (\mathbf{l}_2 - \mathbf{l}_1)^T \\ (\mathbf{l}_3 - \mathbf{l}_1)^T \\ \mathbf{u}^T \end{bmatrix}, \quad \mathbf{t} = \begin{bmatrix} -(\mathbf{l}_2^0 - \mathbf{l}_1^0)^T \mathbf{u} \\ -(\mathbf{l}_3^0 - \mathbf{l}_1^0)^T \mathbf{u} \\ 0 \end{bmatrix},$$

and \mathbf{u}^0 is the desired moment of the fixed axis. Solve Eqs. 2 & 3 for each desired moving axis of a CC dyad to find

the unique corresponding fixed axis that guides the moving body exactly through the 3 prescribed locations.

2.2 Mixed Synthesis Algorithm

We now consider the synthesis of CC dyads that guide a moving body exactly through 2 pick & place locations and approximately through n guiding locations. First a desired moving axis $\hat{\mathbf{v}}$ is selected. Next, we seek a corresponding fixed axis $\hat{\mathbf{u}} = (\mathbf{u}, \mathbf{u}^0)$ for the dyad. We proceed by identifying the spherical image of the CC dyad. Duffy showed that associated with each spatial CC dyad there is a spherical image consisting of a spherical RR dyad whose link lengths are the angular twists of the CC dyad. Moreover, he proved that the spatial CC dyad and its associated spherical RR image have the exactly the same angular relationships and motions [1, 9]. Therefore the synthesis of the spatial CC dyad can be decomposed into two subproblems; (1) the angular synthesis or the synthesis of the link twist angles of the CC dyad and (2) the moment synthesis or the synthesis of the link length of the CC dyad. We address the former first.

The angular synthesis of the spatial CC dyad can be solved by performing the synthesis of its spherical RR image. The direction of the fixed axis is found by solving n 3 orientation problems to yield a set of fixed axis directions $\mathbf{u}_i, i = 1, 2, \dots, n$. The 3 orientation problems are derived from the 2 pick & place locations along with 1 of the guiding locations. Hence, there are n unique 3 orientation problems (Eq. 2) that are solved to obtain n fixed axis directions $\mathbf{u}_i, i = 1, 2, \dots, n$. It was shown in [7] that the direction of the fixed axis that will guide the moving body as desired is the normalized sum of these directions of $\mathbf{u}_i, i = 1, 2, \dots, n$,

$$\mathbf{u} = \frac{\sum \mathbf{u}_i}{\|\sum \mathbf{u}_i\|}. \quad (4)$$

We now focus on the moment synthesis problem; finding the desired moment \mathbf{u}^0 of the fixed axis $\hat{\mathbf{u}}$.

The moment synthesis of the spatial CC dyad can be solved by utilizing the geometric interpretation of Eq. 1; that $\hat{\mathbf{u}}$ must lie on the screw perpendicular bisector associated with the pick & place locations of the desired moving axis $\hat{\mathbf{v}}$. For the CC dyad to reach exactly the pick & place locations Eq. 1 must hold true in both locations. Write Eq. 1 for the pick & place locations and take the difference to yield,

$$\hat{\mathbf{u}} \cdot (\hat{\mathbf{l}}_{\text{place}} - \hat{\mathbf{l}}_{\text{pick}}) = 0. \quad (5)$$

Eq. 5 is the equation of the screw perpendicular bisector of $\hat{\mathbf{l}}_{\text{pick}}$ and $\hat{\mathbf{l}}_{\text{place}}$ [9]. The set of screws $\hat{\mathbf{u}}$ that satisfy Eq. 5 is a two parameter set whose axes intersect and are orthogonal to $\hat{\mathbf{B}}$ as shown in Fig. 2. Note that $\hat{\mathbf{N}}$ is the common normal to $\hat{\mathbf{l}}_{\text{pick}}$ and $\hat{\mathbf{l}}_{\text{place}}$, $\hat{\mathbf{V}}$ is the midpoint screw, and $\hat{\mathbf{B}} = \hat{\mathbf{N}} \times \hat{\mathbf{V}}$. Recall that the direction of $\hat{\mathbf{u}}$ has been previously found from Eq. 4. Therefore finding a point on the fixed axis $\hat{\mathbf{u}}$ is sufficient for determining the unknown moment \mathbf{u}^0 . From the properties of the screw perpendicular bisector it is known that $\hat{\mathbf{u}}$ must intersect and be orthogonal to $\hat{\mathbf{B}}$; we now determine this point of intersection and use it to determine the unknown moment $\hat{\mathbf{u}}^0$.

For the prescribed moving axis $\hat{\mathbf{v}}$ solve n 3 location problems to yield a set of fixed axes $\hat{\mathbf{u}}_i, i = 1, 2, \dots, n$. The 3 location problems are derived from the 2 pick & place locations along with 1 of the guiding locations. Hence, there

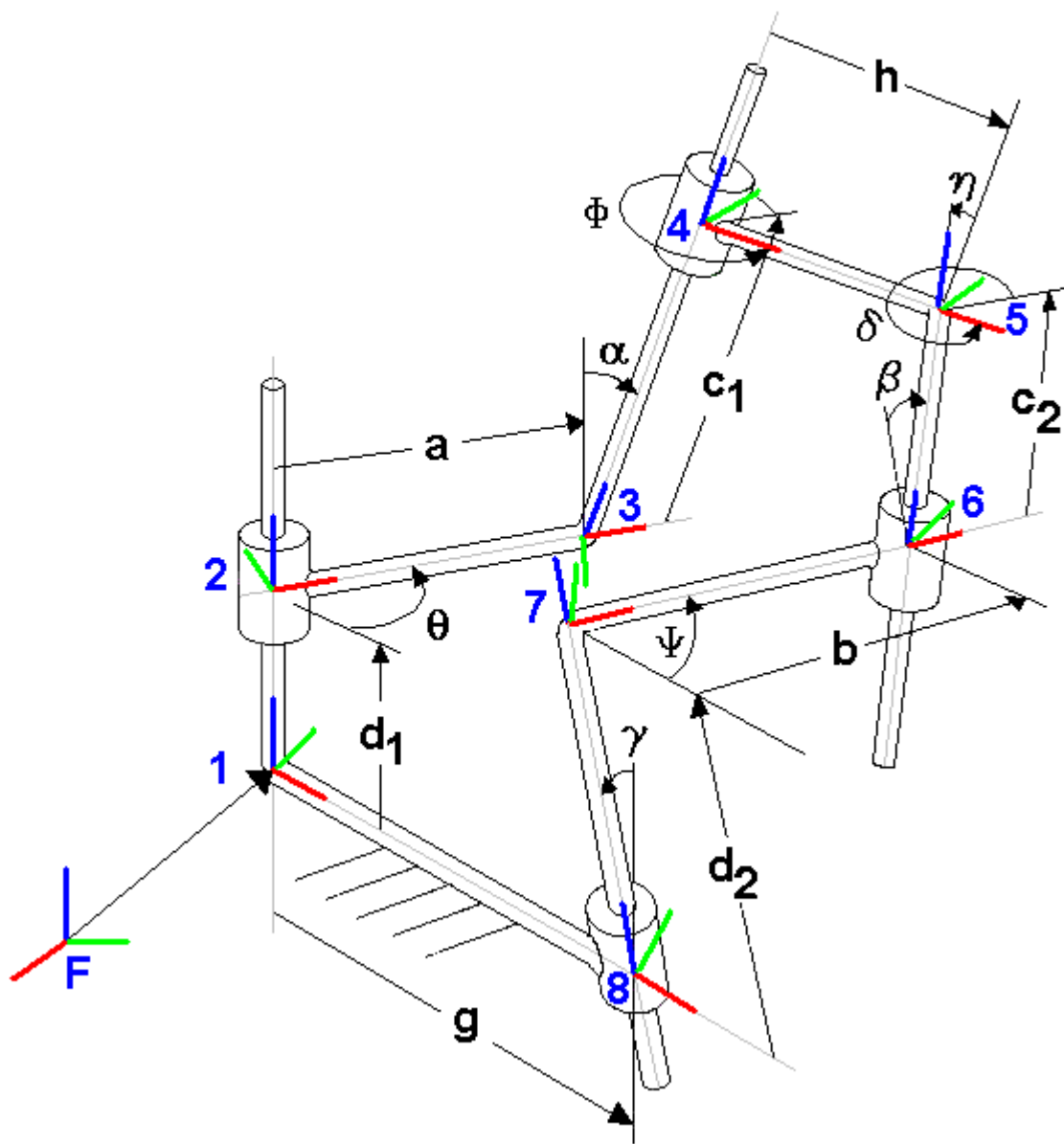


Figure 1. Spatial 4C Mechanism: Geometry & Nomenclature.

are n unique 3 location problems (Eqs. 2 & 3) that are solved to obtain n fixed axes $\hat{\mathbf{u}}_i, i = 1, 2, \dots, n$. Because each of these CC dyads guide the body exactly through the pick & place locations their fixed axes also intersect $\hat{\mathbf{B}}$. Note that if each of these n CC dyads exactly reach all of the guiding locations then their n fixed axes $\hat{\mathbf{u}}_i, i = 1, 2, \dots, n$ intersect $\hat{\mathbf{B}}$ in a unique point. In general the CC dyads will not be capable of exactly reaching the n guiding locations and the intersections of their fixed axes with $\hat{\mathbf{B}}$ will not be a unique point. Next, determine these n intersection points $\mathbf{p}_i, i = 1, 2, \dots, n$. The desired point \mathbf{p} on the fixed axis $\hat{\mathbf{u}}$ is the average of these intersection points,

$$\mathbf{p} = \frac{\sum \mathbf{p}_i}{n}. \quad (6)$$

Finally the unknown moment may be determined from $\mathbf{u}^0 = \mathbf{p} \times \mathbf{u}$. The CC dyad with prescribed moving axis $\hat{\mathbf{v}}$ and fixed axis $\hat{\mathbf{u}}$, as determined with the above algorithm, guides the moving body exactly through the pick & place locations and near the n guiding locations.

3. Example

We employ the preceding methodology and design a 4C spatial mechanism to guide a moving body exactly through two pick & place locations and near 3 guiding locations as defined in Tb. 1 where $[A] = [Rot_z(lng)][Rot_y(-lat)][Rot_x(rol)]$ and all angles are expressed in degrees. Two CC dyads are synthesized independently and then their floating links are joined to yield a 4C closed-chain mechanism.

For dyad #1 a moving axis was prescribed,

$$\hat{\mathbf{v}}_1 = \begin{bmatrix} 0.2673 \\ 0.5345 \\ -0.8018 \\ 0.0000 \\ 0.8018 \\ 0.5345 \end{bmatrix}.$$

The mixed synthesis algorithm presented above yielded,

$$\mathbf{u}_1 = \begin{bmatrix} -0.1292 \\ 0.4342 \\ 0.8915 \end{bmatrix},$$

$$\mathbf{p}_1 = \begin{bmatrix} 0.7935 \\ -0.0109 \\ -1.1956 \end{bmatrix},$$

and fixed axis,

$$\hat{\mathbf{u}}_1 = \begin{bmatrix} -0.1292 \\ 0.4342 \\ 0.8915 \\ 0.5094 \\ -0.5529 \\ 0.3431 \end{bmatrix}.$$

The resulting CC dyad's link lengths are: $a = -2.34$ and $\alpha = 121.15$ (deg).

For dyad #2 a different moving axis was chosen:

$$\hat{\mathbf{v}}_2 = \begin{bmatrix} 0.5774 \\ -0.5774 \\ 0.5774 \\ -0.5774 \\ -0.5774 \\ 0.0000 \end{bmatrix}.$$

The mixed synthesis algorithm yielded

$$\mathbf{u}_2 = \begin{bmatrix} -0.6675 \\ 0.5265 \\ 0.5265 \end{bmatrix},$$

$$\mathbf{p}_2 = \begin{bmatrix} 2.5000 \\ -1.0968 \\ 0.0968 \end{bmatrix},$$

and fixed axis,

$$\hat{\mathbf{u}}_2 = \begin{bmatrix} -0.6675 \\ 0.5265 \\ 0.5265 \\ -0.6284 \\ -1.3809 \\ 0.5842 \end{bmatrix}.$$

The resulting CC dyad's link lengths are: $b = 4.70$ and $\beta = 112.67$ (deg). When the two dyads are combined to form a spatial 4C mechanism the fixed link length is $g = 0.72$ and $\gamma = 38.34$ (deg) and the length of the coupler link is $h = 0.78$ and $\eta = 128.11$ (deg). This 4C mechanism has a non-Grashof $0 - \pi$ double-rocker spherical four-bar image [6, 1].

To verify the motion of the moving body the CC dyad constraint equations were evaluated in each of the 5 locations; the left-hand side of Eq. 1, i.e $\hat{\mathbf{u}} \cdot [A]\hat{\mathbf{v}}$, is reported in the right columns of Tb. 1. Note that the inner product between the fixed and moving lines of each CC dyad is identical in the pick & place locations thereby verifying that the moving body does in fact reach the pick & place locations exactly.

4. Conclusions

A novel dimensional synthesis technique for solving the mixed exact and approximate motion problem for spatial CC open and 4C closed kinematic chains has been presented. The methodology uses an analytic representation of the spatial CC dyad's rigid body constraint equation in combination with classical geometric motion synthesis techniques to yield designs that exactly reach two prescribed pick & place locations while approximating n guiding locations. Such tasks are common in automated assembly and production systems. An example was presented to demonstrate the synthesis procedure.

5. Acknowledgments

Collaborations with Prof. Chintien Huang of National Cheng Kung University (NCKU) of Tainan, Taiwan are sincerely acknowledged. This material is based upon work supported by the National Science Foundation (NSF) under Grant #1132629. Any opinions, findings, and conclusions or recommendations expressed in this material are those of the author(s) and do not necessarily reflect the views of the NSF.

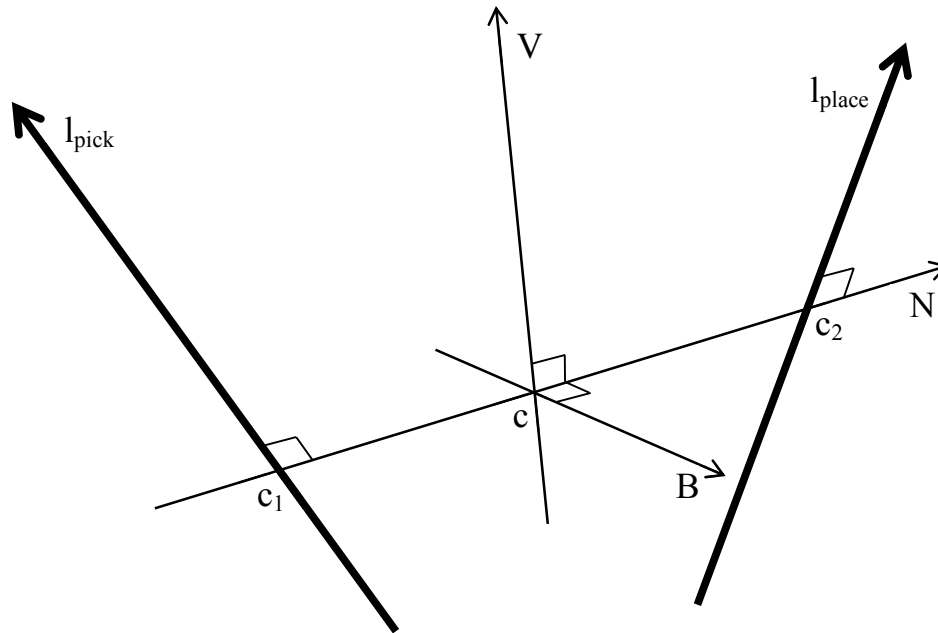


Figure 2. Spatial CC Dyad & The Screw Perpendicular Bisector.

Table 1. Five Prescribed Locations & Synthesis Results.

Longitude	Latitude	Roll	X	Y	Z	Motion Type	Dyad #1 Constraint	Dyad #2 Constraint
0.00	0.00	0.00	3	5	-1	exact	$-0.5173 + 2.0058\epsilon$	$-0.3854 - 4.3362\epsilon$
0.00	25.00	10.00	4	4	-2	approximate	$-0.8074 + 1.9092\epsilon$	$-0.1617 - 5.3040\epsilon$
20.00	45.00	20.00	2	3	-3	approximate	$-0.8760 + 2.0811\epsilon$	$-0.3371 - 4.6082\epsilon$
65.00	65.00	10.00	5	2	-4	approximate	$-0.5801 + 2.2399\epsilon$	$-0.5922 - 2.7565\epsilon$
90.00	90.00	0.00	1	1	-5	exact	$-0.5173 + 2.0058\epsilon$	$-0.3854 - 4.3362\epsilon$

References

- [1] J. Duffy. *Analysis of Mechanism and Robotic Manipulators*. Wiley and Sons, 1980.
- [2] J. Ketchel and P. Larochele. Self-collision detection in spatial closed chains. *ASME Journal of Mechanical Design*, 130, 2008.
- [3] P. Larochele. *Design of Cooperating Robots and Spatial Mechanisms*. The University of California at Irvine, PhD Dissertation, 1994.
- [4] P. Larochele. On the design of spatial 4c mechanisms for rigid-body guidance through 4 positions. In *Proc. of the ASME Design Engineering Technical Conferences*, pages 825–832. ASME, 1995.
- [5] P. Larochele. Spades: Software for synthesizing spatial 4c mechanisms. In *Proc. of the ASME Design Engineering Technical Conferences*, number MECH-5889. ASME, 1998.
- [6] P. Larochele. Circuit and branch rectification of the spatial 4c mechanism. In *Proc. of the ASME Design Engineering Technical Conferences*, number MECH-14053. ASME, 2000.
- [7] P. Larochele. Synthesis of part orienting devices for spatial assembly tasks. In *Advances in Robot Kinematics: Analysis & Design*, pages 79–87. J. Lenarčič and P. Wenger (editors), 2008.
- [8] P. Larochele and S. Dees. Approximate motion synthesis using an svd-based distance metric. In *Advances in Robot Kinematics: Theory and Applications*, pages 483–490. J. Lenarčič and F. Thomas (editors), 2002.
- [9] J. McCarthy. *Geometric Design of Linkages*. Springer-Verlag, 2011.
- [10] A. Murray and J. McCarthy. Five position synthesis of spatial cc dyads. In *Proc. of the ASME Design Engineering Technical Conferences*, volume DE-70, pages 143–152. ASME, 1994.
- [11] J. Nisbett. *A Geometric Approach to the Spatial Equivalent of Burmester Curves*. The University of Texas at Arlington, PhD Dissertation, 1998.
- [12] B. Ravani and B. Roth. Motion synthesis using kinematic mappings. *ASME Journal of Mechanisms, Transmissions, and Automation in Design*, 105:460–467, 1983.
- [13] B. Roth. The design of binary cranks with revolute, cylindrical, and prismatic joints. *Journal of Mechanisms*, 3(2):61–72, 1968.
- [14] L. Tsai and B. Roth. Design of dyads with helical, cylindrical, spherical, revolute, and prismatic joints. *Mechanism and Machine Theory*, 7(1):85–102, 1973.

Heterogeneous Collaborative Swarms of Autonomous Agents with Varying Capabilities

Joshua Weaver
University of Florida
josh.n.weaver@ufl.edu

Dr. A. Antonio Arroyo
University of Florida
arroyo@mil.ufl.edu

Gautam Dash
University of Florida
gbdash@ufl.edu

Dr. Eric M. Schwartz
University of Florida
ems@mil.ufl.edu

ABSTRACT

The overall purpose of this paper is to develop a heterogeneous collaborative swarm of entities with varying capabilities operating within different levels of information clouds where knowledge is shared either between vehicles, between vehicles and base stations, or between different clouds. The entities, or agents, may be of robot form (ground, air or sea vehicles) or human form and will have different specializations for knowledge gathering and sharing. Agents will combine to make a single group or collection of groups to form the entire Swarm as they work individually or collectively to accomplish various goals. The Swarm will consist of two levels of information clouds, one global and many local, that allow information to be collected and shared. The local cloud may be a collective cloud, where all information is stored via a single entity such as a base station while individual agents may communicate with each other, or the cloud may be disjointed where information is only sent and the relevant knowledge is received by individual agents. The local clouds will all be connected via a single global cloud where information is sent to a central database and operations center. At the global cloud level, information is used to decide on mission objectives or is passed to other clouds to be used. Research will focus on the different aspects of the two cloud types, how knowledge is shared and used, and how each agent reacts to the information given mission parameters.

Keywords

Swarm Intelligence, Heterogeneous Swarm, Sensor Fusion, Centralized and Decentralized Control

1. INTRODUCTION

It seems today there is always a new article or report on robotics. Whether it is academia, the military, or just for fun, many people seem to be excited about the potential of robots that can perform jobs and tasks on their own. Many of these same groups are not just interested in how robots may work autonomously, but how they may work together. Interest has gathered about robots that cooperatively work together, while various other groups focus on a more biologically inspired idea such as swarm cooperation.

There are many different ways to define cooperative and swarm robotic systems. In some definitions, a cooperative system

revolves around a set of autonomous agent, sometimes at little as two, which will occasionally rely on and work with each other to accomplish a task. An agent within a cooperative system is typically capable of handling a set of tasks alone; however, they often share world knowledge and arbitrate on how specific tasks should be completed. One such group is focusing on hierarchical network control for cooperative robotics with military application [1]. A swarm system is typically made of a large group of robots, a minimum of three, which work closer together at accomplishing a specified task than a cooperative system. Swarms typically share knowledge as a group memory, are very robust, and handle most tasks together; however, they are themselves usually not very capable vehicles. Most swarms cannot accomplish very difficult tasks and rely heavily on communication abilities between vehicles in the swarm [2].

Though there have been various levels of research on cooperative or swarm systems, it has mostly been held to specific control or sensor fusion schemes. Some cooperative systems focus on how behaviors are chosen between vehicles depending on the world model. Various swarm systems follow some of the same patterns, but focus heavily on how information is stored and shared or emergence. More so, it is very rare to see either of these systems that focus on how vehicles of different areas (ground, air, sea) will work together to accomplish either a swarm or cooperative system.

The goal of our research is to develop a heterogeneous collaborative swarm of entities working with different levels of information clouds in a real environment. This paper discusses the cloud structure while explaining the different types of agents that will exist within the system. Communication schemes between systems within the cloud will be detailed in terms of a centralized and disjointed scheme. Finally, a few of the expected system outcomes will be detailed.

2. Cloud Structure

As described, the cloud structure will be made of a single global cloud and many local clouds. The purpose of the various clouds is to be communication pathways between agents, cloud levels, and end users. Knowledge sharing within local clouds depends on which cloud structure is used (centralized versus disjointed). Knowledge is gathered by multiple local clouds and is then passed

to the global cloud, which is contained within the Internet. The global cloud will describe the state of the world knowledge for all clouds as well as current mission objectives and progress. Knowledge from the global cloud may be reproduced in a single Operations Center where it is viewed by end users, processed, and mission objects are modified as needed. Knowledge from the global cloud may also be passed to other local clouds within the Swarm.

Though information is typically simply sent and received between clouds and mission parameters are sent down from the global cloud, certain agents (human) are able to modify mission parameters if they are part of a given cloud. While implementation of the cloud is not specific, the current cloud structure and communication is performed within the Google Cloud using Google App Engine.

One focus for both the centralized and disjointed cloud structure will also be handling the ability for all agents to communicate with the cloud. Occasionally an agent may leave the communication range of the base station for the cloud. In this situation, a mixed form of bridging (or repeating) communication will be used between multiple vehicles to pass information from the external agent through agents within the communication range of the base station.

2.1 Centralized Local Cloud

The centralized local cloud structure resembles more closely to a Swarm behavior structure. The overall structure focuses on intercommunication within a single cloud between agents of that cloud acting as a squad and a central base station acting as a squad leader. The base station may be a more specialized and capable agent or simply a computer station. In implementation, the base station will hold multiple forms of communication (Wi-Fi, RF, 3G/4G modem, etc.) on a single tower as well as a high-speed computer at the base. The cloud is further made up of multiple agents with their own specializations. Knowledge gathered by the individual agents is directly shared with the base stations and may be indirectly shared with other agents within the cloud. Local level tasks may be decided upon by the base station given parameters of the mission and world knowledge. These tasks can then be directed at specific agents or groups of agents to complete said task. Task goals and progress are shared as knowledge.

2.2 Disjointed Local Cloud

The disjointed local cloud structure resembles a mixed topology of Swarm and Cooperative/Distributive behaviors. The cloud is made up of virtual connections between agents with no central agent processing the knowledge. A central tower is still in place for communication; however, this tower mainly represents the connection of the virtual cloud to the global cloud. Knowledge is broadcasted from each agent within the cloud. All knowledge is directly gathered into the global cloud, while only relevant knowledge is retained for agents given their own specializations. Given that no central base station is used to decide on local level tasks, each agent must be capable of arbitrating new tasks given the collected knowledge and mission parameters. A cost function and consensus/voting scheme may be used between agents to decide how tasks are completed.

3. Swarm Agents

The Swarm consists of robotic agents (ground, air or sea) or human agents. Each agent has its own purpose and specializations within their given clouds. Agents are formed

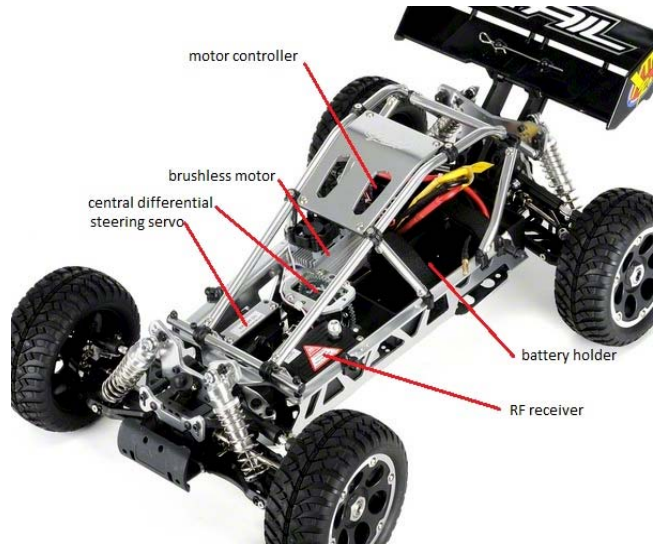


Figure 1. The XTM Rail

within local clouds as needed and desired by mission parameters and tasks given by the global cloud.

3.1 Robotic Agents

Each robotic agent will hold its own level of control and survival behaviors, only receiving any type of directional commands via trajectories or GPS waypoints from the local cloud. Robotic agents have specific abilities that allow them to accomplish certain tasks, e.g., sonar and GPS for basic object detection [4], cameras for computer vision, etc. Robotic agents have communication abilities to send and receive data directly to local clouds via Wi-Fi or RF, while only using 3G/4G in special circumstances. Commands or mission object updates will be sent to robotic agents only from base stations, while intercommunication of knowledge may be shared between other robotic agents or base stations. At times, if an agent moves out of range of a base station, communications may be established with agents that are within range to pass information to the base station. At times, human agents through the cloud may indirectly control robotic agents.

An example of one such agent used within this system as a robotic agent is the XTM Rail 1/8 scale buggy (as seen in Figure 1). This vehicle was used in previous research focused on single vehicle swarms with emergence [3] and a recent paper focused on developing those swarms with more behaviors [4].

3.2 Human Agents

Human agents share multiple purposes in the cloud swarm. In most situations, human agents have the ability to directly affect the mission objects for various clouds. Information from the global cloud is sent directly or indirectly (through base stations) to human agents. With this information, human agents may change mission objects or directly move agents to areas of interest, therefore overriding or removing them from the current mission object for a limited time. Human agents may also share information with the cloud, either through special abilities (sensors, GPS, etc.) located on the human agent or through knowledge updates/commands sent from the human agent.

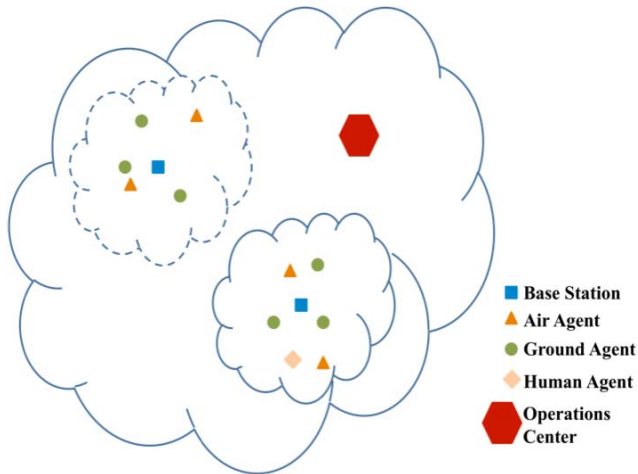


Figure 3. A Description of the complete cloud structure. The solid cloud represents the centralized local cloud, while the broken cloud represents the disjointed cloud. All clouds and components are contained within a larger global cloud.

4. Swarm Communication and Control Application

The overall structure of the cloud and the related components is shown in Figure 3. The method and pathways, as given in sample form (see Figure 2), for communication and control is described below.

4.1 Pathways within a Centralized Cloud

Data passes in multiple directions when dealing with the various clouds. At the low level, agents travel throughout their environment gathering knowledge and performing tasks given their specializations. Knowledge takes the form as objects or points of interest found in the environment, or as task updates. In a centralized cloud, as knowledge is gathered, that information is shared directly with a base station and indirectly with other agents. Knowledge is then passed from the base station of the local cloud to the global cloud within the Internet. From here, information may either be passed to other local clouds if needed, or to a central Operations Center. Knowledge at the Operations Center is used for end users to view the Swarm world knowledge. Either the computers in the Operations Center or the end users may modify mission parameters if desired. From the Operations Center, via the global cloud, mission parameters are sent to each local cloud. Given world knowledge of the local cloud and any other relevant local cloud, as well as mission parameters, a base station will arbitrate and decide tasks for individual or groups of agents.

Human agents may be contained within a local cloud and behave slightly different than robotic agents. Knowledge is gathered by a human agent either indirectly (sensors, GPS, etc.) or directly (information entered into cloud). This information follows the same pathways as robotic agents, except in terms of direct commands given by a human agent. While in a cloud, a human agent can redirect or change a mission parameter for an individual or group of robotic agents. When finished, a human agent can then release said robotic agents back to the control of the base stations.

4.2 Pathways within a Disjointed Cloud

At the low level, information travels differently in a disjointed cloud versus the centralized cloud. As agents travel throughout the environment gathering knowledge, the knowledge is broadcast between all vehicles. Knowledge is either collected by the global cloud or by agents who may use the knowledge given their specializations. Once in the global cloud, the knowledge is treated the same as was in the centralized cloud, resulting in mission commands or modifications being sent to local clouds. When a mission command is received within the disjointed virtual local cloud, each agent received the updated mission command. Using the gathered world knowledge, current mission objectives, and any updated mission objectives from the global cloud, all local agents will adjudicate on all information and come to a consensus on individual or groups of agents needed to complete a task.

In the disjointed cloud, the human agent behaves the same way as in the centralized cloud.

5. Research Focuses

Various research focuses will be followed during the development and work on the previously described system. Each is described below in detail as to what areas are currently being reviewed.

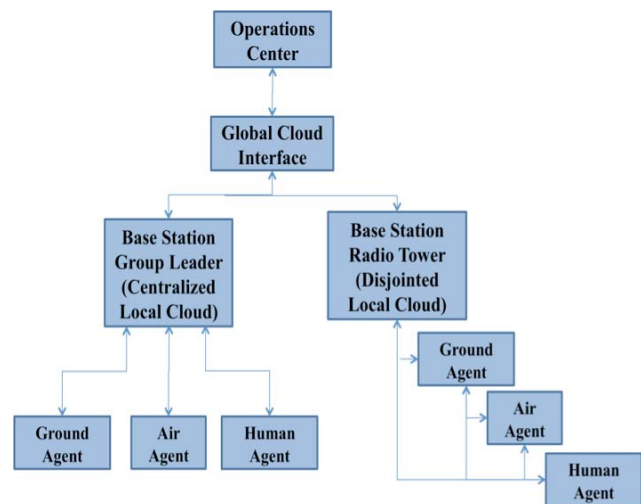


Figure 2. A sample Hierarchical design of information packets passed between local clouds, global clouds, and operations center.

5.1 Swarm Environment Map Building

With a heterogeneous group of robots with different sensing capabilities, the principal goal would be to use all the sensor data to compile a model of the environment around the cloud. We could start with a priori knowledge of the lay of the land (from a map with GPS coordinates or an overhead image) and start filling in the details as the agents explore and sense their surroundings and update the local cloud.

Based on the data available, the local cloud could then decide upon points of interest to investigate. This could be done by the base station in case of a centralized cloud or by each individual agent in a distributed cloud. Points of interest could also be identified by the Operations Center and pushed down through the Global cloud. The local cloud would then have to decide on a

configuration that would cover all these points and come up with trajectories to transition to those configurations.

5.2 Cloud Based Trajectory Planning

Trajectory planning approaches would be different for different cloud structures. The challenges faced here would be developing efficient trajectories for non-holonomic robots in an unstructured environment with hidden/unknown obstacles [5]. For a centralized cloud, the base station would use the overall desired configuration to develop trajectories for each agent and pass them on to each agent as waypoints. For a distributed cloud, each individual agent would have to generate trajectories relative to the other agents, which would result in the cloud reaching the desired configuration.

Trajectory planning could be done using optimal observer based models or heuristic based approaches. Based on constraints for each mission, different techniques could be exploited. For example, in the centralized control scheme, an exhaustive optimal observer based model could work if the base station has enough processing power to tackle the problem. However, in the distributed approach, a less computationally expensive, heuristic based approach could be called for with cost functions based on coverage and time, tailored to help the decision making process. Trajectories could even be developed and pushed down from the global cloud.

5.3 Cloud Transitioning

The agents should also be capable to transition from centralized cloud to disjointed cloud and back. Should the base station drop out, the agents should still be able to complete the mission at hand, working as a disjointed cloud. If the base station were to come back up, the disjointed cloud should be able to utilize its superior processing power and transition back to a centrally controlled cloud.

5.4 Centralized versus Decentralized Control

For a centralized cloud, the base station is aware of the agents and the desired goal. Hence it makes sense to have an orchestration algorithm running on the base station or the cloud, which computes trajectories for each agent and the agents track these trajectories. Various orchestration algorithms could focus on different cost functions, like maximizing coverage while minimizing time or optimizing effort.

The problem with centralized controllers is that the base station or the cloud has to be in constant communication with the agents. That would limit the effectiveness of the swarm. Hence a decentralized control approach would be much more effective in regions where the robots would have to move in and out of communication with the rest of the swarm but be in constant contact with the nearest neighbor [5]. However, if there is a constant chatter of control signals, the swarm would lose bandwidth required for sensor data. Hence the best control algorithms would maintain connectivity without having to exchange control signals between robots.

5.5 Multiple Levels of Arbitration

When a mission gets authorized from the global cloud, the local cloud would have to break it down into individual tasks for each robotic agent. For example, an air vehicle could be tasked to scout

out the area of interest to locate possible targets which would then be passed on to the ground vehicles. If the local cloud were a centralized cloud, the base station would be in charge of distributing the mission tasks amongst the various robots in the cloud. The base station would also monitor and collect data from various members in the local cloud and pass it on to the global cloud.

To handle orchestration at the local cloud level, the base station would need to have better computational capabilities than the other robots in the swarm. If the orchestration layer were deployed on the global cloud, then the base station would receive individual mission parameters for each robot. It would have to collect state information from each robot and relay data to the global cloud. Such a system would not require the base station to have more computational resources compared to the other robots.

However in a distributed local cloud, the mission parameters would be received by all the robots in the cloud. Based on their capabilities and the position of the targets, each robot would generate an expected completion metric of all the tasks in the mission. The robots would broadcast these metrics on to the local cloud. The swarm would then reach a consensus based on these metrics and the tasks in the mission would be assigned to the appropriate robot. The task assignments would then be relayed to the global cloud which could monitor progress and completion.

5.6 Sensor Fusion with Heterogeneous Agents

Sensor data from different robots in a heterogeneous group with different sensing capabilities could be used to build a better position and orientation estimate for each robot in the group [6]. The estimation algorithm could be centralized or decentralized. Also with different heterogeneous robots, different perspectives of the environment can be used to anticipate obstacles and determine paths of least effort while maximizing coverage.

6. Demos

Various demos are planned for 2013 that demo the abilities of the collaborative swarm and cloud. Search and Rescue will demo how air vehicles will be used to perform reconnaissance and place the information on the cloud while various ground vehicles will collect the gathered information and identify any targets of interest. Urban Exploration will show how both the air and ground vehicles work together to explore an enclosed area with tall buildings and multiple hidden corners for a human agent to transverse. Perimeter Maintenance will show how air and ground vehicles may be used to protect a specified mobile perimeter with a high level of coverage given the various levels and types of vehicles.

Vehicles will operate in the Ubuntu environment with the cloud existing within the Google App Engine. A human agent can either view or control various aspects of the cloud via an Android Tablet that gives status updates and control to the user. This information is passed from the tablet into the cloud for processing. An operations center will also be used to start and modify missions.

7. Conclusion

In this paper we described a heterogeneous collaborative swarm of entities that operate within a real environment with different levels of information clouds. We went into detail of how the various levels of the cloud structure work together as well as how the various types of agents within the swarm communicate and

Empowering Robots via Cloud Robotics: Image Processing and Decision Making BoeBots

Siavash Rastkar, Diego Quintero, Diego Bolivar, Sabri Tosunoglu

Department of Mechanical and Materials Engineering
Florida International University
10555 W Flagler St
Miami, Florida, USA

954-592-8007, 786-877-5916, 305-215-4405, 305-348-1091

srast002@fiu.edu, dquin024@fiu.edu, dboli004@fiu.edu, tosun@fiu.edu

ABSTRACT

Technological advancements have skyrocketed ever since the invention of the computer. While the computer power increases, restrictions on the hardware in use still exist. These constraints may vary from shortened battery life to limited software capabilities. Cloud computing, and subsequently cloud robotics have risen as an alternative to offer solutions to the expanding needs in robotics. Rather than limiting the robot to use only the onboard software, cloud robotics offers access to vast resources; in most cases through wireless internet to complete computational needs remotely. This paper shows an example of how a very restricted robot platform such as the BoeBot mobile platform will benefit from cloud robotics. We will use a local network and an external camera to control the robot and perform image recognition utilizing the cloud system. Furthermore, through this analysis, a conclusion of its economic implications will be reached. Economically speaking, cloud robotics minimizes the need of hardware, which traditionally translates to lower prices for products that are highly technologically advanced. Cloud robotics is additionally appealing due to the simple way in which it can be continuously improved and easily shared.

Keywords

Cloud Robotics, Mobile Platform, Image Processing, Remote Control, Wireless Connection.

1 INTRODUCTION

Development in the field of robotics is strongly linked to advances in electronics. Code written into microcontrollers is usually restricted to the capacity of their drives, making the function of the robotic parts it controls somewhat limited. In the past few years cloud computing has revolutionized the way robots and humans interact. Cloud computing functions by sharing codes and other resources over a network, with the creation of the Internet and

wireless connections, robots can now be controlled from any distance and with almost no limit on its programming size or source of the codes. This is called cloud robotics. This system takes robots to a level where, for instance, artificial intelligence can be implemented with little onboard hardware. The purpose of this paper is to show how a very simple platform such as the Parallax BoeBot can perform computationally demanding tasks by utilizing the cloud robotics concept.

1.1 Parallax BoeBot

The BoeBot robots used in this project are produced by the Parallax Company. These platforms have an aluminum structure, which holds the electronic and mechanical components. Each robot has two ultrasonic sensors in front and back, two servos and two whiskers on the left and right sides, and also two photo-resistor sensors can be mounted on it (Fig. 1). The Basic-Stamp software is used to program the platform, and the debugged code is transferred to the BoeBot by using a USB connection.

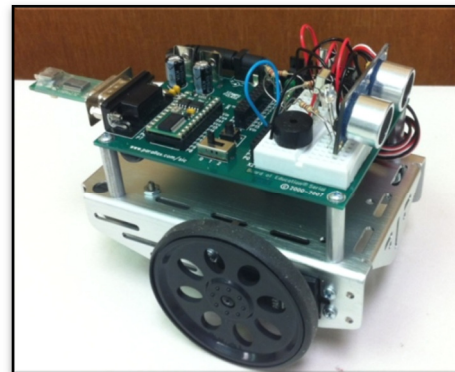


Figure 1. A BoeBot with an ultrasonic sensor in front

1.2 Cloud Robotics

In the 1960s, after the invention of computers, the need for computers as a public service was realized. It was not until 30 years later, with the creation of the Internet, that allowed launching cloud computing to what it is today (Fig. 2).

Cloud computing refers to sharing of computational resources over a network. Although seemingly a simple concept, it relieves remote devices from the burden of carrying out extensive computations and complex decision-making procedures. It also allows even the simplest devices to have access to an unlimited supply of software resources [1].

Cloud robotics (Fig. 3), on the other hand, builds on this concept and includes the possibility of sharing hardware resources in addition to software. For instance, decisions on the availability of hardware and the most suitable configuration for a given task can be identified relatively quickly. This resource is used to minimize the amount hardware embedded on devices and lower the consumption of power. It also saves time by being able to send the same codes and programs to many robots [2].

In conventional robotics, every task such as moving a foot or grasping an object is programmed and executed on the processor which is carried by robot. However, by taking advantage of cloud robotics, CPU-heavy tasks can be offloaded to remote servers and robot simply sends its workspace data to the cloud and receives executable commands from the cloud [3].

A noteworthy effort has been initiated at Stanford University. The ROS (Robotic Operating System) is an open-source platform, which is a spinoff of the Stanford AI Robot (Quigley). The ROS software is developed on a Unix-like platform although an experimental version for the Mac OS exists [4].

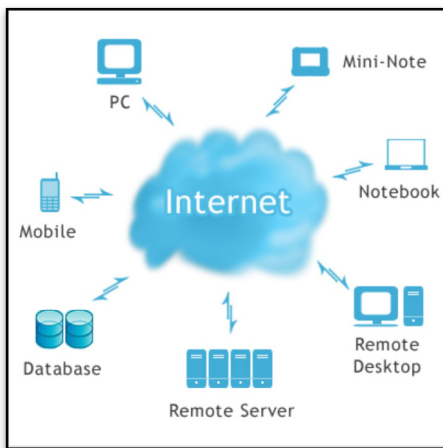


Figure 2. Cloud computing

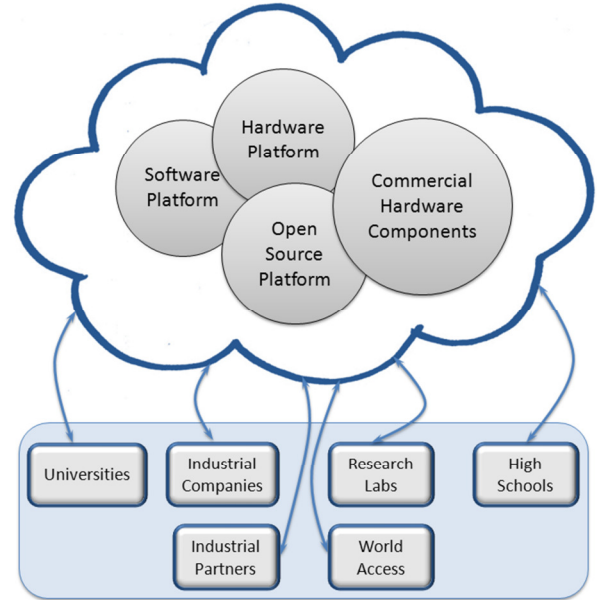


Figure 3. Cloud robotics

Another platform for cloud computing is the MS Cloud OS known as Windows Azure, which is a commercial platform, backed by Microsoft. It is originally envisioned as a general-purpose cloud-computing platform [5].

Generally we can say that the benefits of using a cloud server are:

- Sending and receiving data to and from external servers.
- Complicated processes can be handled by the server allowing the user to employ smaller and less expensive robots with less power consumption.
- Robots can be easily controlled remotely.
- Cloud server can provide a platform for robots to collaborate with each other.
- Software maintenance is significantly eased. Updating of the software and drivers can be handled easily and uniformly across all robots.

In this paper, Microsoft Windows operating system is used to perform the role of cloud server; a communication channel between the mobile platform and the server is developed with a wireless hub. A special MATLAB code developed in this work captures workspace data sent by the moving platform and makes decisions for the platform and guides it.

2 CLOUD ROBOTICS FRAMEWORK

In this research, tasks are divided into three steps: (1) Establishing a wireless connection between moving platform and the server, (2) Controlling the moving

platform through a website, and (3) performing an image processing task to show data transferring and processing capabilities of the developed cloud robotics framework. In each step, two different types of codes and programs are required, one to be run on the platform and the other to control the server.

2.1 Wireless Connection

Wireless connection between the server and the platform is established by using a wireless hub and wireless USB adapter¹. As figure 4 illustrates, the wireless hub is mounted on top of the BoeBot.

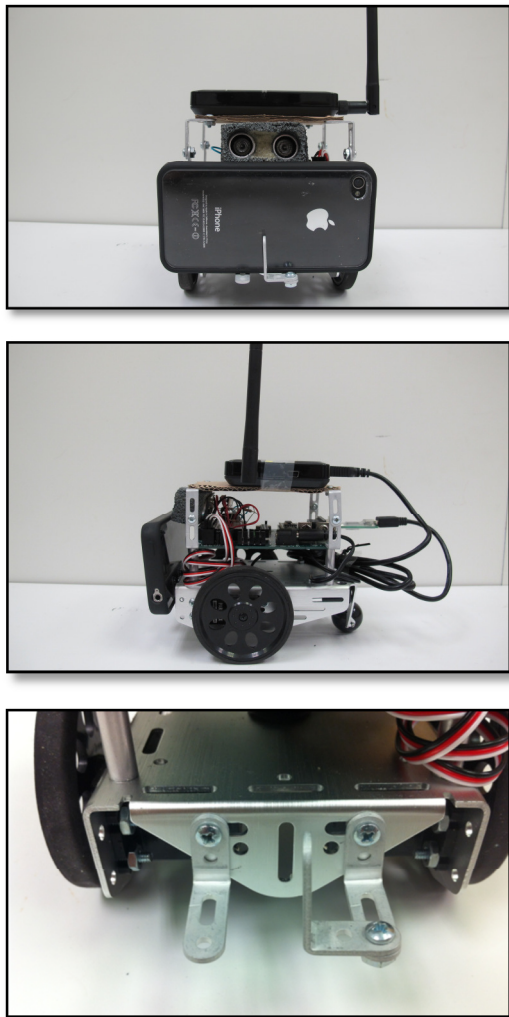


Figure 4. BoeBot with wireless hub and camera

¹IOGEAR GUWH104 USB wireless hub

Three small brackets are attached to BoeBot’s front panel to provide a holder for wireless camera. A specific ‘COM’ port is dedicated to the wireless USB adapter and this port is used both on the server and the platform codes as the communication channel. For sending videos from the mobile platform to the server, an iPhone is mounted on the platform and by using an application called “Mini Web” from the Apple Store, we were able to send the information to a local host. This is exactly same as what IP (Internet Protocol) cameras can do.

2.2 Remote Controlling the BoeBot

A Basic Stamp code is loaded to the platform which can give different motion commands (forward, backward, left, right, stop) based on the value of a string variable which will be read through the ‘COM’ port. Also, this code can send sensor readings through the same ‘COM’ port to our server. Figure 5 shows a section of the Basic Stamp code. As shown in this figure, the SEROUT command gets, and the SERIN command sends data through a serial port. This is used to communicate with the external server. In these commands, the serial pin number of the BoeBot, Baud mode rate and target variables are to be specified.

The first line sends out the readings of the ultrasonic sensor and the second line monitors the serial port for a string variable as motion command.

```
SEROUTsPin, Baud, [DEC Distance, LF]
SERINsPin, Baud, [command]
```

Figure 5. Sample basic stamp code

Five different subroutines are developed in our Basic Stamp code. Each generates appropriate commands for servo motors to provide either forward, backward, left or right turn motion or the stop command.

Generally, it can be said that the platform gathers data from its workspace and sends them to the server. Server does all the required processing on the raw data and returns a suitable motion command to BoeBot. This motion command sends a signal to the platform’s actuators to execute the desired motion.

A website is designed which contains a panel for controlling the platform (Fig. 6). In the camera address bar of this website, the user can enter the IP address of the wireless camera installed on the platform. By pressing each button, a motion command is stored in a text file in website’s root folder. The remote controlling code, written in MATLAB, continuously monitors this file and whenever a new command is sent to it, MATLAB acquires that and

by using the developed wireless communication channel, transfers it to the BoeBot.

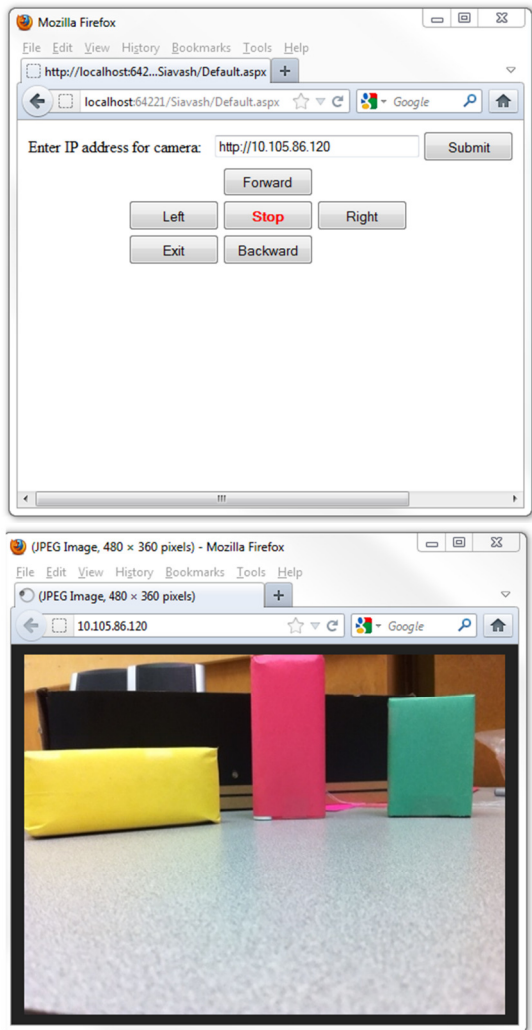


Figure 6. Webpage with control panel and live video streaming

In Figure 7 a sample MATLAB code is shown. In this code, the first line opens the developed wireless channel, the second line sends the data to this channel and the last line closes the port and shows that the communication is completed.

The website (Fig. 6) can be easily accessed wherever an internet connection is available and the user can remotely control the BoeBot's motion and also receive an online video from its workspace. Another advantage of using a website as a remote control medium is that it can be accessed via smart phones.

2.3 Image Processing

The whole idea of developing the cloud framework is to be able to accomplish tasks which require high processing power by a robot which has a simple onboard processor. Image processing can be a very good example of such a purpose; it can very well test both data transfer capabilities (by streaming online video) and processing power (by processing the online video) of our cloud system.

This section demonstrates the power of cloud robotics by accomplishing the image processing on the cloud instead of utilizing the onboard microprocessor of the mobile platform. For this purpose, the BoeBot is placed in a workspace which has objects with different colors.

```
fopen(portname);
fprintf(portname, command);
fclose(portname);
```

Figure 7. Sample MATLAB code

Then BoeBot will stream an online video from the environment and this video will be processed by MATLAB. An object with a specific color is defined as the target (here we are looking for the green object), BoeBot scans its workspace until the program on the server computer² says that it has found the target and then the same program will guide the platform toward it.

In MATLAB, images are stored as 3D matrices with three layers and each layer shows the values of red, green and blue channels of each pixel's color [6]. So, for finding a target with a specific color, a maximum and minimum threshold for each color channel is defined and when the BoeBot starts streaming video, MATLAB will capture frames of the video in predefined time intervals.

Then, colors of all of the pixels in that image are compared against the reference value. If a pixel has our desired values, its color will be changed to white; else it is going to be transformed to a black pixel. After this step, the group of white pixels are attached together to form an object, noises are filtered from the processed image and probable holes in the white region are patched.

As we mentioned earlier, performing an image processing task here is to demonstrate the extra capabilities that a simple platform like a BoeBot can gain after being

²Intel Core 2 Duo CPU T5550 @ 1.83 GHz / 2.00 GB RAM

connected to a cloud server. Hence, for simplicity it is always assumed that there is one and only one target with desired color in our workspace.

In the next step, centroid of the white object is calculated and it is compared with the center of the picture frame. If the object is in the right or left half of the picture, then a command is sent to the BoeBot to turn to the right or left, respectively. If the object is in the center of the picture, then a command is sent to the BoeBot to keep its current direction. The amount of the rotation is defined as a function of the distance between white object's centroid and the picture's center.

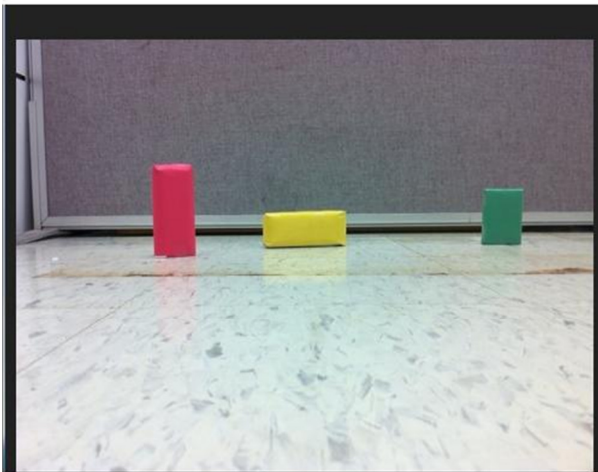


Figure 6. A frame captured from online video

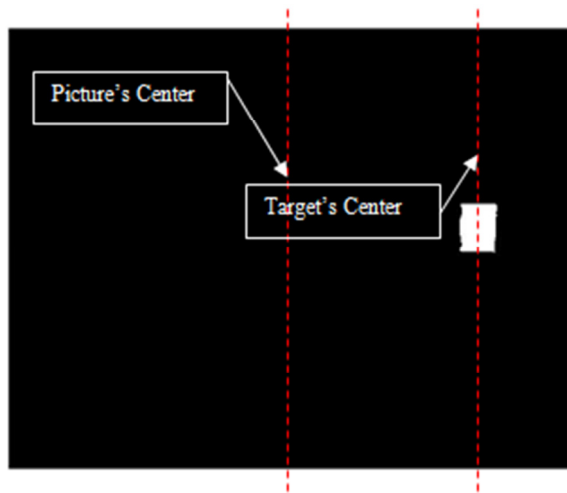


Figure 7. Processed image

After BoeBot aligns itself with the target, forward motion command is sent to it and the platform starts to move forward. While BoeBot is in motion, MATLAB grabs new picture frames from the wireless camera in predetermined

time intervals and checks BoeBot's direction. If any correction is required, a left or right rotation command is sent to the BoeBot. This process continues until the reading of front ultrasonic sensor says that the BoeBot is reached within 1 inch distance of the target. At this point, the server sends a stop command to the BoeBot to end the task.

Figure 8 shows a frame capture from the online video and Figure 9 illustrates the processed image. As shown in Figure 9, all of the green pixels are converted to white and the rest is colored black – as our stated goal was to identify the color green in this test. Based on the distance between the white object's centerline ("Target's Center" in Figure 9) and picture frame's centerline ("Picture's Center" in Figure 9), BoeBot aligns itself towards the target.

3 CONCLUSION

The idea of this research was built on the concept that includes the possibility of sharing hardware resources in addition to software. By a relatively modest modification on a simple robot like the BoeBot, we were able to connect it to a more powerful processing and analyzing resources. At the first step, a webpage was developed and a connection between this page and the platform was established which gave us the capability of controlling the platform via the web. The main advantage of this method is that it can be accessed through smart phones and also it can be easily developed for controlling more than one robot.

Furthermore, to exemplify how a very restricted robot platform such as the BoeBot will benefit from cloud robotics. A local network and an external camera were used to control the robot and perform image recognition. Economically speaking, cloud robotics minimizes the need of hardware, which traditionally translates to lower prices for products that are highly technologically advanced, as it was observed throughout the research. With very minimal expense, in relation to the robot's hardware, relatively complex tasks were successfully completed as a benefit of using cloud robotics. In other words, BoeBot was able to execute tasks that it could never attempt without the cloud robotics infrastructure. It must also be noted that cloud robotics is additionally appealing due to the simple way in which it can be improved on and easily shared.

4 REFERENCES

- [1] P. Mell, T. Grance, The NIST Definition of Cloud Computing, National Institute of Standards and Technology Special Publication 800-145, 2011.
- [2] E. Guizzo, Robots with Their Heads in the Clouds, IEEE Spectrum, March 2011.
- [3] E. Guizzo, Cloud Robotics: Connected to the Cloud Robots Get Smarter, IEEE Spectrum, January 2011.

[4] M. Quigley, E. Berger, and A. Y. Ng, STAIR: Hardware and Software Architecture, Association for the Advancement of Artificial Intelligence (AAAI), pp. 31-37, 2007.

[5] B. Gourley, Cloud Computing and Cyber Defense,

white paper to the National Security Council and Homeland Security Council, 2009.

[6] Maria Petrou, Costas Petrou, Image Processing: The Fundamentals, John Wiley and Sons, New York, May 2010.